Mooring Analysis For A TLP Supporting A 15 MW Wind Turbine

Identifying critical design parameters that influence the design life of a mooring system regarding higher-order loads for a TLP supporting a 15 MW wind turbine

Kevin Leenders

Supervisors:
Dr. O.C. Géné (TU Delft)
Dr. Ing. S. Schreier (TU Delft)
Dr. Ir. M.R. Karimi (Bluewater Energy Services)
Dr. Ir. D. Van der Heul (Bluewater Energy Services)

A thesis presented for the degree of
MSc Offshore Engineering

3ME
TU Delft
Netherlands
April 12, 2023

Abstract

With the pressing matter of climate change, the importance of renewable energy sources is increasing day by day. A large portion of this renewable energy is to be generated with the use of wind turbines, which are commonly located onshore. In recent decades, great effort has been put in the development to place these turbines offshore, because of a higher yield in energy production, as a result of higher wind speeds, greater consistency and less interference from human-made objects. These offshore turbines can be placed on floating or bottom-founded structures. Only 20% of all possible wind farm locations are suitable for the application of a bottom-founded wind turbine, due to its depth restriction. Therefore, a great deal of development is focused on the application of floating wind turbines. In essence, there exist three different types of floating structures: semi-submersible, SPAR and TLP.

In this thesis, the TLP is considered for a floating foundation because to its superior motion characteristics compared to the other structures. The TLP obtains its stability from its mooring system due to excessive buoyancy, which causes the mooring lines to be under tension. This in turn causes the TLP to have compliant and constrained DOFs. These constrained DOFs cause the eigenfrequencies of the system to be out of reach of first-order wave loading. However, from the oil & gas industry it is known that this type of structure does have a high-frequency response. This is known as springing and ringing, where this thesis is devoted solely to springing. Springing is identified as the resonance of the constrained DOFs of the TLP caused by the subsequent wave loading on the floater. Bluewater Energy Services is currently also developing and studying floating offshore wind substructures for different sites and wind turbine sizes. Therefore, they are also interested in the effects of springing and how these can be mitigated.

From initial evaluations of the motion characteristics of the case model TLP, it is seen that there are eigenfrequencies of the system that coincide with both the high frequency tail of the first-order wave load spectrum and the second-order wave load spectrum. Therefore, first- and second-order wave loads are considered. These forces are evaluated with the use of potential theory and calculated with OrcaWave and Hydrostar, which are commercially available diffraction programmes. Springing is subsequently evaluated using time-domain analysis with OrcaFlex, which is a commercially available software capable of performing time-domain analyses with aero-hydro-servo-elastic coupled models.

From initial simulations, it is seen that springing events are indeed present in the system and are mainly affecting the fatigue life of the tendons. Additionally, slack tendon events are present to a larger degree and are correlated to the whipping of the tower and RNA. This mainly causes the exceedance of structural limits. As springing is a resonance problem, only adjustments to the mooring system are considered that influence the location of the eigenfrequency. In this thesis, adjustment of the axial stiffness and inclination of the tendon are considered. Adjusting the axial stiffness did not produce the desired effect, because the range of common values in the mooring industry is rather limited to invoke any considerable change in the motion characteristics of the TLP. Furthermore, the TLP showed a large number of slack tendon events. that are correlated with the whipping of the tower and consequently caused the exceedance of structural limits. Adjusting the axial stiffness is not able to prevent these events. Adjusting the tendon angle did show promising results. For the case study, an optimum angle of 16° is found, which on average halves the tendon tensions. A reason for this is that with the introduction of a tendon angle, the TLP rotates around a certain focal point. At 16°, this focal point is located at the RNA. Thus, the TLP tends to rotate around the RNA instead of the other way around. This change of motion behaviour also prevents the occurrence of slack tendon events. Although not preventing the occurrence of springing events, the optimal tendon angle does reduce the effect and rate of occurrence of springing to a satisfactory level.

List of Acronyms

Below is the list of acronyms that are used throughout this thesis listed in alphabetical order:

CAPEX	CAPital EXpenditure	iii
CALM	Catenary Anchor Leg Mooring	iii
COG	Centre Of Gravity	6
COM	Centre Of Mass	iii
CFD	Computational Fluid Dynamics	iii
DLC	Design Load Case	28
DNV	Det Norske Veritas	iii
DOF	Degree Of Freedom	xxi
EOM	Equation Of Motion	6
FD	Frequency Domain	8
FFT	Fast Fourier Transform	iii
FLS	Fatigue Limit State	iii
FPSO	Floating Production, Storage and Offloading	iii
FSO	Floating Storage and Offloading	iii
FNV	Faltinsen, Newman & Vinje	iii
GBS	Gravity Based Structures	iii
HF	High-Frequency	iii

HFL	High-Frequency Limit	iv
IFORM	Inverse First-Order Reliability Method	123
JONSWAP	Joint North Sea Wave Project	iv
LCOE	Levelized Cost Of Energy	iv
MBL	Minimum Breaking Load	iv
MBS	Minimum Breaking Strength	iv
NREL	National Renewable Energy Laboratory	iv
NSS	Normal Sea State	iv
OPEX	OPerating EXpenditures	iv
QTF	Quadratic Transfer Function	xii
RAO	Response Amplitude Operator	43
RNA	Rotor Nacelle Assembly	10
SPAR	Sing Point Anchor Reservoir	iv
SPM	Single Point Mooring	iv
SSW	Steel Strand Wire	29
3-T	Tension, Time and Temperature	iv
TD	Time Domain	8
TLP	Tension Leg Platform	iv
ULS	Ultimate Limit State	iv
WLSQ	Weighted Least Squares Estimate	122

Nomenclature

Below is the nomenclature of indices, sets, parameters, and variables that are used throughout this thesis.

Subscripts

a	Amplitude
i, j, k	Direction indication
n	Normal component
t	Transverse component
t	Index for time step

Superscripts

(i)	Indication of order (i=1,2,3)
w	Incoming wave component
d	Diffracted wave component
r	Radiated wave component
β	Order of spectral moment

Parameters

a	Radius of vertical column [m]
A_{kj}	Added mass force coefficient in direction k due to a motion in direction j
B_{kj}	Damping force coefficient in direction k due to a motion in direction j
C_{kj}	Stiffness force coefficient in direction k due to a motion in direction j
c	Wave group velocity [m/s]
f_n	Natural/eigenfrequency [Hz]
g	Gravitational acceleration [9.81 m/s^2]

R_e	Reynolds number
N	Indication of quantity
m_β	β^{th} order spectral moment of spectral density distribution
S	Wave steepness
H_s	Significant wave height [m]
T_p	Wave peak period [s]

α_{SI}	Return period used for IFORM
β_{SI}	Safety Index used for IFORM
γ	Peakedness factor
Δt	Time discretization step
$\Delta\omega$	Wave frequency discretization step
ρ	Water density [1024 kg/m^3 for sea water at 20°C]

Variables

F	Force [N]
h	Water depth [m]
H	Wave height [m]
k	Wave number [rad/m]
$\vec{n}$	Surface outward pointing unit normal vector
p	Pressure [N/m^2]
T	Wave period [s]
T_e	Encounter wave period [s]
S_ζ	Wave spectrum [m^2/Hz]
t	Time [s]
$\vec{u}$	Water particle velocity vector [m/s]
u	Horizontal (x-direction) water particle velocity [m/s]
$\vec{x}$	Space vector

β	Heading [rad]
β_e	Encounter heading [rad]
ε	Phase [rad]
ζ	Free surface elevation [m]
λ	Wave length [m]
Φ	Fluid potential [m^2/s]

Ψ	Nonlinear potential served as a correction to the linear potential used in the derivation of the FNV model $[m^2/s]$
ω	Wave frequency [rad/s^1]

Contents

List of Figures

List of Tables

1

Introduction

With the pressing matter of climate change, where the focus is on becoming energy independent from polluting resources, several types of renewable resources have been investigated. A leading resource in this story is the use of wind energy generated by wind turbines. These wind farms are commonly located onshore. However, in recent decades, the focus has been on moving these farms offshore. This is because offshore wind farms have a higher yield compared to onshore wind farms, due to higher wind speeds, greater consistency and less interference from human-made structures.

As seen in Figure 1.1, there are in essence two types of foundation used for offshore wind turbines. These are bottom-founded and floating. Currently, mainly the application of monopiles is considered, as the structure is simple by design and relatively easy to install. However, a disadvantage for the use of monopiles is the depth restriction of approximately 40-50 metres (Cape Holland, 2022). This restriction for bottom-founded structures can be extended upto 60 metres with the use of jacket structures (Horwath et al., 2020), but is usually not considered as this is a costly alternative and therefore not profitable.

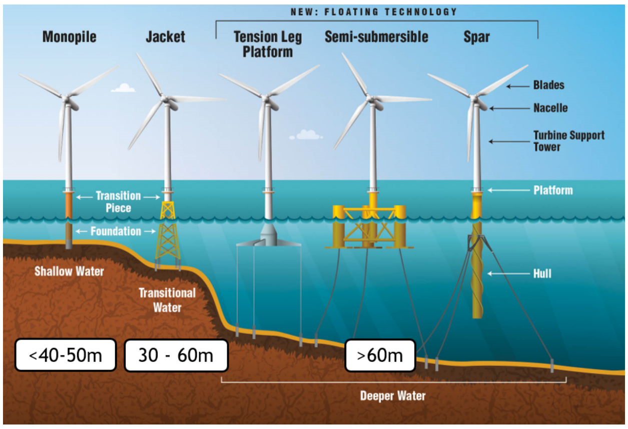

Figure 1.1: Different types of offshore wind turbine foundations.

According to WindEurope (2021), of all possible locations for the realisation of an offshore wind farm, only 20% are suitable for bottom-founded structures. This means that 80% must be considered with the use of floating structures. As seen in the figure above, there are three types of floating structures: TLP, semi-submersible, and SPAR. In this thesis, the focus is on the use of the TLP. The TLP has, compared to the other two floating foundations, superior motion characteristics, the lowest production costs, and uses the least amount of material. In theory, this results in the highest return of investment, as the yield of the turbine is the highest for minimal motions and the investment is lower due to the reduced size of the floater.

1.1 Subject

Compared to the semi-submersible and SPAR foundations, where a large portion of their stability is a result of their hydrostatic properties, the TLP gets its stability from its mooring system. This is achieved by a surplus of buoyancy, which causes the tendons of the system to be under tension. As a result, the TLP reacts as a compliant structure for surge, sway, and yaw DOFs, while heave, roll, and pitch acts as the constrained DOFs of the TLP. This constraint causes the eigenfrequencies of the system to be outside the reach of first-order wave forcing (first-order meaning wave forces that scale linearly with incoming wave frequencies), consequently having a low response, which is favourable for the efficiency of a wind turbine.

However, as often mentioned in the literature for oil & gas related structures (e.g. Faltinsen (1990); Davies et al. (1994); Natvig (1994), etc.), a significant response of these high-frequency eigenmodes (modes with response frequencies above the wave frequency spectrum encountered) is often observed. These are named as springing and ringing. Springing is identified as a periodic steady-state response occurring in mild & severe sea states (Davies et al., 1994), while ringing is a strong transient response triggered by the passage of a high and steep wave front (Jefferys & Rainey, 1994). Their difference is exemplified in Figure 1.2. Due to the periodic nature of springing, the event is mentioned to have a large influence on the fatigue of the mooring system, while ringing, which occurs less frequently, is more important for the ultimate loading conditions of the mooring system.

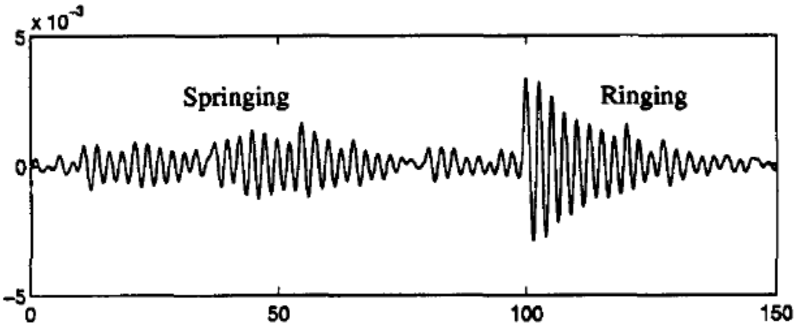

Figure 1.2: Characteristic time history course for the events of springing and ringing.

From articles such as Roald et al. (2014) and Bachynski & Moan (2014), it can be determined that these responses are also important for wind industry related TLPs. In these articles, the high-frequency eigenmodes of the TLP are in the range of 0.3-0.5 Hz or even higher have been recorded, which is outside the range of first-order wave forcing (e.g. 0.14-0.20 Hz for the North-Sea (Lavidas & Polinder, 2019)). Therefore, a higher-order wave loading model might be needed to correctly describe these high-frequency responses, as these do have frequency components that coincide with the eigenfrequencies of the system. Due to the location of the eigenfrequencies, it is often mentioned that springing is the result of high-frequency first-order loading or second-order sum-frequency loading (Roald et al., 2014; Journée & Massie, 2008), while ringing is related to third- or higher-order loading (Faltinsen et al., 1995; Bachynski & Moan, 2014).

Bluewater Energy Services, further on in this document referred to as Bluewater, is currently also in the design process for a floating wind turbine supported by a TLP, for which its concept is illustrated in Figure 1.3. They have requested to investigate the effects of these high-frequency responses on the mooring lines of their concept TLP, and to determine whether adjustments can be made to minimise the effect of these responses.

Figure 1.3: Wind turbine based on a TLP floater (Bluewater, 2022)

To ensure a viable project time, the scope is limited to the adjustments of the mooring system of the TLP, as these previously described high-frequency responses affect mainly the tendons of the floater. Therefore, adjustments to the geometry of the TLP floater or tower are not considered. In addition, no mooring-soil interaction is considered. Therefore, the connection point is assumed to be rigid. It is not believed that this will have a large influence on the tension signals of the tendons or the motion characteristics of the floater, as the anchor points should remain in place during the operational life of the structure. Furthermore, as mentioned in the introduction, the use of this structure is expected to be in intermediate to deep waters. Therefore, shallow-water conditions are not considered. Last but not least, springing and ringing are considered important high-frequency responses of the TLP system. However, only the effects of springing are investigated to ensure a viable time planning. The evaluation of the ringing response is only considered in the literature to indicate the difference between the two responses.

1.2 Company profile

Bluewater, founded in 1978, is an expert in the design, manufacture, supply, and installation of FPSOs and FSOs. In their company life time, they have designed ten, of which five are still in their operational fleet up to this day. The company is also known for their development of SPMs, CALM buoys, turret mooring and towers with multiple risers. The company also provides operational, logistic management and support for FPSOs and FSOs. Since 2006, the company is also heavily involved in the development of renewable energy solutions. As mentioned above, they are currently looking into floating platforms for the wind turbine. But this is not the only subject they are tackling. They are also interested in floating tidal energy converters, e-buoys, and floating solar.

It can be said that Bluewater is a well-known and established company within the offshore oil & gas industry. In addition to its efforts in the renewable energy section, the company will maintain its current market position, as stated in its mission and vision, and will play a vital role in the energy transition (Bluewater, 2022).

1.3 Thesis Research Question

To answer the request given by Bluewater, to investigate the effects of higher-order high-frequency loading on the tendon lines of a TLP supporting a wind turbine, the question is summarised into the following research question:

What aspects of a mooring system for a TLP supporting a wind turbine have to be considered during the preliminary design to minimise the influence of springing on the structural integrity of the mooring tendons?

1.3.1 Sub Questions

To help answer the main research question mentioned above, four additional sub questions are formulated. These will focus mainly on how these high-frequency responses can be recognised and modelled with commercially available tools, and will go into investigating viable mitigating solutions within the current mooring design.

- What is the cause for springing to occur in the motion of a TLP?
- To what extent is it possible to model springing of a TLP with the use of available software?
- Which properties of the mooring design have an influence on the response of a TLP due to springing types of loading?
- To what extent can optimal ranges for mooring design properties be identified to minimise the occurrence and effect of springing?

This first sub-question will give an answer on why this high-frequency response occurs for the TLP. A better understanding of the root cause will give clues as to the extent to which the mooring system can prevent these types of response. The second question will give an answer to whether it is possible to model this high-frequency response and which software is capable of computing it. This will help to formulate the method statement. The third question will focus on finding properties that will influence this high-frequency response. Identifying these properties will be important in the investigation, as they will be adjusted in order to minimise the magnitude of these types of response. The last question will tackle the minimisation part of the research question, where an optimum value for a particular adjustment will be searched, to minimise the effects of the high frequency response on the TLP.

1.3.2 Goal

As a means of working towards a target, the intent of the investigation is summarised into two goals. The first goal of this research is to give an optimal range for particular properties of the mooring system in the preliminary design phase, with the use of available modelling software, in order to minimise the influence of higher-order high-frequency loading and, subsequently, increasing the service life of the floating wind turbine. The second goal of this research is to clarify the subject of springing and ringing, to gather knowledge about these responses from the oil & gas industry and to see what connection they have in the offshore floating wind industry.

1.4 Reading guide

Here below, a description is given on the structure of the thesis to guide the reader.

- **Chapter 1**: An introduction to the subject of this thesis is given. The need for this topic is explained and an approach is given for solving the problem.
- **Chapter 2**: A literature study is conducted on topics related to the evaluation of springing. It starts with an evaluation of motion characteristics, a description is given for both springing and ringing and details are given about the hydrodynamic loading.
- **Chapter 3**: The method statement is described for the analysis of the problem. Key parameters for evaluation purposes and mooring adjustables are selected. Subsequently, the means of evaluating the results are outlined. In addition, the case model TLP is presented and details of its motion characteristics are described.
- **Chapter 4** In this chapter, the results are processed and evaluated. First, the results for the diffraction analyses are presented. After that, the results of the time-domain analyses are evaluated, where the effectiveness of a particular mooring adjustments stands central.
- **Chapter 5** A small reflection is given on the results and answers are formulated for the research questions mentioned in the introduction.
- **Chapter 6**: Recommendations are given for future research topics. These are mostly topics related to ideas and objectives that are not completed during the course of this thesis.

2

Loading & Responses

2.1 Motions

As the occurrence of high-frequency responses is related to the system eigenmodes, the theory regarding characteristic motion is considered. It starts with the evaluation of the Equation Of Motion (EOM) in Chapter 2.1.1 and how these result in the evaluation of eigenfrequencies. Furthermore, the stiffness of the mooring system is an important feature of a TLP, as its stability depends on it. Therefore, a method to estimate the stiffness of a typical TLP is presented in Chapter 2.1.2.

2.1.1 Equation of motion

For the description of motions for a floating structure, the use is often made of a coordinate system. A representation of such a coordinate system is shown in Figure 2.1. For the location of the origin of the coordinate system, the coordinates x and y related to the Centre Of Gravity (COG) of the floating structure are taken, while the z coordinate is usually taken at the mean free surface level.

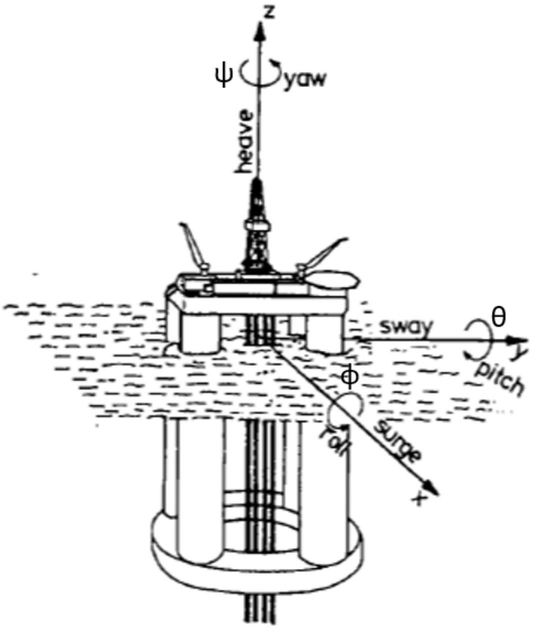

Figure 2.1: Coordinate system of floating structure (Faltinsen, 1990)

	Symbol	Name
1	x	Surge
2	y	Sway
3	z	Heave
4	ϕ	Roll
5	θ	Pitch
6	ψ	Yaw

Table 2.1: DOFs within the coordinate system.

The system thus consists of a collection of 6 DOFs (see Table 2.1). The eventual EOM is derived with the use of Newton's second law, where the acceleration of a body is defined by the imposed force divided by the mass of the object in a certain DOF. Translating the 6 DOFs into a single container vector $\vec{x}$ results in the following description of the EOM.

$$\ddot{\vec{x}} = \sum_{j=1}^{6} \vec{F}_j / m, \tag{2.1.1}$$

where $\ddot{\vec{x}}$ indicates the second time derivative of the vector assigned previously. For floating structures, the force on the right-hand side of the equation consists of four separate terms. These are as follows:

$$\vec{F}_j = \vec{F}_j^r + \vec{F}_j^s + \vec{F}_j^w + \vec{F}_j^d. \tag{2.1.2}$$

Here, $\vec{F}^r$ are the forces caused by the motions of the floating structure, $\vec{F}^s$ are the static forces acting on the body of the ship, $\vec{F}^w$ are the forces on the floating structure caused by the incoming wave (also known as the Froude-Krilov forces) and $\vec{F}^d$ are the forces caused by the diffraction of the incoming waves. The evaluation of $\vec{F}^w$ and $\vec{F}^d$ are tackled in Chapter 2.2. $\vec{F}^s$ and $\vec{F}^r$ are forces caused by the static and dynamic position of the floating structure. Thus, these depend on the motion vector $\vec{x}$. Assuming that the motion is linearly related to incoming harmonic waves, the effect of these forces can be substituted to the left-hand side of Equation 2.1.1, resulting in the following equation:

$$(\mathbf{M} + \mathbf{A}) \cdot \ddot{\vec{x}}(t) + \mathbf{B} \cdot \dot{\vec{x}}(t) + \mathbf{C} \cdot \vec{x}(t) = \vec{F}^w(t) + \vec{F}^d(t). \tag{2.1.3}$$

Here, **A** and **B** are known as the hydrodynamic coefficients, **C** is the hydrostatic coefficient, and **M** is the mass matrix of the floating structure. The coefficients are 6x6 matrices due to the coupling of the different DOFs. The evaluation of the hydrodynamic coefficients is considered in Chapter 2.2, the evaluation of the hydrostatic matrix is partially evaluated in the following chapter, and the mass matrix of a floating structure can be defined as follows.

$$\mathbf{M} = \begin{bmatrix} m & 0 & 0 & 0 & m \cdot z_{CG} & -m \cdot z_{CG} \\ 0 & m & 0 & -m \cdot z_{CG} & 0 & m \cdot x_{CG} \\ 0 & 0 & m & m \cdot y_{CG} & -m \cdot x_{CG} & 0 \\ 0 & -m \cdot z_{CG} & m \cdot y_{CG} & I_{44} & I_{45} & I_{46} \\ m \cdot z_{CG} & 0 & -m \cdot x_{CG} & I_{54} & I_{55} & I_{56} \\ -m \cdot y_{CG} & m \cdot x_{CG} & 0 & I_{64} & I_{65} & I_{66} \end{bmatrix} \tag{2.1.4}$$

where m is the total mass of the floating structure, x_{CG}, y_{CG}, z_{CG} are the distances between the COG of the floating structure and the origin of the coordinate system and I_{ij} are the inertia terms (collection of the inertia terms is sometimes also called an inertia tensor).

Equation 2.1.3 is the equation presented in Time Domain (TD). For the response analysis of a floating structure, the motion characteristics are often presented in Frequency Domain (FD). For linear motions, this is done with the assumption that forces and motions are represented by harmonic equations. Using complex notation, these can thus be represented as follows:

$$x_j(t) = Re\left\{\hat{X}_{a,j} \cdot e^{-i\omega t}\right\}, \tag{2.1.5a}$$

$$F_j(t) = Re\left\{\hat{F}_{a,j} \cdot e^{-i\omega t}\right\}. \tag{2.1.5b}$$

Where $\hat{X}_{a,j}$ and $\hat{F}_{a,j}$ are the complex amplitudes, indicated by $\hat{}$ (complex) and subscript a (amplitude), and ω represents the frequency of the incoming wave. The complex amplitudes will thus give the magnitude of the amplitude and also the phase between the motion/force and incoming wave. Substituting these complex equations into EOM results in the following:

$$\left[-(m_{kj} + a_{kj}(\omega))\omega^2 - i\omega b_{kj}(\omega) + c_{kj}\right] \cdot \hat{X}_{a,j}(\omega) = \hat{F}_{a,j}(\omega). \tag{2.1.6}$$

Where the subscripts kj indicate a force in direction k due to a motion in direction j.

For the EOMs, the system has the property to oscillate in the absence of any force. These are called the eigenfrequencies of the system and can be found by equalling the left-hand side with zero (eigenvalue problem). To simplify the problem, the damping term is neglected, as this will not influence the location of an eigenmode, as it will only affect the magnitude of this eigenmode. This then results in the following equation for the eigenfrequency:

$$\omega_n = \sqrt{\frac{c_{kj}}{m_{kj} + a_{kj}(\omega)}}. \tag{2.1.7}$$

Thus, for a TLP, where the stiffness of the system is large, indicates that the eigenfrequencies are located in the higher region of the frequency range. Additionally, TLP are often associated with a low mass for the floater (relative to the semi-submersible and SPAR), thus also causing the eigenfrequencies of the TLP to be located in the higher frequency regions.

2.1.2 Mooring stiffness

As mentioned in the Introduction, the stability of TLP originates from the mooring system. Therefore, the stiffness used in the EOM is an important feature to determine. To give an indication of these stiffness values and to see which terms contribute primarily to the total stiffness of the system, a simplified parametric estimation is performed.

First, the stiffness values for the roll / pitch DOFs are performed, as these are the most difficult to determine due to the distributed mass. For the estimation, the simplified 2D representation of the case model TLP is considered (see Figure 2.2).

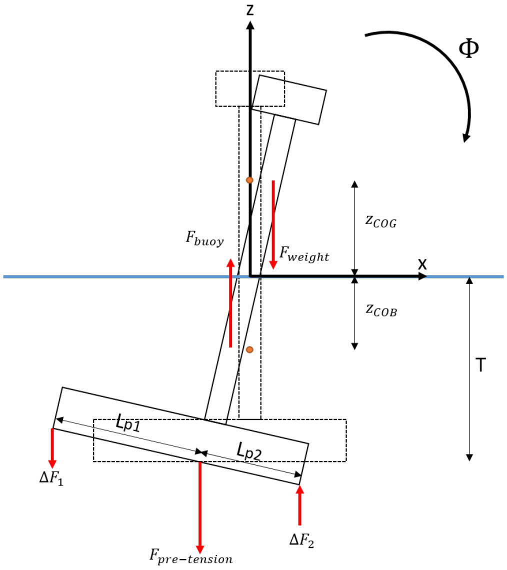

Figure 2.2: Simplified TLP model to estimate roll/pitch stiffness terms.

In this model, the pontoon and the tower are assumed to be rigid. The sum of moments around the origin can be written as follows:

$$\sum M_{tot} = M_{\Delta F_1} + M_{\Delta F_2} + M_{\text{pre-tension}} + M_{\text{buoy}} + M_{\text{gravity}}, \tag{2.1.8}$$

where the centre of buoyancy is at half the draught (T), the distance to the centre of gravity is represented by z_{COG}, where the pretension is equal to the buoyancy force minus the total weight, and where the change in tendon tension is represented as:

$$\Delta F_1 = -\frac{N_{tendons} \cdot EA}{L_{tendon}} \cdot L_{P1}^2 sin(\varphi), \tag{2.1.9}$$

$$\Delta F_2 = -\frac{2N_{tendons} \cdot EA}{L_{tendon}} \cdot L_{P2}^2 sin(\varphi). \tag{2.1.10}$$

Using the information given above, the different moments are as follows:

$$M_{\Delta F_1} = -\frac{EA}{L_{\text{tendon}}} \cdot L_{P1}^2 \cdot \sin(\phi), \tag{2.1.11a}$$

$$M_{\Delta F_2} = -\frac{EA}{L_{\text{tendon}}} \cdot L_{P2}^2 \cdot \sin(\phi), \tag{2.1.11b}$$

$$M_{\text{pre-tension}} = -(F_{\text{buoy}} - m_{tot} \cdot g) \cdot T \cdot \sin(\phi), \tag{2.1.11c}$$

$$M_{\text{buoy}} = F_{\text{buoy}} \cdot z_{COB} \cdot \sin(\phi), \tag{2.1.11d}$$

$$M_{\text{gravity}} = m_{\text{tot}} \cdot g \cdot z_{COG} \cdot \sin(\phi). \tag{2.1.11e}$$

Summing the moments, linearising the dependency of ϕ, and turning the factor into an up-righting rotational stiffness term, leads to the following equation for the roll / pitch stiffness term:

$$C_{44} \,\&\, C_{55} = \frac{N_{tendon} \cdot EA}{L_{tendon}} \cdot [L_{P1}^2 + 2L_{P2}^2] + F_{\text{buoy}} \cdot (T - |z_{\text{COB}}|) - m_{\text{tot}} \cdot g \cdot (z_{\text{COG}} + T)\,. \tag{2.1.12}$$

Using preliminary values for the case model TLP (see Chapter 3.2), it can be calculated that approximately 97% of the total stiffness is the result of the mooring system (first term in Equation 2.1.12). The evaluation of the hydrostatic component is not taken into account, as this will be calculated with the modelling software used. A preliminary value shows that this accounts for less than 1% of the total roll / pitch stiffness, therefore, the majority of the stiffness is the result of the mooring system.

For the heave response, the derivation of the stiffness coefficient is less complicated, as the stiffness term is represented by the changing tension of the tendons and the surface-piercing column. Thus, the heave static restoring coefficient is represented as follows:

$$C_{33} = \frac{3N_{\text{tendons}}EA}{L_{\text{tendon}}} + \rho \cdot g \cdot A_{\text{waterline area}}, \tag{2.1.13}$$

where the first term is the stiffness resulting from the mooring system, and the second term is the hydrostatic stiffness. Using preliminary values of the case model TLP, it can be calculated that the hydrostatic stiffness term only accounts for less than 0.5% of the total heave static stiffness component. Thus, as is the case for the roll / pitch stiffness, the stiffness comes mainly from the mooring system. This excessive stiffness in the system causes the high-frequency motion characteristics of the TLP on which this thesis is focused.

The stiffness coefficients for the compliant DOFs (surge, sway and yaw) are as follows:

$$C_{11} \ \& \ C_{22} = \frac{F_{buoy} - m_{tot}g}{L_{tendon}} \tag{2.1.14a}$$

$$C_{66} = \frac{L_{P1}^2 \cdot (F_{buoy} - m_{tot}g)}{L_{tether}} \tag{2.1.14b}$$

2.1.3 Tower effects

As shown in the previous chapter, for the calculation of the roll / pitch stiffness coefficients, there is an additional influencing factor that is not normally seen in the oil & gas industry. This is of course the addition of the tower and Rotor Nacelle Assembly (RNA). These cause, to a greater degree, an increase in the inertia term. Taking Equation 2.1.7, will result in eigenfrequencies that are consequently lower, compared to TLPs for the oil & gas industry. This subsequent location of the eigenfrequency is important because it determines the method for hydrodynamic load evaluations. From the oil & gas industry, responses such as springing are seen as a resonance problem, where the eigenfrequencies are far away from fist-order wave loading, consequently requiring higher-order wave loading models. However, due to the properties related to the wind industry TLPs, where the increased inertia due to the presence of the tower and RNA, shifts the eigenfrequency towards the first-order load spectrum. Thus, the excitation of the constrained DOFs (roll and pitch) could also partially be the result of the first-order high-frequency wave load.

Additionally, the inclusion of a tower with a suspended mass will also influence the natural roll / pitch frequency in a different way. This is as follows. If it is assumed that the TLP is fixed and the tower is flexible, the motions of the RNA can be represented as in the illustration below.

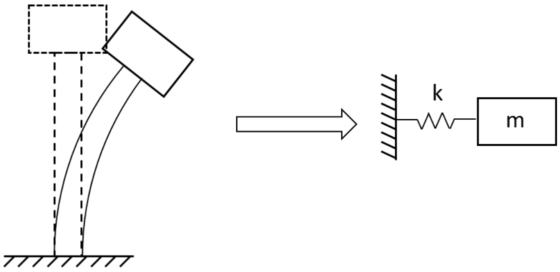

Figure 2.3: Tower bending

The bending of the tower with an end mass is equivalent to a mass-spring system, where m represents the mass of the RNA and k represents the stiffness of the bending tower. This system also has an eigenfrequency (see Equation 2.1.15) which can be determined using the so-called "forget-me-not" equation from Den Hartog (2012). Using preliminary values, it is seen that the eigenfrequency of the bending tower and the roll / pitch eigenmode of the TLP might have eigenfrequencies that are closely located. From Den Hartog (1947), it is known that if two coupled masses with a low mass ratio, for which their eigenfrequencies are closely located, might have an influence on their coupled eigenfrequency. It is to be seen in the analysis from the case model, to what degree this plays a role. This is explored in Chapter 3.2.

$$\omega_{\text{beam \& mass}} = \sqrt{\frac{3 \cdot EI}{m \cdot L^3}} \tag{2.1.15}$$

2.1.4 Response

As mentioned in the previous chapter and the introduction, the expected responses for the constrained DOFs of the TLP are springing and ringing. Information from available literature (mainly from the oil & gas industry) is summarised in the chapters below, where attention is paid to its definition, their effects, and how to recognise them.

2.1.4.1 Springing

As described previously, high-frequency responses are expected due to the high-frequency characteristics of the TLP. One of which is springing, which can be identified to be a resonant effect of the constrained DOFs of the TLP due to hydrodynamic loading. From Chapter 2.1.2, it is determined that these constrained DOFs are heave, roll, and pitch. This high frequency behaviour of the floater will translate itself into high frequency tension signals occurring in the mooring system of the TLP. This will have an impact on the fatigue life of the mooring system as resonance causes a large number of tension cycles. In addition, the resonance effect is seen in the higher frequency ranges, for which damping is usually low in value, therefore causing large "undamped" displacements of the floater, which consequently accompanies these high-frequency loading cycles with high tensions in the mooring system.

It is noted in several articles (Faltinsen, 1990; Chakrabarti, 2005; Roald et al., 2014; DNV-RP-F205, 2019), that the occurrence of springing in TLP type floating structures is usually the result of a second-order hydrodynamic load, since this type of load will have frequency loading components that correspond to the high natural frequencies of the TLP system. However, as suggested in Chapter 2.1.3, the presence of a tower with a RNA might shift the constrained DOFs toward the first-order loading spectrum. Nevertheless, it is not known to what extent this is the case. Therefore, the inclusion of first- and second-order wave loading models are considered in the loading evaluation for a springing response of the TLP.

There is no official set of identification criteria for the occurrence of springing in the response of floating structures. Davies et al. (1994) suggested to label a response as springing if the extreme HF tendon tension does not exceed 5 to 6 times the standard deviation of this tension time history and if the kurtosis of the HF tension is less than or equal to 5.0. These can be evaluated by performing the TD analysis and transforming the data into FD, which is also mandatory for the springing analysis (DNV-RP-F205, 2019; IEC-61400-3-2, 2019). As springing can be seen as a resonance problem, peaks in the spectral density of the tendon tension signals of the TLP coinciding with constrained eigenfrequencies may also indicate the occurrence of springing.

Zou & Kim (2000) conducted research on when springing is expected for TLP and GBS type structures, when subjected to an irregular wave train. It is stated that springing is to be expected when the wave train consists of weakly asymmetric waves. Supplementary, Wang & Zou (2006) showed that the probability of springing is a non-Gaussian distribution, see Figure 2.4. To correctly model these non-Gaussian instances, the application of a quadratic Volterra model would be needed to handle non-Gaussian wave input. Winterstein et al. (1994) & C. H. Kim (2008) showed however, that a Gaussian representation is sufficient for the estimation of extreme and fatigue forces, for systems with stiff characteristics for particular DOFs.

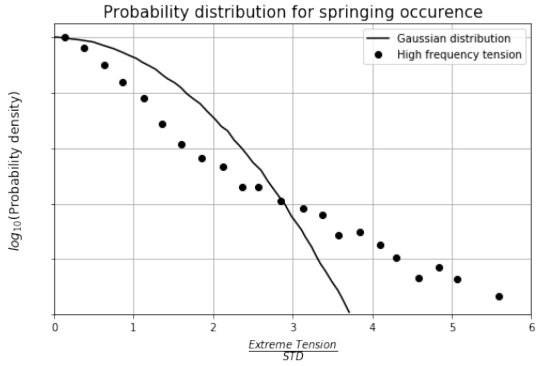

Figure 2.4: Distribution of extreme high-frequency tension categorized as a springing phenomena (Wang & Zou, 2006).

C. H. Kim (2008) stated that springing can be simulated for significant wave heights less than 9m and Zou et al. (1997) validated springing to occur for a TLP compared to model tests, using a JONSWAP spectrum with $H_s = 8m$, $T_p = 12s$ and $\gamma = 1.7$. These can be used as starting points for the identification of susceptibility to springing in TLP type structures.

2.1.4.2 Ringing

As previously described, another high-frequency response, linked to higher-order wave loading, is the appearance of ringing. Springing and ringing are thus both linked to higher-order wave loading and occur both in the higher frequency ranges, but they are not the same. Gurley & Kareem (1998) defined springing to be a steady state response due to second-order sum frequency wave loading, occurring in both mild and severe sea states. In contrast, ringing is a strong transient response observed under severe loading conditions triggered by the passage of a single high and steep wave train. This difference is observable in Figure 2.5. The response in this figure is displayed as a sudden increase in tendon tension followed by a damped tension trajectory until returning to "normal" tension levels. In contrast to springing, where the response is believed to have an effect on the fatigue life of the mooring tendons, the occurrence of ringing is believed to have an effect on the ultimate loading conditions of the mooring system. Furthermore, the rate of occurrence of ringing is much lower than springing (Natvig, 1994), therefore it is not believed to significantly affect the fatigue life of the mooring system.

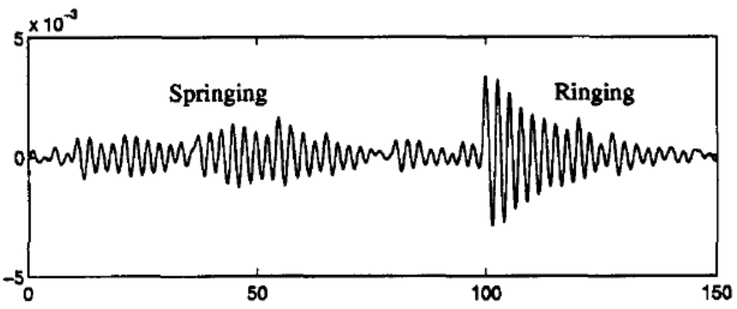

Figure 2.5: Wave characteristics for a springing and ringing event (Gurley & Kareem, 1998).

Literature confirms this description for the occurrence of ringing, as Faltinsen et al. (1995), Stansberg et al. (1995) and Wang & Zou (2006) showed that ringing occurs for wave trains with strong asymmetric waves and where Botros et al. (1996) and Natvig (1994) showed in the response assessment of the Heidrun TLP, that ringing occurs for sudden surges in wave height. Faltinsen et al. (1995) also stated that marine structures with structural periods in the range of 1 to 5 seconds are susceptible to ringing responses. Therefore, this is of importance for the tendon analysis for the TLP in this research, since heave and pitch DOFs have natural periods between 3 to 5 seconds (Faltinsen, 1990).

The following criteria are collected from literature for the possible occurrence of ringing:

- Presence of surface-piercing columns.
- High Froude number [1], $Fr > 0.4$ (Grue et al., 1993).
- Long-wave regiment / low-diameter wavelength, ${}^{D}/_{\lambda} < 0.2$ (Faltinsen et al., 1995) or $ka < 0.63$ (Krokstad et al., 1998).
- Wave height comparable to the cross section of the column, $\zeta_a/a = \mathcal{O}(1)$ (Faltinsen et al., 1995).
- Low Keulegan-Carpenter numbers, $KC < 5$ (Grue & Huseby, 2002).

The criteria are comparable to the criteria found in Bachynski & Moan (2014). The calculation of the ringing response is an even more difficult phenomenon to compute compared to springing. The fact that ringing occurs at a frequency that is triple the frequency of the incoming wave suggests that ringing is caused by a third- or even higher-order wave load

---

[1] Grue et al. (1993) mentioned that the Froude number is determined by "the particle velocity at the wave crest, the cylinder diameter and the acceleration due to gravity". For the case of the TLP, this cylinder diameter would be the surface-piercing tower.

(Faltinsen, 1990; Bachynski & Moan, 2014). Third- and higher-order potentials need to be solved in order to accommodate this force in the model description. However, there is a simplification of this third-order force using the FNV model from Faltinsen et al. (1995), only valid for a vertical cylinder with constant cross section, where Krokstad et al. (1998) showed that it compared well with the full third-order diffraction potential up to $ka = 0.4$.

For the identification of ringing, no official system is established, as is the case for springing. However, the same characteristic parameters, used to identify springing, can be used for this identification process. Jefferys & Rainey (1994) suggested that it can be identified as ringing if the extreme high frequency tension of the tendon is greater than seven times the standard deviation and if the kurtosis is greater than 5. In the case of ringing, the same non-Gaussian behaviour can be observed as with springing (see Figure 2.6).

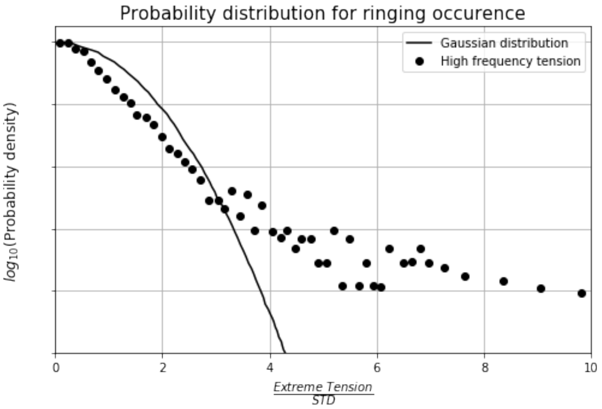

Figure 2.6: Distribution of extreme high-frequency tension categorized as a springing phenomena (Wang & Zou, 2006).

An additional remark presented in the paper from Grue et al. (1993) is the occurrence of a so-called secondary loading if the wave height exceeds a particular value. The forcing occurs a quarter wave period after the main peak load and has a magnitude of 11% compared to this peak load. This secondary loading cycle is caused by a negative pressure at the back of the cylinder, a so-called suction force. This suction force is not taken into account with the use of FNV or the description of a third-order potential. In recent studies, it has been successfully modelled with the use of CFD. However, Xu & Wang (2021) showed with the use of CFD simulations that this secondary loading cycle is not a prerequisite to induce a ringing behaviour of the structure.

For evaluating ringing in time domain simulations, it is often required to implement forces up-to third order. These evaluations are very complex and computationally expensive to include. However, a simplified method exists to combat this. This takes into account certain environment conditions for which a ringing response is seen and a simplified explicit equation is formulated. This is called the FNV method. As mentioned in the scope (see end of Chapter 1.1), the inclusion of ringing is not considered in this thesis. Thus, this FNV model is not incorporated in the subsequent analyses. Nevertheless, details about the method and its implications are found in Appendix A.5.

2.2 Hydrodynamic Loading

To be able to describe the effect of wave loading on structures, the use of hydrodynamic models is required, which will be investigated in this chapter. It is common practise to use loading models that scale linearly with incoming harmonic waves, also known as first-order wave loading. However, since the eigenfrequencies of the TLP are substantially higher compared to other ordinary floating structures (Faltinsen, 1990), the use of wave loading considering only first-order approximations may be insufficient to describe the response of a TLP, since first-order models present little or no energy in this higher frequency range. Therefore, it is necessary to also incorporate higher-order wave loading, as these have loading components at a multiple of the incoming wave frequency. As mentioned in Chapter 2.1.4, it is believed that incitement of springing may be caused by second-order hydrodynamic loading, while ringing is believed to have frequency characteristics at three times the incoming wave frequency, indicating a third or higher order hydrodynamic load.

Before diving into describing these linear and higher-order loading models, it is important to choose the appropriate model for the calculation of wave-induced forces. Two important theories that are commonly used in the offshore industry are Morison's equation and potential theory. The choice of using a specific model depends on which flow regime is to be considered during the calculation. In Figure 2.7, the influence of different flow regimes is summarised to determine which types of forces are important. When the structure is large compared to the wave length, the forces resulting from radiation and diffraction become important. With decreasing structure size, the influence of these forces decreases. As the wave height increases, the importance of including viscous effects increases. In higher waves, viscous drag dominates the damping term, and radiation damping can be neglected.

Based on these considerations, the appropriate model would be Morison's equation for the simulation of forces on the TLP, as it is a relatively slender structure near the free surface. However, the response of the TLP, which this research focusses on, is located in the HF region of the response spectra. This is usually caused by higher-order wave forces, for which the term slenderness must be reconsidered, as the HF region involves significantly shorter wave lengths (Roald et al., 2014). Kvittem et al. (2012) also showed the limitations of computing high-frequency responses using Morison's equation, which can be attributed to the fact that second-order diffraction forces do not decay exponentially with depth (Faltinsen, 1990; M. Kim & Yue, 1990; M. Kim, 1991). Therefore, it is decided to use the potential theory for the calculation of forces on the TLP.

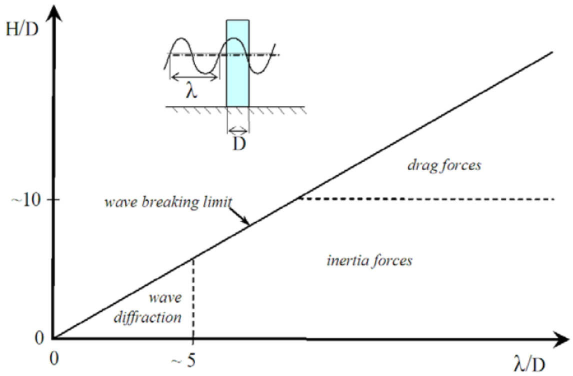

Figure 2.7: Estimation wave load regime (Faltinsen, 1990).

The forces in the diffraction region are the result of the fluid velocity exerting pressure on the submerged structure. In potential theory, this fluid velocity is represented as the gradient of a potential. Thus, the velocity of the fluid is represented by $\nabla\Phi$, which is written in the following condition:

$$\nabla^2\Phi(\overrightarrow{X},t) = 0. \tag{2.2.1}$$

Here, Φ satisfies the Laplace equation. Substituting Equation A.1.3 into the Navier-Stokes equation and assuming that the fluid is incompressible, inviscid, and irrotational will result in the Bernoulli equation for calculating hydrodynamic pressures, represented by Equation 2.2.2.

$$p(\overrightarrow{X},t) = -\rho\left(\frac{\partial\Phi}{\partial t} + gZ + {}^1\!/\!_2 \cdot (\nabla\Phi)^2\right). \tag{2.2.2}$$

To solve the equation, boundary conditions are formulated. These are as follows:

1. No flow through the seabed.

$$\frac{\partial\Phi}{\partial Z} = 0 \text{ for Z} = 0. \tag{2.2.3}$$

2. The component of the fluid velocity normal to the hull should be equal to the normal component of the velocity of the hull itself.

$$\vec{n}\cdot\nabla\Phi = \vec{n}\cdot\left(\frac{\partial\overrightarrow{X}}{\partial t} + \vec{\Omega}\times\overrightarrow{X}\right). \tag{2.2.4}$$

   Where Ω is the angular velocity of the body.
3. The dynamic boundary condition, which indicates that the pressure at the instantaneous position of the free surface is equal to the atmospheric pressure.
4. The kinematic boundary condition, which states that a fluid particle cannot leave the free surface. This is represented by the following equation, taken from Journée & Massie (2008):

$$\frac{\partial^2\Phi}{\partial t^2} + g\frac{\partial\Phi}{\partial Z} + 2\nabla\Phi\cdot\nabla\frac{\partial\Phi}{\partial t} + {}^1\!/\!_2\nabla\Phi\cdot\nabla\left(\nabla\Phi\right)^2 = 0. \tag{2.2.5}$$

   Which only holds at the instantaneous position of the free surface.
5. The radiation condition, stating that the potential decays at infinity.

Although the Laplace equation is a linear equation, particular boundary conditions are not. This results in the equation being difficult to solve. A common workaround is the use of the perturbation expansion method, where the wave steepness is assumed to be small on the basis. This results in the following equation:

$$\Phi(\overrightarrow{X},t) = \Phi^{(1)}(\overrightarrow{X},t) + \Phi^{(2)}(\overrightarrow{X},t) + \Phi^{(3)}(\overrightarrow{X},t) + ... \tag{2.2.6}$$

Here $\Phi^{(1)}$ is the potential related to first-order forces, $\Phi^{(2)}$ to second-order forces, etc. Regarding the perturbation method used for the derivation, $\Phi^{(2)}$ is a nonlinear correction to $\Phi^{(1)}$ and where $\Phi^{(2)}$ is asymptotically dominated by $\Phi^{(1)}$. For the description of springing and ringing, it is believed that the inclusion of potentials up to $\Phi^{(3)}$ is needed.

A method to solve the first-order forces is tackled in Chapter 2.2.1 and the second-order forces are tackled in Chapter 2.2.2. All of these methods depend on the description of the surface elevation. A commonly applied representation and additional information are given in Chapter 2.2.3.

2.2.1 First-order loading

For the calculation of the first-order forces, the first-order potential $\Phi^{(1)}$ is considered. The eventual force on the submerged body is calculated by the first-order pressure acting on the body. This pressure is calculated by the Bernoulli equation, for which only the first-order terms are kept. This results in the following equation:

$$p = -\rho \frac{\partial \Phi}{\partial t}, \tag{2.2.7}$$

The fact that the equation for the potential is linear allows the following decomposition of the potential:

$$\Phi = \Phi^w + \Phi^d + \Phi^r. \tag{2.2.8}$$

Φ^w is the potential related to the incoming wave, while Φ^d is the potential related to the deflection of the incoming waves assuming that the body is stationary, also known as diffracted waves. The last potential, Φ^r, known as the radiation potential, is related to radiated waves caused by oscillations of the body in still water.

The radiation potential leads to the evaluation of the hydrodynamic coefficients a & b as mentioned in Chapter 2.1.1. These are transformed into a 6x6 matrix and can be solved using a method as described in Chapter A.2. This uses a panel method for which the hydrodynamic coefficients are calculated with the following equations for every incoming wave frequency (ω).

$$a^\omega_{kj} = -\rho \sum_{p=1}^{N} Re\left\{\phi^\omega_{j_p}\right\} n_{k_p} \Delta S_p, \tag{2.2.9a}$$

$$b^\omega_{kj} = -\rho\omega \sum_{p=1}^{N} Im\left\{\phi^\omega_{j_p}\right\} n_{k_p} \Delta S_p. \tag{2.2.9b}$$

Subsequent forces on the submerged body caused by the incoming and diffracted wave potentials are also required in this solving method and will also result in the forces required. These can be calculated with the following equations.

$$F^{ex}_k(\omega, t) = \rho\omega^2 \zeta_a e^{-i\omega t} \left[\sum_{p=1}^{N} \phi_{0_p} n_{k_p} \Delta S_p + \sum_{p=1}^{N} \phi_{7_p} n_{k_p} \Delta S_p\right], \tag{2.2.10}$$

where ϕ_0 is the velocity potential of the incoming wave (Φ^w) and ϕ_7 is the velocity potential of the diffracted wave (Φ^d). The evaluation of these calculations are computed with commercially available diffraction software.

2.2.2 Second-Order Loading

Second-order loading means that the loads are proportional to the wave amplitude squared (ζ_a^2). Contributions to this second-order loading can be attributed to the same factors that play a role in the first-order calculation. These are the excitation forces ($F^{ex} = F^w + F^d$) and the radiation forces (F^r).

$$F^{(2)}_{tot} = F^{r(2)} + F^{w(2)} + F^{d(2)}. \tag{2.2.11}$$

Here, the subscript $^{(2)}$ indicates that the force is of second order. This equation can be simplified as the second-order radiation forces ($F^{r(2)}$) are the same as for the first-order loading since the radiation potential does not change (Journée & Massie, 2008; Roald et al., 2014). Thus, the calculation of higher-order loads can focus on the determination of the second-order wave and the diffraction potential ($\Phi^{w(2)}$ & $\Phi^{d(2)}$).

2.2.2.1 Near field method

It is common practise to obtain second-order loads on a floating body by using a method called the "near-field method" or the "direct integration method". In this method, the forces on a body are calculated by integrating the pressure on the time-varying submerged part of the floating structure, where only forces of the second order are kept, which will result in the desired total second-order wave force. To start with the derivation of this method, a coordinate system is introduced and shown in Figure 2.8. The remaining derivations are based on the work of Pinkster (1980) and Journée & Massie (2008).

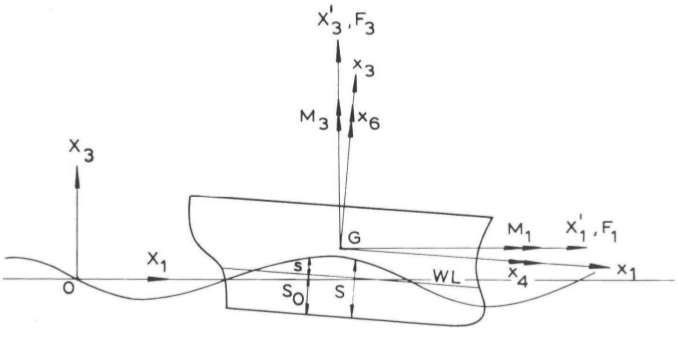

Figure 2.8: Coordinate system used for in the near field method (Pinkster, 1980).

Using this definition of the coordinate system, using the non-linear Bernoulli equation and keeping only terms up to second order, leads to the following equation of the pressure:

$$\begin{aligned} p = &- \rho g \left[X_3^{(0)} + \varepsilon X_3^{(1)}\right] - \rho \left[\varepsilon \frac{\partial \Phi^{(1)}}{\partial t} + \varepsilon^2 \frac{\partial \Phi^{(2)}}{\partial t} + \varepsilon \vec{X}^{(1)} \cdot \varepsilon \vec{\nabla} \frac{\partial \Phi^{(1)}}{\partial t}\right] \\ &- \frac{1}{2}\rho |\varepsilon \nabla \Phi^{(1)}|^2. \end{aligned} \tag{2.2.12}$$

This equation also has to suffice for the non-linear free-surface condition, which is as follows:

$$\frac{\partial^2 \Phi^{(2)}}{\partial t^2} + g \cdot \frac{\partial \Phi^{(2)}}{\partial X_3} = 2 \cdot \left(\vec{\nabla} \Phi^{(1)} \cdot \vec{\nabla} \frac{\partial \Phi^{(1)}}{\partial t}\right) + \frac{\partial \Phi^{(1)}}{\partial t} \cdot \left(\frac{\partial^2 \Phi^{(1)}}{\partial X_3^2} + \frac{1}{g} \cdot \frac{\partial^2}{\partial t^2} \left(\frac{\partial \Phi^{(1)}}{\partial X_3}\right)\right). \tag{2.2.13}$$

For calculations of the forces resulting from the near-field method, the Froude-Krylov method can be applied (Equation 2.2.10), where the integration over the submerged part of the hull is divided into an integration of the mean submerged surface (S_0) and a time-varying part (s) as represented in Figure 2.8. Subsequently, only keeping terms of second order leads to the following equation for the second-order hydrodynamic force:

$$\begin{aligned} F^{(2)} = -\frac{1}{2}\rho g \int_{WL} \zeta_r^{(1)} \vec{n} dl - \iint_{S_0} -\frac{1}{2}\rho |\vec{\nabla} \Phi^{(1)}|^2 \vec{n} dS, \\ - \iint_{S_0} -\rho \vec{X}^{(1)} \vec{\nabla} \frac{\partial \Phi^{(1)}}{\partial t} \vec{n} dS + R^{(1)} \times m \cdot \vec{X}_g^{(1)} - \iint_{S_0} -\rho \left(\frac{\partial \Phi^{w(2)}}{\partial t} + \frac{\partial \Phi^{d(2)}}{\partial t}\right) \vec{n} dS. \end{aligned} \tag{2.2.14}$$

Here $\zeta_r^{(1)}$ is the relative wave height and m is the inertial mass of the floating object. From the equation, it can be seen that the second-order wave force is the result of a combination of first-order terms and the result of the second-order potential. These are often named as the *quadratic* and *potential* loads, respectively. As it is the case of first-order evaluations, the second-order force can also be solved with the use of diffraction software.

2.2.2.2 Quadratic Transfer Function

The near field method presented in the previous chapter shows the exact formulation of the second-order force (Equation 2.2.14) for a floating body. However, these functions are time-inefficient and impractical to use. Therefore, the use of QTFsis presented as a replacement.

For the computation of QTFs, a bichromatic wave description is used and substituted into the formula of the second-order near-field method, from which transfer functions for the difference and sum frequencies can be derived. Documentation for these transfer function derivations is numerously provided in the common literature, for example, by Pinkster (1980) or M. Kim & Yue (1990). Calculations for complexly formed floating bodies are commonly done by diffraction analysis software such as Hydrostar, Ansys Aqwa, WAMIT, etc.

Once these QTFs are obtained, a time-dependent formulation can be generated to use these second-order transfer functions in a TD analysis.

$$F_{tot}^{(2)}(t) = Re\left\{\sum_{i=1}^{N}\sum_{j=1}^{N}\zeta_{a,i}\zeta_{a,j}QTF^{-}e^{i(\omega_i-\omega_j)t} + \zeta_{a,i}\zeta_{a,j}QTF^{+}e^{i(\omega_i+\omega_j)t}\right\}, \tag{2.2.15}$$

where QTF$^-$ is related to complex transfer functions for the difference frequencies and QTF$^+$ is related to the sum frequencies, N represents the number of harmonic waves in the irregular wave pattern, ω_i and ω_j are the oscillating frequencies for the wave pairs and subsequently $\zeta_{a,i}$ and $\zeta_{a,j}$ their amplitudes. To calculate the force, a Fourier transform is needed on all incoming wave pairs. The equation in question can also be simplified to represent the in-phase and out-of-phase components, thus eliminating the complex number.

$$\begin{aligned} F_{tot}^{(2)} = & \sum_{i=1}^{N}\sum_{j=1}^{N}\zeta_{a,i}\zeta_{a,j}P_{ij}^{-}\cos((\omega_i-\omega_j)t+(\varepsilon_i-\varepsilon_j)) \\ & +\sum_{i=1}^{N}\sum_{j=1}^{N}\zeta_{a,i}\zeta_{a,j}Q_{ij}^{-}\sin((\omega_i-\omega_j)t+(\varepsilon_i-\varepsilon_j)) \\ & +\sum_{i=1}^{N}\sum_{j=1}^{N}\zeta_{a,i}\zeta_{a,j}P_{ij}^{+}\cos((\omega_i+\omega_j)t+(\varepsilon_i+\varepsilon_j)) \\ & +\sum_{i=1}^{N}\sum_{j=1}^{N}\zeta_{a,i}\zeta_{a,j}Q_{ij}^{+}\cos((\omega_i+\omega_j)t+(\varepsilon_i+\varepsilon_j)), \end{aligned} \tag{2.2.16}$$

where P$_{ij}^{\pm}$ represents the in phase QTFs recognised by its cosine term and Q$_{ij}^{\pm}$ represents the out phase QTFs recognised by its sine term.

2.2.3 Waves

2.2.3.1 Regular waves

A common description of a wave is the regular or harmonic wave, where the wave pattern can be described by a sine function. In Figure 2.9, a description of a regular wave is sketched for a time-fixed or space-fixed situation, where the most important properties of the wave are defined. In both coordinate systems, the origin of the axis system is located at the mean water level, the z-axis is positive upward and the wave propagates in the positive x-direction.

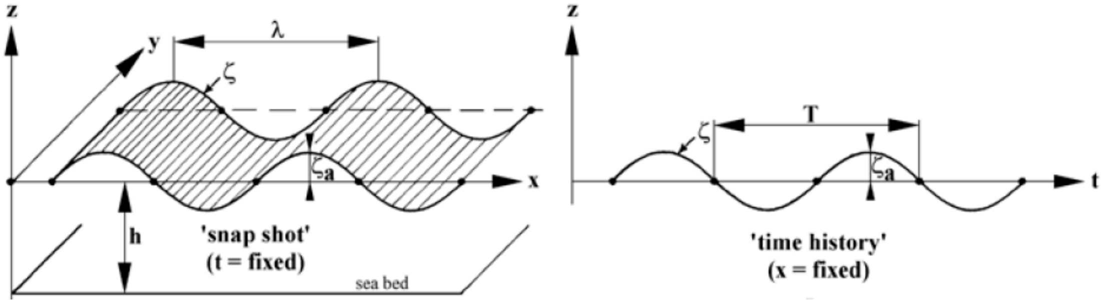

Figure 2.9: Regular wave description (Journée & Massie, 2008).

The depth of the seabed is indicated with h, thus located at $z = -h$ in the coordinate system. The distance between the highest point of the wave (crest) and the lowest point of the wave (through) is the wave height (H). Thus, for a harmonic wave, the amplitude of the wave (ζ_a is equal) to half the height of the wave. The horizontal distance between waves is indicated by the wave length (λ). The period between two successive waves is called the wave period (T). These parameters can be described as follows:

$$\lambda = \frac{2\pi}{k}, \tag{2.2.17a}$$

$$T = \frac{2\pi}{\omega}. \tag{2.2.17b}$$

Here, k is indicated as the wave number and ω as the wave frequency. From these arguments, the phase velocity c can be characterised as:

$$c = \frac{\lambda}{T} = \frac{\omega}{k}. \tag{2.2.18}$$

The description of the elevation for a positive x-direction wave can be characterised by the following equation:

$$\zeta = \zeta_a \cos(kx - \omega t). \tag{2.2.19}$$

From the kinematic boundary condition of the free surface represented by Equation A.1.26, the so-called *dispersion relation* can be derived, which establishes the relation between ω and k.

$$\omega^2 = kg \cdot \tanh(kh). \tag{2.2.20}$$

2.2.3.2 Irregular waves & statistics

The wave described in the previous chapter is a first-order approximation of the free surface. For realistic ocean descriptions, the use of a harmonic equation is not sufficient, as the oceans tend to be highly irregular. However, this irregularity can be approximated with the sum of different harmonic components. As the first-order approximation of the potential and the free-surface are linear expressions, the description of the potential for irregular waves can also be represented by the summation of potentials belonging to individual regular wave components due to the superposition principle. This is exemplified with the following equation:

$$\zeta(t) = \sum_{i=1}^{N} \zeta_{a,i} \cos(k_i x - \omega_i t + \varepsilon_i). \tag{2.2.21}$$

Knowing that a measured time series of a wave elevation can be represented by a summation of multiple harmonic wave components, each with its own frequency and direction of propagation component, a Fourier transformation can be applied, which gives the ability to study frequency characteristics of particular wave conditions. A common frequency analysis is the use of energy density spectra. In Figure 2.10 a visual representation is given of how the Fourier analysis relates the spectrum to the time signal. The energy density can be calculated with the following equation:

$$S_\zeta(\omega_n) \cdot \Delta\omega = \sum_{\omega_n}^{\omega_n+\Delta\omega} \frac{1}{2}\zeta_{a_n}^2(\omega). \tag{2.2.22}$$

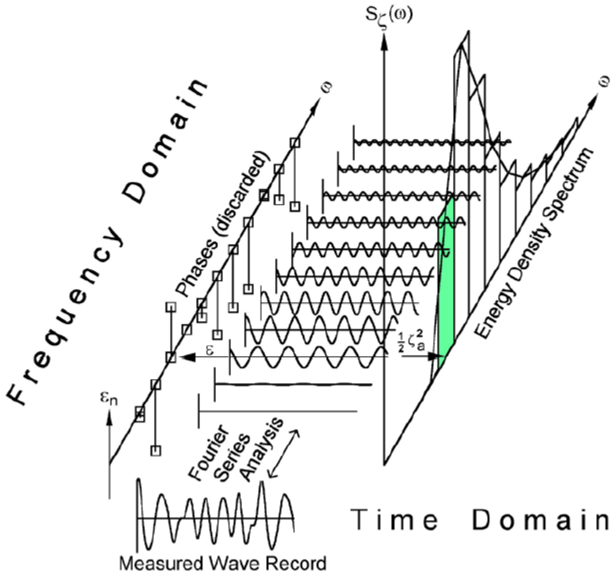

Figure 2.10: Wave record analysis (Journée & Massie, 2008).

If the energy density spectrum of a wave elevation time series is known, characteristics such as significant wave height (H_s) and wave period (T) can be determined. This is done with the help of a spectral moment represented in the equation below.

$$m_{\beta\zeta} = \int_0^\infty \omega^\beta \cdot S_\zeta(\omega) \cdot d\omega. \tag{2.2.23}$$

Here, β indicates the order of the spectral moment. For calculating the significant wave height, the following equation is used.

$$H_s = 4 \cdot \sqrt{m_{0\zeta}}. \tag{2.2.24}$$

The mean wave period (T_1) and the mean zero-crossing wave period (T_2) can be calculated with the following equations:

$$T_1 = 2\pi \cdot \frac{m_{0\zeta}}{m_{1\zeta}} \tag{2.2.25a}$$

$$T_2 = 2\pi \cdot \sqrt{\frac{m_{0\zeta}}{m_{2\zeta}}} \tag{2.2.25b}$$

2.2.3.3 Nonlinear waves

The previous chapters are based on the use of a harmonic description of a wave. The advantage of using this description is the availability of using the superposition principle, which is used to describe irregular waves (Chapter 2.2.3.2) but also to calculate potential diffraction forces (see Chapter 2.2.1). With the use of non-linear wave description, this superposition principle will no longer be applicable, and wave induced forces have to be based on Morison's equation. As stated in the introduction of this chapter, the calculation of forces is done with the use of potential theory, and thus the inclusion of nonlinear waves is not possible in this context and are limited to the use of Airy waves.

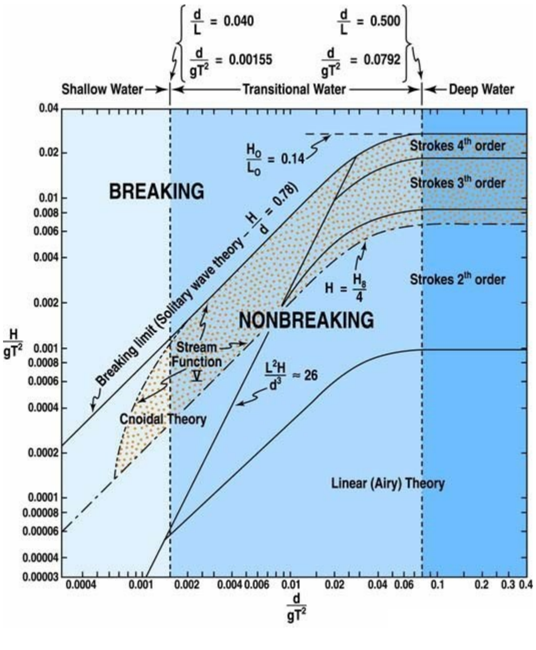

Figure 2.11: Applicability of various wave theories (LeMéhauté, 1976).

In Figure 2.11, the range of applicability of various wave theories is illustrated. For the applicability of regular waves or Airy wave theory in deep water, which this research is focused on, the following limit applies.

$$\frac{H}{gT^2} < 0.001. \tag{2.2.26}$$

2.3 Mooring system

2.3.1 Key parameters

Figure 1.3 illustrates a typical representation of a TLP. The concept pretensions the tendons by incorporating excessive buoyancy in the volume of the floater. This system of pretensioned tendons will then act as a stiff spring for the heave, roll and pitch DOFs, while acting as a soft spring for the surge, sway and yaw DOFs. For the design of the TLP, there are a multitude of mooring properties, which can be altered in the design phase. This can vary from the length of the supporting pontoon arms to the number of cables at each of these pontoon arms. To ensure a viable project scope, only adjustable key parameters consisting of the tethers of the TLP will be considered, this excludes the end terminals. These adjustable parameters will be the following:

- Axial stiffness (EA)
- Effective weight per metre
- Tendon angle
- Number of tendons per pontoon arm
- Pre-tension
- Tendon length

Only limited knowledge exists about the effects of adjusting mooring properties for offshore wind related TLPs. Identifying and quantifying these influences are the aims of this research. Milano et al. (2018) has however already presented a paper, which showed results of changing the tendon angle for a TLP wind turbine. It showed promising results in decreasing the excursions of surge, but it seems to increase the motions in heave and pitch as the angles of the tendons are increased. The study also only uses linear theory for the hydrodynamic modelling, thus investigating the effect of inclined angles including higher-order loading, is still an area of interest to take into account for the tendon assessment. Common parameters used to describe the properties of mooring lines are as follows:

MBL This describes the maximum force under a straight free length of rope, to which it can be exposed before line failure occurs. The term MBS is commonly used for fibre ropes.

T-N curves This curve defines the number of cycles (N) to failure within an effective tension range (T). This is comparable to a S-N curve, where the object is subjected to a stress range.

3-T This is a design curve that represents the load capacity of synthetic materials. The capability is based on three critical parameters *temperature*, *tension* and *time*.

2.3.2 Materials

The choice of material is an important factor in the design of the mooring lines. For application in a TLP, the type of mooring line is limited to steel wire / tubes and fibre ropes, e.g. Dyneema, aramid, etc. There are a multitude of material applications available in the offshore industry. The goal of this research is to provide optimal ranges for key parameters of the mooring system presented in Chapter 2.3.1.

2.3.2.1 Steel tubes

The offshore industry has relied on the use of steel tube tethers for oil & gas related TLPs. Examples are the Snorre platform located in the North Sea or the Mars TLP located in the Gulf of Mexico.

The structural strength of these tendons depends on the type of steel that is being used. The steel tube tendons can be designed in such a way that they are either solid or neutrally buoyant. For neutrally buoyant tendons, the inner diameter is increased while minimising the increase in wall thickness. This causes the displaced volume to increase and level out with the weight of the tendon. This in turn will decrease the total load at the connection point of the platform. The downside of this is that the bending stiffness will decrease, due to decreased wall thickness. Another disadvantage of using steel pipes is that they are limited in depth due to the hydrostatic pressure exerted at these greater depths. Last but not least, the use of steel presents the hazard of corrosion that will affect the structural integrity of the tendons. This effect is usually taken care of by adding additional material to maintain structural integrity despite losing material to corrosion throughout the design life or by coating the tendons to be corrosion resistant.

The use of steel pipes as tendons for the TLP has provided a good and reliable solution for use in structures related to the offshore oil and gas industry. These need a strong and reliable tendon to withstand the environmental loads acting on the large dimensions of the body. For the case of floating wind turbines, the loads, sizes and weights are a few orders in size smaller. The possibility therefore arises to use more affordable types of mooring lines, such as steel wire ropes or fibre ropes. Using the fact that a multitude of wind turbines are being used in a wind farm to impose any viable amount of energy produced, the use of more affordable tendons could significantly reduce the CAPEX of a project, therefore increasing the LCOE. The use of ropes also mitigates the problem of the depth limit of steel pipes, and with the use of fibre ropes, the problem of corrosion can be mitigated. In light of this research, the objective of finding optimal ranges for the mooring system will focus primarily on the use of steel wire ropes.

2.3.2.2 Steel wire ropes

As mentioned above, the use of steel wire ropes could serve as an affordable alternative to steel pipes for the use of tendons of the TLP. In Figure 2.12, a few common configurations of steel wire ropes are illustrated.

Figure 2.12: Steel wire rope configurations

The most common type of wire rope is the stranded rope. The construction includes a series of strands around a centre core of wire, all woven in the same rotational direction. The number of wires and strands depends on the required axial and bending strength. This rope has the property of generating torque, when subjected to an increasing tension force. The other type of wire rope is the torque-balanced spiral rope. Half-locked or full-locked coil wire rope falls into this same category. The construction is made up of layers of wires woven in opposing directions. This causes the rope to have balanced torque characteristics that do not change when subjected to a tension force. The half-locked and full-locked coil wires use a shaped outer layer, making it resistant to water intrusion, preventing the wire from unraveling and serves as protection against abrasion.

In DNV-OS-E304 (2020), it is stated that for long-term design requirements, the use of spiral ropes is considered, due to their high strength to size ratio. Additionally, the rope has less exposed wire material compared to strand wire, making it more corrosion resistant. For offshore purposes, the ropes can also be protected with plastic sheathing, increasing its resistance to corrosion. This sheating is also necessary for ropes with a design life of more than 15 years, according to DNV-OS-E301 (2020). Therefore, this is a viable solution for the use as a mooring tendon for the TLP. The use of half-locked or full-locked coil wire ropes also seems a match for the use in the mooring system, they have a higher concentration of metallic area than spiral ropes. The purpose of these types of ropes, however, is to provide high abrasion resistance. This is not needed for the TLP. In addition, coiled wire ropes need a higher bending radius, increasing their difficulty in handling during the transportation and installation phase. Additionally, the cost of coiled ropes is significantly higher than that of spiral strands. Thus, the use of half-locked or full-locked coil wire ropes is not considered further in this research.

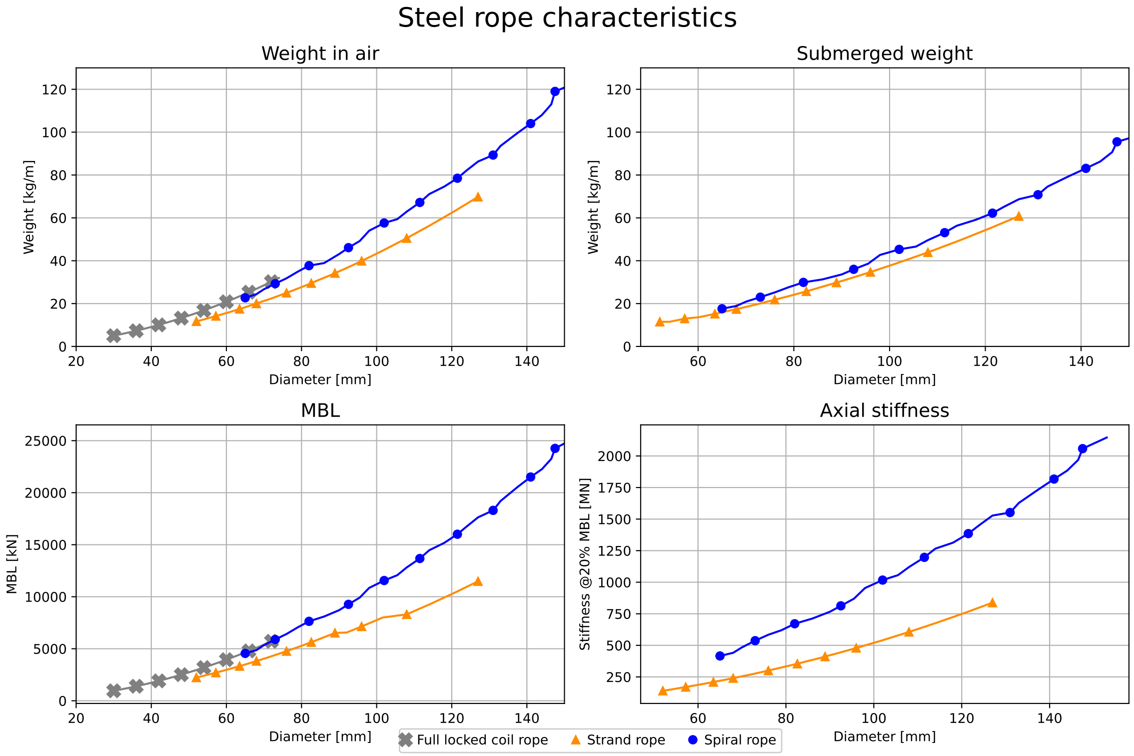

Figure 2.13: A collection of steel wire rope characteristics, showing the difference between weight, MBL and axial stiffness for the different type of ropes

In Figure 2.13, characteristics of the different types of rope are presented. Values are based on a catalogue from Bridon (2011). It clearly shows the differences in strength and weight between spiral and stranded ropes. It gives some realistic values for the key parameters defined in Chapter 2.3.1 and will serve as a check if the optimal values of the key parameters are realistically viable. The figure shows that if the eigenfrequencies of the TLP need to be increased, this can be achieved with increased tendon diameter, as this will increase the stiffness of the system. The added benefit is that the MBS will also increase. The downside of this is that if the eigenfrequency needs to be lowered, MBS will also be subsequently lowered, which is unfavourable for ULS calculations. It is to be determined from the simulations how this will play out. The figure also gives a visual confirmation on why to exclude half-locked and full-locked coil wire ropes, as the commercial available range of rope characteristics is far below that of spiral and stranded wire rope. A summary of the range of key parameters is provided in Table 2.2.

Rope type	**Range of values**			
	Diameter [mm]	Weight [kg/m]	MBL [kN]	Axial stiffness [MN]
Strand	52 - 127	12 - 70	2.230 - 11.484	140 - 838
Spiral	65 - 153	23 - 123	4.453 - 25.302	416 - 2.146
Coiled	30 - 74	5 - 32	958 - 6.043	-

Table 2.2: Common values for key parameters for steel wire ropes.

3

Method

3.1 Methodological approach

This research aims to determine the critical mooring design properties for the TLP in the preliminary design phase and to find their optimal values, to minimise the influence of high-frequency responses of the TLP. These high-frequency responses have been identified as springing and ringing. Due to time constraints of this project, the evaluation of ringing has not been considered. Thus, the subsequent method is based on the evaluation of springing for the TLP system.

As concluded in Chapter 2.1.4.1, springing is a resonance problem for the constrained DOFs of the TLP. This might be the result of high-frequency first-order wave loads or second-order sum-frequency wave loads. From Chapter 2.2.1 & 2.2.2, it was mentioned that these forces can be obtained with use of diffraction analysis software. For this thesis, OrcaWave and Hydrostar are used, which are commercially available diffraction software. No model test data are available for the case model TLP, therefore, for validation purposes, a step-simplification study is performed. At every step, the geometry is built up in order to have more resemblance to the TLP structure, where each step is validated with available literature. Furthermore, the choice for the use of two diffraction software rather than a single programme is because the subsequent results will be cross-validated with each other, to ensure greater confidence in the final results.

The model used for this research is a three pontoon-supported tension leg platform for supporting a 15 MW wind turbine. Details are provided in Chapter 3.2. The evaluation of springing is done with the use of time-domain analyses simulated with OrcaFlex, which is a commercially available aero-hydro-servo-elastic modelling software. As springing is identified as a resonance problem, only mooring system variables that influence the eigenfrequency of the total system are considered. These are the following:

- Axial stiffness (EA)
- Effective weight per metre
- Tendon angle
- Number of tendons per pontoon arm
- Pre-tension
- Tendon length

The values for mooring adjustables can be found in Chapter 2.3.2. However, in practise it is not realistic to adjust these variables univariately (see Figure 2.13). Furthermore, some variables are expected to have insignificant effects on the results (e.g. effective weight per metre). Therefore, only the angle of the tendon and the axial stiffness will be adjusted, where the adjustment of the axial stiffness is based on the material properties commonly used in the offshore industry.

Characteristics that will serve as an indication for performance improvement, are the occurrence rate of HF signals in tendon tensions and platform motions, the improvement of fatigue life and the change in maximum values occurring in the tendon tension, accelerations at the RNA, bending moments at the base of the tower, etc. The tools to measure these performance characteristics will be the following:

Spectral density plot (FFT) As described in Chapter 2.1.4.1, it is believed that the presence of a peak coinciding with the constrained DOFs of the TLP, is a reason to identify the response as springing. This can be done by applying a Fourier transform to the tendon tension signals in order to obtain a spectral density plot.

Rainflow counting Due to the high-frequency cyclic nature of springing, accompanied by large tendon tension amplitudes, it is believed that springing will largely affect the fatigue of the mooring system. A method to assess fatigue is rainflow counting, which is a tool available in OrcaFlex. This method estimates the cycles and stress ranges, where with the use of an S-N/T-N curve, the damage to the tendon can be calculated. Usually, it depends on the client which curve is to be used, thus there is a freedom of choice, therefore, both are calculated first and compared. Afterward, a single curve is chosen for further analyses. Material properties for SSW for the application of the S-N curve are taken from DNV-OS-E301 (2020), and properties for the T-N curve are taken from API (2005).

Time history graphs In Chapter 2.1.4.1, a method is considered for the recognition of springing in oil & gas related TLP structures. In this method, the time signals of the tendon tensions are filtered for their high-frequency content and subsequently screened if certain characteristic values (e.g. standard deviation and kurtosis) are exceeded, which indicate the occurrence of a springing event. It is to be seen whether the method is also applicable for wind industry related TLPs.

Probability of exceedance graphs The reason for the application of this tool is the same as for the tool presented previously (time history graphs). Springing is shown to result in a non-Gaussian distribution, as represented in Figure 2.4. Once again, it is to be seen whether this is also the case for the wind industry related TLPs.

For the investigation of high-frequency responses, a case study is considered for the application of the model. The choice of relating the research to a case study ensures that the influence of these effects is evaluated under realistic environmental conditions. Inspiration is drawn from research such as Bachynski & Moan (2014) and T. Kim & Kim (2015), where a similar approach is considered. For this research, the Korean Strait is chosen for the location of the wind farm, where an average depth of 130m-140m is determined.

To represent realistic environmental conditions in the time-domain simulations, use is made of Design Load Cases (DLCs) as described in IEC-61400-1 (2019). To limit the number of simulations, only a selection of these DLCs is considered. It is often mentioned in literature that the effects of high-frequency responses are most notable in mild to severe sea states. Therefore, load cases are chosen that represent these severe sea states. A choice has been made to select DLCs 6.1 & 6.4, for which DLC 6.1 is used to calculate the ULS of the system, while DLC 6.4 is used to calculate the FLS condition of the system. An additional reason to choose these DLCs is that the turbine is kept in idling mode. During simulations, it was seen that the turbine pitch controller caused a large variation in the total result. Therefore, keeping the turbine in idling mode mitigates the influence of the pitch controller on the final results of this thesis. Subsequent environmental characteristic values are determined from metaocean data for the Korean Strait using a self-developed contour plotter. The final contour plots are illustrated in Figure 3.1.

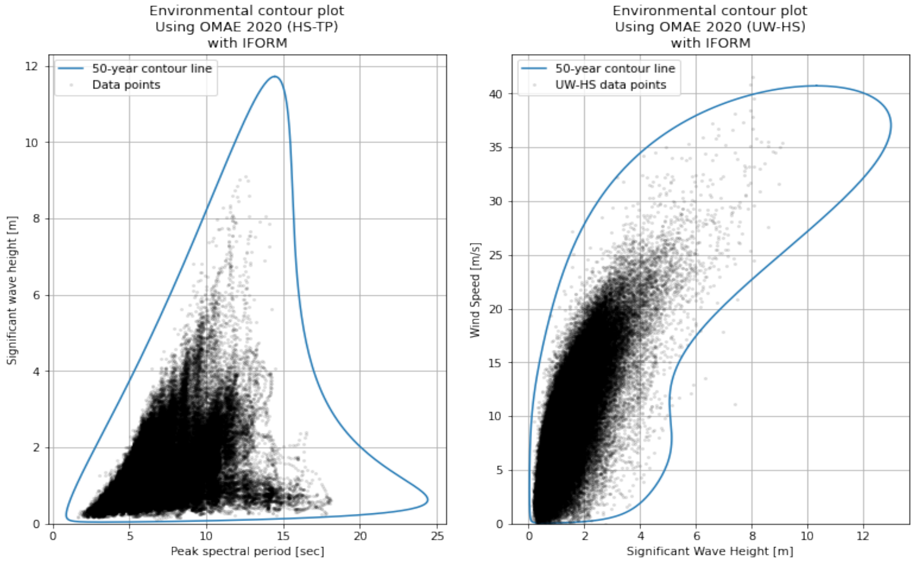

(a) **(b)**

Figure 3.1: Estimation of the environmental parameters for the DLCs using bivariate environmental contour lines. In subfigure (a), the environmental contour plot for the significant wave height and peak spectral period is illustrated. In subfigure (b) the environmental contour plot for the significant wave height and wind speed is illustrated.

Initially, the mooring adjustments will be individually changed incrementally, with values occurring within industry common limits, and the individual adjustments will be rated according to how strongly they improve or worsen the high-frequency response of the TLP. If relations between adjusters can be established to improve the overall motion characteristics of the TLP, the search for combinations between adjusters is followed to obtain an optimal mooring configuration that combats high-frequency responses in the TLP.

3.2 Case model

3.2.1 Model properties

The case model for the floating wind turbine will be a 15 MW wind turbine supported by a three-legged TLP, each leg having 2 vertical Steel Strand Wire (SSW) tendons. Details of the geometry are summarised in Table 3.1, supplementary visualised by Figure 3.2. Because the project developer has not yet selected the actual wind turbine generator, the analysis will be based on a generic offshore wind turbine generator, the IEA-15-240-RWT turbine. Specifications can be found in Gaertner et al. (2020).

Item	Value	Unit
Total mass	4500	ton
Submerged volume	9380	m^3
Hub height	143	m
Rotor diameter	115	m
Pontoon length	46	m
Draft	24	m
Tendon length	116	m
Axial stiffness	2.146e6	kN

Table 3.1: Floating wind turbine parameter summarization.

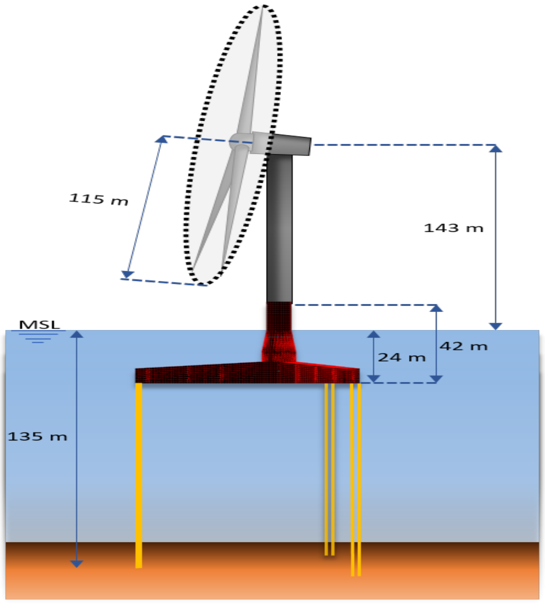

Figure 3.2

Figure 3.3: Geometry description of floating wind turbine concept.

3.2.2 TLP eigenfrequencies

For the estimation of the eigenfrequencies of the TLP, the modal analysis option is used within OrcaFlex. This will result in realistic values for the eigenfrequency as the elasticity of all the components in the system is accounted for (e.g. flexibility of the tower and pontoon arms). The eigenfrequencies are summarised in Table 3.2. For surge, sway, heave, and yaw DOFs, the values are comparable to other floating wind related TLPs, e.g. UMaine TLP (Roald et al., 2014), or the ranges indicated by Faltinsen (1990) (3-5 s). However, the eigenfrequency for the roll / pitch DOFs is lower than commonly reported, for example, the UMaine TLP has a roll / pitch eigenfrequency of 2 rad/s Roald et al. (2014) and in Matha (2010), the eigenfrequencies are approximately 1.5 rad/s. The reason for this low roll / pitch eigenfrequency is the application of a 15MW wind turbine. Comparable research only goes up to 10MW turbines. This, due to the size of the blade, has resulted in a larger tower and a heavier RNA. As explained in Chapter 2.1.3, this increases the inertia for these particular DOFs, consequently lowering the natural frequencies. Furthermore, as suspected at the end of Chapter 2.1.3, it was suggested that the bending eigenfrequency of the tower and RNA will influence the total eigenfrequency of the system. Applying the properties of the TLP and substituting these into Equation 2.1.7, results in an eigenfrequency for roll/pitch of 1.7 rad/s. The same frequency is seen in the OrcaFlex modal analysis if the tower is set to rigid. Thus, the flexibility of the tower causes the pitch eigenfrequency to shift from 1.7 rads/ to 1 rad/s.

Eigenfrequencies		
DOF	rad/s	s
Surge	0.18	34.5
Sway	0.18	34.5
Heave	2.82	2.27
Roll	0.98	6.41
Pitch	0.98	6.41
Yaw	0.33	18.83

Table 3.2: Eigenfrequencies of the case model TLP.

If a 10MW turbine[1] had been used in the investigation, the pitch eigenfrequency would be 17% higher compared to the case of a 15MW turbine. This difference would be even greater for a 5MW turbine[2], where the eigenfrequency would be 60% higher compared to the case of 15MW, again showing the effects of using a 15MW turbine.

The eigenfrequencies in Table 3.2 are illustrated in Figure 3.4. In this figure, the expected first-order loading spectrum is graphed for sea states corresponding to the DLC 6.1 loading case. It is observed that the roll/pitch eigenfrequency is still in the range of some substantial first-order forcing. Additionally, since the second-order sum frequency wave load is acting at twice the incoming wave frequency, a second-order force peak can be expected at the roll/pitch eigenfrequency as well. Thus, both may have a contributing factor in the occurrence of springing, which justifies why both forces should be included in the analysis. It is to be seen from the analyses, which is the main contributing factor.

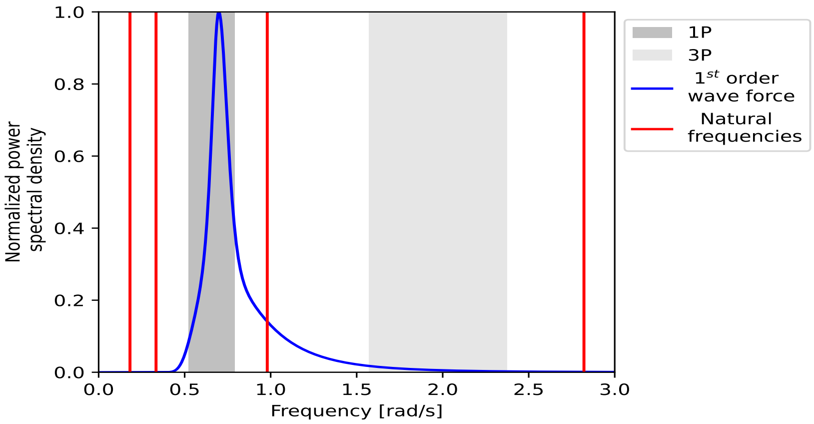

Figure 3.4: Location of eigenfrequencies for the case model TLP.

---

[1] The DTU 10MW turbine is chosen as reference where the hub height is at 115m.

[2] The NREL 5MW wind turbine is chosen as reference where the hub height is at 90m.

3.3 Model adjustment

3.3.1 Axial stiffness

In Table 2.2, characteristic values commonly used in offshore engineering for steel tendons are shown. The axial stiffness of the steel wire rope ranges between 400 and 2200 MN. It is recognised that altering the axial stiffness will influence the weight, diameter, and other properties of the tendons, and these will be adjusted accordingly.

From the initial simulations, common loads within the tendon were around a value of 14 MN. Therefore, taking into account the safety factor (IEC-61400-3-2, 2019), axial stiffness values will be chosen that correspond to MBS /MBL greater than 19 MN. This limit is represented by the red dashed dotted line in Figure 3.5, which shows the indication between the breaking load and the axial stiffness of the common mooring tendons, bearing in mind that the stiffness values for steel wire ropes above a breaking strength of 25 MN are estimates. As different properties result in different dimensions for the tendons, changes in the tendons will be based on the consequent values for steel wire rope. Therefore, the range of axial stiffness is 1500 to 3000 MN, where the extrapolation of values is used after an axial stiffness of 2100 MN. Eight values are chosen using a Gauss-Lobatto sampling method, where the values are compared with commercially available tendons (or extrapolated values based on commercially available data), and reference is made to Bridon (2011) for the subsequent values needed.

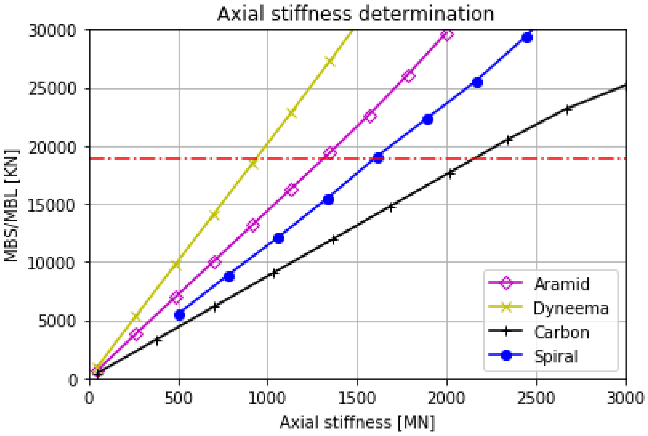

Figure 3.5: Correlation between axial stiffness and breaking load for mooring tendons

3.3.2 Tendon angle

Adjusting the angle of the tendons is a straightforward procedure, in which the length is increased until the same static position of the TLP is obtained. Values from 0 to 30 degrees are selected with the use of a Gauss-Lobatto sampling method. These adjustments are implemented into OrcaWave and Hydrostar by adjusting the stiffness matrix and are implemented into OrcaFlex by adjusting the configuration and the length of the tendons.

3.3.3 Summary

In Table 3.3, a summary is given for the mooring adjustables.

Cases	**Adjustables**	
	Axial stiffness [MN]	**Tendon angle** [°]
1	1017	1
2	1266	4
3	1528	8
4	1736	12
5	2058	17
6	2468	21
7	2777	25
8	3024	28
9	-	30

Table 3.3: Simulation cases.

4

Results

4.1 Diffraction analysis

In Chapter 4.1.1, both diffraction programmes, OrcaWave and Hydrostar, are validated, benchmarked and compared with results from available literature. In Chapter 4.1.2, the setup is described for the diffraction model of the case model TLP and the first- and second-order analysis results are presented in Chapters 4.1.3 & 4.1.4 respectively. In Chapter 4.1.5, the diffraction analysis for the model adjustments (tendon angle and axial stiffness) is shown. The chapter is concluded with a combination of the two adjustments.

4.1.1 Validation diffraction analysis

To validate the diffraction analysis of the TLP geometry, a step simplification study is performed. At every step, the geometry is built up in order to have more resemblance with the TLP structure. Each simplified geometry is compared with available literature. This analysis also allows to compare the accuracy of Hydrostar and OrcaWave and to gain knowledge on how to improve the diffraction analysis for this particular type of structure. The steps taken for the simplified geometries are as follows:

1. A bottom-mounted cylinder with a circular cross section compared to the results from Eatock Taylor & Hung (1987), who performed the diffraction analysis analytically. Furthermore, OrcaWave supplied a validation report that compared the results with the same paper and compared the results with WAMIT.
2. The OC3-Hywind SPAR platform. Multiple articles are presented on the model, providing information on the geometry, mooring properties, and providing load and motion RAOs.
3. A TLP structure developed by the University of Maine. The comparison will be based on the analysis performed by the NREL, for which the results are presented in Roald et al. (2014). In this paper, first- and second-order results are presented, and specifications are given about the geometry and mooring system.

4.1.1.1 Eatock Taylor and Hung

In the paper from Eatock Taylor & Hung (1987), a bottom-mounted cylinder with a radius and height of 1m is used. In Hydrostar, it is possible to create a bottomless cylinder mesh within Hydrostar itself. For OrcaWave, the mesh has to be imported and cannot be created within the software. However, OrcaWave accepts Hydrostar format mesh files. For the OrcaWave mesh, the inclusion of a bottom is needed since earlier calculations showed that a bottomless cylinder resulted in erroneous solutions for the sum QTFs.

Figure 4.1 illustrates the meshes that are used for the analysis. A top mesh is added to both cylinders (transparent in Figure 4.1a and green in Figure 4.1b), which is used to mitigate the effects of irregular frequencies. A key aspect of the mesh is the refinement near the free surface. This improves the quality of the diffraction analysis in the higher frequency ranges.

To replicate that the cylinder cannot move, motion constraints are assigned in all DOFs. This is important for the second-order load analysis, as Equation 2.2.14 contains terms of first-order body motions. In OrcaWave, this constraint is applied by selecting all DOFs as fixed. However, this option does not exist in Hydrostar. To solve this problem, the constraint is mimicked by adding an additional stiffness matrix with very high stiffness values and setting the damping at 100% for all DOFs.

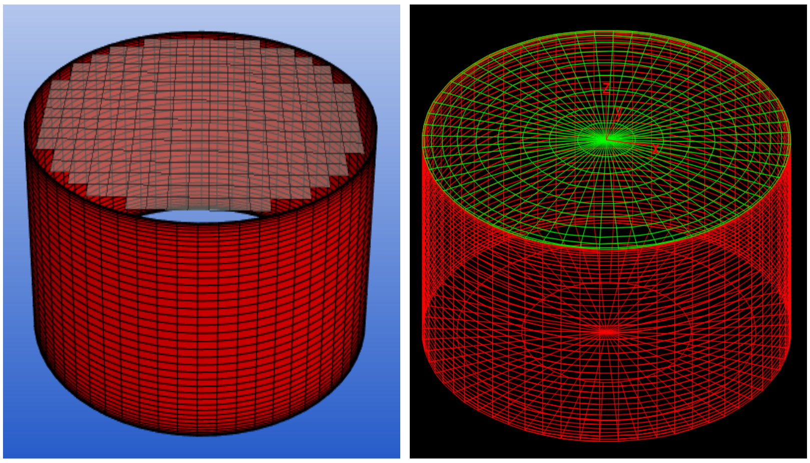

(a) Hydrostar mesh **(b)** OrcaWave mesh

Figure 4.1: Geometry used for the bottom-mounted cylinder to replicate the structure in the paper from Eatock Taylor & Hung (1987). In Figure 4.1a, the cylinder for Hydrostar is illustrated and in Figure 4.1b the cylinder for OrcaWave is illustrated. Both cylinders are classified as R60H40, meaning that 60 elements are used along the circumference of the cylinder and 40 elements over the height.

Load RAO

First, the surge load RAO is compared. The mesh size is changed by either adjusting the number of panels along the circumference of the structure or by adjusting the number of panels over the height of the structure. Figure 4.2 illustrates the mesh convergence study for the evaluation of the load RAOs [1]. The error is calculated by integrating over the total load RAO and comparing this integrated value with the analytical results. Overall, OrcaWave shows a better approximation of the analytical results compared to Hydrostar. As expected, an increase in the number of panels along the circumference of the cylinder seems to be the leading factor in obtaining convergence. For Hydrostar, a significant increase in the number of panel elements is needed to obtain the same convergence as for OrcaWave. However, an error of 0.4% is considered sufficient.

---

[1] This is the only validation step where an actual mesh convergence study is performed due to the availability of an analytical solution. For subsequent mesh convergence studies, the focus is on reducing the change in results for increased mesh refinements

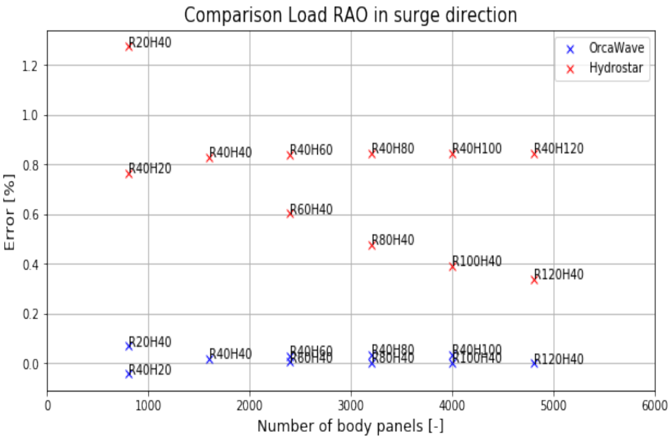

Figure 4.2: Mesh convergence study for the surge load RAO.

Drift load

Next, the mean surge drift load is compared. The results are illustrated in Figure 4.3. The convergence rate compared to the analytical results is better for OrcaWave than for Hydrostar, although it does not differ much.

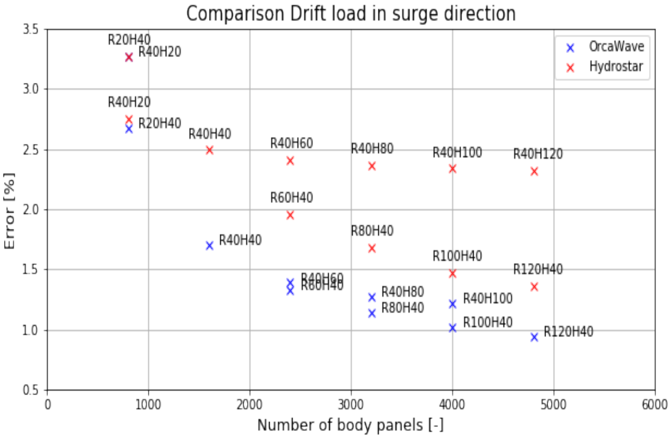

Figure 4.3: Mesh convergence study for the surge mean drift load

However, the error in Figure 4.3 does not give a complete picture of the convergence, as the error is calculated by comparing the area below the curve across the entire frequency range. In Figure 4.4, the mean drift load is plotted. The difference between OrcaWave and Hydrostar occurs mainly above a frequency of 3 rad/s. This is attributed to the following. When plotting all the results in a single figure, it is seen that an increase in the number of panels along the circumference of the cylinder results in a better convergence of the drift load peak (around 2.5 rad/s in the figure), while an increase in 'H' results in a better convergence of the drift load in the higher frequency ranges. Since the refinement of the mesh near the free surface is different between OrcaWave and Hydrostar, might explain why there is a difference in the total convergence error.

Additional methods to compare the convergence rate of drift loads in the higher frequency ranges are to compare the approximated solution calculated with the far-field method (only available in Hydrostar) or to use the theoretical HFL. This shows that the drift load converges to a particular limit, as the structure does not react to waves with a considerably high frequency. For a cylinder, this limit is determined analytically:

$$F_{lim} = {}^{2}/{}_{3} R\rho g\zeta_a^2 \tag{4.1.1}$$

This limit is also shown in Figure 4.4. OrcaWave seems to underestimate this limit slightly for the same number of panels as Hydrostar, but the difference is negligible.

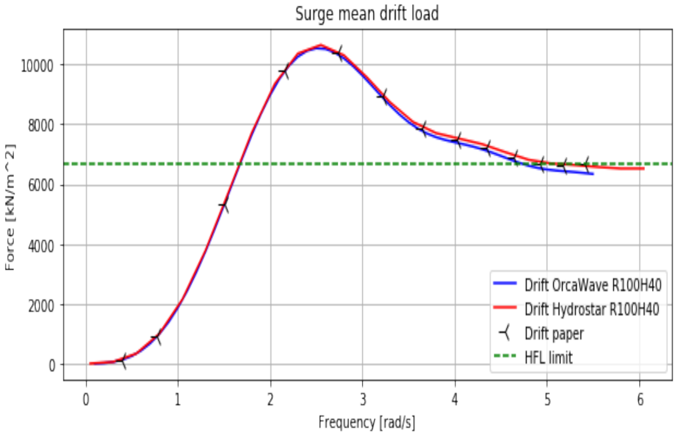

Figure 4.4: Mean surge drift plot

Sum QTF

As mentioned in Chapter 2.2.2, the second order wave force consists of a quadratic and a potential load. This potential term is evaluated by the diffraction method or by the Haskind analogue method, also called direct and indirect methods, respectively. For these methods, it is possible to evaluate the integral without taking into account the free-surface forcing. According to several literature (e.g. Orcina creator of OrcaWave, Roald et al. (2014), etc.), this is justified for the lower frequency ranges. However, since this thesis looks at higher frequencies, the inclusion of free-surface forcing must be considered, therefore, requiring a free-surface mesh. Hydrostar has a built-in function to accommodate this, but OrcaWave does not. In order to accommodate a free-surface mesh for OrcaWave, a Python script is created that can recreate the Hydrostar mesh.There are three additional parameters for the free-surface mesh that influence the accuracy of the free-surface forcing.

1. Radius of the circle identifying the quadrature zone
2. Number of sections in the asymptotic ring
3. Number of annuli for the quadrature zone

Figure 4.5 illustrates different zones present for the second-order free-surface calculation. The asymptotic ring identifies the boundary from which asymptotic approximations are used to solve the potential for radii going to infinity. The quadrature zone uses a simplified integral evaluation method to speed up the calculation and the panelled zone is used to solve second-order boundary problem. However, it is challenging to determine the best settings for these three parameters.

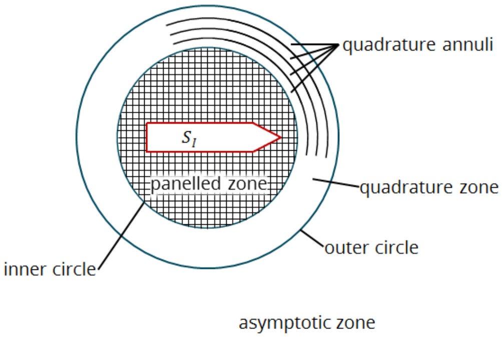

Figure 4.5: Free surface zone identification used in sum QTF calculations (OrcaWave)

To evaluate the optimal setting, the following method is set up. Since the quadrature zone is used purely to speed up the calculations, the initial calculations will only be performed with a panelled and asymptotic zone. From several sources in literature (e.g. Roald et al. (2014), M. Kim (1991), etc.), it was concluded that the outer radius of the paneled zone is not of great importance, but more so is the density of panels within the paneled zone. Thus, convergence is achieved by increasing the number of panels in the panelled zone. For the analysis, a partition radius of 15m with 100 individual sections is used for the asymptotic zone, as recommended by the Hydrostar manual.

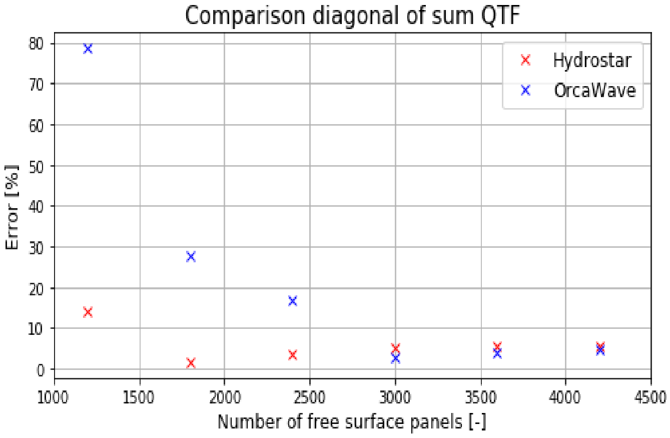

Figure 4.6: Comparison of the diagonal of the sum QTF in surge direction.

The discretization error is evaluated by comparing it with analytical results and by comparing the direct and indirect solutions from OrcaWave (not available for Hydrostar). The results are illustrated in Figure 4.6, from which it is observed that after a few increments in the number of panels, the error does not diminish upon further refinement of the mesh.

Although convergence between the two diffraction programmes are in agreement (with a remaining insignificant difference), the number of free-surface panels seems excessive for such a simple structure, and thus a closer inspection of the results is conducted. Figure 4.7 illustrates the results of the QTF calculations. It can be seen that both Hydrostar and OrcaWave converge to a different value from the analytical solution for frequencies exceeding 3 rad/s. This indicates that waves with a smaller wavelength are not calculated correctly with the current panel size. This is not correctly captured in the error plot in Figure 4.6, as the error is calculated by integrating throughout the total frequency range.

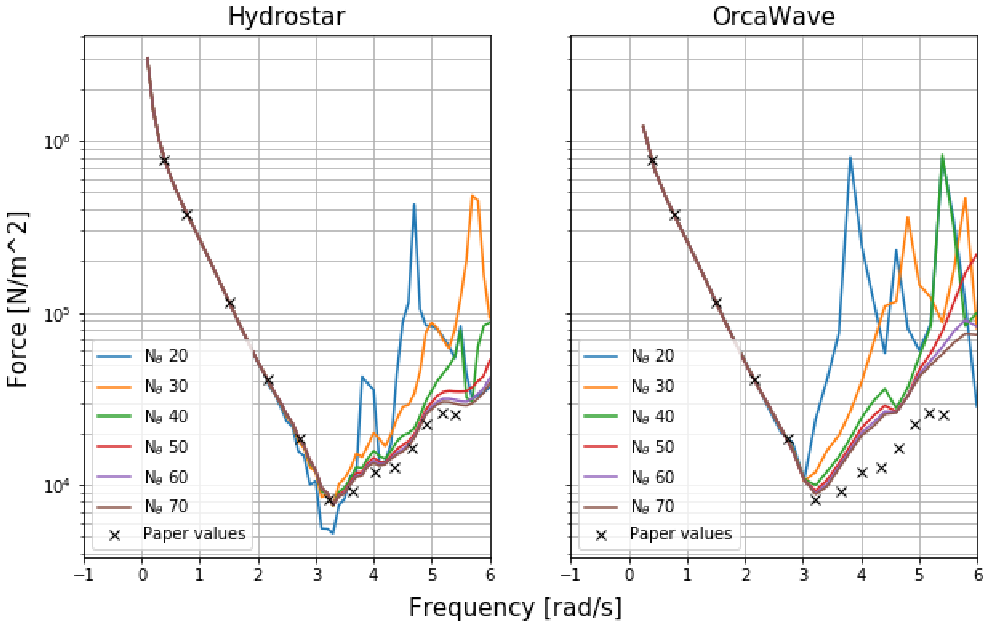

Figure 4.7: Diagonal of the sum frequency QTF for different free-surface meshes with a partition radius of 15m.

It is concluded from the OrcaWave validation page that to capture the maximum wave frequency of 5.5 rad/s, a maximum panel length of 0.08m is allowed. Since the free-surface mesh is a simple structure, the maximum panel length can be formulated as follows:

$$d_{max} = R\sqrt{2(1 - cos(^{2\pi}/_{N_\theta}))}, \tag{4.1.2}$$

where R represents the partition radius of the panelled zone and N_θ the number of divisions along the circumference of the surface piercing object. The plot of this function for several partition radii is shown in Figure 4.8. To obtain a correct panel size for the diffraction analysis, it is more beneficial to decrease the partition radius compared to increasing the number of divisions along the circumference of the body, as an increase of N_θ has a greater influence on the computation time. Additionally, increasing panel density has a greater influence on the diffraction analysis compared to the partition radius, as previously concluded from a review of the literature on the subject.

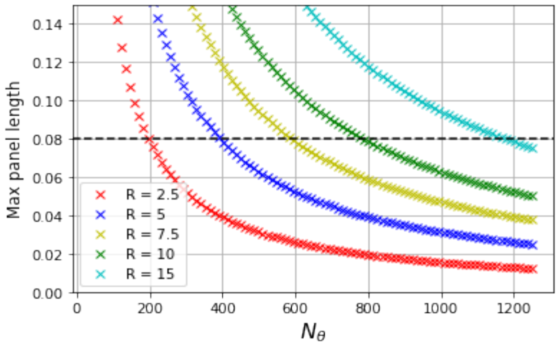

Figure 4.8: Max panel length for different partition radii plotted over a range of N_θ.

A rerun is conducted with a partition radius of 2.5m and 5m retaining the same number of panels, results in Figure 4.9. It can be seen that the error is significantly reduced for a smaller partition radius, which confirms the observation and conclusion about the maximum panel length in the previous sum QTF analyses. The convergence rate is similar for the different partition radii, but far fewer panels are needed to reduce the error.

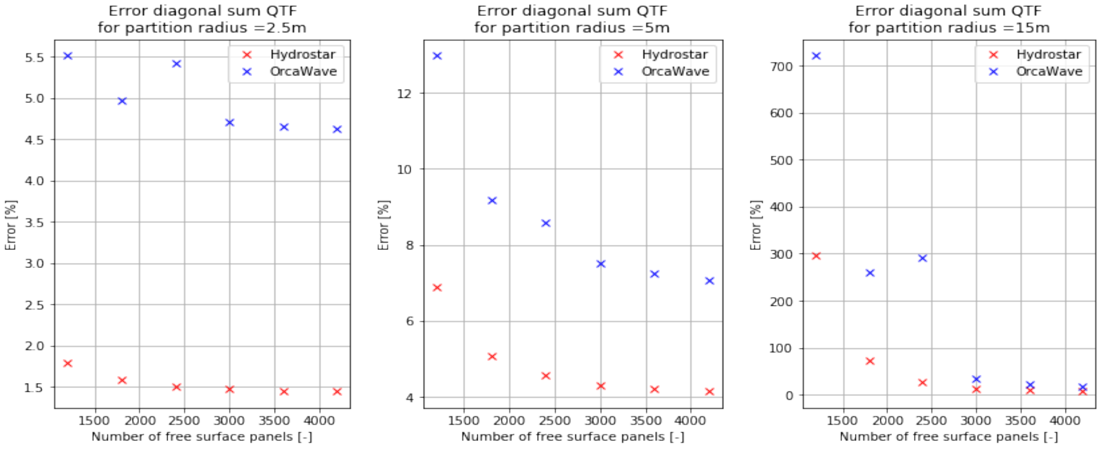

(a) (b) (c)

Figure 4.9: Error plot of the diagonal of the sum frequency QTF for different partition radii.

The difference between the direct and indirect potential loads calculated with OrcaWave show similar convergence. This is illustrated in Figure 4.10. With a decreasing partition radius, the difference between direct and indirect potential loads decreases significantly.

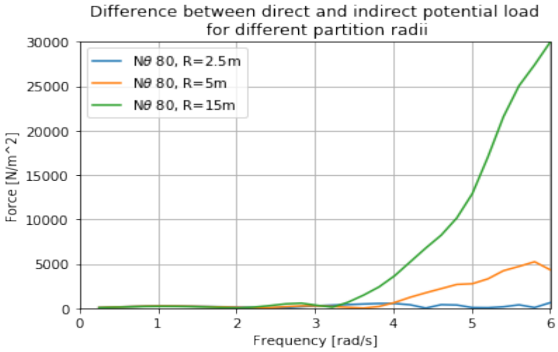

Figure 4.10: Absolute difference between the indirect and direct calculated potential load for varying the partition radius. The most refined free-surface mesh ($N_\theta = 80$) is used for comparison.

In Figure 4.9, there is a clear difference between the results from Hydrostar and OrcaWave. Hydrostar seems to better approximate the analytical values compared to OrcaWave. This problem was presented to Orcina, the developer of OrcaWave, who responded with the following findings. Orcina ran the simulations with a partition radius of 3m and systematically reduced the average panel size of the body and free surface. For an average panel size of 0.02m, the error nearly disappears. Thus, this shows that OrcaWave is capable of accurately reproducing the results of Eatock Taylor & Hung (1987) and that convergence for the sum frequency loads is a balancing act between the partition radius, the body mesh, and the free surface mesh. A rerun with Hydrostar showed a similar behaviour of the error.

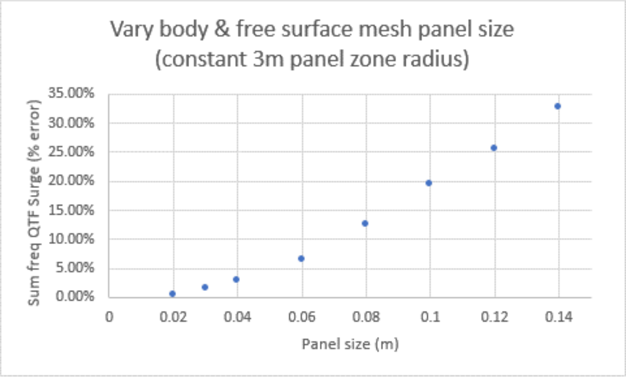

Figure 4.11: Convergence study performed by Orcina for the diagonal of the sum frequency QTF.

4.1.1.2 Spar OC3-Hywind (NREL)

For the second step in the validation, a diffraction analysis is performed for a SPAR structure. This introduces the addition of a mooring system and a supersurface structure in the form of a wind turbine. For reference, the OC3-Hywind SPAR is chosen for comparison, as extensive data for comparison of the results is available in literature.

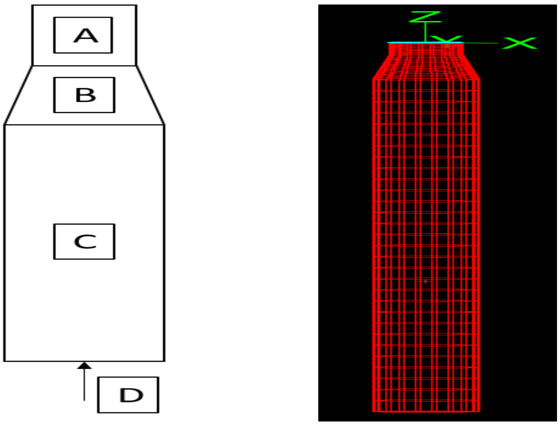

(a) (b)

Figure 4.12: In subfigure 4.12a, the distribution of the mesh for the SPAR is represented. In subfigure 4.12b, an example of the distribution is given. This example is the 600 panels variant.

Geometric and physical properties are taken from Jonkman (2010) and the results are taken from Roald et al. (2014). As before, the mesh generation is performed by Hydrostar. In Roald et al. (2014), several meshes with different number of panels are used. A step in mesh refinement is defined by splitting the panels of the coarser mesh in half. However, nothing is mentioned about the distribution of the mesh across the entire structure. A 1:1:3:1 ratio for mesh area's A:B:C:D (see Subfigure 4.12a) is applied for the number of panels over the height of the structure, where the coarsest mesh sequence is 20 panels over the circumference of the structure and 10 panels for the height (R=40 and H=10). Quarter symmetry could not be used for the simulation, as Hydrostar requires half symmetry for the second-order analysis. Four mesh versions are made with 600, 2400, 5400 and 9600 panels, respectively. The inclusion of the mooring system of the SPAR platform is introduced as an external stiffness matrix, for which the values are taken from Roald et al. (2014) and no viscous damping is applied to the structure.

First order results

First of all, the load RAOs are compared. In Figure 4.13, the results of Hydrostar and OrcaWave are presented for the mesh sizes described above. Sway and roll are not included in the figure, as they have a negligible value because of body symmetry in the YZ-plane. The same applies to yaw, since the round shape of the SPAR will not induce a significant load. From the figure, it can be seen that for surge, 2400 panels is enough to obtain convergence, while for pitch, 5400 panels are needed and for heave, a small difference still occurs between 5400 and 9400 panels. In general, the rate of convergence is mainly determined by convergence in the higher frequency range ($\omega > 3$ rad/s).

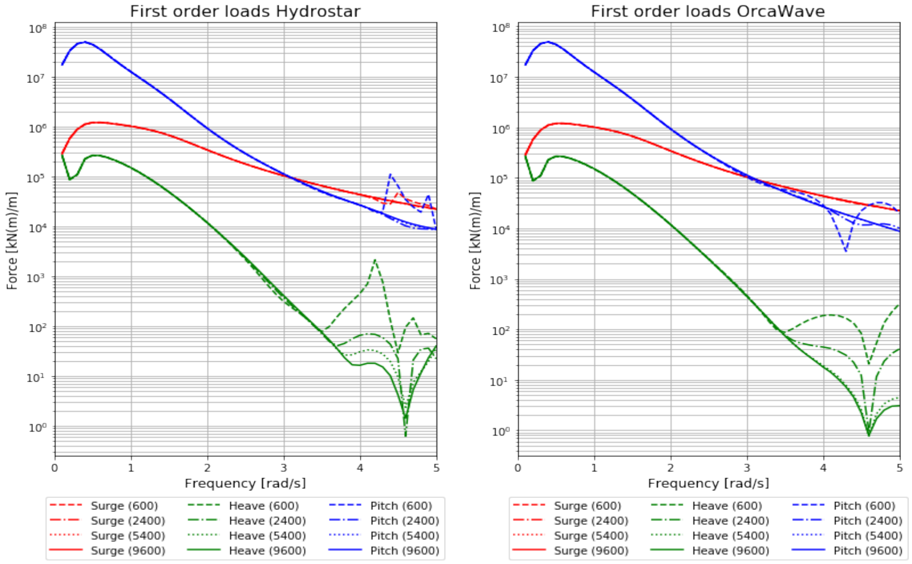

(a) (b)

Figure 4.13: First-order load results for the OC3-Hywind SPAR platform.

Figure 4.14 illustrates the error for the load RAOs. From the figure it can be observed that convergence for the different DOFs is reached for the larger numbers of panels. The error for surge and pitch also converges to an acceptable limit considering the error introduced by the webplot digitiser. However, for heave, the error is significantly higher.

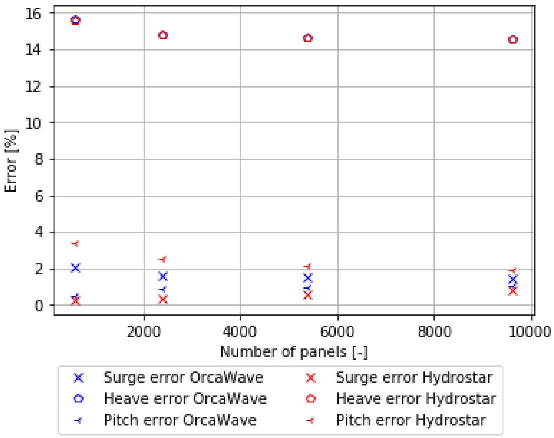

Figure 4.14: Error of the first-order load RAOs of the SPAR platform, comparing the values from Hydrostar and OrcaWave with the results presented by the NREL.

To explain this large heave error, the results for the heave load RAO calculated with the smallest panel size and the heave load RAO from the NREL is plotted on a semi-logarithmic scale in Figure 4.15. It can be seen that after a frequency of 2 rad/s, the values start to diverge significantly. This can be attributed to the fact that the graphs from Roald et al. (2014) are not on a logarithmic scale, making it difficult to select these values with the webplot digitiser. Thus, the load RAOs for heave can be considered correct. Additionally, the figure brings to light a small difference between Hydrostar and OrcaWave for frequencies above 3.5 rad/s. However, the values are negligibly small and are expected to have no large effect on the second-order analysis.

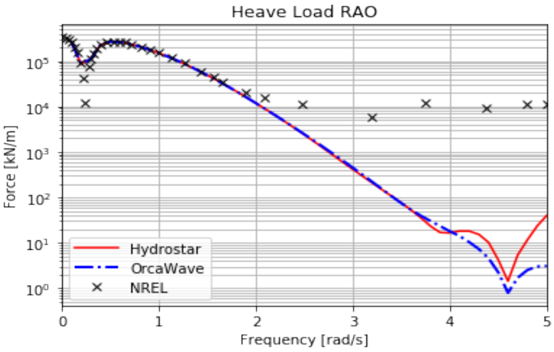

Figure 4.15: Comparison of heave load RAO

Last but not least, interest is focused on the value of the heave load Response Amplitude Operator (RAO) around 0.2 rad/s. The values presented in Roald et al. (2014) tend to go to zero. This is initially not seen in the OrcaWave and Hydrostar simulations, but is resolved when a refined frequency step is applied for the analysis (see Figure 4.16). The dip occurs because the downward force acting on the tapered section and the upward force acting on the bottom of the SPAR cancel each other out at this specific frequency. This means that if the cylinder is to be completely uniform over the height, this dip would not be observed, as the heave force only acts at the bottom. This behaviour can be seen in Figure 4.16, which confirms that the dip is physical.

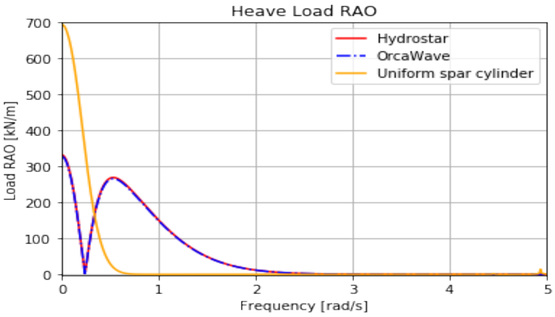

Figure 4.16: Heave load RAO with a refined frequency step for the analysis. Additional uniform SPAR cylinder is analysed.

Differences in damping values can also be compared. This is shown in Table 4.1, where the most refined mesh is used for the comparison. Damping for only a particular selection of DOFs could be compared, as the plots in Roald et al. (2014) and Jonkman (2010) are too zoomed out. The results overall are in good agreement, where the large error for B33 is again attributed to the accuracy of the webplot digitiser.

	Error [%]						
	B15	B22	B24	B33	B42	B51	B55
OrcaWave	0.3	-0.69	-0.93	9.22	-0.23	-2.6	-0.65
Hydrostar	2.1	1.52	1.46	10.09	2.16	-0.26	1.85

Table 4.1: Comparison damping terms for the SPAR platform.

As the added mass is simply a straight line in the paper from the NREL, it is difficult to compare the detailed graphs from the diffraction analysis. Therefore, the values between OrcaWave and Hydrostar are compared with each other. These show some minor differences (less than 1%), which will not have a significant effect on the end result.

The last part of the first-order comparison is the evaluation of the motion RAOs, which will give an indication of how well the interaction of mooring stiffness is modelled and to what extent the differences in hydrodynamic coefficients influence the solution for the motions. Taking first the OrcaWave results (see Figure 4.17), there is an absence of peaks, as seen in Roald et al. (2014). The phase suggests that there are eigenmodes for frequencies below 0.5 rad/s, and thus a refinement for the frequency step is needed to calculate the expected peaks.

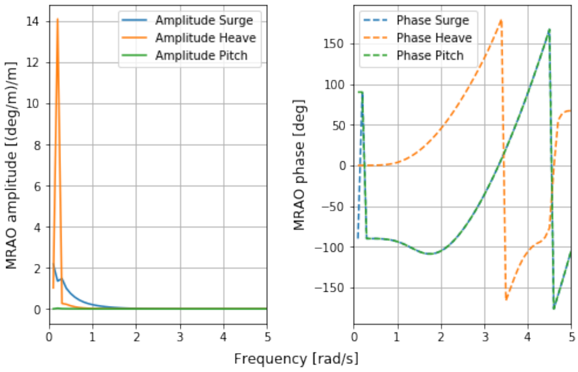

Figure 4.17: SPAR motion RAOs from OrcaWave first attempt.

This refinement is done for a frequency range of 0 to 0.5 rad/s, since this is where the peaks for the eigenmodes occur. In Figure 4.18, the results of this frequency refinement calculated with both OrcaWave and Hydrostar are illustrated. Only the mesh with 5400 panels is used for the calculation to avoid unnecessary simulations.

In Figure 4.18, the result of this frequency refinement is shown. The motion RAOs show a much closer resemblance to those illustrated in Roald et al. (2014). Peaks coinciding with the eigenfrequencies of the system occur at the same frequencies as those presented in the paper. The height of the peaks is not the same, which is caused by the use of different frequencies during the simulation. However, this is not a problem, since the peaks are not actually a physical representation of the actual motion RAOs. This is because the matrices in the EOM are singular near an eigenfrequency of the system. The application of viscous damping would mitigate this problem. However, this is not applied in Roald et al. (2014) and therefore is not taken into account. The location of the eigenfrequencies is a good match between Hydrostar, OrcaWave and the NREL, which shows that inertia and mooring stiffness are properly incorporated. One remark is the small shift of the pitch peak between Hydrostar and OrcaWave, which is deduced to be a result of differences found in the added mass.

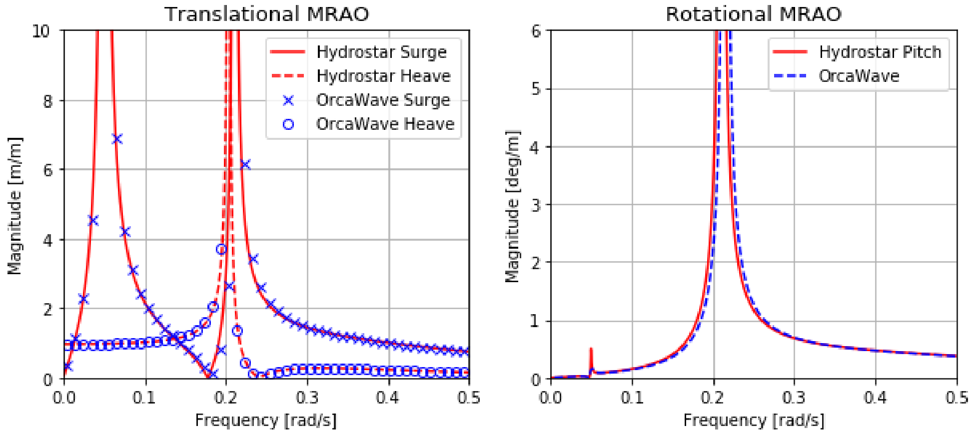

Figure 4.18: SPAR motion RAOs with a refined frequency step. The analysis for both Hydrostar and OrcaWave are shown.

Second order results

First, the mean wave drift force in surge direction is calculated. The results are presented in Figure 4.19 for both Hydrostar and OrcaWave. For Hydrostar, convergence between panel sizes is already obtained at 2400 panels, whereas no convergence is obtained for OrcaWave. In Chapter 4.1.1.1, it was concluded that the convergence of the peak of the drift force was mainly influenced by the number of panels along the circumference of the cylinder, while the number of panels along the height greatly influenced the convergences of the drift load in the higher frequency ranges. Obtaining better results for the drift load would mean an increase in radial panels for Hydrostar and an increase in the number of panels over the height for OrcaWave. However, this drop in HFL is a known problem for OrcaWave, as confirmed by Orcina themselves, thus increasing the number of panels may not result in a correct solution (this problem is solved in a later stage of this research and is presented in Chapter 4.1.1.3). On the subject of HFL, the limit can be calculated once again with Equation 4.1.1, where the radius of the upper cylinder is chosen, since for very high wave frequencies, the influence on depth will be concentrated mainly near the free surface. Hydrostar seems to approach this limit correctly and, not surprisingly, OrcaWave does not.

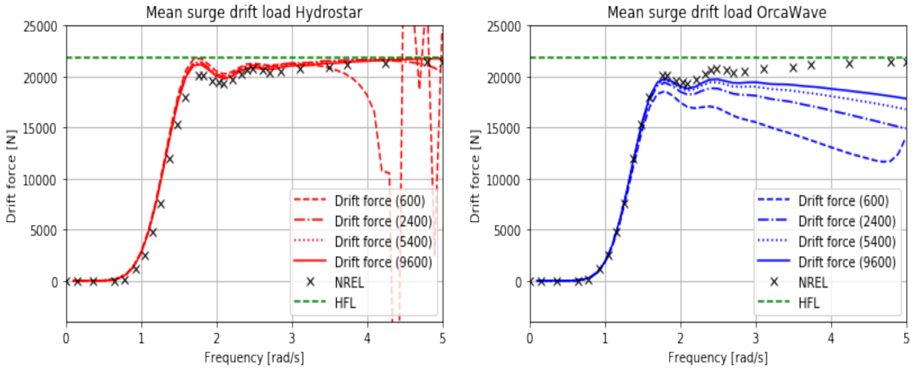

(a) (b)

Figure 4.19: Mean surge drift load for the SPAR platform.

The next part is the comparison of the full QTFs. Both the difference frequency and sum frequency QTFs are provided by Roald et al. (2014), but only the sum frequency QTFs will be compared, as this is the focus of this thesis. The papers also show the quardratic load part of the sum frequency QTFs, thus the analysis starts with OrcaWave, as Hydrostar does not have the ability to split these contributions.

The same free-surface mesh type as represented in Chapter 4.1.1.1 is used for the SPAR. No mesh convergence study for the free surface is needed as this is already done in the paper. There, it is stated that satisfactory results are achieved with a partition radius of 140m and with a body mesh containing 5400 panels. The free surface is created with a self-developed Python code. The same frequency range of 0.26 to 1.5 rad/s is used for the calculations. A key indicator of whether sum frequency calculations have converged, is to compare results calculated with the direct and indirect methods, which is illustrated in Figure 4.20.

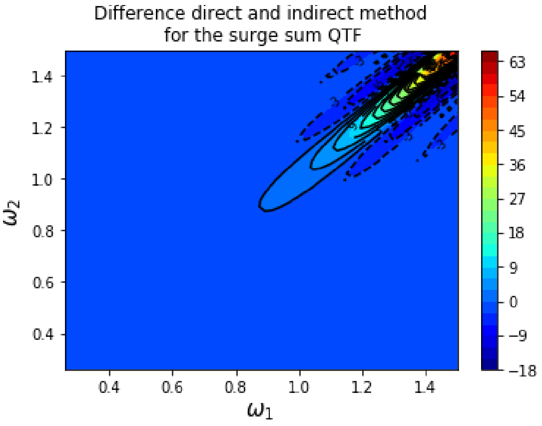

Figure 4.20: 2D surface plot indicating the difference between the direct and indirect solutions for the surge sum frequency QTF of the SPAR platform.

This figure shows that the results are not convergent by any means. The same result is seen for the other DOFs. In previous validation steps, the indirect method showed to have a more stable output. The results calculated with the indirect method are shown in Figure 4.21. This shows that for heave and pitch, the results are already quite similar, value-wise and shape-wise. Small differences can be expected since no mesh convergence study is conducted for this case study. However, the surge plot shows some larger discrepancies. The maximum value is around 166 kN/m^2 for OrcaWave, while 80 kN/m^2 is presented by the paper. This discrepancy is better presented when the diagonals of the QTF are plotted. This can be seen in Figure 4.22. For heave and pitch the results are comparable, but there is a large difference in value and shape for the surge DOF.

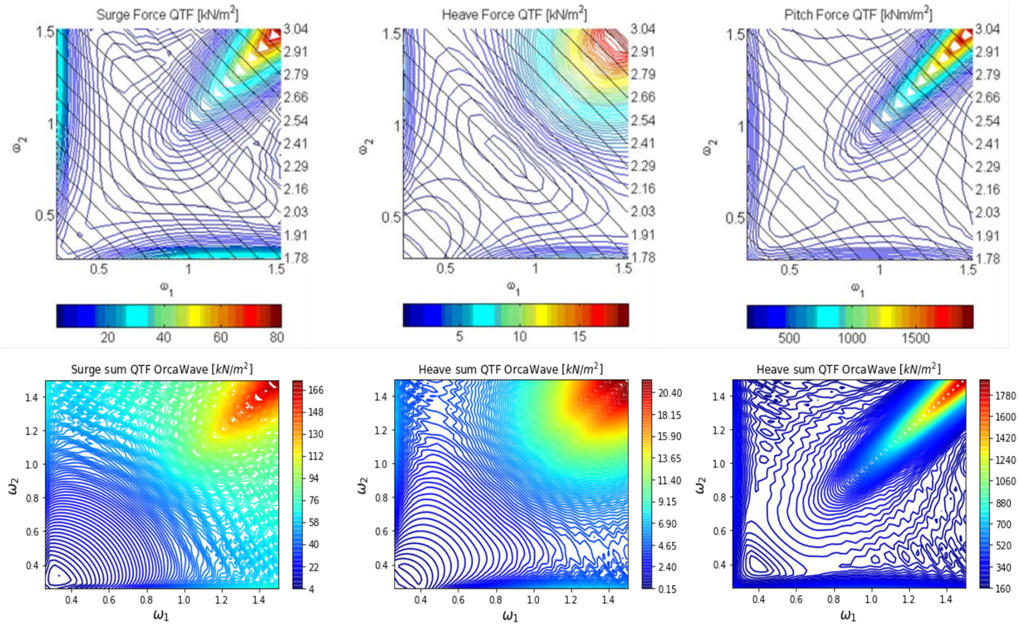

Figure 4.21: Comparison of sum frequency results. The results from Roald et al. (2014) are illustrated in the top row, while the results from OrcaWave are illustrated in the bottom row, for which the OrcaWave results are calculated with the indirect method.

To follow up on this difference in the surge direction, the quadratic load part is compared to exclude any errors in the incorporation of the SPAR characteristics. The results are illustrated in Figure 4.23. The results show an exact match to those presented in the paper. Therefore, differences in the sum frequency QTF for surge can be attributed to the solution of the potential load part.

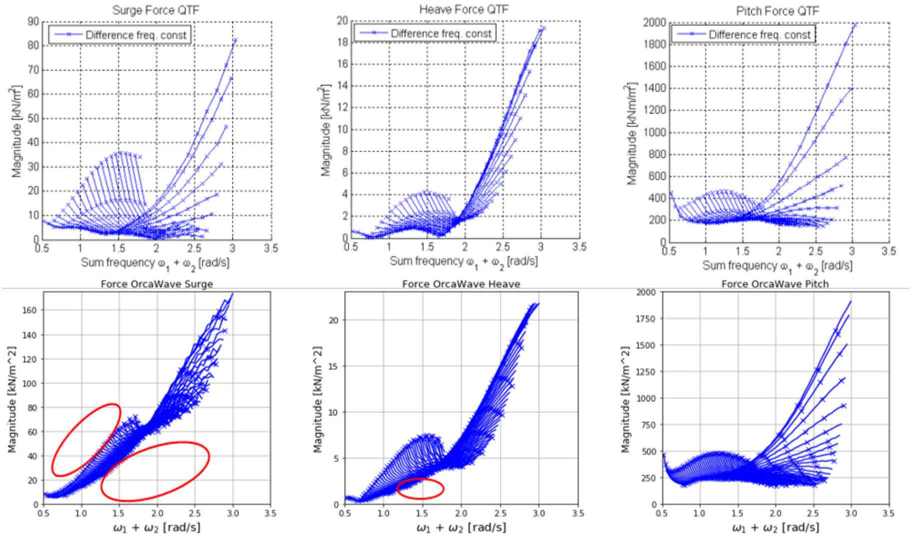

Figure 4.22: Diagonal of sum frequency QTFs for the SPAR platform. The line presents the value for which the difference of the two incoming wave frequencies are constant. The red circled areas indicates where differences are identified.

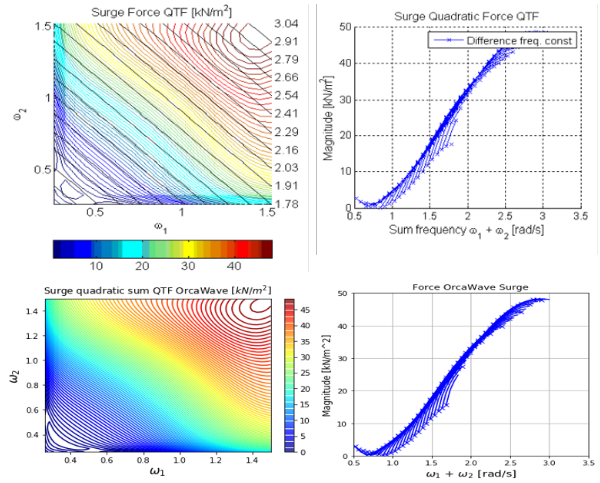

Figure 4.23: Comparison of the surge quadratic load part of the sum frequency QTF. The graphs in the top row are the results from Roald et al. (2014) and the graphs in the bottom row are the results from OrcaWave.

The left circle in the surge graph illustrated in Figure 4.22 suggests that energy is missing in the lower range of the chosen frequency band. An eigenmode is located near this lower frequency band (see Figure 4.18), which explains the sudden increase in value as presented in the paper. High values encountered near an eigenmode in the solution of the potential load part are believed to be a result of the presence body motion related terms in the second-order boundary condition (see Equation 2.2.13), which is used to solve the second-order potential. As mentioned in the evaluation of the motion RAOs, the locations of the eigenfrequencies are close, but not necessarily exact. Therefore, an additional sum frequency analysis is performed with an adjusted lower frequency range of 0.23 rad/s. The results are plotted in Figure 4.24. This figure does show the sudden increase in the sum frequency QTF value, which is why this part is missing from the first analysis.

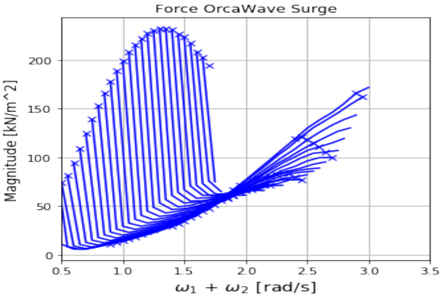

Figure 4.24: Diagonals of surge sum frequency QTF with the extended lower boundary for the frequency calculation range.

Last but not least, is the overestimation of the sum frequency QTF force for both surge and heave around 1.5 rad/s. There are no eigenfrequencies within this range, there is no difference in the quadratic load part of the QTF force near this region, and other factors are not believed to have affected the solution of the second-order potential. In a later stage of the project, it was found that this was the result of an improper addition of the quadratic load part to the potential load part. In the script for plotting the results, the addition of the individual magnitudes was performed, which is mathematically incorrect, as the contributions should first be summed and, thereafter, the magnitude should be calculated. Subsequently, this was corrected in the model and resulted in the graphs illustrated in Figure 4.25. This solved the problem and showed good agreement with the plots of Roald et al. (2014).

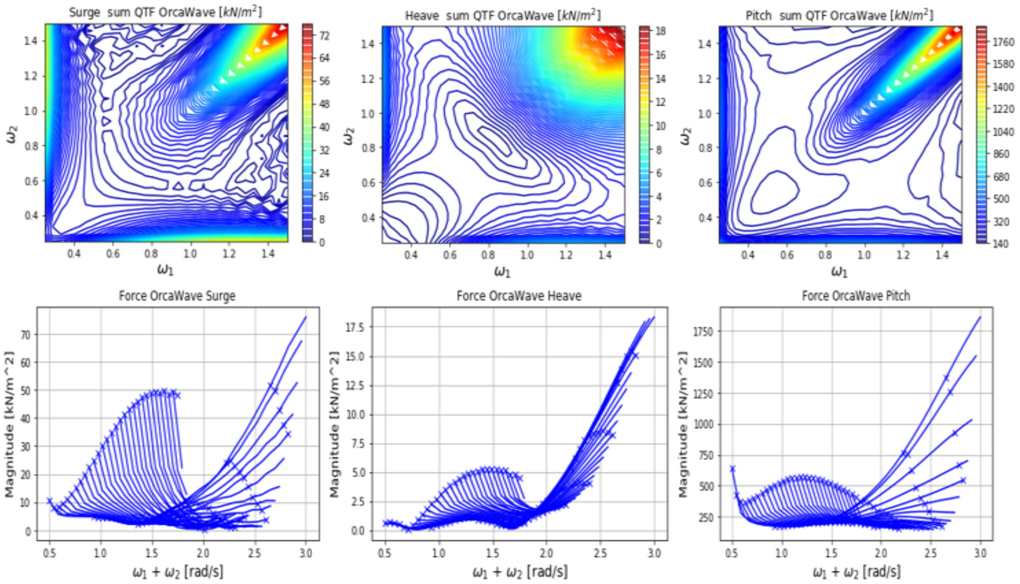

Figure 4.25: SPAR sum frequency QTFs with the corrected model.

Applying the lessons learnt from OrcaWave to Hydrostar and performing the sum frequency analysis, results in the graphs illustrated in Figure 4.26. The graphs have roughly the same shape and value, compared to the graphs from the Roald et al. (2014). Surge, however, shows some discrepancies in the upper left and lower right corners. This is believed to be caused by the shift in the eigenfrequency, as observed in the motion RAOs (see Figure 4.18). This can significantly influence the solution for the second-order potential, as seen with OrcaWave.

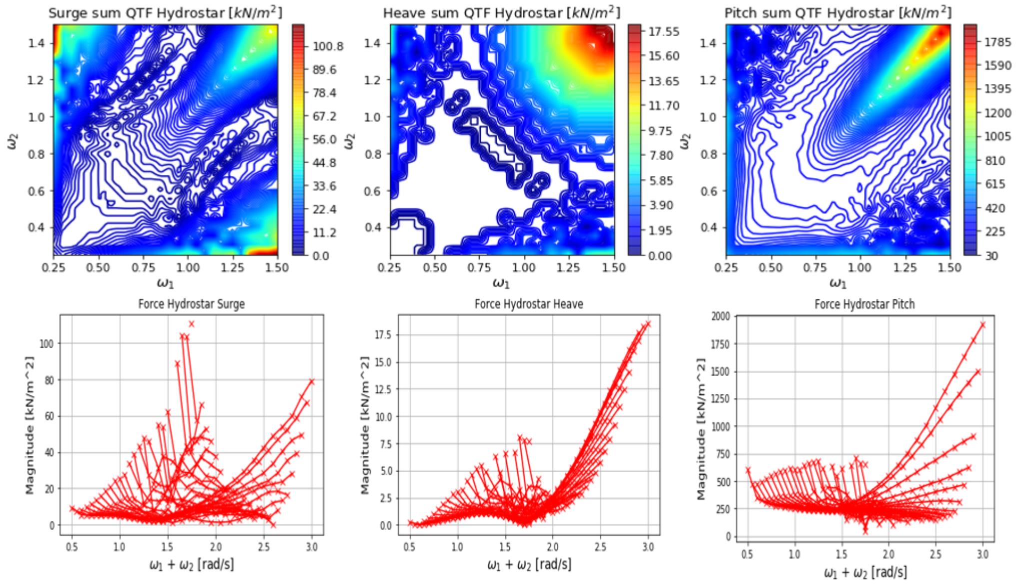

Figure 4.26: Results for the sum QTF analysis with Hydrostar for the SPAR platform. The top row illustrates the surface plot of the sum QTFs, while in the bottom rule, the diagonals are plotted.

As a final note on the solution using a free-surface mesh, the analysis with the refined mesh still showed a large discrepancy between the direct and indirect methods in the higher sum frequency ranges, which indicates that the type of free-surface mesh structure is insufficient for large deep-water structures. The error can mainly be attributed to the large panels on the edge of the free surface, thus a revision of the mesh is needed. This revision will be addressed in the following chapter, where a comparison is performed for a TLP type structure.

4.1.1.3 UMaine TLP (NREL)

For the last step in the validation process, a diffraction analysis is performed for a TLP structure. This will provide valuable information if the diffraction softwares are able to correctly capture the HF characteristics of the TLP in the first- and second-order analyses. For reference, the TLP from the University of Maine is chosen, as the NREL has also performed multiple analyses with this structure. Furthermore, the second-order results are displayed in the same way as in Chapter 4.1.1.2, making the comparison straightforward. Once again, all results will be taken from Roald et al. (2014) and digitally converted using a webplot digitiser for a better comparison.

A detailed geometry specification is given in Koo et al. (2012) and illustrated in Figure 4.27. As the mesh is more complex than the first two validation steps, the use of Hydrostar to create the mesh proved to be problematic. Therefore, the complex geometry is created with the use of Salome Meca, an open-source meshing software. Two points of attention appeared during the creation of the model. The first is the transition of the arm to the lower centre column. In Figure 4.27, it shows that the transition is direct. However, this creates gaps in the mesh of the pontoon arms. To avoid this, the pontoon arm is extended horizontally out of the cylinder for 0.5m, and then the slope is introduced. This is believed to have a negligible effect on the total result.

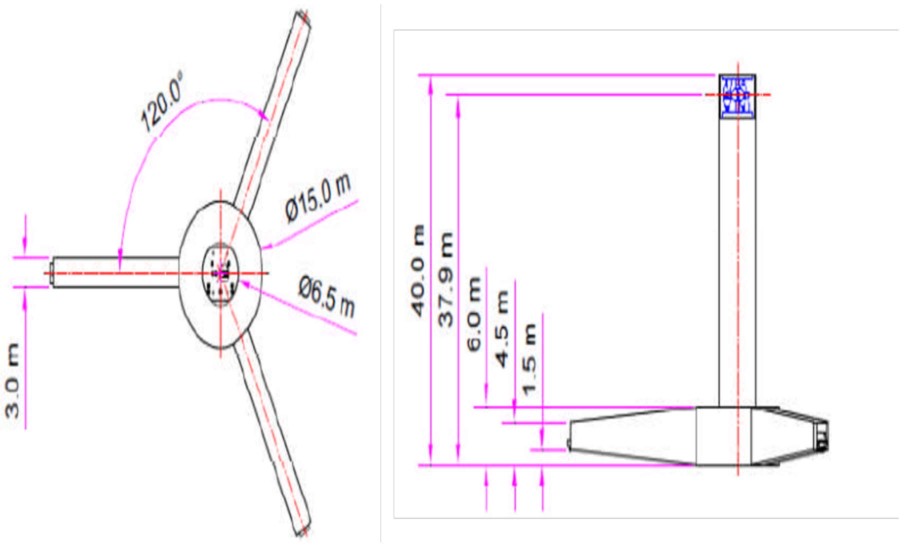

Figure 4.27: Global dimension for UMaine TLP (Koo et al., 2012).

The second point of attention is the mention of the draught in Roald et al. (2014). A draught of 24m is mentioned. However, this resulted in erroneous results, for example, an overestimation of the heave load RAO. An overestimation of such a RAO indicates that the structure needs to be lowered, due to the exponential depth dependence of the potentials. Other literature mention a depth of 30m, which is subsequently used. This adjustment resulted in the correct heave load RAO, This is seen in Figure 4.28, which confirms that lowering the structure reduces the magnitude of the heave load RAO.

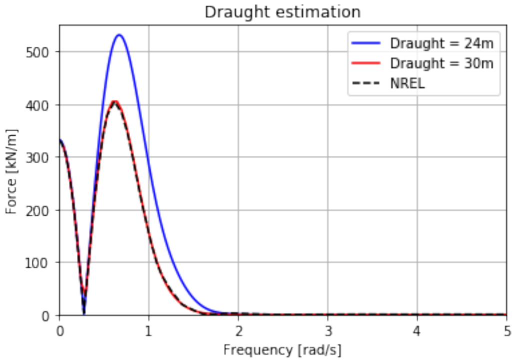

Figure 4.28: Heave load RAO for UMaine TLP for different draughts. A draught of 30m is the correct value when compared to the results from Roald et al. (2014).

For the mesh convergence analysis, four different mesh versions with XZ-symmetry are created with 2350, 5050, 8000 and 10500 numbers of panels, respectively. In addition, cosine spacing is applied on the central column near the free surface, which helps improve the potential solution in the higher frequency ranges. An example is shown in Figure 4.29. The addition of the mooring system and superstructure is incorporated in the same way as in Chapter 4.1.1.2.

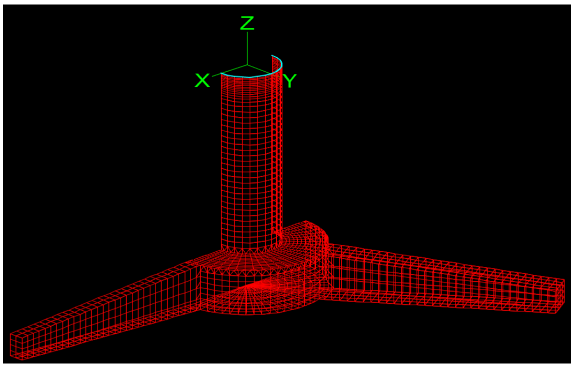

Figure 4.29: Mesh of UMaine TLP with 5050 panels.

First-order results

First of all, the load RAOs are compared. Figure 4.30 illustrates the results for Hydrostar and OrcaWave. As is the case for the SPAR structure, only the surge, heave, and pitch DOFs are considered. For OrcaWave, the load RAOs have already converged with the coarsest mesh for the surge and pitch DOFs. For heave, satisfactory convergence is obtained for 5050 panels. For Hydrostar, the convergence of the surge and pitch DOFs is obtained with 5050 panels, while the heave load RAO is not yet fully converged.

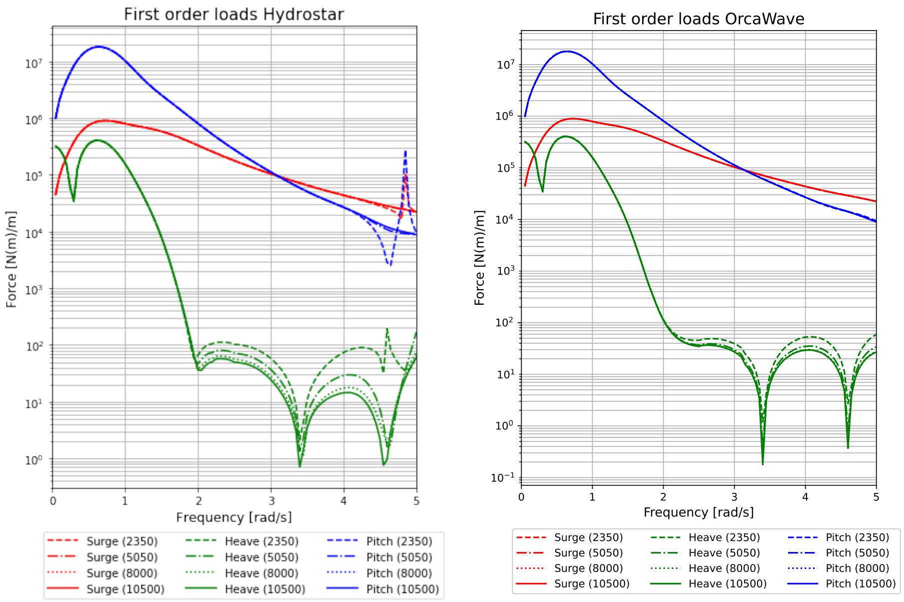

(a) **(b)**

Figure 4.30: First-order loads results for the UMaine TLP.

It is believed that this is the result of the mesh for the pontoon arms. Adjusting the level of discretization in Salome Meca mainly impacts the number of panels in the two centre columns. The number of panels located on the pontoon arms in the heave direction hardly changes. Adjusting the refinement of the panels on these pontoon arms would therefore help with the convergence rate of the heave load RAO. However, this refinement is not performed, because the lack of convergence is located near an HF eigenmode of the system, for which a diffraction analysis is unable to perform the analysis correctly. Additionally, combining the fact that the magnitude of the RAO after 2 rad/s is a few orders lower compared to the magnitudes in the wave frequency region, therefore having a low influence on the motion RAOs. In addition, an upper range of 1.5 rad/s is applied to perform the second-order diffraction analysis. In Figure 4.31, the error of the load RAO is illustrated. For the coarsest panel variant, the error is already at a satisfactory level and for 5050 panels, the error is below 1%. In general, Hydrostar and OrcaWave show comparable output.

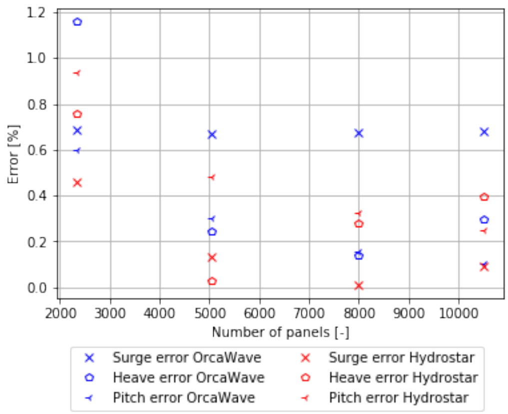

Figure 4.31: Error of the first order load RAOs for the UMaine TLP, comparing the values from Hydrostar and OrcaWave with the results presented by the NREL.

Next, the damping values are compared. As is the case for the SPAR platform, only particular DOFs are compared. The difference between these values and the values calculated using the finest mesh is summarised in Table 4.2. Overall, the values are in good agreement with each other. The error is believed to be largely caused by the accuracy of the webplot digitiser.

	Error [%]						
	B15	B22	B24	B33	B42	B51	B55
OrcaWave	-1.81	0.36	-0.66	4.41	-0.23	-0.27	1.91
Hydrostar	-0.09	2.89	1.03	4.46	1.63	1.61	2.75

Table 4.2: Comparison damping terms for UMaine TLP.

For the added mass, the average values are comparable to those presented in the paper. Comparing the results between Hydrostar and OrcaWave once again resulted in some minor changes which, as seen for the SPAR structure, are not believed to have a large impact on the end results.

The last part of the first-order analysis, is evaluation of the motion RAOs, for which the results are illustrated in Figure 4.32. The motion RAOs for surge and heave are plotted on a semi-logarithmic scale. This method of plotting brings to light some differences, especially for heave. This can be attributed to small differences observed in some terms of the EOM. Nevertheless, the differences are occurring for a frequency range above 2 rad/s, thus it is expected that this has no significant effect on the second-order analysis, as the analysis is performed up to 1.5 rad/s and the magnitudes are once again negligibly small. Another noticeable difference is the height of the peaks coinciding with an eigenmode. However, this is not seen as a problem because of the lack of physical meaning of these peaks, as the matrices are singular at frequencies corresponding to an eigenmode, consequently resulting in an incorrect solution.

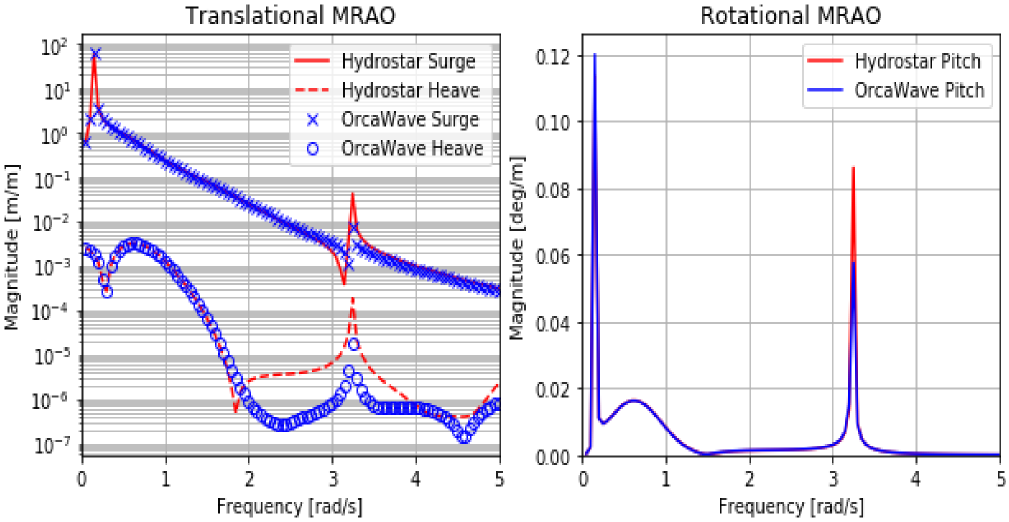

Figure 4.32: Motion RAOs for the UMaine TLP.

Second-order results

For the second-order results, it is started with evaluating and comparing the mean surge drift load. As observed in the diffraction analysis of the SPAR platform (see Chapter 4.1.1.2), the results for OrcaWave showed to be insufficient. Therefore, a different calculation method is used, namely the middle field method developed by Chen (2004). This uses a control surface for the computations. Both OrcaWave and Hydrostar are able to do such computations. Hydrostar automatically creates the control surface, while it needs to be created by a separate programme for OrcaWave. Regardless, it is unknown what shape the control surface should be. In the paper from Chen (2004) and in Hydrostar, a box-like shape is used to represent the control surface, while the example files in the OrcaWave validation report and the WAMIT manual suggest that the shape should approximate the shape of the body. To obtain the optimal control surface, 3 versions are created: a box, a cylinder, and a TLP shape control surface. As a rule of thumb, a minimum distance of 2m is applied between the control surface and the body, and the size of the control surface panels is equal to the size of the body panels.

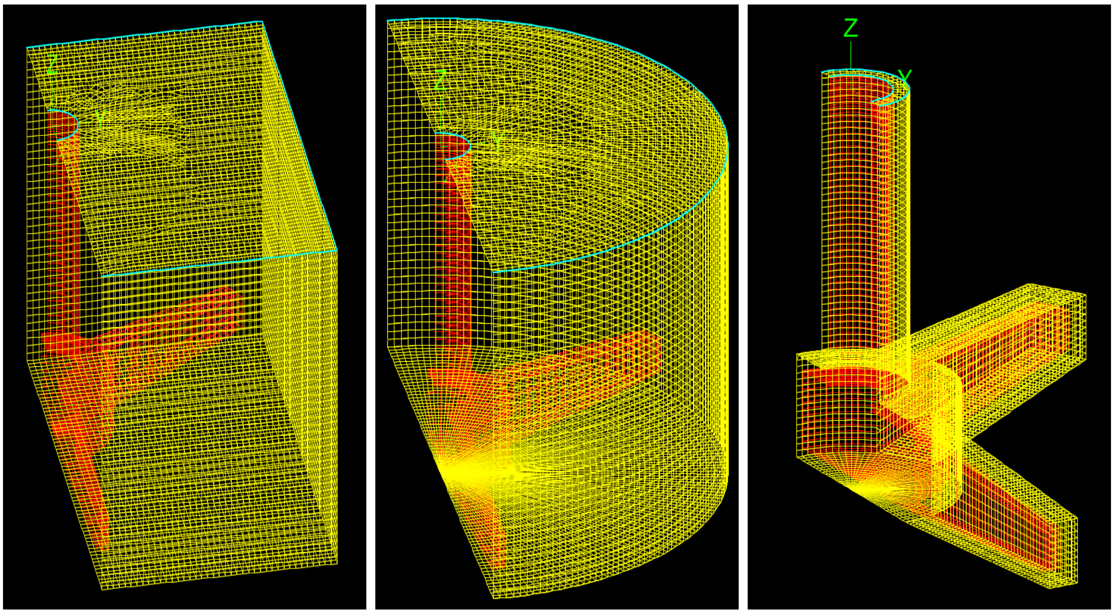

(a) (b) (c)

Figure 4.33: Example of control surfaces for the UMaine TLP. The red and yellow color is an indication for the body and control surface mesh respectively.

The results of these calculations are illustrated in Figure 4.34. It is observed that all three types of control surface shapes show good agreement with the results presented by the NREL until an incoming wave frequency of 2.5 rad/s. After that, the drift load should asymptotically approach the HFL, which is not the case, as the drift force seems to start to oscillate in this region. Nevertheless, of the three variants, the control surface with a TLP type shape returns the best results for the drift load calculation. This version is also slightly faster in calculation time, which can be attributed to having the lowest number of control surface panels.

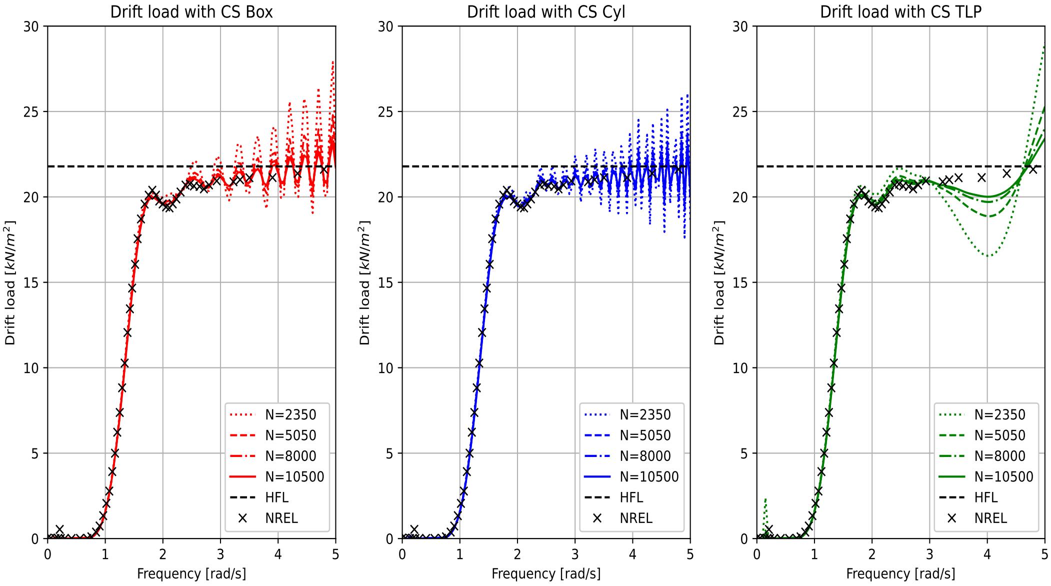

Figure 4.34: Summary of drift calculations using three different shapes for the control surface.

The real gain for using the control surface for drift load computations in OrcaWave is seen when results are compared with the drift load calculated with the pressure integration method (near-field). This comparison is illustrated in Figure 4.35, where a clear underestimation of the surge drift force is observed.

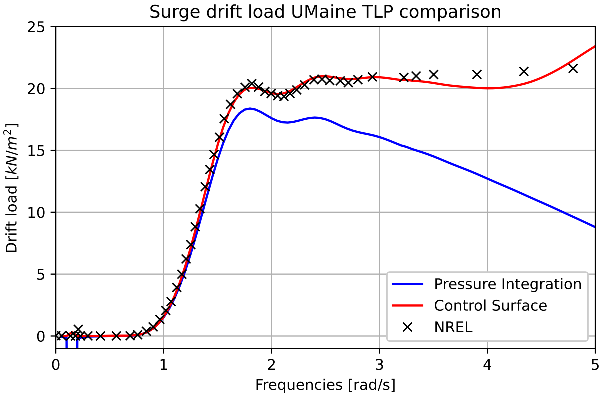

Figure 4.35: Comparison of surge drift load calculation within OrcaWave, using the pressure integration and control surface methods. The calculations are performed on with the body mesh containing 10500 panels.

Since the drift load is diverging at a higher frequency, this is believed to be the case due to the absence of panel refinement near the free surface for the control surface. This is because in a higher frequency range, the influence of wave loads is concentrated near the free surface, due to the decreasing exponential depth dependency in the velocity potential equation. An update to the control surface is performed, where an equivalent refinement near the free surface is performed as applied to the body. This is illustrated in Figure 4.36.

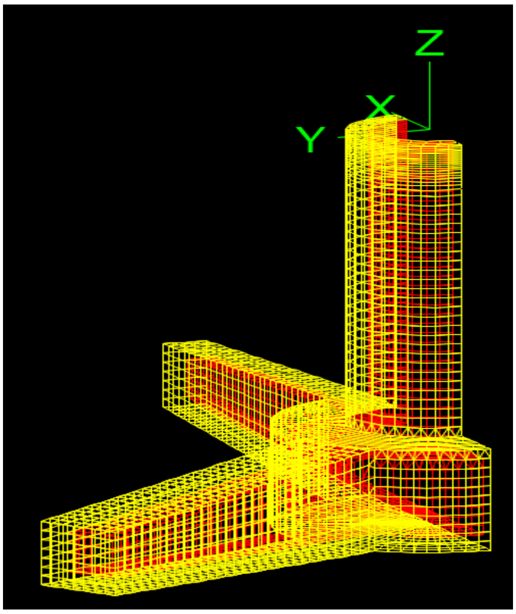

Figure 4.36: Control surface with adjusted refinement near the free surface for the UMaine TLP

The results are illustrated in Figure 4.37. In this figure, it can be observed that the refinement of the mesh near the free surface has significantly improved the convergence of the drift load in the HFL. The mesh with 5050 panels already shows that the drift load has approached the solution presented by the NREL.

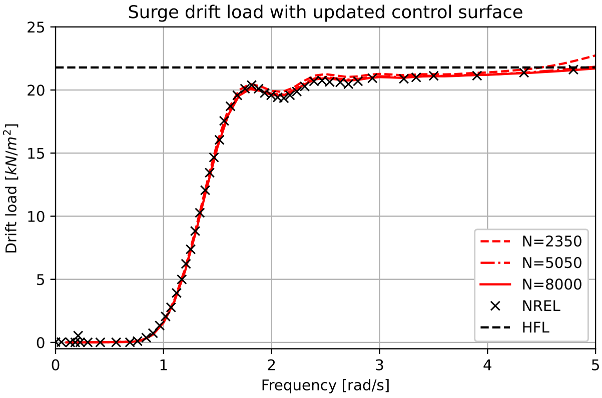

Figure 4.37: Surge drift load with adjusted control surface. Mesh with 10500 panels is not considered as convergence is already obtained with 8000 panels.

The next step in comparing second-order results is to evaluate the sum frequency QTFs. Roald et al. (2014) suggests a partition radius of 100m. Additionally, as is the case in the preceding validation steps, no application of a quadrature zone is considered. From Chapter 4.1.1.2, it was concluded at the end of the second-order analysis that the Python generated free-surface mesh was insufficient. However, with the introduction of Salome Meca, this problem could now be solved. In the paper from the NREL, an example for the shape of the free-surface mesh is presented, which could be recreated with Salome. Additionally, a free-surface mesh is generated using the 2D NETGEN algorithm, which simplifies the procedure of creating a free-surface mesh.

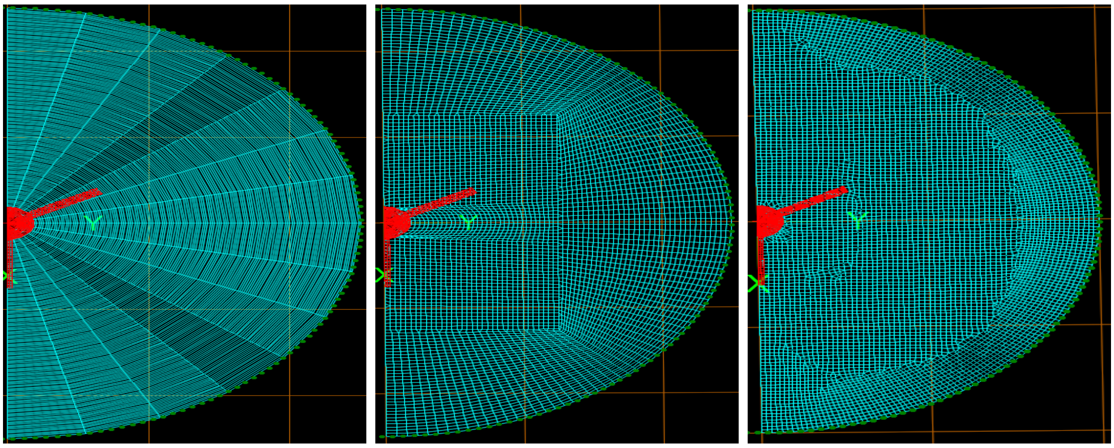

(a) (b) (c)

Figure 4.38: Examples of free surface mesh for the UMaine TLP. From left to right, the Python, the NREL and the NETGEN free surface meshes are illustrated respectively.

Only the body meshes with 2350 and 5050 panels are considered for the evaluation, as OrcaWave consumes a large portion of the memory (more than 16.8GB for a single thread for a body mesh with 5050 panels). For an indication of mesh convergence for the solution, the indirect and direct methods are compared. As can be seen in Figure 4.20, the largest differences occur along the diagonal of the potential load ($\omega_1 = \omega_2$). Therefore, the convergence is based on this diagonal, for which the results are illustrated in Figure 4.39.

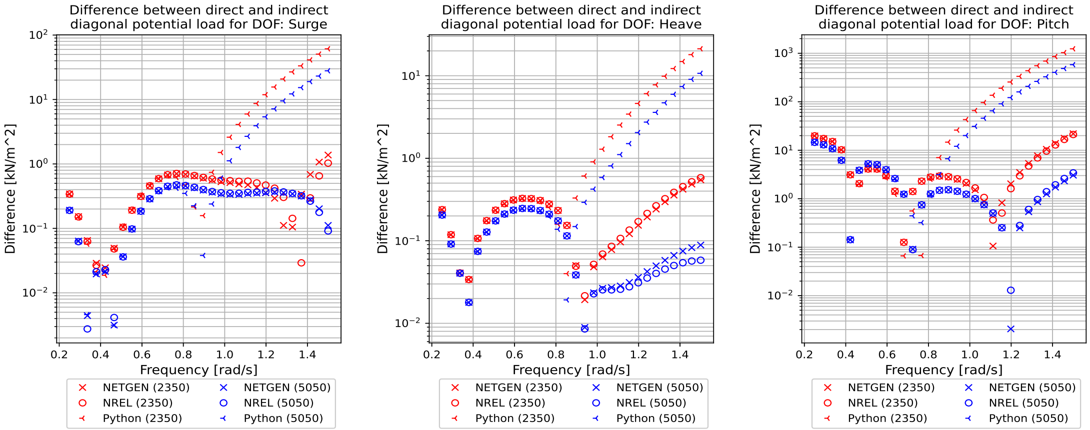

(a) (b) (c)

Figure 4.39: Absolute difference between the direct and indirect solution for the diagonal of the sum frequency potential load.

Overall, there is a clear difference in accuracy between the mesh generated by Python and those generated by Salome. The free surface mesh based on the one from the NREL and the one generated with the NETGEN algorithm seem to perform equally well in terms of convergence. A noticeable difference between the two is that the running time of NETGEN is considerably longer, which can be attributed to the fact that the NETGEN mesh on average has 40% more panels compared to the NREL. In general, it can be stated that the absolute difference is quite low ($<$ 1kN), but a statement on convergence cannot be given, since only a single partition radius is applied without varying the size of the mesh panel.

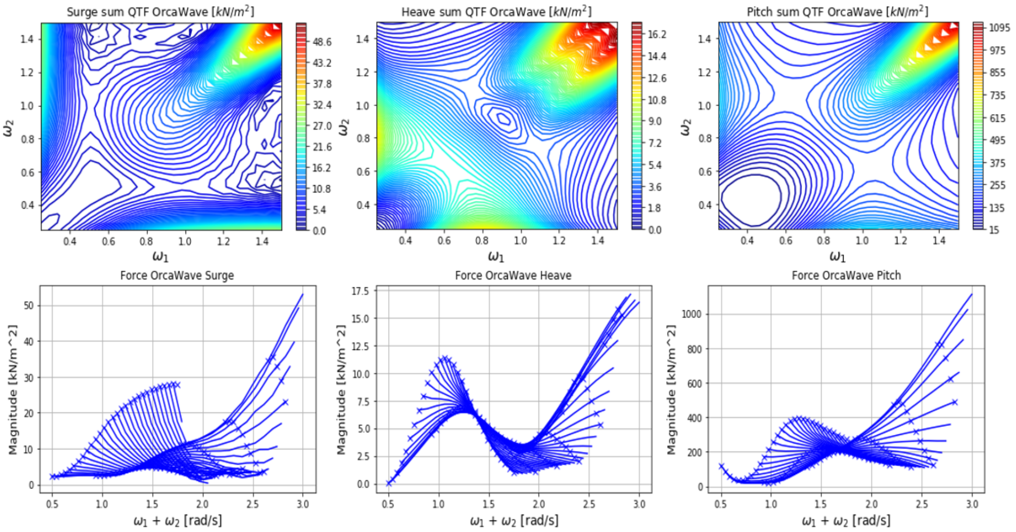

Figure 4.40: Sum frequency QTF results for the UMaine TLP calculated with OrcaWave.

In Figure 4.40, the results of the sum QTFs are illustrated. It can be seen that the solution does not have any similarity to the results in Roald et al. (2014). The results of the NREL are believed to be incorrect and those calculated with OrcaWave are in the right direction. This can be concluded on the basis of the following clues.

The first major clue is given by Roald et al. (2014) itself. For the difference frequencies, it is stated that the analysis is performed incorrectly and that all results should be discarded. However, no statement is made about the sum frequencies. The way the sum and difference frequencies are calculated is quite similar, thus whatever has affected their difference frequency calculation should also have affected their sum frequency calculations. The second clue is seen in the surface graph for the total sum frequency QTFs, where the three DOFs show identical shapes for the surface graphs, which is highly unlikely considering the difference in shape and motion behaviour between the DOFs. The third clue is seen in the comparison of the quadratic loads. The results calculated with OrcaWave are illustrated in Figure 4.41.

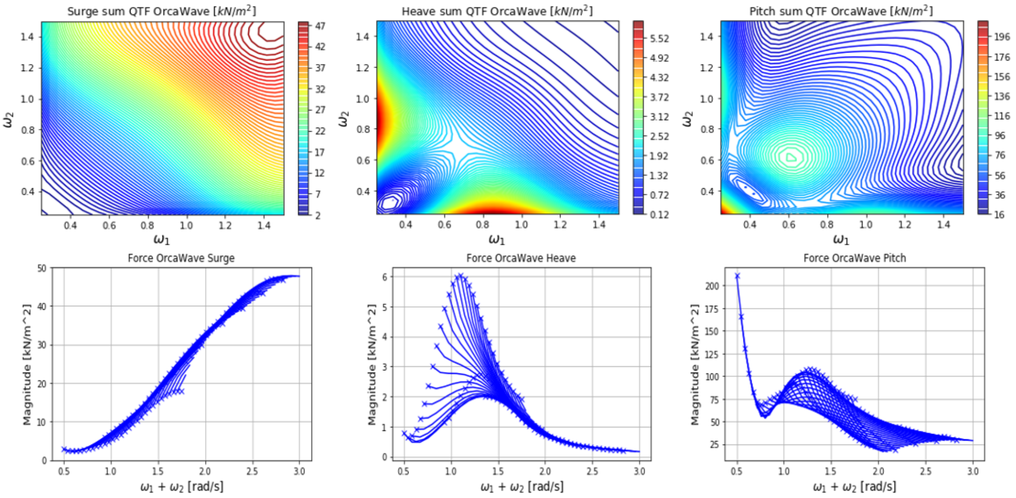

Figure 4.41: Quadratic load part of the sum frequency QTFs for the UMaine TLP calculated with OrcaWave.

As the quadratic loads there a result of first-order body motions and first-order potential solutions, which have shown to be almost identical to the ones presented in the paper, no differences should be expected for these calculations. However, this is not the case. In addition, some carryover is expected between the SPAR and the geometry of the TLP, which is seen, to a lesser extent, in Figure 4.23. The fourth clue is the comparison with Hydrostar. The total sum frequency QTFs are illustrated in Figure 4.42. These show a good comparison with those calculated with OrcaWave. A note should be added that these are calculated with the Python generated free-surface mesh, thus improvement is still to be expected.

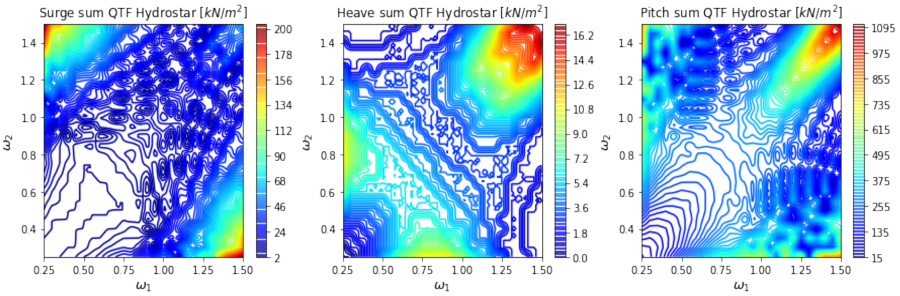

Figure 4.42: Sum frequency QTF for the UMaine TLP conducted with Hydrostar.

Returning to the question of the quadratic load, the fifth clue is seen in the surface plot in Roald et al. (2014). In general, a peak in quadratic load can be expected if a peak in motion RAO is located near this frequency. In the surface plot for the surge DOF, a peak is observed for an incoming wave frequency of 0.6 rad/s, while no peak in motion RAO is seen near this frequency. The sixth and final clue is seen when time simulations are compared with model test data. The NREL concluded that a large overestimation of the second-order force is seen with the time domain simulations. The values of the sum QTF presented by the NREL are a factor 5 to 30 times higher than the values found by OrcaWave and Hydrostar. This could explain why this overestimation is present. Combining these six clues and the fact that the sum frequency analysis for the SPAR structure showed almost identical results, a cautious conclusion can be drawn that the sum frequency results in Figure 4.40 are correct. However, an improvement in the results could be obtained by conducting a convergence study. However, this is saved for the case study TLP from Chapter 3.2 as this is the main focus of this thesis.

As mentioned above, an improvement in the calculation is expected for Hydrostar if a more refined free-surface mesh is applied. This is achieved by integrating the free surface mesh file into the body mesh file. Only the NREL free surface mesh will be used, since it had a favourable running time and showed an accuracy comparable to that of the NETGEN free surface mesh. To see the difference in results, the absolute difference between a simulation with a Python generated and a NREL based free surface mesh is compared. Due to the speed of Hydrostar, the body mesh with 10500 panels could be calculated, this is used for the comparison illustrated in Figure 4.43. There is a significant improvement using the refined free surface, which shows once again the importance of a correctly refined free surface mesh. As expected, the difference is mostly located near the higher range of the incoming wave frequencies, as this is where free surface forcing will be more important. After this refinement is applied, compared to the results of OrcaWave, there is a distinct difference in quality between the two. It is yet to be decided whether this quality difference has an influence on the time-domain simulations within OrcaFlex.

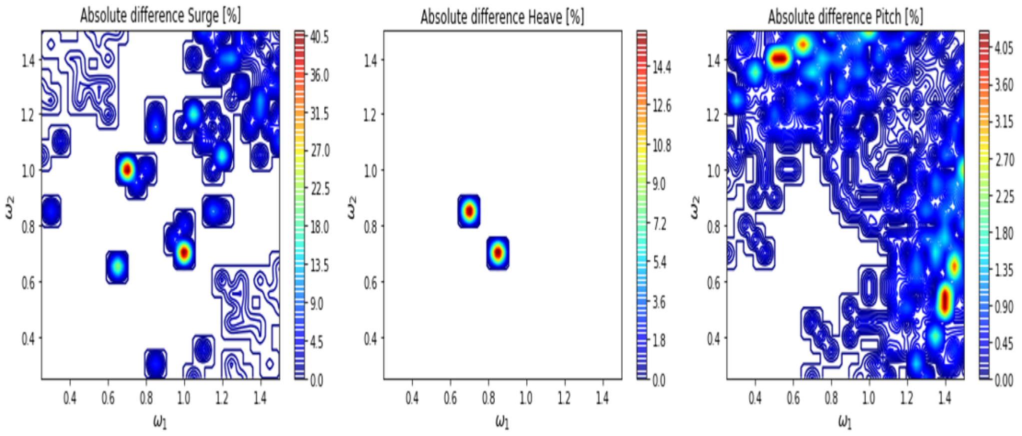

Figure 4.43: Absolute difference in percentage between the sum frequency solution using a Python generated free surface mesh and applying the NREL based free surface made in Salome Meca. Body mesh with 10500 panels is used for the calculation.

To obtain more certainty, an additional run with Hydrostar is performed, where the sum frequency parameters are automatically adjusted during the calculation, the so-called quad method (not available in OrcaWave). This method almost triples the calculation time, which is the reason why it is not applied in the first set of simulations. The results of this simulation are illustrated in Figure 4.44, where the body mesh of 10500 panels is used for the evaluation. This option greatly improves the quality of the Hydrostar calculation. Although the calculation takes a considerable amount of time compared to the previous method, the running time is still only a fraction of what is needed for OrcaWave and the quad method will therefore be used for subsequent analyses.

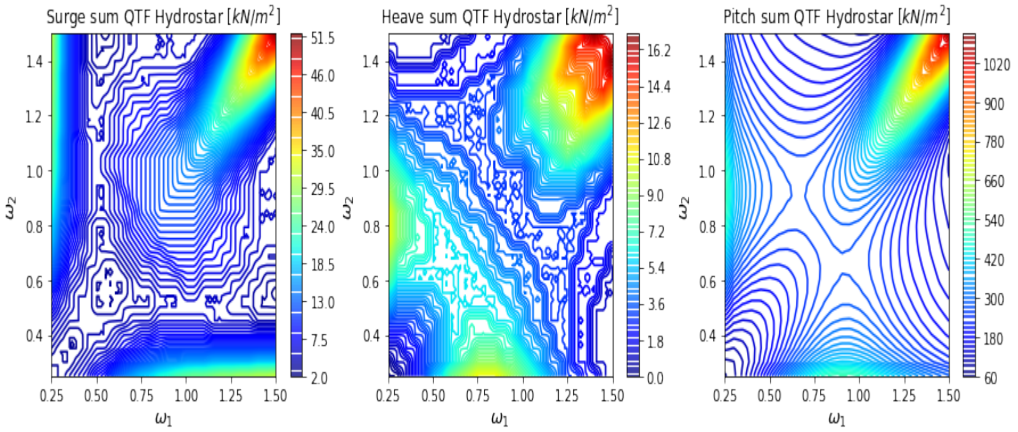

Figure 4.44: Sum QTF of the UMaine TLP applying the quad method from Hydrostar for the evaluation.

4.1.2 Set-up diffraction model

In this chapter, the setup of the diffraction model is discussed. First, the mooring stiffness properties of the TLP are determined in Chapter 4.1.2.1 and the inertia matrix in Chapter 4.1.2.2. Thereafter, the first-order diffraction analysis is conducted in Chapter 4.1.3 followed by the second-order diffraction analysis in Chapter 4.1.4.

4.1.2.1 Mooring stiffness properties

OrcaFlex presents a feature to provide the stiffness properties of the mooring of the total model. Their values are represented in Table 4.3.

	TLP					
wrt global	**X**	**Y**	**Z**	**RX**	**RY**	**RZ**
X	4.19E+02	6.83E-07	1.44E+01	1.07E-01	-7.66E+03	-9.77E-04
Y	3.99E-07	4.19E+02	4.60E-03	7.44E+03	1.07E-01	6.66E+02
Z	1.44E+01	4.60E-03	9.03E+04	8.69E-02	-1.62E+03	-2.14E-01
RX	1.07E-01	7.44E+03	8.69E-02	9.48E+07	-2.82E-02	1.58E+03
RY	-7.66E+03	1.07E-01	-1.62E+03	8.46E-02	9.48E+07	-4.68E+00
RZ	-9.75E-04	6.66E+02	-2.14E-01	1.21E+03	-4.90E+00	8.89E+05

Table 4.3: Mooring stiffness report for the base case model in OrcaFlex.

Two methods are applied to validate the values obtained in the mooring stiffness report. The first method is to calculate the stiffness by applying an incremental load and obtaining the static displacement. The stiffness is calculated by dividing the force by the static displacement and taking the mean of all these values. The second method is to use the analytically derived stiffness equations (see Chapter 2.1.2), where the equations are given for the diagonal of the stiffness matrix.

Applying the force-displacement method in OrcaFlex results in the values summarised in Table 4.4. The estimates are observed to be close to those presented in the mooring stiffness report.

	Diagonal of stiffness matrix					
	C11	**C22**	**C33**	**C44**	**C55**	**C66**
Report	4.19E+02	4.19E+02	9.03E+04	9.48E+07	9.48E+07	8.89E+05
Estimation	4.18E+02	4.18E+02	9.09E+04	9.44E+07	9.44E+07	8.89E+05
Difference	0.05%	0.06%	0.68%	-0.46%	-0.47%	0.00%

Table 4.4: Summarization of stiffness estimation using the force-displacement method.

In Table 4.5, the results of the analytically derived diagonal stiffness terms are shown and compared to the values from the mooring stiffness report. As the approximation uses a rigid model, the stiffness of the flexible elements in the floater are increased to more resemble the rigidity. This could only be performed until a certain value as this caused errors for the static convergence analysis in OrcaFlex. This is why there still exists a small difference between the reported stiffnesses and the analytically derived one. The largest difference is seen for the heave DOF, which is the result of the pontoon arms not being completely rigid. This does not have a large influence on the roll/pitch DOFs due to the fact that only one side of the TLP is put under extra tension when rotated.

	Diagonal of stiffness matrix					
	C11	**C22**	**C33**	**C44**	**C55**	**C66**
Report	4.19E+02	4.19E+02	1.12E+05	1.09E+08	1.09E+08	8.91E+05
Analytical	4.29E+02	4.29E+02	1.17E+05	1.094.E+08	1.09E+08	8.55E+05
Difference	2.38%	2.38%	4.46%	0.44%	0.43%	-4.04%

Table 4.5: Summarization of stiffness estimation using the updated analytical model and comparing the values with the mooring stiffness report.

Only the diagonal elements of the stiffness matrix have been checked as these are the most important ones. Off-diagonal elements can also be controlled with the first method described in this chapter. However, this is not performed as their values are less significant compared to the diagonal terms.

4.1.2.2 Inertial matrix

For the diffraction analysis, only the submerged part is modelled. However, there is also an influence from the structure above the waterline, for example, the tower, RNA, and additionally placed mass objects. To account for these objects, a combined inertial tensor has to be considered. OrcaFlex is capable of obtaining data from individual objects and extracting their inertial components.

		COM wrt to O(0,0,0)		
	mass (te)	**X**	**Y**	**Z**
TLP	2727.1	-0.002	0.000	-13.537
Tower	698.035	-0.139	0.000	68.528
Turbine	385.5794	-12.592	0.000	144.396
Nacelle	630.888	-8.484	0.000	145.621
Additional mass	67.5	-0.107	0.000	55.859
Total	4509.10	-2.2881	0.00	35.980

Table 4.6: Superstructure mass and location with respect to the origin of the model located at (0,0,0).

Using the parallel axis theorem, the following inertia tensor could be calculated for the superstructure with respect to the COM of the total structure.

	Total inertia tensor		
	RX	**RY**	**RZ**
RX	2.15E+07	3.42E+01	1.12E+06
RY	3.42E+01	2.16E+07	-1.74E+01
RZ	1.12E+06	-1.74E+01	1.60E+06

Table 4.7: Calculated inertia tensor to represent the superstructure on top of the TLP. The inertia tensor is calculated with respect to the COM.

This will be added in the diffraction analysis for both OrcaWave and Hydrostar. The added benefit of performing the static calculations of the model is to validate whether the total mass is accounted for in the inertia calculation by comparing it with the static tension in all the tendons. This can be done with the following formula:

$$F_{\text{pre-tension}} = (F_{\text{buoyancy}} - \text{Weight})/N_{\text{tendon}}. \tag{4.1.3}$$

Taking into account the change in submerged volume from the initial volume displayed in Table 3.1, due to a change in static position of the TLP, results in a mass difference of 0.09% compared to Table 4.6. The total mass and the value of the pretension can thus be accounted for.

4.1.2.3 Diffraction mesh

For the creation of the mesh, Salome Meca is used, as this showed to be a reliable and easy-to-use programme, when the mesh was constructed for the UMaine TLP in Chapter 4.1.1.3.

Body mesh

From previous analyses, it was observed that 6700 panels is on the edge of computational efforts. Therefore, this is set as an upper boundary for the creation of the body meshes. Five versions with an increasing number of body panels are created, namely 1200, 2500, 4000, 5000 and 6700 panels, respectively. Special attention is paid to the inclusion of refinements near the free surface and the use of XZ-symmetry to reduce computational effort.

The mesh exported for Salome Meca is a *.dat* extension file. This is transformed to a *.hst* file using Python, which both OrcaWave and Hydrostar can read, ensuring that both diffraction programmes use the same mesh for calculation.

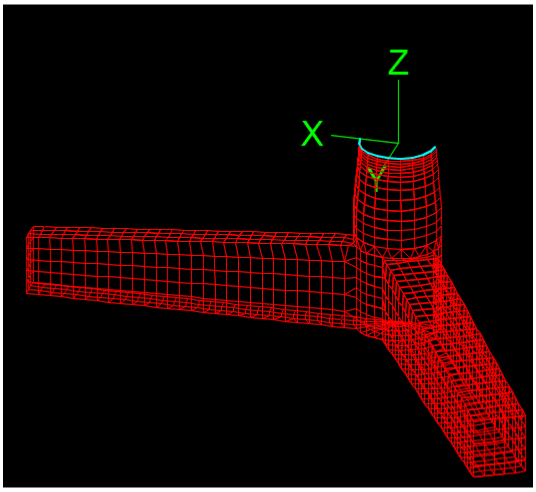

Figure 4.45: Coarsest version of the TLP mesh (1200 panels).

Control-surface mesh

In OrcaWave, the calculation of the mean wave drift force using pressure integration was found to be unreliable (see Chapter 4.1.1.1). This could be resolved by providing a control surface for the application of the mid-field calculation method. In Chapter 4.1.1.3, it was shown that a control box, which mimics the geometry of the body, had the best result. A minimum distance of 2m was applied between the body and the control surface, and the panels between the two meshes were roughly the same size. Special attention was directed toward refinement near the free surface, which had a large influence on the convergence of the HFL. These considerations are taken into account for the creation of the case model control surface. Figure 4.46 illustrates this created control surface.

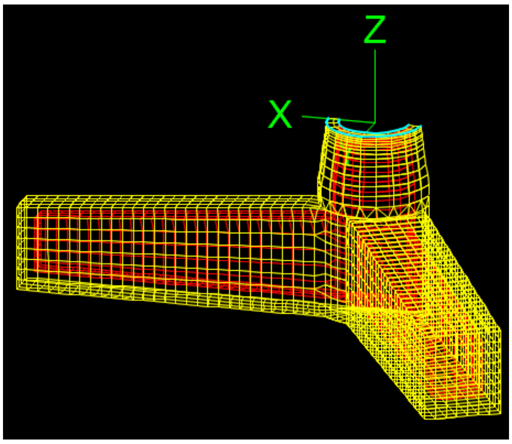

Figure 4.46: Coarsest version of the control surface used for the calculation of mean wave drift force. The red panels represent the mesh for the body, while the yellow ones are the panels for the control surface mesh.

Free-surface mesh

In Chapter 4.1.1.3, a sensitivity analysis was performed to obtain the optimal free-surface mesh structure used in the sum frequency QTF calculations, balancing computational effort and quality. From this analysis, an optimal mesh was found as depicted in Figure 4.47. The optimal parameter for R is to be decided from the second-order sum frequency QTF mesh convergence study, which is performed in Chapter 4.1.4.

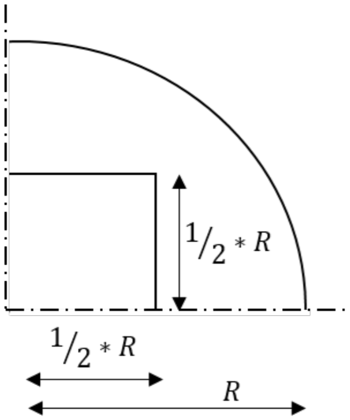

Figure 4.47: Parameterized free-surface mesh analogous to the NREL. Only quarter symmetry is displayed.

4.1.2.4 Viscous drag

As seen in Chapter 4.1.1, problems arise for the diffraction analysis when the calculation frequency coincides with eigenfrequencies. Unrealistic high peaks appear in the motion RAOs, which in turn influences the calculation of quadratic and potential loads. These peaks occur because the matrices of the radiation potential are singular in the eigenfrequencies of the system. This causes the denominator in the solution of the EOM to become zero, resulting in no solution of the RAO at this particular frequency. The occurrence of singularities is caused by the absence of viscosity. Including these effects is done with the inclusion of Morison drag elements.

Both OrcaWave and Hydrostar allow for this inclusion. These elements are applied to the mooring, pontoon arms, and the submerged part of the tower. Values corresponding to these elements are summarised in Table 4.8, where the pontoon arms and tower are assumed to have uniform geometry.

	Morison Parameters				
	Drag diameter [m]		**Drag Coefficients [-]**		
	Normal	**Axial**	**X**	**Y**	**Z**
Pontoon Arm	8.67	0.0	2.2		0.0
Tower	11.0	0.0	1.0		0.0
Mooring line	0.175	0.175	1.2		0.1

Table 4.8: Parameters of Morison elements for the TLP

These Morison elements are sea-state dependent. Therefore, two cases are needed, one of which belongs to DLC 6.1, a ULS case, and the other to DLC 6.4, a FLS case. The values for the significant wave height and peak period are determined from the metaocean data of the location of the case study and are summarised in Table 4.9.

	Hs [m]	**Tp [s]**
FLS	8.0	11.0
ULS	10.9	12.5

Table 4.9: Metaocean parameters for the use of Morison drag elements.

Subfigure 4.48a illustrates an example of the Morison drag model used in OrcaWave, and Subfigure 4.48b illustrates the motion RAOs for the cases with and without viscous damping. As expected, the peaks in the graph remain in the same location as these are related to stiffness and mass. Only the height of the peaks has changed due to the addition of viscous damping, where the ULS case shows a larger damping effect compared to the FLS case.

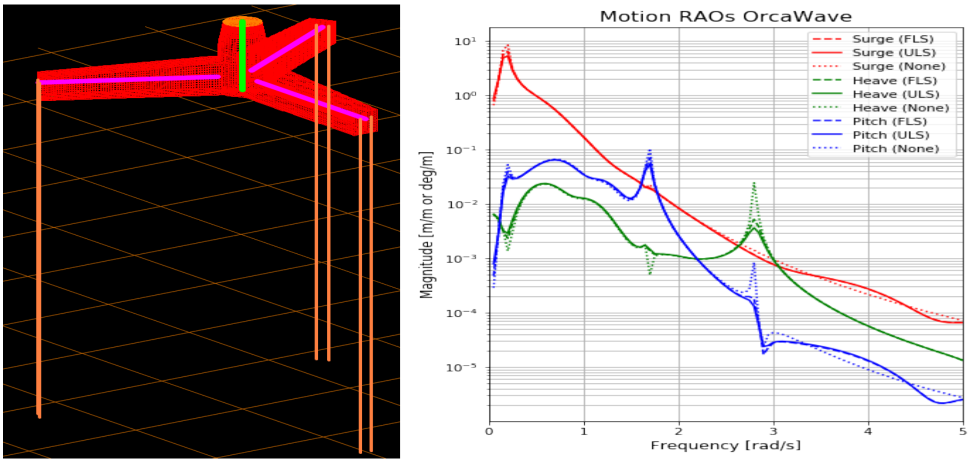

(a) **(b)**

Figure 4.48: Viscous drag model in OrcaWave for the case model TLP. Subfigure 4.48a illustrates the model for which the colored lines represent the Morison drag elements. Subfigure 4.48b illustrates the motion RAOs for the case without viscous and for the cases with viscous damping (FLS & ULS).

Similar results are found with Hydrostar, when applying the same Morison characteristics. However, an error is introduced if the wave direction is changed. The viscous damping of the motion appears to act only in the 0° and 180° wave heading. Therefore, if a wave heading of 90° is applied, the motion RAO in sway resembles the undamped motion RAO. Therefore, linear damping is applied to the total system to eliminate this error. The amount of linear damping is estimated by matching the height of the peaks with the Morison drag model.

4.1.2.5 Inclusion of tower flexibility

As seen in Chapter 3.2.2, it was concluded that the flexing of the tower caused the pitch eigenfrequency of the system to change from 1.7 rad/s to 0.98 rad/s. It is not possible to incorporate this DOF of the tower into the diffraction programmes used. However, the paper of Gueydon et al. (2015) suggests adjusting the global stiffness of the system so that the eigenfrequency matches that of the system with a flexible tower. This can be done by calculating the new stiffness value using Equation 2.1.7. An iterative scheme is applied, due to the frequency-dependent added mass component in the equation, to approach the correct value. The approach to the correct value is illustrated in the figure below and resulted in an adjusted stiffness value of $34 \cdot 10^{6}$ kN/m.

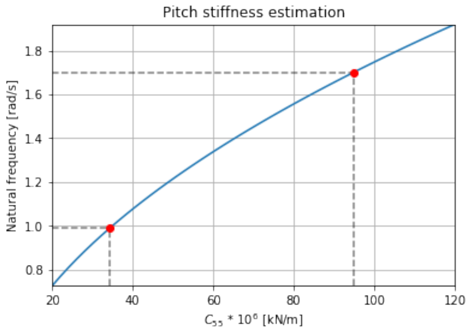

Figure 4.49: Pitch stiffness estimation for the TLP. For the correct pitch eigenfrequency of 0.98 rad/s, an adjusted stiffness of $34 \cdot 10^{6}$ kN/m is estimated.

Incorporating this newly calculated stiffness into the OrcaWave constraints, results in the motion RAO illustrated in Figure 4.50. It is seen that the motion RAO with adjusted stiffness now results in a correctly located pitch eigenfrequency. The downside of this adjustment is that the amplitude in the wave frequency region (0.1-1.4 rad/s) is significantly higher. This is attributed to the fact that, as a result of lowering the stiffness, the total structure is now more susceptible to lower wave frequency excitation. The peak at 0.98 rad/s for the OrcaFlex generated motion RAO is not the result of the stiffness of the mooring alone, but is a consequence of the interaction between the floater mooring stiffness and the flexibility of the tower. his overestimation of wave frequency related motions is also seen in the paper from Gueydon et al. (2015). Although correctly calculating the eigenfrequency peak, differences in the wave frequency are considered too large. Therefore, another option is explored to approximate the correct motion RAO.

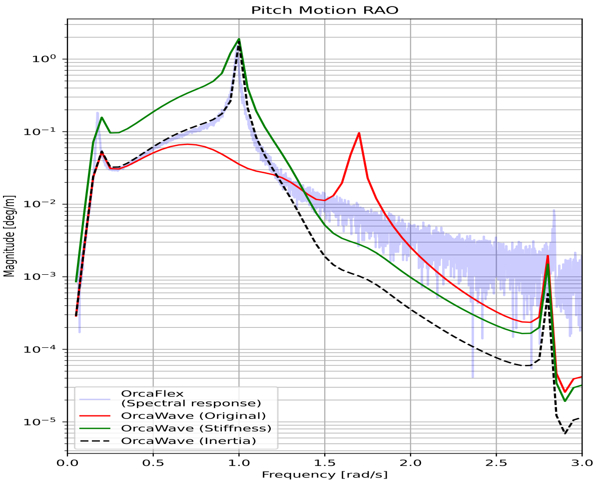

Figure 4.50: Comparison of motion RAO in the pitch DOF for the TLP. Different adjustment methods are applied in order to have more resemblance with the white noise generated motion RAO.

This other option is to adjust the inertia term in Equation 2.1.7. The same method as before is applied, resulting in a value for the inertia term of $80 \cdot 10^9 \ kg \cdot m^2$, for which an illustration is also included in Figure 4.50. This approaches the OrcaFlex signal significantly better in the wave frequency region. Only after 1.3 rad/s is a divergence from OrcaFlex observed. This is as expected, as the increase of inertia will resist, to a larger degree, the motions situated in the higher wave frequency ranges. In terms of second-order analysis, it is expected that the quadratic loads will be approximated with more accuracy, since the motion is correctly predicted in the frequency ranges, where the magnitudes of these motions are relatively large. Divergence occurs only for magnitudes in motion below 0.01 deg/m, therefore, it will have a low contribution to the sum frequency QTF.

Taking into account the two possibilities of adjusting the motion RAO as discussed above, the adjustment of the inertia term seems the most promising method. This is due to the better approximation of the motion RAO in the important wave frequency range. Additionally, the adjustment of the inertia is an easier method, as the mooring system will be adjusted. This adjustment in the mooring system would alter the stiffness properties, for which, in every iteration, the correct stiffness is to be calculated based on newly generated spectral response graphs. It is expected that this is not needed for the inertia method, as the inertia remains the same for all mooring system adjustments and therefore already approximating the correct pitch eigenfrequency.

4.1.3 First-order results

4.1.3.1 Load RAO

For the start of the first-order analysis, the load RAOs are evaluated. Only surge, heave, and pitch are taken into account, since the other DOFs have a negligible value due to the symmetry in the TLP. Figure 4.51 illustrates these RAOs. from which it is observed that the results are quite similar to those of the UMaine TLP, which is due to similarities in the geometry of the structure and mooring characteristics. Below a frequency of 3 rad/s, almost no difference is observable between the different meshes. Above a frequency of 3 rad/s, larger number of panels is needed to obtain absolute mesh convergence. The eigenfrequencies of the floater are, however, below this frequency, thus a coarser body discretization can be acceptable for first-order wave load simulations. This may, however, not be the case for the second-order analysis. Thus, the final acceptable body mesh depends on the mesh convergence study for the second-order diffraction analysis.

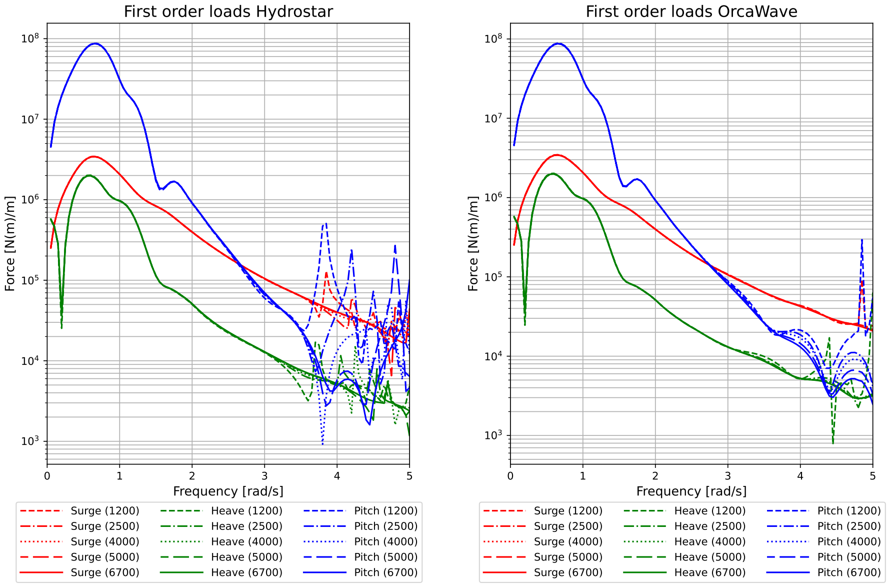

(a) (b)

Figure 4.51: First order loads results for the case model TLP.

In terms of convergence, the mesh variant of 6700 panels is used as a reference. Figure 4.52 illustrates the mesh convergence for different mesh variants. OrcaWave tends to have a better convergence rate than Hydrostar. This is mainly attributed to the approximation of the load RAO after 3 rad/s. For Hydrostar, the convergence with respect of the most refined mesh variant is 2% compared to 0.25% for OrcaWave.

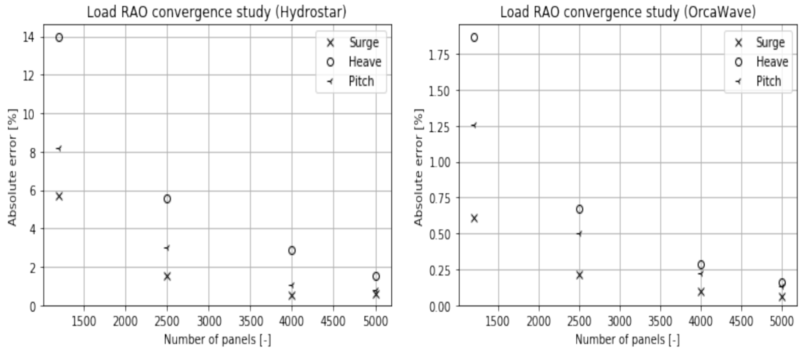

(a) **(b)**

Figure 4.52: Convergence study for the load RAOs of the case model TLP. Convergence is referenced to the finest mesh size of 6700 panels.

4.1.3.2 Hydrodynamic coefficients

The results for the hydrodynamic coefficients are summarised in Appendix B.1. Only the relevant DOFs are illustrated. For the added mass, it can be seen that overall the values are almost identical between Hydrostar and OrcaWave. An small shift is seen, for which an explanation cannot be given. In the validation for the OC3-Hywind spar and UMaine TLP, a similar shift was observed, which did not result in significant differences for subsequent analyses.

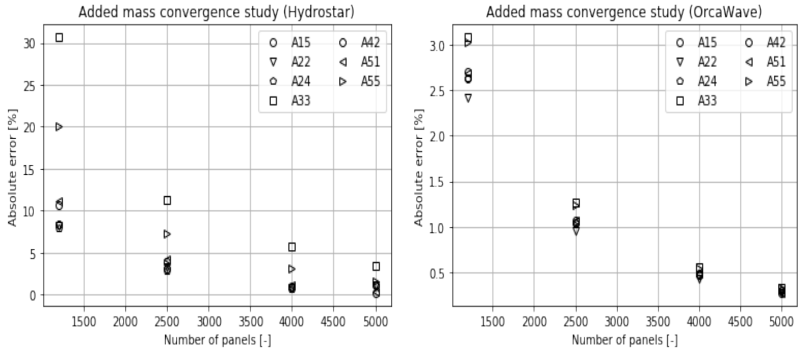

(a) **(b)**

Figure 4.53: Convergence study for the added mass of the TLP. Convergence is referenced to the finest mesh size of 6700 panels.

For the overall convergence of the added mass, where the most refined mesh is used for reference, some noticeable difference is observed between OrcaWave and Hydrostar. Based on Figure 4.53, OrcaWave has an overall convergence of 0.25%, while Hydrostar only reaches a convergence of 4%. For both programmes, the added mass in heave is the leading factor for which mesh convergence is difficult to obtain. Nevertheless, the location where these differences occur is in the higher frequency region, for which the influence on the total results will be negligible due to its subsequent low magnitudes.

For the damping coefficients, almost no difference is seen, not even on the logarithmic scale. It is only after 4 rad/s that the curve for OrcaWave seems to diverge. This is attributed to the discretization error of the body. A larger number of body panels should reduce this difference, but the results are significantly low in value. As concluded for the added mass, these small differences do not have a large influence on the motion RAOs, so no refinement of the body mesh is needed.

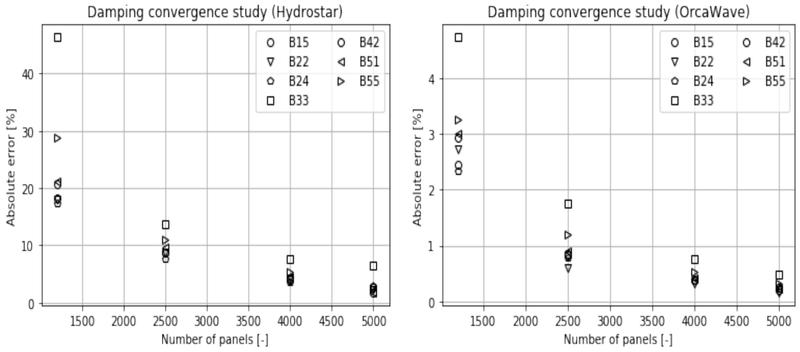

(a) **(b)**

Figure 4.54: Convergence study for the hydrodynamic damping of the case model TLP. Convergence is referenced to the finest mesh size of 6700 panels.

In terms of convergence for the damping term, the results are comparable to those for the added mass. Overall, OrcaWave tends to have better convergence with coarser mesh sizes than Hydrostar does. This can also be attributed to the stability of the solution after 4 rad/s.

4.1.3.3 Motion RAO

For the mesh convergence study considering the motion RAOs, is performed that includes the effects of viscous fluids and the effects caused by tower flexibility, for which the results are illustrated in Figure 4.55.

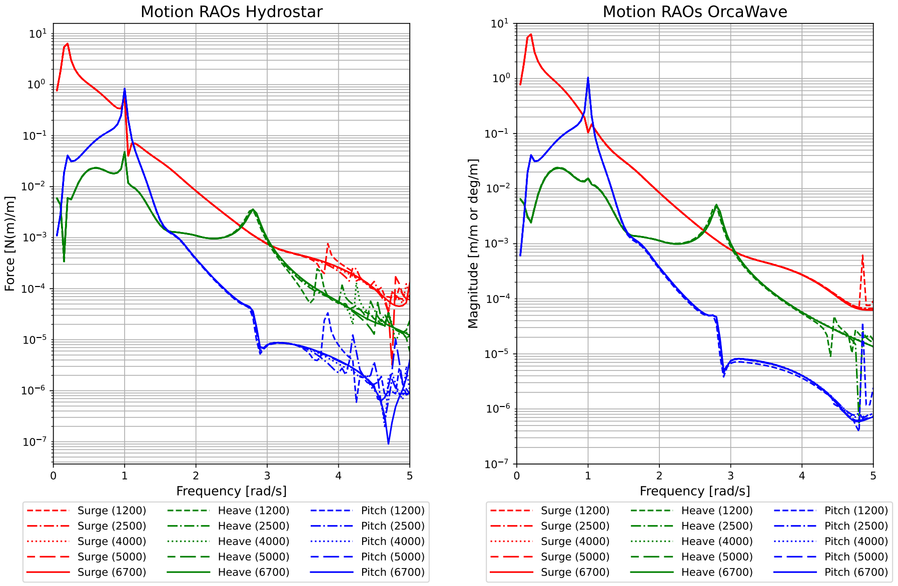

(a) **(b)**

Figure 4.55: Motion RAOs for the case model TLP. The flexibility of the tower is included and the analysis is done for the ULS viscous drag case.

As was seen with the previous first-order results, the results for OrcaWave seem to be more convergent than those for Hydrostar. This convergence is also mainly present after 4 rad/s for OrcaWave and after 3 rad/s for Hydrostar. For the lower frequencies, some small differences are present between the two. These are mainly related to the influence of pitch eigenfrequencies on the motion RAOs in surge and heave DOFs. This coupling between these DOFs seems to be greater in Hydrostar than in OrcaWave. This coupling difference is also present in calculations without any inertia and viscous drag adjustments. Therefore, it is not known why this is the case. Consequently, some differences around this pitch eigenfrequency are expected to be present in the second-order analysis, especially for the quadratic load calculations.

Figure 4.56 illustrates the motion RAOs mesh convergence study, where the most refined body mesh is chosen as a reference. This confirms the difference in the convergence rates between the two programmes. Taking into consideration the accuracy and the calculation time for the second-order analysis, it is decided that for OrcaWave, the 4000 panels body mesh variant is chosen for the full QTF calculations and for Hydrostar, the 6700 panels body mesh variant as this is much faster in the calculation process.

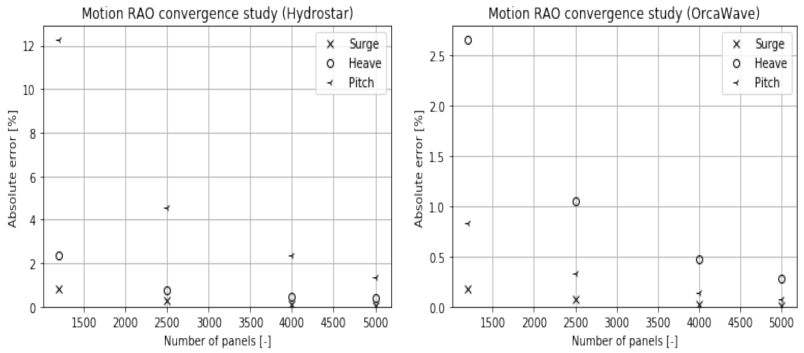

(a) **(b)**

Figure 4.56: Convergence study for the motion RAOs of the TLP. Convergence is referenced to the finest mesh size of 6700 panels.

4.1.4 Second-order results

4.1.4.1 Mean drift force

For the calculation of the drift force, the control surface is used for OrcaWave, as the integration of direct pressures appeared to be unreliable (see Chapter 4.1.1.3). For Hydrostar, the far-field method is used. The results are illustrated in Figure 4.57. The FLS viscous drag case is used for comparison. For both Hydrostar and OrcaWave, the results seem to be converging as the mesh is refined. A new large peak is observed, which is not seen before in drift calculations made in Chapter 4.1.1. This is the peak in the pitch eigenfrequency, which obtains a large value due to the presence of a substantial amount of wave energy at this distinct wave frequency and a large value in the motion RAOs. The first peak is related to the surge DOF. In the higher frequency range, both Hydrostar and OrcaWave seem to be approaching the HFL correctly.

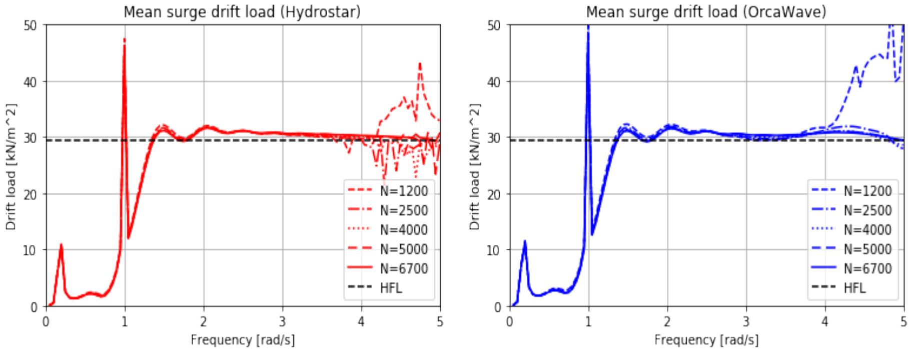

(a) **(b)**

Figure 4.57: Mesh convergence study considering the mean surge drift force for the case model TLP.

In Figure 4.58, the convergence study is illustrated. For Hydrostar, the convergence is only 4% compared to the most refined mesh, while OrcaWave already has up to 0.25% convergence for the 4000 panel mesh variant. This confirms the conclusion for the body mesh selected in Chapter 4.1.3.3, that 4000 panels are enough for the QTF analysis with OrcaWave, while 6700 panels are needed for Hydrostar. This large difference in convergence is mainly due to instabilities in the HFL calculations.

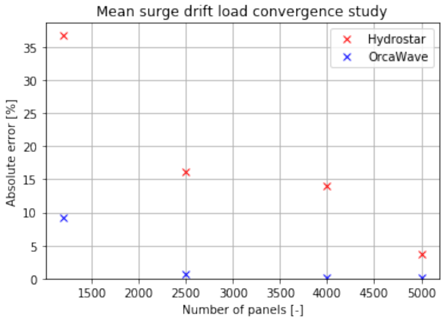

Figure 4.58: Mesh convergence study for the mean surge drift load for the case model TLP. The convergence is referenced to the finest mesh size of 6700 panels.

Furthermore, the mean surge drift load is directly compared between the two programmes in Figure 4.59. This shows almost identical results, thus concluding that the previously found differences in the motion RAOs, do not have a large influence on the drift calculations.

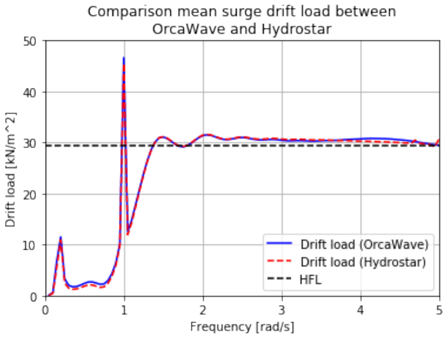

Figure 4.59: Comparison of the mean surge drift load for Hydrostar and OrcaWave. The most refined body mesh is used for the comparison.

4.1.4.2 Full QTF

For the complete QTF calculation, a more extensive mesh convergence study is needed. This is done with the following method, as explained in Roald et al. (2014). There are in essence three parameters to be adjusted if the calculation is done without a quadrature zone. The partition radius (PartR), the scaling factor between the free surface and body panels (Scale), and the number of panels on the body (NPan). This mesh convergence study is done with OrcaWave for which the focus will be on the potential load, as the convergence of the quadratic load depends on the mesh convergence of first-order terms. Roald et al. (2014) recommends to calculate two incoming wave frequencies, 1 and 1.35 rad/s, respectively. The results are illustrated in Appendix B.2.1. For further calculations, the ULS viscous drag model is used.

For PartR, different values for the radius are between 75m and 300m with increments of 25m. From the figures presented in Appendix B.2.1.1, it is concluded that the results stabilise at a partition radius of 175/200m, where the relative change in the result is 2% for heave and 0.1% for surge and pitch. A choice is made for a partition radius of 175m, as this will reduce computational effort (see Figure 4.60). An additional observation is the difference between direct and indirect solutions for a changing partition radius. This difference between the two seems to remain constant. This can be explained due to the fact that the overall solution depends on the accuracy of the evaluation of the asymptotic simplification at the partition radius. This is mainly influenced by the size of this radius, so convergence in the asymptotic evaluation is reached at 175m. However, the scaling and body discretization remain the same, therefore showing a constant discrepancy between the direct and indirect solutions.

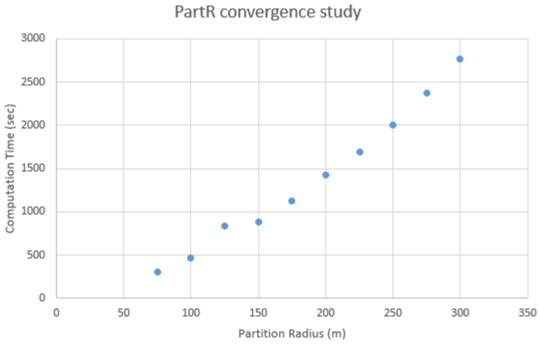

Figure 4.60: Computational effort for the PartR convergence study. The analysis is done with OrcaWave, using a body mesh of 4000 panels (NPan) and a scale of 2 (Scale) for the free-surface panels. The results show a linearly increasing computing time for an increasing partition radius.

The next phase of the mesh convergence study is the scaling of the free-surface panels. For this, the previously selected partition radius of 175m is applied, combined with the original used body mesh of 4000 panels. The results are illustrated in Appendix B.2.1.2. This shows that the scaling of the free-surface panels has a large influence on the convergence between the direct and indirect methods. This is expected because it is often mentioned in the literature that the panel density of the free-surface mesh has a large influence on the accuracy of the evaluation. It is also observed that the indirect method shows an earlier stabilisation of the results compared to the direct method. This is in line with what was observed with the sum frequency QTF analysis for the OC3-Hywind spar in Chapter 4.1.1.2. It is therefore more reliable to use the indirect method for the final solution. Large bumps in computational effort are seen between scaling increments, therefore, a scale of 1.5 is chosen for the final calculation, as this shows only a 1% difference in results between mesh discretization steps for all three DOFs, while maintaining reasonable computational effort.

The last part of the mesh convergence study is to adjust the refinement for the body mesh. For this, the previously generated body mesh discretizations are used. For the free surface, a partition radius of 175m and a scale of 1.5 are used. The results are illustrated in Appendix B.2.1.3. This also shows a more stable output of the indirect method for the solution. In general, the choice of selecting 4000 panels for body mesh seems sufficient, as the change in results is limited to 1.5%. The number of panels also just allows to be run on all the available threads of the computer. For quadratic loads, the average change in results between the body mesh discretization steps is found to be around 0.5%, while the results for the difference frequencies have converged to an average value of 1%.

For the calculation of the full frequency range, it is important to select frequencies such that all natural frequencies are captured. However, as mentioned previously, the calculation times for OrcaWave are on the order of days. A rough estimate is illustrated in Figure 4.61. A calculation until the eigenfrequency of heave (≈ 3 rad/s), which is the highest in the system, takes almost 5 days to complete. Due to time constraints in this project, the maximum incoming wave frequency is restricted to 2.5 rad/s, which will almost half the total calculation time.

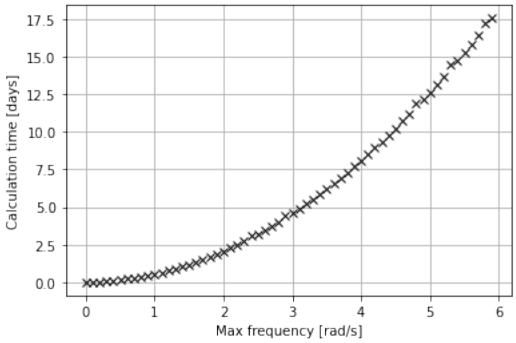

Figure 4.61: Estimated calculation time for an OrcaWave simulation. This is based on a 16 thread computer with 64GB of memory. The frequency step in the simulation is 0.05 rad/s.

As a starting point, the solution for the potential load is compared using the direct and indirect methods. This is illustrated in Figure 4.62. There are still some differences between the two solutions. These are mainly located in the higher frequency ranges. The mesh convergence study is only performed until an incoming wave frequency of 1.35 rad/s. Extending this to 2.5 rad/s would be a better option. However, the analysis is already on the computational limit. Therefore, no refinement of the model will be performed. Nevertheless, in the early stages of this research, differences between the direct and indirect solutions were observed in the ranges of GN's, thus overall there is a large improvement. From the analyses done in Chapter 4.1.1 and from the mesh convergence study, the solution from the indirect method has shown to be more robust. Therefore, this method is chosen in further analyses.

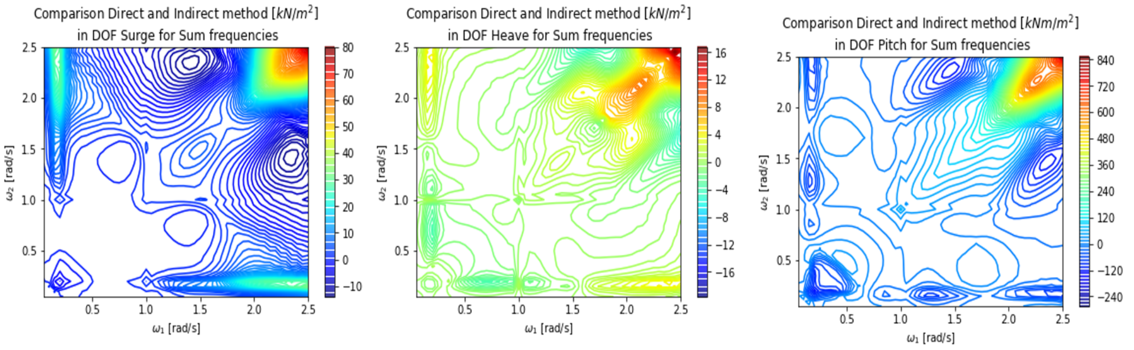

Figure 4.62: Comparison of the potential load using the direct and indirect methods.

The results of the total sum QTFs are illustrated in Figure 4.63. The first finding is the influence of the pitch eigenfrequency at 1 rad/s. This locally increases the value of the QTF for all three DOFs. This increase in value is also present in the surge eigenfrequency. Apart from the influence of the pitch eigenfrequency, the results look similar to those found for the UMaine TLP (see Chapter 4.1.1.3).

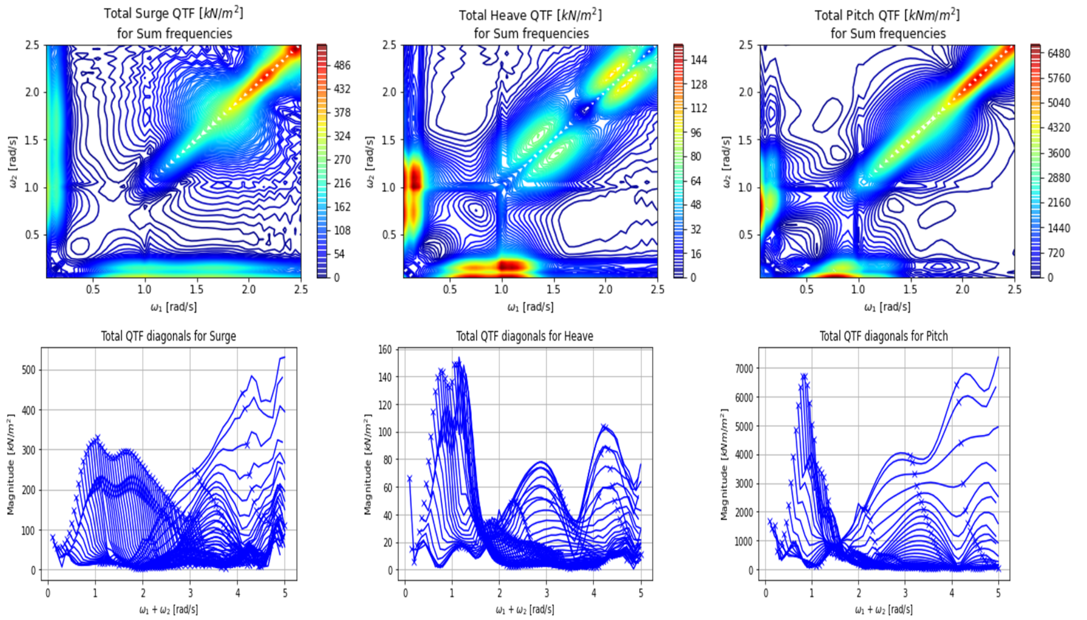

Figure 4.63: Total QTFs for the case model TLP. The solution is calculated using the control surface for the quadratic load part and the indirect method for the potential load part. The analysis is performed with OrcaWave. The top row represents the surface plot, while the bottom row represents the diagonals for which the difference between the two incoming wave frequencies is constant ($\omega_1 - \omega_2$ =constant).

Furthermore, the contribution of the quadratic loads is illustrated in Figure 4.64. This logically shows the presence of eigenfrequencies as well. It is also seen that the forces are mainly located near the lower frequency range. This absence of large values in the higher frequency range is caused by the low values of body motions and first-order potential values. This shows the need to include the potential load, where the values are mostly high in the higher frequency ranges.

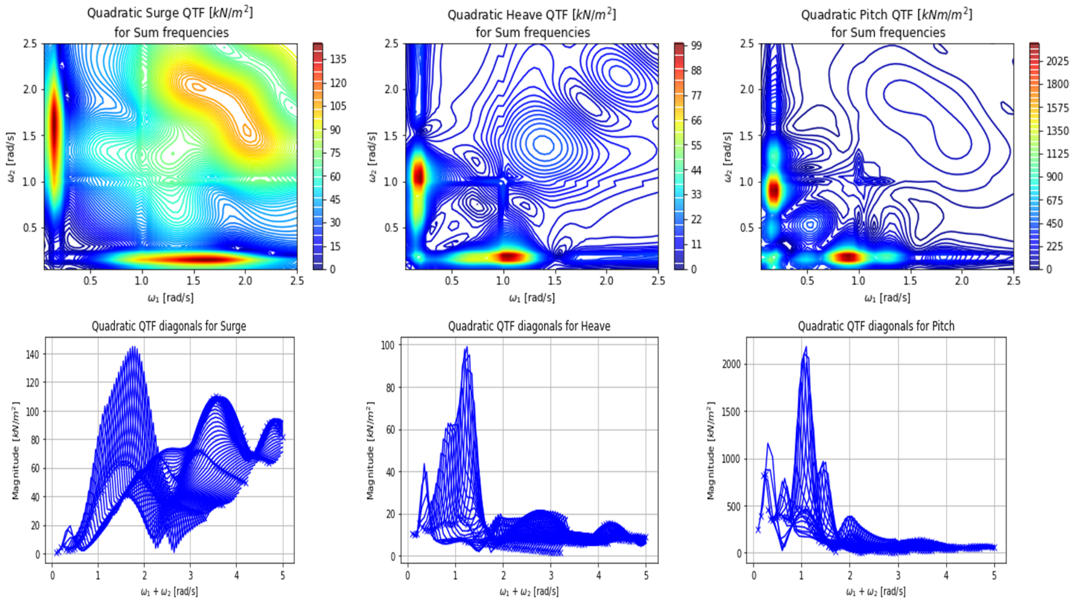

Figure 4.64: Quadratic load QTFs for the case model TLP. The solution is calculated using the control surface method. The analysis is performed with OrcaWave. The top row represents the surface plot, while the bottom row represents the diagonals for which the difference between the two incoming wave frequencies is constant ($\omega_1 - \omega_2 =$constant).

For completeness of the full QTF analysis, the difference frequencies QTFs are illustrated in Appendix B.2.2. Compared to the sum frequencies, the difference frequencies show overall fewer differences between the direct and indirect methods, attributed to the fact that is far easier to obtain convergence in the solution. Therefore, a mesh convergence study is not necessary if such a study is performed for sum frequencies QTFs. An additional check for the difference frequencies QTF, is to compare the diagonal of the difference frequency QTF with the mean drift load calculation, as these should result in the same answer. This is illustrated in Figure 4.65, which shows that this indeed is the case.

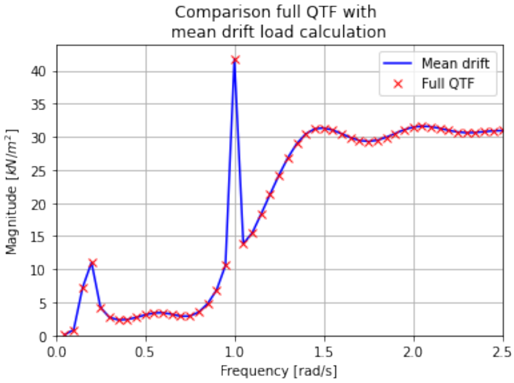

Figure 4.65: Comparison between the mean drift load calculation, and the diagonal of the full difference frequencies QTF calculation for the DOF of surge.

Hydrostar results are illustrated in Figure 4.66. These show good similarity to the OrcaWave results (see Figure 4.63). Even the presence of the pitch eigenfrequency in the QTFs seems identical in shape and value. However, differences are noticeable around the eigenfrequency of the surge DOF. This can be attributed to the damping model. In Chapter 4.1.2.4, it was decided to apply linear damping, since the Morison elements seemed to only dampen the motion if the heading is 0° or 180°. Nevertheless, solutions that exclude regions near an eigenfrequency seems almost identical.

The quadratic load calculations cannot be performed with the control surface method, as this showed erroneous results for Hydrostar. Therefore, these are calculated using the near-field method, which might also cause some differences between the two diffraction programmes. However, the differences are considered negligible. For subsequent reiterations of the diffraction analyses due to changing mooring characteristics, a choice may be directed to Hydrostar for its optimal running time (almost 5 times less than with OrcaWave).

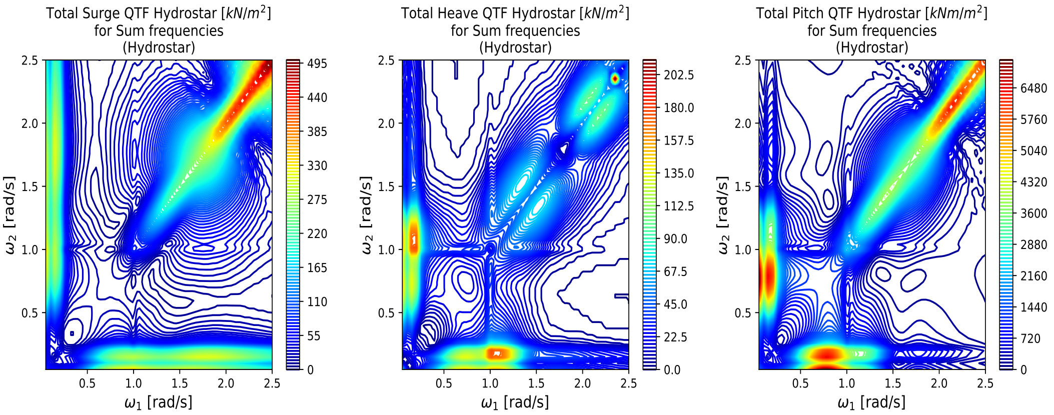

Figure 4.66: Total sum frequency QTFs for the case model TLP. The solution is calculated with Hydrostar using the pressure integration for the quadratic load part and the indirect method for the potential load part.

The difference frequency QTFs calculated with Hydrostar is also considered and illustrated in Appendix B.2.2. These show results similar to OrcaWave, but with the same issue of having some small differences near the eigenfrequency of the system. However, these differences are again considered negligible.

4.1.5 Diffraction analyses of adjusted models

4.1.5.1 Tendon angle adjustment

The tendon angles presented in Table 3.3 are used for the TLP. For every tendon angle, the stiffness of the system should be adjusted. This is done in the same matter as presented in Chapter 4.1.2. Additionally, a check is performed with a spectral response graph, calculated with OrcaFlex, to see if the motion RAOs matches those generated from OrcaWave.

This introduces a problem. As concluded in Chapter 4.1.2.5, the inertia term is adjusted in order to capture the shift in pitch eigenfrequency due to the flexibility of the tower. However, a larger mismatch in pitch eigenfrequency appears to occur as the angle of the tendons increases. This can be explained as follows. Inclining the tendons causes a large coupling between surge and pitch. In Figure 4.67, the eigenmode of surge is shown for the system, with increasing tendon angles. When the tendons are at a 0° inclination, thus the classical TLP configuration, the "surge" eigenmode seems to be a pure motion in surge direction, therefore, not affecting the pitch eigenmode. However, this changes when an inclination is introduced. For the "surge" eigenmode, the system is rotating around a fixed point instead of showing a pure translational motion. It is not an easy task to mimic this behaviour with a globally applied stiffness matrix, which is used in both diffraction programmes. Therefore, OrcaWave and Hydrostar underestimate the eigenfrequency peak of surge in the motion RAOs and miscalculate the behaviour of the TLP around the pitch eigenfrequency. Therefore, the tendon angles will only be adjusted up to 21°, since from this point on the mismatch is too large between OrcaFlex and the diffraction programmes, as the increased coupling between surge and pitch seems to disappear after 21°.

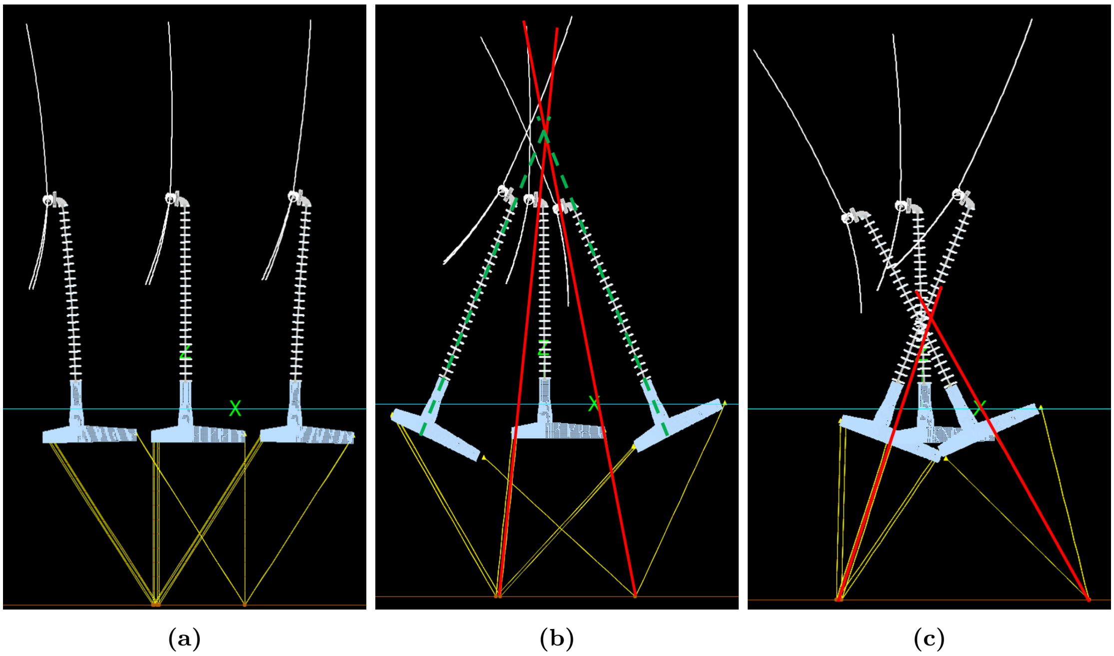
(a) (b) (c)

Figure 4.67: Surge eigenmode for the TLP. From left to right, the tendon angles are 0°, 12° and 30°.

This increasing coupling of surge and pitch is also seen when plotting the spectral response graphs for all the adjusted tendon angles. This is illustrated in Figure 4.68. It can be seen that with an increasing tendon angle, the peak located at the pitch eigenfrequency increases in the spectral response graph for surge, and the peak located at the surge eigenfrequency increases in the spectral response graph for pitch. Additionally, the increase in the surge eigenfrequency peak is also present in the spectral response graph for heave and influences, to a larger degree, the location of the heave eigenfrequency. This shift in heave eigenfrequency is also not captured with OrcaWave or Hydrostar. The surge peak in the spectral response graph for surge is logically decreasing due to the restriction in this DOF.

An additional observation from Figure 4.67, is that the rotation point is located in the crossing of the lines extending from the angled mooring lines (red lines in the figure). It is known that nacelle acceleration imposes a large requirement on the structure, as this need to be as low as possible. Therefore, the location of the rotation point in the nacelle is expected to have an optimal effect on the life of the turbine.

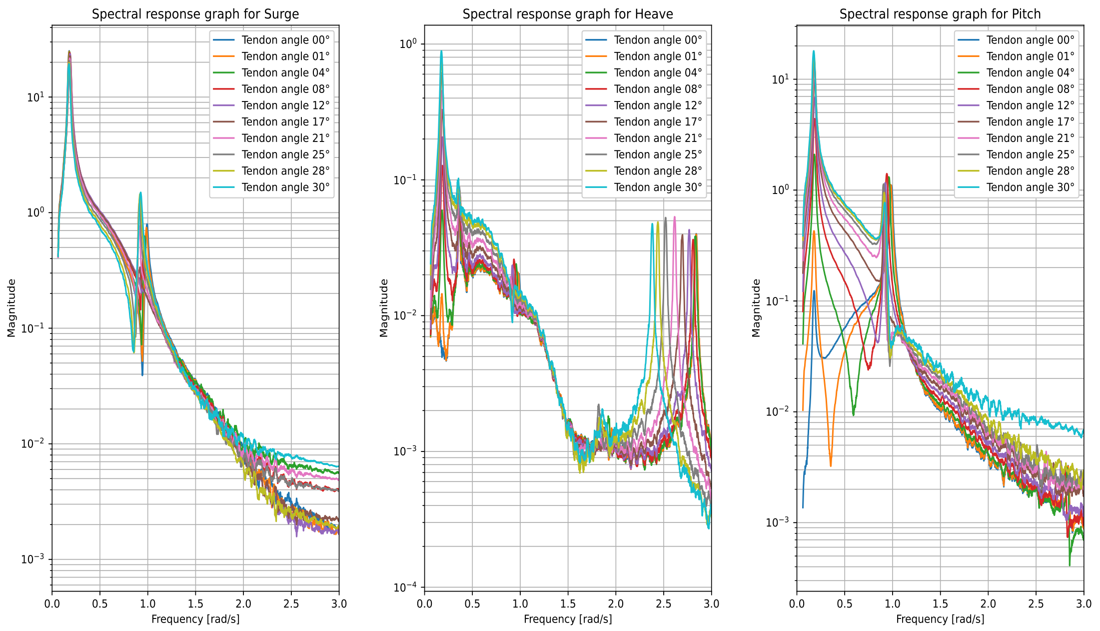

(a) **(b)** **(c)**

Figure 4.68: Spectral response graphs calculated with OrcaFlex, for the DOFs surge, heave and pitch. In the graphs, all the tendon angle adjustments are considered.

This mismatch between the full nonlinear model in OrcaFlex and the simplified model in OrcaWave and Hydrostar have no influence on the first-order calculations, due to the absence of body motions in those calculations. However, differences will occur in the second-order diffraction analysis. Especially for quadratic load calculations and, to a lesser degree, for the potential load. Yet to date, it is not possible to incorporate total nonlinear models into available diffraction software, and the second-order results will be less accurate as the tendon angle increases.

The results for the sum QTFs are summarised in Appendix B.3.1. From these QTFs, the following can be observed. As the angle of the tendon increases, the magnitudes near the pitch eigenfrequency become smaller. However, after a particular angle, the influence of the pitch eigenfrequency on the QTF magnitudes increases, surpassing the magnitudes of the base case tendon configuration. The same is observed in Appendix B.3.2, where the differences between the classical and inclined configurations are illustrated. This is related to the way the TLP changes its motion behaviour as the tendons are inclined. From the comparison, it can also be seen that the changes are mainly located near the lower and wave frequency regions. This is due to the fact that the only changes in the calculation for inclined tendons are the motion RAOs. Since these motion RAOs have a negligible value in the higher frequency ranges, the value of the QTF will depend only on the shape of the body, which remains the same.

For high-frequency responses, it is favourable to avoid forcing in these high-frequency eigenmodes. Therefore, it is believed that inclining the tendons too much, might have an unfavourable effect in decreasing the occurrence of springing. It is to be seen from TD analyses if this expectation is indeed correct.

4.1.5.2 Axial stiffness adjustment

The stiffness values presented in Table 3.3 are incorporated into the TLP mooring system. Because the tendon angles remain vertical, no inertia adjustment is necessary when changing the stiffness of the tendon. The difference in behaviour at the first-order level is shown with the OrcaFlex generated motion RAOs (spectral response graphs). This is illustrated in Figure 4.69, from which the following can be observed. In general, increasing the stiffness of the tendon mainly influences the heave eigenfrequency. An increase in stiffness causes the heave eigenfrequency to shift to a higher frequency. Taking into account Equation 2.1.13, this is as expected. This shift to a higher frequency also seems to lower the amplitude of heave, which is a result of lower wave energy in the high frequency tail of the wave spectrum. The eigenfrequency peak for surge is not affected, which is also expected according to Equation 2.1.14a, where there is no dependence on the axial stiffness.

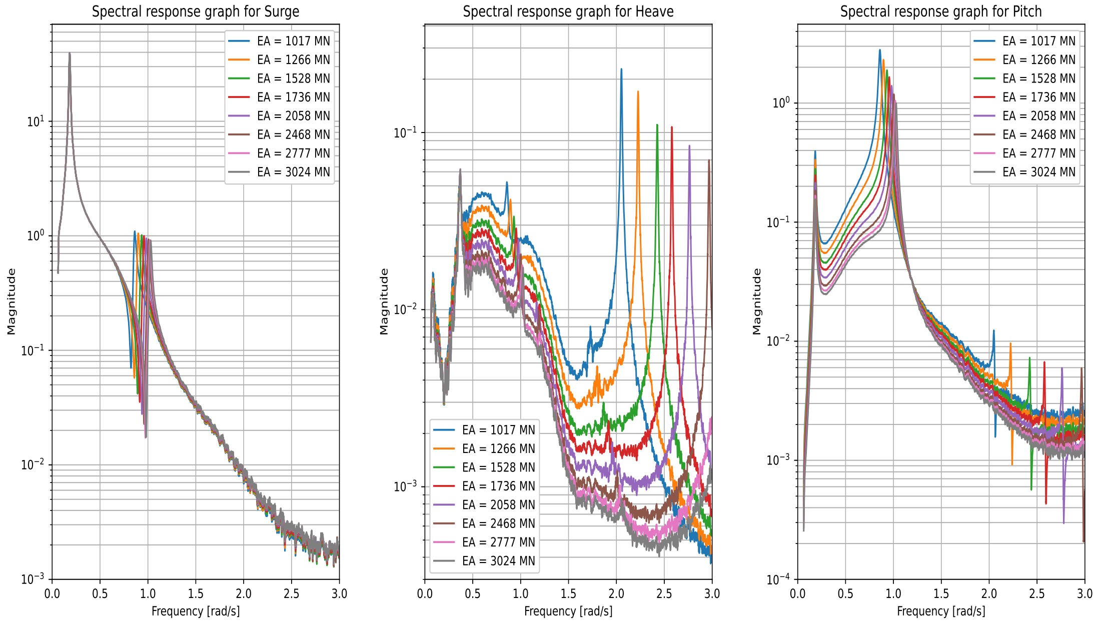

(a) **(b)** **(c)**

Figure 4.69: Spectral response graphs calculated with OrcaFlex, for the DOFs surge, heave and pitch. In the graphs, all the stiffness adjustments are considered.

For the pitch DOF, the same is observed as for the heave DOF, where an increase in stiffness causes a shift of the eigenfrequency towards the higher frequency range. However, the rate of this shift is lower than expected. From Equation 2.1.12, the slope of the increase in natural frequency, due to an increase in tendon stiffness, is a factor three times higher than what is observed with OrcaFlex (see Figure 4.70). The differences between the theoretic and OrcaFlex generated eigenfrequencies are mainly the result of simplifications for the theoretic part and due to a number of non-rigid components still present in the system, in particular the tower and the RNA.

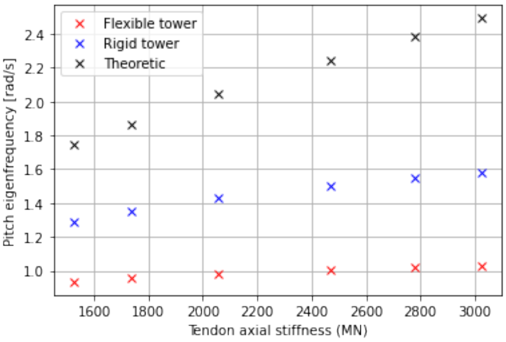

Figure 4.70: Estimation of the natural frequency for the pitch eigenmode. The values for the flexible and rigid tower are estimated using the OrcaFlex modal analysis option. The theoretic values are computed from Equation 2.1.12.

The figure clearly depicts how the flexibility of the tower limits the shift of the pitch eigenfrequency for an increase in tendon stiffness. Therefore, the effect of decreasing and increasing the axial stiffness of the tendon is expected to be very limited, due to the inability of shifting the eigenfrequencies away from the wave frequency region. Only a very large increase in the axial stiffness of the tendons could cause the pitch eigenfrequency to shift far enough from the wave frequency region. However, the axial stiffnesses used are already slightly beyond the limits of the mooring industry. Therefore, increasing the number of tendons would be a better alternative if the tendon angles remained parallel. However, this is not considered in this study.

In Appendix B.3.3 the sum frequency QTFs are summarised. No large differences can be observed for a change in axial tendon stiffness. This can be explained because the motion RAOs do not change significantly. Only the heave RAO changes significantly around 2.5 rad/s, which is slightly outside of the applied calculation range, but the overall difference will be insignificant because the magnitude is negligible after 1.5 rad/s. Therefore, the value of the sum QTF is determined mainly by the shape of the submerged structure in these higher frequency ranges, which remains the same. The only noticeable difference is around the pitch eigenfrequency, where the second-order force in this eigenfrequency tends to increase with increasing axial stiffness of the tendon. This is related to the fact that the amplitude of the motion RAO at this particular frequency decreases with increasing tendon stiffness, therefore consequently lowering the amplitude of the quadratic load part. Therefore, some reduction in the springing amplitude can be expected if the second-order sum frequency load aligns with the pitch eigenfrequency of the system. However, the effect will be marginal due to the fact that overall, the values of second-order forces are lower and the change is rather limited for increasing tendon stiffness, when compared to the base case.

4.1.5.3 Combination adjustment

At the end of Chapter 4.2.2.2, an idea was formulated that altering the axial stiffness of the tendon with an inclined TLP mooring configuration could show promising results, as this would combine the improving characteristics of both types of adjustment. A choice is made to use the optimal angle of 16°, found in Chapter 4.2.2.1. For the case of the axial stiffness, it is questioned that the optimal axial stiffness can depend on a specific set of variables. Increasing the stiffness would mean increasing the natural frequencies of the system, but it is uncertain whether or not the fatigue life would improve. If the shift is not large enough to prevent the excitement of the natural periods, tendon damage could increase. The same can be reasoned for decreasing the axial stiffness. Therefore, to find the optimal configuration, all the stiffness variations in Table 3.3 are used in the analysis.

In Figure 4.71, the OrcaFlex generated motion RAOs (spectral response graph) are illustrated. These show, to a greater degree, similarities with the univariately adjusted tendon angle of 16° and the increase in tendon axial stiffness shows effects similar to those of Chapter 4.1.5.2. The heave eigenfrequency increases significantly, while only slightly altering the pitch eigenfrequency. However, the magnitude of the pitch peak does decrease, which could be beneficial, as it reduces the second-order loading.

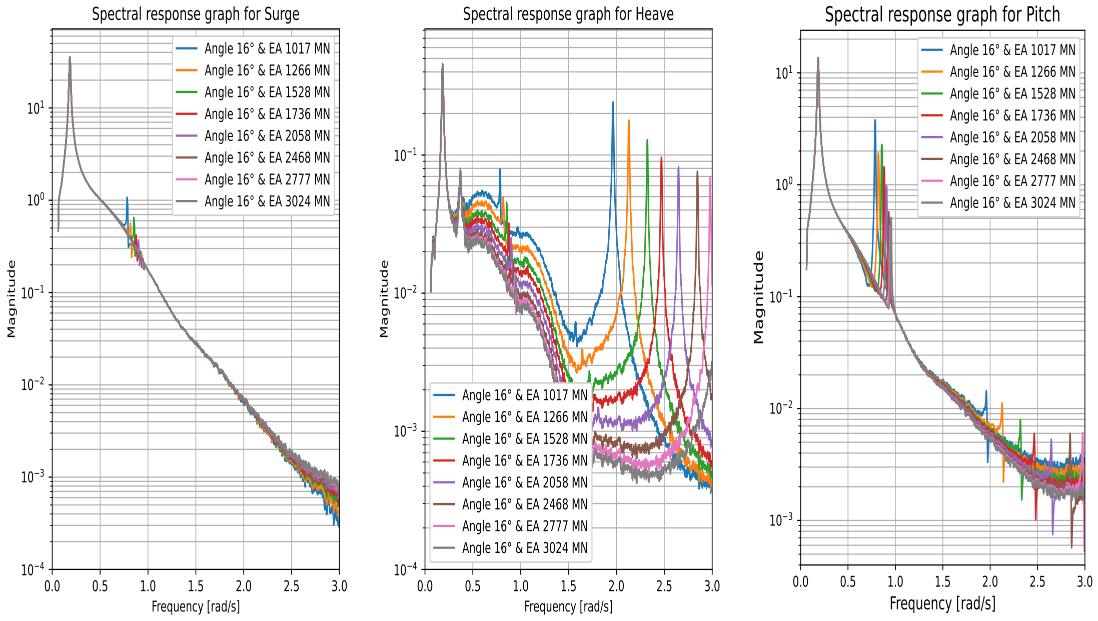

(a) (b) (c)

Figure 4.71: Spectral response graphs calculated with OrcaFlex, for the DOFs surge, heave and pitch. In the graphs, all the tendon angle adjustments are considered.

The results for the sum frequency QTF calculation are summarized in Appendix B.3.5. As is the case for the univariately adjusted axial stiffness, no large differences occur in the results. The magnitudes of the force remains relatively the same. The differences are mostly related to the marginal shifting in eigenfrequencies and the change in magnitude of those eigenfrequencies. Based on the fact that the loading pattern remains the same, but the magnitude of this pattern decreases with an increasing axial stiffness, it is expected that the overall loading and fatigue life will improve.

4.2 Fully coupled time domain analysis

In this chapter, the time domain analyses are performed with the fully coupled model generated within OrcaFlex. Geometry and details are described in Chapter 3.2. The analysis starts by performing the time domain analyses for the base model. The problem of the high-frequency response of the floater will be investigated and what aspects of loading this can be attributed to. Base values for the performance parameters will be calculated as these will be used for reference. The analysis will then focus on the performance change due to the adjustment of a mooring characteristic. The performance parameters will be compared to the base case to quantify the effect of a particular adjustment.

4.2.1 Base case simulations

The first step of the time domain analysis is to analyse the behaviour of the base case model. As this research is focused on high-frequency responses, which occur in severe sea states, the environmental conditions will solely represent these severe states. Therefore, the turbine will be kept in idling mode. In Chapter 4.2.1.1, research is conducted on the effect of the different types of hydrodynamic loading and what the overall response is for the model. And in Chapter 4.2.1.2, calculations are performed for the chosen DLCs to retrieve characteristic values for later comparison, when adjustments are made to the mooring system.

4.2.1.1 Hydrodynamic loads & overall response

For a first look at the loads and responses of the model, a simulation is performed that resembles the environmental conditions of DLC 6.1. A significant wave height (H_s) of 10.9m with a corresponding peak spectral period (T_P) of 12.5s is chosen (estimated from Figure 3.1). A turbulent wind field is applied in the simulations corresponding DLC 6.1 conditions and has been generated with Turbsim.

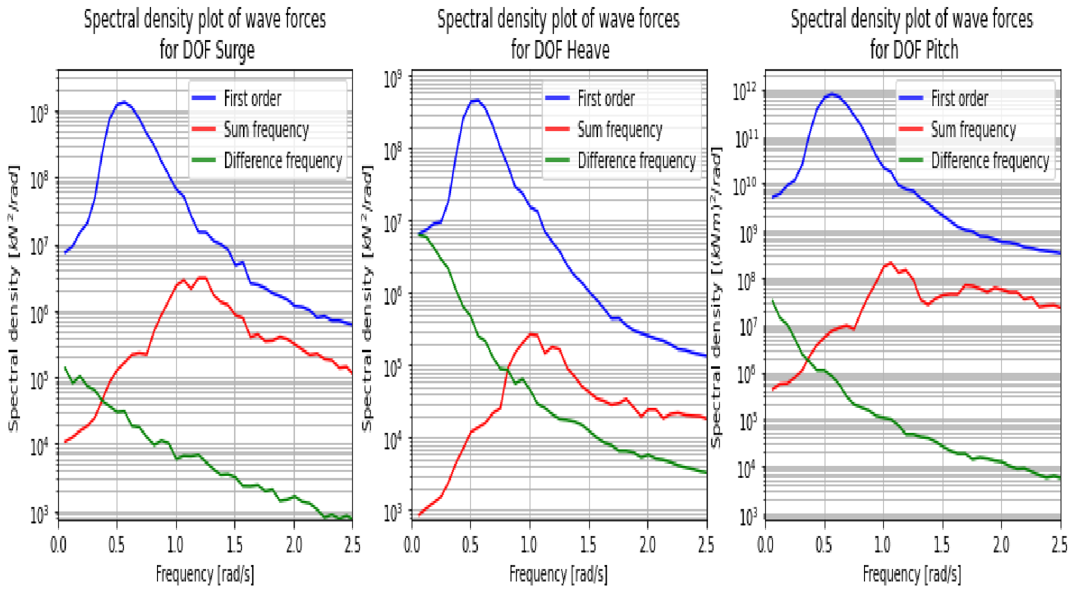

Figure 4.72: Spectral density plot for the wave forces acting on the case model TLP. The forces are plotted for the DOFs surge, heave and pitch.

In Figure 4.72, the contributions for the different wave forces are illustrated for the important DOFs. From the figure, it is observed that the main and largest contribution is from the first-order wave forces, which is as expected due to the asymptotic approximation of potential theory. Its peak is in line with the assigned wave spectrum peak period. The two smaller and in magnitude equally comparable lines are related to the second-order wave forces. The difference frequencies are located mainly in the lower frequency range. And, as expected, the sum-frequency wave forces are located after the main wave frequencies, with a peak at twice the incoming wave frequency peak. An important feature to note is that at the pitch eigenfrequency of 1 rad/s, the first-order wave force is still present and larger than the sum frequency wave force. This high-frequency tail of the first-order force, will therefore greatly contribute to the excitation of the pitch eigenmode of the system, consequently causing a springing response to be seen in the tendon tension.

For the occurrence of springing in the tendons, several methods are described in Chapter 2.1.4. One of the methods is to look at the spectral density plots for the tendon tensions. A peak near the pitch eigenfrequency would indicate that springing has occurred in the model. In Figure 4.73, a spectral density plot of the tendons and motions for the TLP is shown. It can be clearly observed that, in addition to the peak at 0.5 rad/s, caused by the chosen wave frequency spectrum, a second larger peak arises at 1 rad/s. This can be labelled as the occurrence of springing in the system. From the motions of the TLP, it can be seen that this springing is mainly caused by the pitch DOF, which is as expected. Additionally, a third, but much smaller, peak is observed at 2.7 rad/s, which is caused by the heave eigenfrequency.

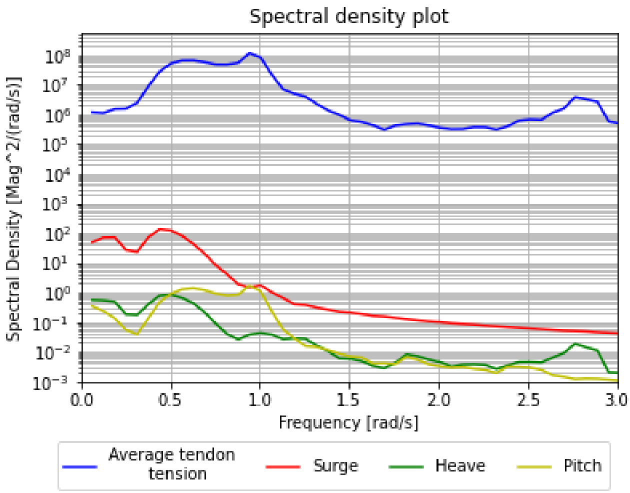

Figure 4.73: Spectral density plot of the average tendon tensions and important DOFs of the TLP.

An additional method is to plot the extreme tensions with respect to the deviations. This is illustrated in Figure 4.74. The distribution of extreme tension events indeed shows the same non-Gaussian behaviour as seen by Wang & Zou (2006) and shows comparable results found in Botros et al. (1996). The event also shows that standardised values above 5 have occurred, which means by standards that springing has taken place.

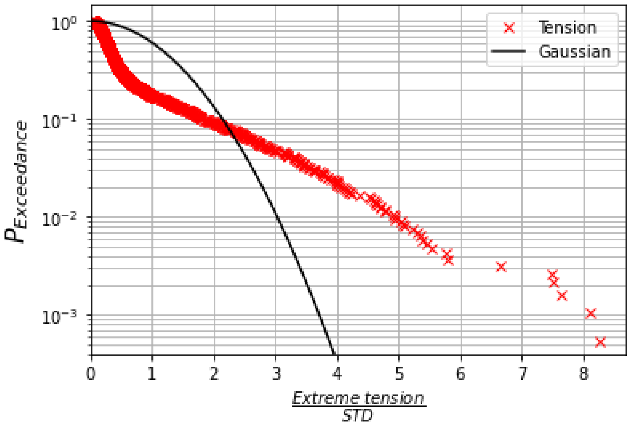

Figure 4.74: Probability of exceedance for the standardized tension peaks.

An interesting feature to note is that standardised values above 8 have occurred as well. This would usually indicate that a ringing event has occurred, which is unlikely as the third-order loading model is not included. A closer inspection of the time series showed the probable cause. In Figure 4.75, a segment of a tendon tension time series is illustrated from which it is seen that tendon tensions below zero have occurred. This indicates a slack tendon event. The aftermath of such an event shows similarities with a ringing event. Thus, such events can be masked as probable ringing events in the analysis.

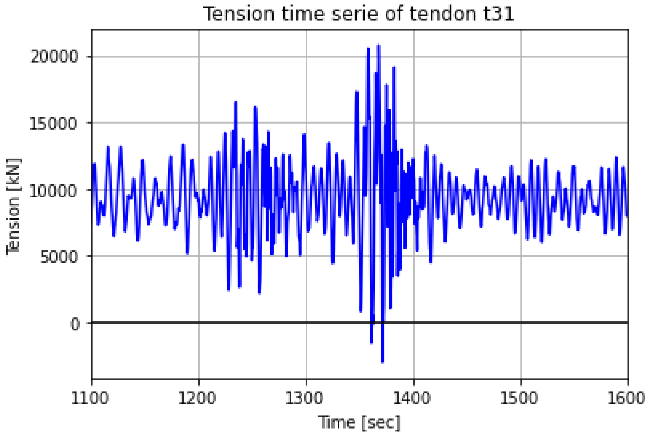

Figure 4.75: Time series segment of the tendon tensions. This segment shows a large slack tendon event, recognized due to the negative value in the tendon tensions.

Increased pretension is believed to reduce the probability of slack tendon events, but only to a limited extent. This is due to the mechanism that causes these events. In Figure 4.76, this mechanism of a typical slack tendon event is shown. It starts with the approach of a large wave front. This pushes the TLP into surge/sway DOF with high acceleration, causing the RNA and the tower to bend the other way, due to inertia effects. This movement in the XY plane also causes the TLP to be pushed down, which consequently causes the TLP to pitch. Afterward, the momentum of the tower and RNA swinging back causes a larger increment in the same pitching direction. This eventually causes a slack tendon event to occur. Tower flexing is believed to be the main factor that contributes to this slack tendon mechanism.

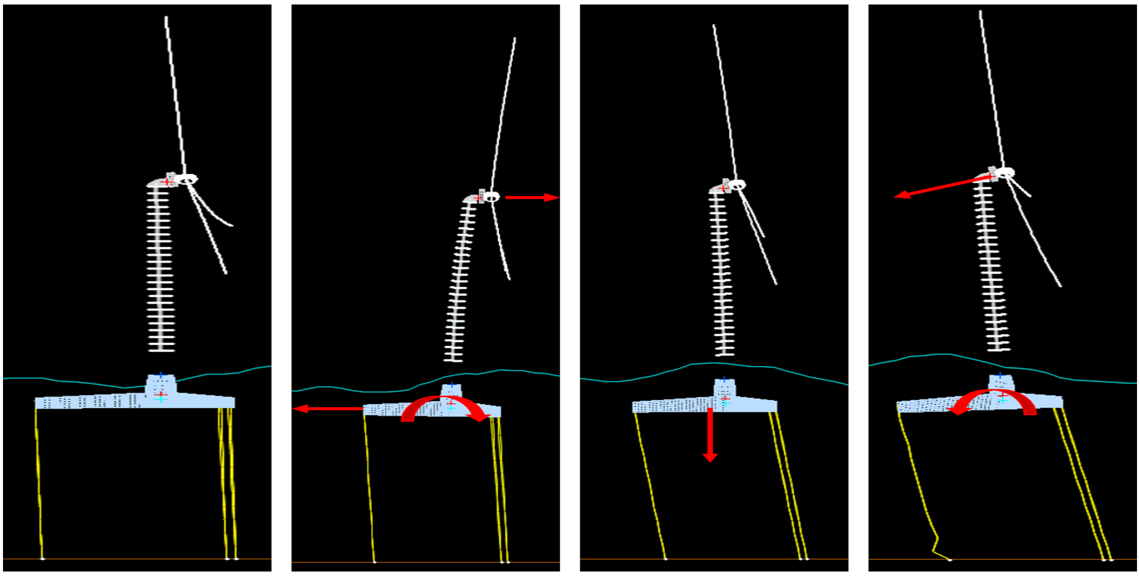

Figure 4.76: Illustration of a slack tendon event, showing the mechanism behind this event.

The last method, described by Davies et al. (1994) and Jefferys & Rainey (1994), which is commonly applied for oil & gas related TLP structures, is to plot the high-frequency part of the tendon tensions and to estimate the exceedance based on particular limits. However, a problem arises for this method. To extract a high-frequency signal from the tendon time series, a cut-off point between wave frequency and high-frequency related forces is needed. In oil & gas related structures, where the stiff eigenfrequencies are located far away from the wave frequencies, it is easy to select a cutoff point that separates the wave frequency part from the high-frequency part. However, for the case model TLP, there is no clear difference between wave frequency and high frequency, due to the low eigenfrequency of pitch. Therefore, it is an unreliable method to use for this concept, as a small change in the cut-off drastically changes the outcome (see Figure 4.77 for an example). For future analyses in this thesis, springing is only measured by means of spectral density plots and time series.

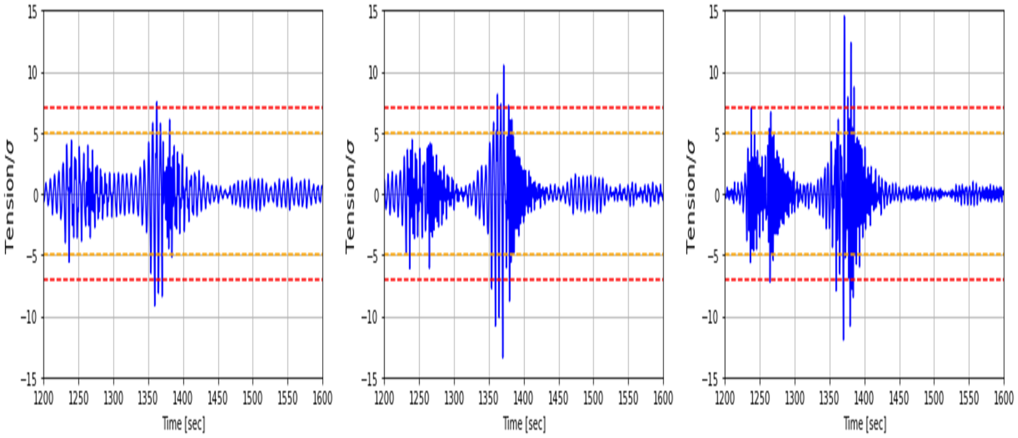

Figure 4.77: Differences in springing and ringing analysis results, as outlined by Jefferys & Rainey (1994). From left to right, a cut-off frequency of 0.15, 0.16 and 0.17 Hz is used for the analysis. Large difference occur between plots, even though the cut-off is only changed slightly. If springing has occurred, values above the orange line will appear. Crossing the red line would mean a ringing event.

4.2.1.2 DLC calculations

DLC 6.1

For this design load case, a sensitivity analysis is performed to see which conditions cause the maximum values of the key parameters. This sensitivity is first focused on the directionality of environmental conditions and then on the peak spectral period.

In IEC-61400-1 (2019) & DTU (2016), a co/multi-directional environment is applied, with a maximum directional spread of 30°. To limit the number of simulations, the directional setting, which results in the highest values of key parameters, will be used for further analyses. Due to symmetry in the TLP design, only 3 different directions are needed for the analysis (see Figure 4.78). As a turbulent wind field is used, only a yaw error of ±8° is required. For the simulations, a peak spectral period of 12.5s is used and, as required, 6 wave seeds per direction are considered. From the simulations, it is concluded that direction 0° resulted in the largest value, with wave and wind conditions being co-directional.

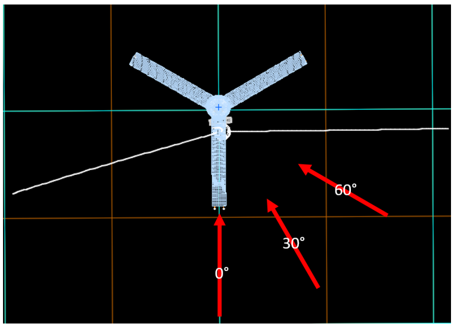

Figure 4.78: Environmental direction plan for DLC 6.1 directional spreading sensitivity analysis.

In the next phase, a sensitivity analysis for the peak spectral period is performed. From the environmental contour plots (see Figure 3.1), it is seen that for a significant wave height of 10.9m, peak spectral periods between 11.5s and 15s are expected. For these periods, a sensitivity analysis is performed to obtain the period that results in the largest key parameter values. A co-directional environment in direction 0° is used, applying 6 different seeds for the wave environment per peak spectral period. The results are illustrated in Figure 4.79, where it is seen that a peak spectral period of 11.5s results in the highest key parameter values.

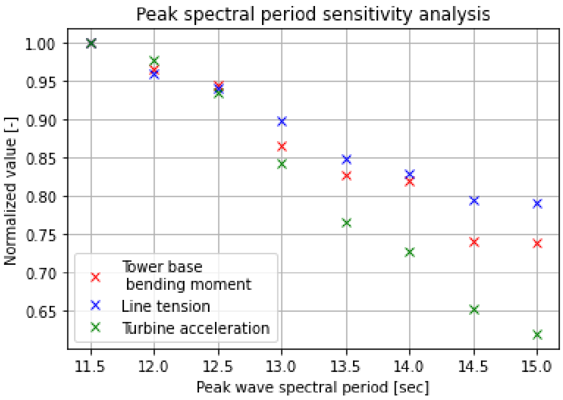

Figure 4.79: Sensitivity analysis for the peak spectral period for DLC 6.1.

Applying the findings of the sensitivity analyses to the entire DLC 6.1 analysis already shows the incapacity of the current mooring system, as they exceed industry standard limits. For the tower, a maximum base moment of up to 500 $MN \cdot m$ is allowed, and the maximum turbine accelerations are commonly constrained at 9 m/s^2. For the tendon tensions, if the safety factor is applied on both the design load and the tendon material (steel), an exceedance of 32% can be calculated. From the simulations, a large portion of this limit exceedance is related to slack tendon events that are currently occurring on a regular basis. In a springing event, maximum values of up to 20 kN are observed, still exceeding the design criteria for the tendons.

In Figure 4.80, the presence of springing events is also clearly depicted, due to the presence of the second larger peak, which does not coincide with the wave spectral period. This will have a large influence on the fatigue life of the tendons due to its high frequency component and the amplitudes accompanying these tendon tensions. As concluded earlier, the incitement of springing is largely caused by first-order wave forces, as there is still a substantial amount of wave energy at the pitch eigenfrequency of ±1 rad/s. In this regard, an optimal eigenfrequency should be above 1.25 rad/s, where little to no first-order wave energy is left.

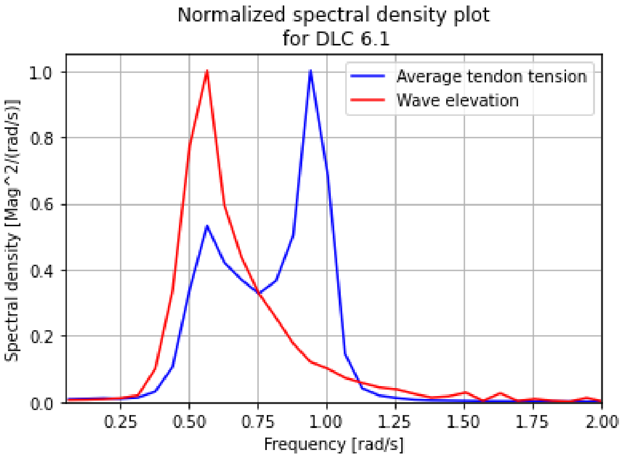

Figure 4.80: Normalized spectral density plot showcasing the presence of springing in the signal for the tendon tensions.

DLC 6.4

For this design load case, the same settings are provided for the wind turbine. For environmental conditions, a NSS is used for the South Korean Sea (the states used are summarised in Table C.1 in Appendix C.1). The environmental conditions correspond to the criteria for DLC 6.4. It should be noted that this does not result in the fatigue life of the tendon, as day-to-day cases are not taken into account (DLC 1.2), because this would vastly increase the number of simulations. The DLC 6.4 analysis will result in hourly tendon damage. For subsequent analyses, the exact damage is not required to know, only if a certain adjustment results in the desired effect.

The results for the sum of the hourly damages are presented in Table 4.10 for all 6 tendons. Fatigue simulations for additional mooring adjustments will be compared with the values presented in this table. The largest tendon damage is found in the tendons t21 and t22, which is logically correlated with the dominant direction of environmental load. As for subsequent analyses, the conditions will remain similar, and comparison of damage values for tendon t21 will be sufficient to indicate any change in performance after a mooring adjustment.

Between the S-N and T-N curves, large differences in tendon damage can be observed. This is mainly related to the fact that damage with the T-N curves is a relationship between the tension and the MBS of the tendon. This is not the case for the S-N curves, thus not taking into account if the MBS of the tendon is exceeded. Post-processing takes considerably longer for the T-N curves, thus a choice is made to evaluate subsequent tendon damages with the S-N curve. This will not affect the end results as only a change in performance is required.

		Tendons					
		t11	t12	t21	t22	t31	t32
Damage	S-N	0.152	0.145	0.453	0.435	0.168	0.190
	T-N	0.341	0.326	1.046	1.004	0.376	0.418

Table 4.10: Summary of tendon damage for DLC 6.4 for the base case mooring configuration of the TLP using both the S-N and T-N curves.

The calculation of all these different environmental conditions also gives some information on which conditions cause the greatest damage. The results are illustrated in Figure 4.81. As expected, under sea conditions, where a low peak spectral period combined with a high significant wave height, the greatest damage will occur to the tendons. This is because the number of stress cycles that the tendon experiences increases with a decreasing wave period, and higher stresses can be expected for increased wave heights hitting the floating unit. However, the largest tendon damage is not found at these described environmental values, but at a rather low significant wave height of 3.5m and a peak spectral period of 6.5s. This is because the peak spectral period coincides with the pitch eigenfrequency of the system (see Table 3.2).

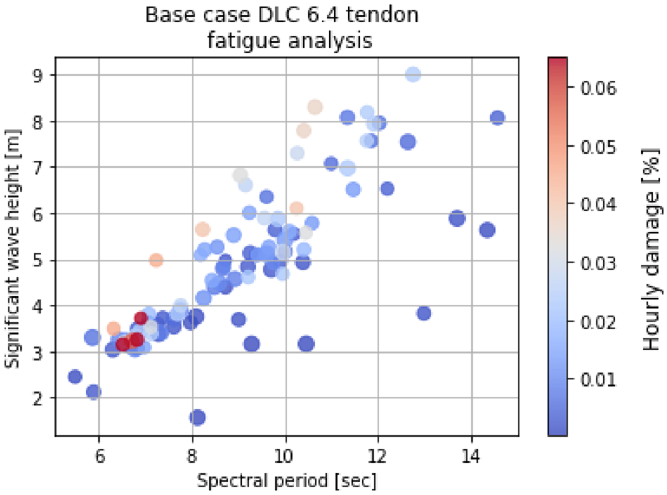

Figure 4.81: Fatigue calculation of DLC 6.4 for the base case mooring configuration. The values represent the hourly damage of all the tendons for different combinations of significant wave height and peak spectral period. The plot is base on the S-N curve.

This increase in tendon damage for sea states with peak spectral periods near the natural pitch period can clearly be observed in Figure 4.82. At a standardised period of 1, where the peak spectral period is equal to the natural pitch period of the TLP, a significant increase in tendon damage can be observed. Therefore, this can be classified as springing, causing more tendon damage. As previously concluded, this springing is not caused by second-order wave loading but rather by the first-order wave loading, as a result of the constrained DOFs having a low eigenfrequency.

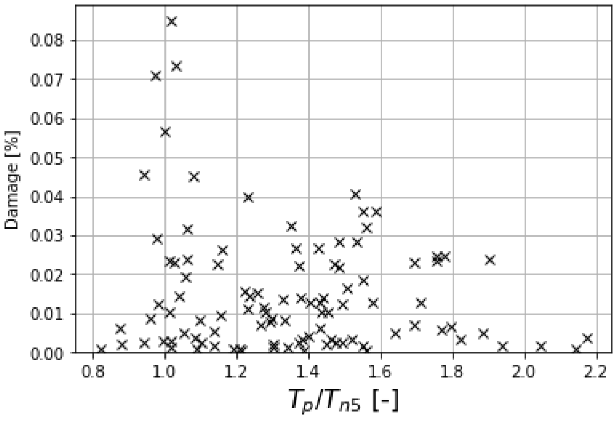

Figure 4.82: Tendon damage plotted against the peak spectral period, which are standardized with the pitch natural period. The plot is based on the S-N curve.

For these special cases, where the first-order wave force mainly causes this springing effect, the spectral densities of the tendon tension are collected and illustrated in Figure 4.83. This figure shows that the response is largely influenced by springing, due to the large peak at the pitch eigenfrequency. No wave frequency peak is observed as this peak coincides with the "springing" peak, meaning that first-order forces are indeed causing this effect. This peak causes large stresses with a large number of cycles in a specific time period, therefore logically causing large amounts of tendon damage.

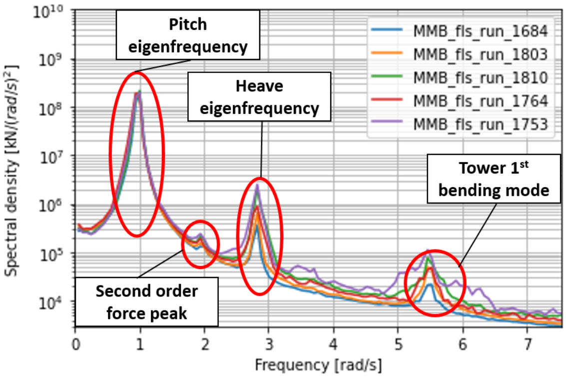

Figure 4.83: Spectral density plot of the tendon tension for environmental conditions which mainly incite springing in the system. Additionally, the cause of several peaks in the signal is identified.

It should be noted that not all environmental conditions, where the wave spectral peak period is equal to the pitch eigenfrequency, results in high tendon damages, as seen in Figure 4.82. This is because for these simulations, there is no unidirectionality of environmental variables present.

From the DLC calculations in this chapter, the following is concluded:

- Springing is present in the system and is not necessarily related to second-order hydrodynamic loading.
- The base case configuration (vertical tendon and 2100 MN axial stiffness per tendon) exceeds the limits for the key parameters.
- Slack tendon events are present.
- The major contributing factor to tendon fatigue is linked to springing.
- The main cause of the problems listed above is linked to the flexibility of the tower and the mass at the end of the tower, causing this lower pitch eigenfrequency.

The problems described in the list above, are show stoppers for the current design concept of the mooring system, which addresses the necessity of this thesis. It is to be seen from the mooring adjustments, addressed in Chapter 4.2.2, how the system will improve or worsen, based on the established reference values.

4.2.2 Adjusted model simulations

In this chapter, the performance of the mooring adjustments is evaluated. The evaluation is based on a comparison with the reference values found in the DLC calculations for the base case model performed in Chapter 4.2.1.

4.2.2.1 Tendon angles

DLC 6.1

The results are illustrated in Figure 4.84. This shows that inclining the tendons can significantly improve the performance of the TLP. The optimum angle is ±16°, which reduces the tendon tension with ±40%, the tower base moment with ±50% and the nacelle acceleration with ±65%. Especially for turbine accelerations, a large reduction in maximum value is obtained compared to the base case. This is mainly attributed to the fact that the rotation point is in the nacelle itself (see Figure 4.67).

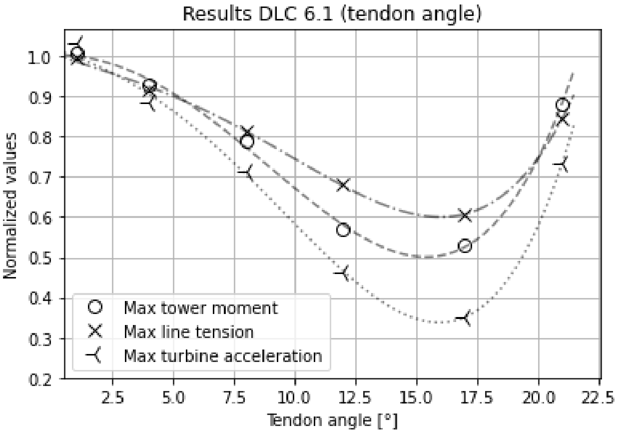

Figure 4.84: Results for DLC 6.1 where the angle of the tendon for the TLP is adjusted.

The probability of slack tendon events follows a similar trend as illustrated in the figure. It was previously concluded that the whipping of the tower has a large influence on these slack tendon events. The rotation of the TLP now being in the nacelle itself means that this whipping effect is mitigated to a greater extent. This explains the reduced incidence of slack tendon events. Furthermore, the statistics of the key parameters for changing tendon angles are transformed into normal distributions and illustrated in Figure 4.85. In this figure, it is seen that for an increasing tendon angle, the mean and standard deviation of the key parameter signals are reducing. The optimum is for the 17° tendon angle case, which will give an indication that fatigue damage is the lowest for this particular case. However, this must be proven from the DLC 6.4 calculation and is addressed in the next subparagraph.

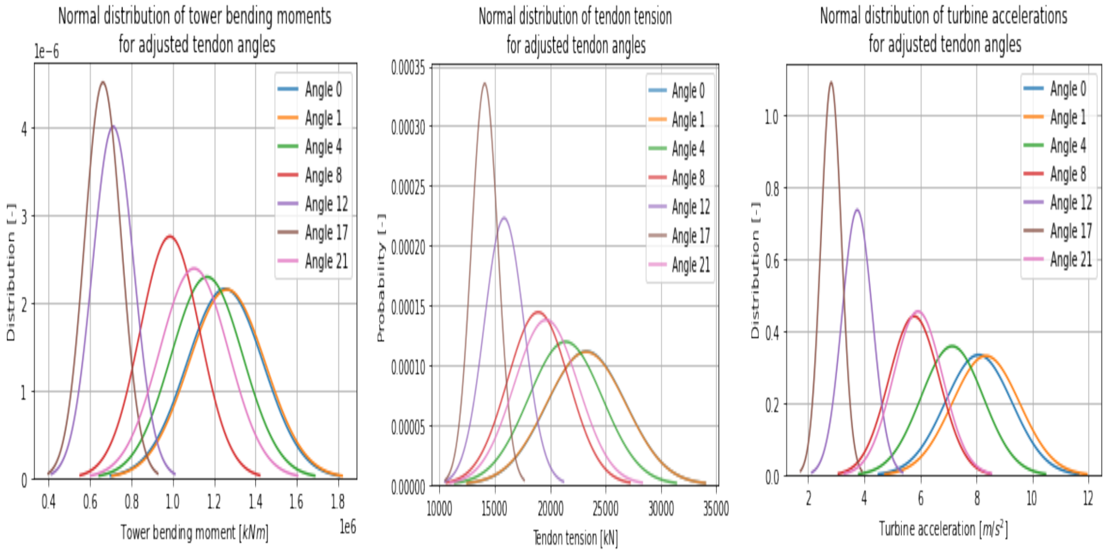

(a) **(b)** **(c)**

Figure 4.85: Normal distributions of the key parameters for changing tendon angles. From left to right, the normal distribution of the tower bending moments, tendon tensions and nacelle accelerations are illustrated.

The last observation made from the DLC 6.1 calculation is the change in the spectral density of the tendon tensions, which is illustrated in Figure 4.86. This shows the decrease in spectral density for the optimal tendon angle, due to the decrease of the tensions in the tendons. Additionally, the ratio between the wave frequency incited tension peak and the peak related to springing events is decreasing, indicating that the amount of springing is reducing in the system. However, increasing the tendon angle too much can worsen the amount of springing in the system.

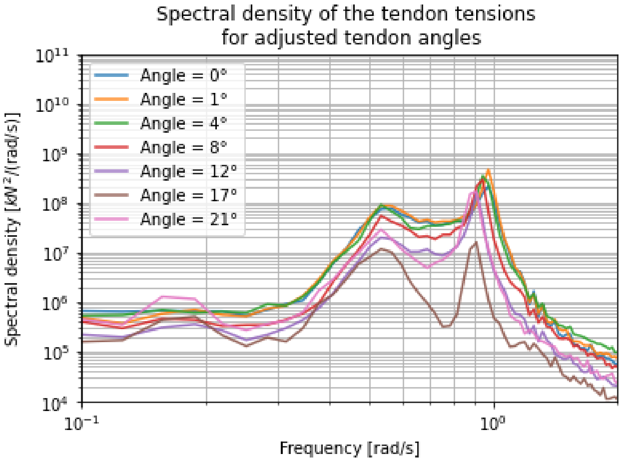

Figure 4.86: Spectral density plots of the tendon tensions for an increasing angle of the tendons for the case model TLP.

DLC 6.4

The results of fatigue damage are illustrated in Figure 4.87. These clearly show a significant reduction in tendon damage for particular tendon angles. As was the case for the DLC 6.1 calculations, an optimum is found at ±16°, where the tendon damage is less than 1% compared to the simulation of the base case.

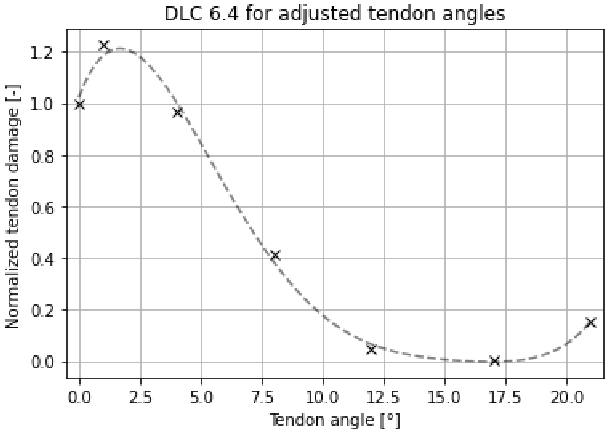

Figure 4.87: Results for DLC 6.4 where the angle of the tendons of the case model TLP are adjusted.

The figure also confirms the prediction made in Figure 4.85, where the low mean narrowbanded distribution of the tendon tension of the 17° tendon angle case will result in the lowest fatigue damage. This is the result of the reduced stress range and also from a decrease in the number of springing events, as seen in Figure 4.86.

This decrease in springing is also observed when Figure 4.81 is recreated for the mooring configuration with a tendon angle of 17° and illustrated in Figure 4.88. In this figure, it is observed that the largest damage no longer occurs in the natural pitch period of the system, meaning that the effect of springing events is reduced for this particular case of inclined tendon angle. The highest damages are now occurring at the largest significant wave heights, which is expected.

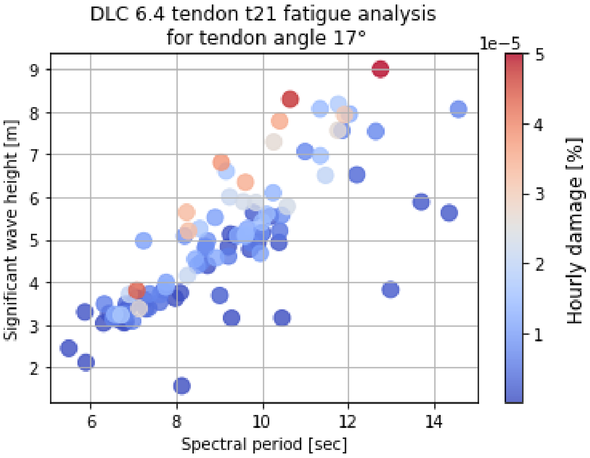

Figure 4.88: Fatigue calculation of DLC 6.4 for the mooring configuration where the tendon angle is 17°. The values represent the hourly damage of tendon t21 for different combinations of significant wave height and peak spectral period.

Additional notion

A notion about this specific optimal tendon angle is to be added. It must be stated that this optimum is found for case study specific parameters, such as the water depth, pontoon length, etc. It is believed that different site conditions will alter the dynamics of the floater. To find out what can cause this difference, a parametric study is performed to identify the causes and see how they influence the stability of the floater.

It is chosen to represent the stability of the floater by calculating the pontoon angle of the floater. The model is simplified using a projection of the TLP. This projection and important parameters to calculate the pontoon angle are illustrated in Figure 4.89.

The angle of the pontoon (ψ) can be related to the points **P1** and **P2** and is calculated as follows:

$$\psi = tan^{-1}\left(\frac{P1,z - P2,z}{P2,x - P1,x}\right). \tag{4.2.1}$$

Where:

$$P_{1,x} = -Lp - H \cdot \left(\frac{cos(0.5\pi - \alpha + \delta\beta)}{cos(\alpha)} - tan(\alpha)\right), \tag{4.2.2a}$$

$$P_{1,z} = H * \frac{sin(0.5\pi - \alpha + \delta\beta)}{cos(\alpha)}, \tag{4.2.2b}$$

$$P_{2,x} = 0.5Lp - H \cdot \left(tan(\alpha) - \frac{cos(0.5\pi - \alpha + \delta\gamma)}{cos(\alpha)} \right), \tag{4.2.2c}$$

$$P_{2,z} = H \cdot \frac{sin(0.5\pi - \alpha + \delta\gamma)}{cos(\alpha)}. \tag{4.2.2d}$$

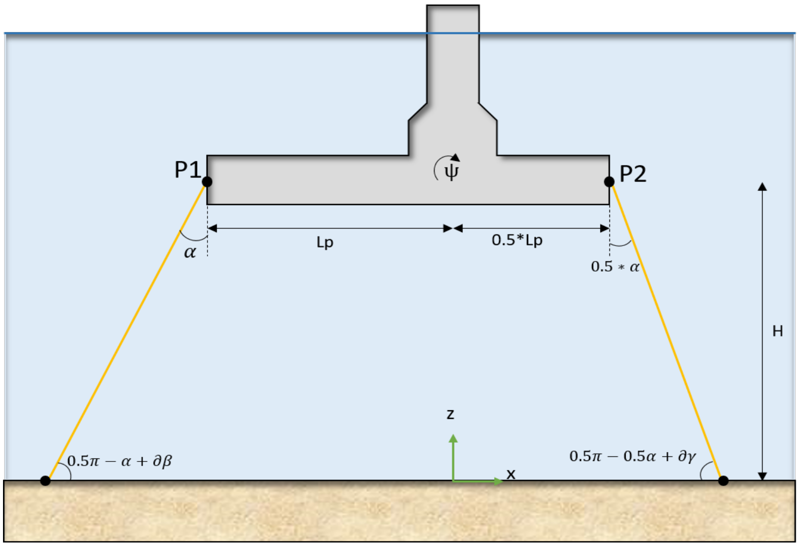

Figure 4.89: Parametric representation of the TLP for calculating the rotation of the pontoon.

The equation for the angle of the pontoon can be solved by assuming an initial angle $\delta\beta$ and incorporating that the pontoon length remains the same if the system is rotated (see Equation 4.2.3). This results in the two unknowns ψ and $\delta\gamma$.

$$^3/_2 Lp = \sqrt{(P_{2,x} - P_{1,x})^2 + (P_{2,z} - P_{1,z})^2}. \tag{4.2.3}$$

Thus, from the equation, it can be observed that the stability depends on the depth of the water, the initial angle of the tendon, and the length of the pontoon. This dependency is shown in Figure 4.90, where the values of the pontoon angle are compared.

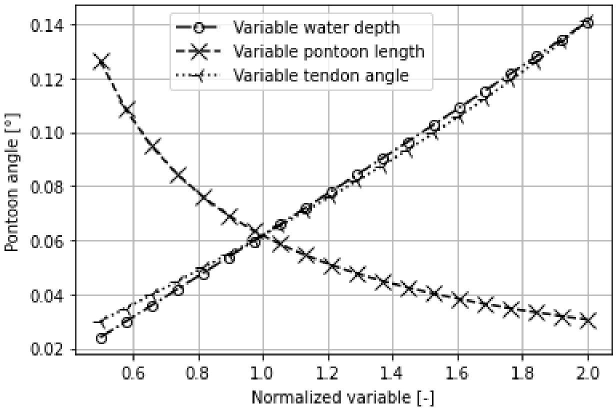

Figure 4.90: Difference in pontoon stability by adjusting the dependent parameters on a univariate basis. For the comparison, $\delta\beta$ is kept at 10° and the variables are normalized based on their initial values ($\alpha = 16°$, $Lp = 46m$ & $H = 135m$).

From this figure, it is observed that increasing the water depth and the initial angle of the tendon tends to decrease the stability of the pontoon because the angle of the pontoon is increasing. This could also explain why slack tendons events reappear at a tendon angle of 21°, due to decreased pontoon stability. A way to increase this stability is to increase the length of the pontoon. Similar trends are believed to be expected for the DLC calculations if these parameters are adjusted accordingly. However, this is beyond the scope of this thesis and shall not be investigated.

The addition of inclining the tendons can be a good solution to minimise the loads and fatigue of the tendons, but caution should be taken with respect to the influencing parameters found in this notion. An ideal configuration could be achieved by taking into account both the length of the pontoon and the angle of the tendon, to minimise the loads on the tendons with respect to the different water depths.

4.2.2.2 Axial stiffness

DLC 6.1

The results are illustrated in Figure 4.91. From the figure, it is seen that decreasing the stiffness of the tendons causes an increase in the values for the key parameters. For an axial stiffness of 1017 MN, an increase of ±35% for the turbine accelerations and tower base moments is observed, when compared to the base case of 2100 MN, while the tendon tension increases with ±20%. This is expected because as the stiffness of the system decreases, the amplitude of the motions increases, consequently amplifying the mechanism behind slack tendon events (see the description of these events in Chapter 4.2.1.1). Increasing the axial stiffness seems to have a limited effect on the key parameters. This is because the increase in stiffness is too small to change the motion characteristics of the system (see Figure 4.69). Slack tendon events are still present in the simulations, consequently causing these large parameter values. Therefore, for this case study, the increase in axial stiffness will not serve as a solution to meet the design requirements. Slack tendon events somewhat mask the effectiveness of altering tendon stiffness.

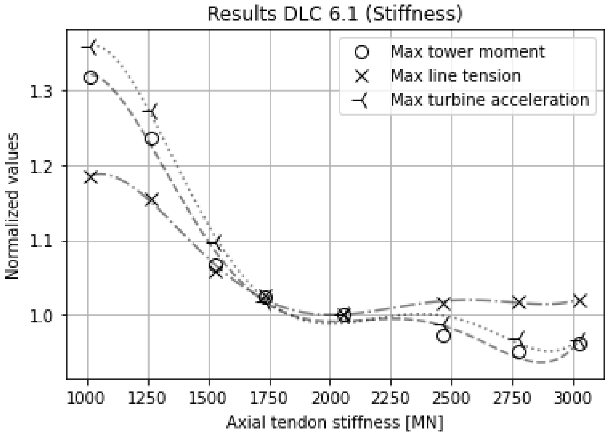

Figure 4.91: Results for DLC 6.1 where the stiffness of the tendon of the TLP is adjusted. The axial stiffness of 2100 MN is the base case for the project.

This marginal effect of changing the stiffness is also seen when displaying the key parameter statistics in the form of a normal distribution. These are illustrated in Figure 4.92. From this figure, it can be observed that the mean and standard deviations are decreasing for the first three stiffness adjustments. After that, the mean stays relatively at the same location, while only slightly decreasing its standard deviation. Therefore, it can be expected that the fatigue life improves significantly for the first few axial stiffness adjustments and then relatively stabilises, towards the same value as that found for the base case. The validity of this prediction will be seen in the next subparagraph, where the results of the DLC 6.4 calculation are evaluated.

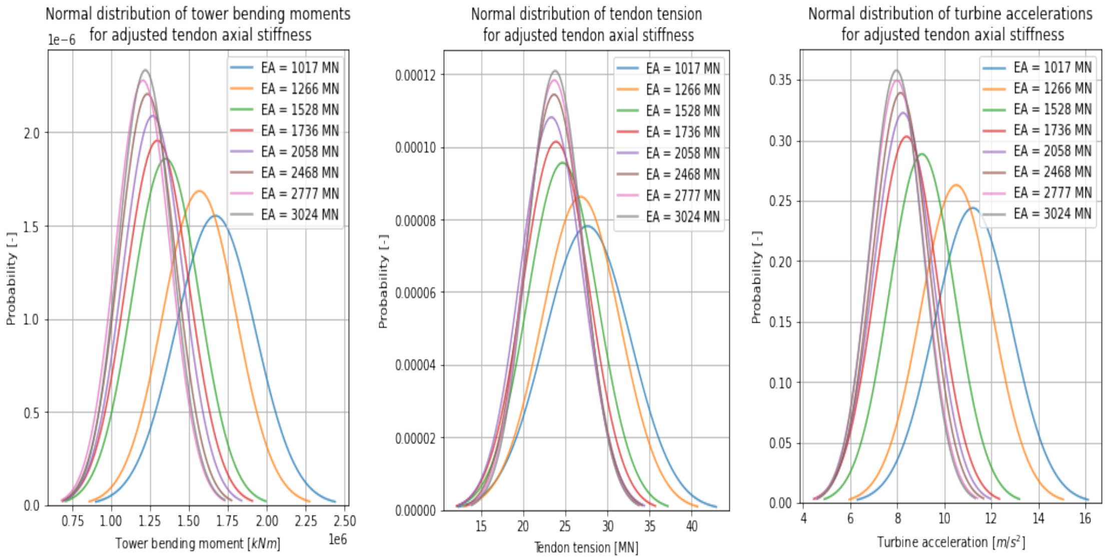

(a) **(b)** **(c)**

Figure 4.92: Normal distributions of the key parameters for changing tendon axial stiffness. From left to right, the normal distribution of the tower bending moments, tendon tensions and nacelle accelerations are illustrated.

The last point of analysis is to examine the tendon tensions of the adjusted models. The results are illustrated in Figure 4.93, where the spectral density of these tendon tensions are plotted. From the graph, a similar projection of the tensions is seen, where the largest differences occur at the first few stiffness adjustments, and after that, stabilises around a particular value. An additional observation seen, is that the peak at ±3.7 rad/s is significantly increasing for the lower range of the tendon axial stiffnesses. This is coinciding at the eigenfrequency of the turbine blades. Decreasing the axial stiffness of the tendons, seems to increase the motions of the blades. It is not known if this decrease in turbine blade excitation is the cause of an increased axial stiffness or if its due to the decrease of slack tendon events.

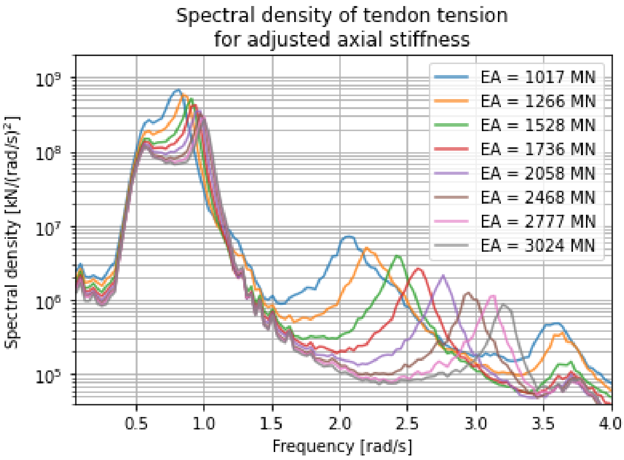

Figure 4.93: Spectral density plots of the tendon tensions for an adjusted tendon axial stiffness for the TLP.

DLC 6.4

Fatigue assessment has two methods for analysis. The first is to relate fatigue by altering the diameter of the tendon to match it with the axial stiffness, or to adjust the stiffness term itself. Changing the stiffness term would imply a different material for which the S-N curves are unknown, making this option not possible. Therefore, the diameters of the tendons are adjusted, based on the values in Table C.2.

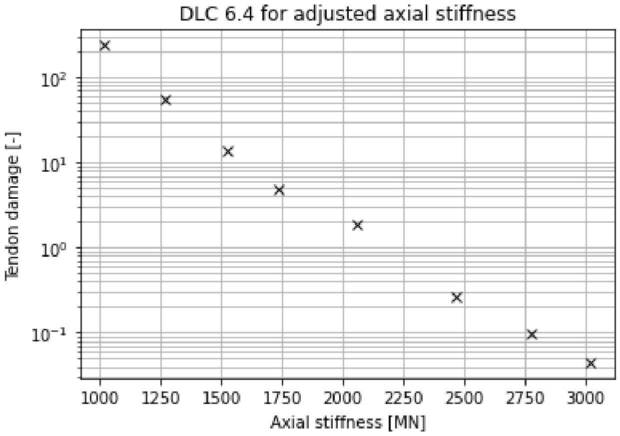

Figure 4.94: Results for DLC 6.4 where the axial stiffness is adjusted for the tendons of the case model TLP.

The results are illustrated in Figure 4.94. These show a clear decrease in tendon damage for an increase in axial stiffness. Contrary to the prediction made in the DLC 6.1 calculation, where it was believed that the damage would only decrease for the first few adjustments in axial stiffness and then remain around the same value. Instead, the value appears to continue to decrease, which is the result of an increase in the diameter of the tendon, which decreases the stress for the same tension.

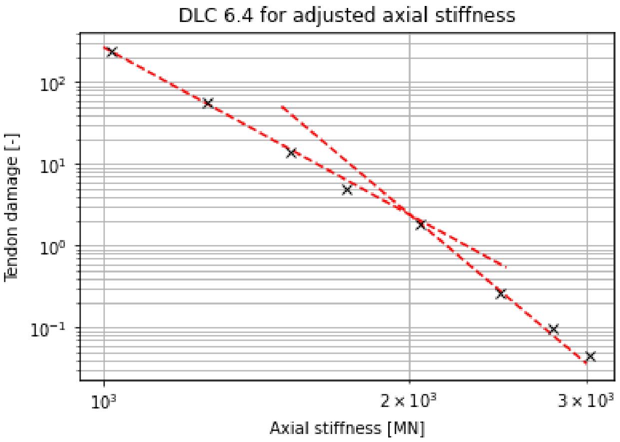

Figure 4.95: Difference in decreasing rate of tendon damages. The damages show a linear relation in a log-log plot, meaning that the decrease follows a power function.

However, the rate of decrease in tendon damage is not constant, as shown in Figure 4.95. This is caused by the marginal change in motion behaviour of the TLP after a particular axial stiffness. For the first few axial stiffnesses, the change in tendon damage depends on the increase in the diameter of the tendon and the decrease in the loads of the tendon. For the other axial stiffnesses, the loads are relatively the same. Thus, the change is related to the increase in the tendon diameter. Nevertheless, increasing the axial stiffness of the tendon does not prevent the damage caused by springing. This is because the motion behaviour remains the same, even for the largest axial stiffness (see Figure 4.96).

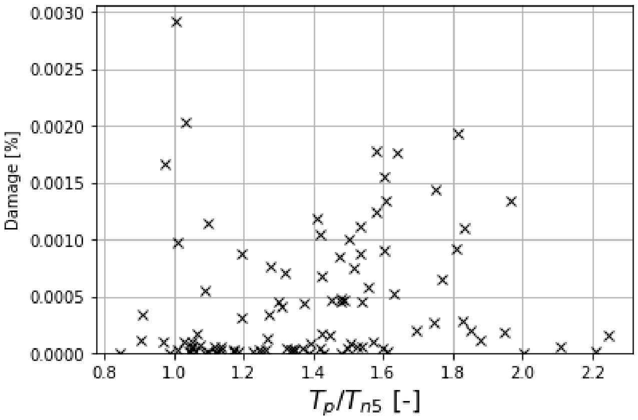

Figure 4.96: Tendon damages related to the pitch natural period, for the axial stiffness case of 3024 MN.

Adjusting the axial stiffness of the tendon is a viable solution to minimise tendon damage. However, this solution is a mitigation of the problem, rather than a preventive one. Additionally, the ULS calculation remains unchanged after the adjustment of the mooring system. As concluded at the end of Chapter 4.2.1.1, the root of the problem is the low pitch eigenfrequency of the system caused by the flexibility of the tower. The increase in axial stiffness is too marginal to invoke a change in the motion behaviour of the TLP. A possibility would be to increase the number of tendons per arm, to ensure a sufficient increase in axial stiffness, to push the natural periods of the constrained DOFs away from the first-order loading frequency range. However, this would be a costly solution and is currently beyond the scope of this thesis. Nonetheless, a possibility arises when the adjustment of the tendon axial stiffness is combined with the inclination of these tendons. This would combine the load minimising properties of inclining the tendons with the fatigue life optimising properties of adjusting the axial stiffness.

4.2.2.3 Combination

For this combination, the optimal inclination of 16°, as found in Chapter 4.2.2.1, is applied to the tendons and different axial stiffnesses are applied. The results of the diffraction analysis in Chapter 4.1.5.3 are implemented in OrcaFlex.

DLC 6.1

The results are illustrated in Figure 4.97. From the figure, it is seen that the evolution of the maximum key parameter follows a nonlinear route. Tendon tensions first decrease until a particular axial stiffness and then start to increase. For the lowest axial stiffness of 1017 MN, an increase of ±10% is seen, while an increase of ±5% is seen for the highest axial stiffness of 3024 MN. The optimal value with regard to tendon tension is the base case axial stiffness of 2100 MN.

A different story is to be told for the progression of the nacelle acceleration and tower base bending moment. First, a large decrease in normalised value is seen for these key parameters until an axial stiffness of 1538 MN, then it starts to increase until the axial stiffness of the base case. After this increment, a second decent is observed in the normalised value followed by the last increase in the normalised value for the axial stiffness of 3024 MN. This behaviour is not observed where the stiffness is altered univariately, probably because slack tendon events overshadowed these signals.

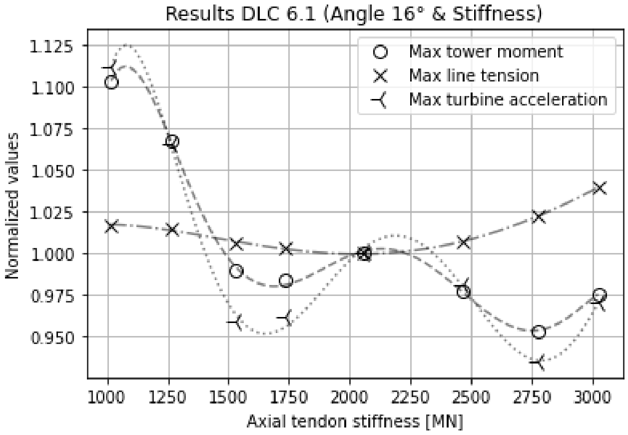

Figure 4.97: Results for DLC 6.1 where the stiffness of the tendons are varied for an inclination of the tendons of 16°. The axial stiffness of 2100 MN is regarded as the base case for this instance.

To try to explain the behaviour of the progression of the maximum key parameter values, Figure 4.98 is used. In the first subfigure, the descents and increments are labelled, which are used for the individual explanations. Sections A-D explain the progression of the accelerations of the nacelle and the base moments of the tower, while Sections E and F explain the progression of the effective tension of the TLP tendons.

- **A** The increase in axial stiffness limits the motion of the TLP and shifting the heave eigenfrequency away from the wave frequency region. This will cause an initial decrease in the nacelle accelerations and the bending moments at the base of the tower.
- **B** Increased axial stiffness causes a peak in the spectral peak of tendon tension near the eigenfrequency of the tower bending mode. This is caused by the change in the eigenfrequency of heave of the TLP. The bending of the tower and heave motion are coupled motions due to the off-centre position of the nacelle. At 2100 MN axial stiffness, this peak is at its maximum, which explain the increase and peak of the line **B**.
- **C** The further increase in axial stiffness is causing this TLP-tower bending coupling to be less strong. Therefore, consequently, lowering the tower base moments and nacelle accelerations.
- **D** The last increase in the base moments of the tower and the accelerations of the nacelles is caused by the eigenfrequency of the heave of the TLP to shift towards the first bending mode of the turbine blades. This bending mode of the blades is translated into accelerating the nacelle and consequently bending the tower beneath. At 3024 MN axial stiffness, the eigenfrequencies are equal and it is expected that these two key parameter values will decrease afterward as the eigenfrequencies move away from each other.
- **E-F** The increase and decrease in the motions of the superstructure will naturally translate into the increase and decrease in the tension of the tendon. The parameter first decreases as a result of a larger restriction of motions as the axial stiffness increases. Subsequently, the tensions increase because of the excitation of superstructure eigenmodes, such as those of the tower and the turbine blades.

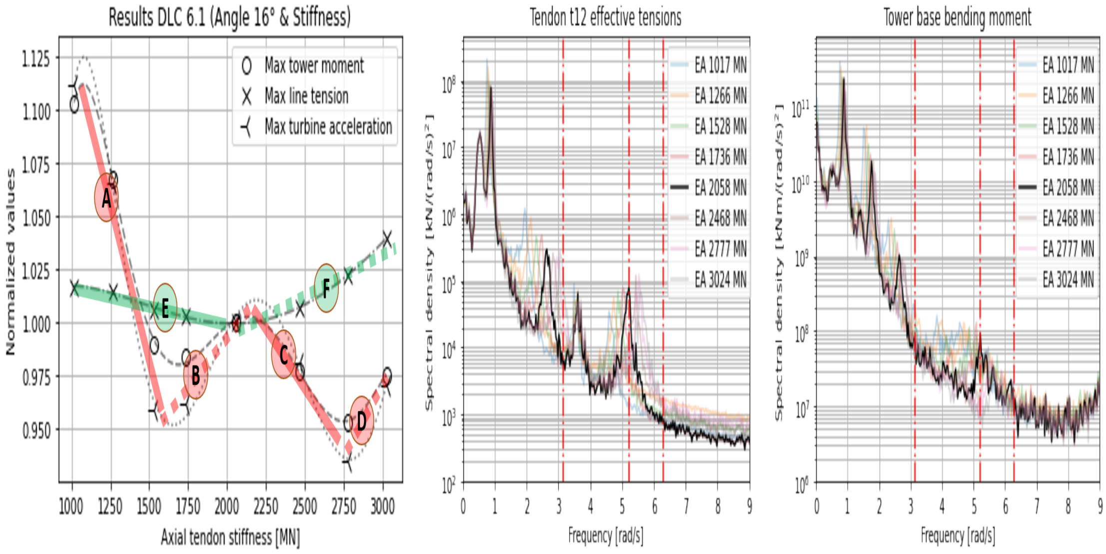

(a) (b) (c)

Figure 4.98: Analysis of the DLC 6.1 results for the combined mooring system adjustment. In the first figure from the left, the different processes are identified for the key parameters, where the tower base bending moment and nacelle accelerations are grouped with each other as they follow a similar progression. In the two figures on the right, the spectral density plots of the effective tendon tension and tower base moment are shown. Additionally, vertical red dash-dotted lines are added in the spectral density plots, to indicate the following eigenfrequencies. 1^{st} turbine blade bending mode (≈ 3.1 rad/s), tower 1^{st} bending mode (≈ 5.21 rad/s) and 1^{st} bending mode of the mooring lines (≈ 6.2 rad/s).

Taking into account Figure 4.97, it is believed that an axial stiffness of 2468 MN or 2777 MN will serve as an optimum for the TLP. This is attributed to two reasons. The first is because the moments at the base of the tower and the accelerations of the nacelle are the lowest for the two axial stiffnesses, therefore improving the service life of the RNA, which can be a large part of the OPEX. The second reason is that although the maximum tendon tension force is increasing, the increase is only marginal and still below the design limit. The final optimum will be the result of fatigue calculations, although this is expected to follow a trend similar to that in Chapter 4.2.2.2.

DLC 6.4

For the evaluation of fatigue life, the same method is applied for the S-N curve as in Chapter 4.2.2.2, where the tendon diameter is adjusted accordingly. Additionally, as a means of comparison, the T-N curve is also used, applying the method highlighted in Chapter 4.2.1. With slack tendon events mitigated with the introduction of a tendon angle, the results for the T-N curve are much more stable. The results are illustrated in Figure 4.99. From the figure it can be seen that the fatigue life shows a trend similar to that of the univariately adjusted axial stiffness case (see Figure 4.94). Both S-N and T-N calculated tendon damages show similar results for the higher axial stiffness, while a divergence between the two is seen for the lower axial stiffness range. This is caused by the decrease in MBS for the T-N curve. Exceedance of the MBS is not taken into account in the S-N curve, which explains why the overall damage is lower for this curve. In the higher axial stiffness range, where the MBS is moving away from the maximum loading, the T-N and S-N curves are converging to the same answer.

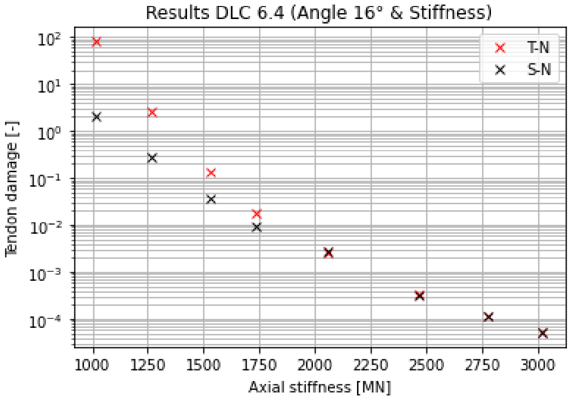

Figure 4.99: Results for DLC 6.4, where the axial stiffness is adjusted for the 16° inclined tendon angles of the TLP. The axial stiffness of 2100 MN serves as the base case simulation.

Based on the conclusion of the DLC 6.1 calculation in which an axial stiffness of 2468 / 2777 MN is stated to be optimal, the same conclusion can be drawn regarding the DLC 6.4 calculation. Both axial stiffnesses show comparable tendon damages and an eventual optimum between the two should be based on total fatigue calculations, thus also including DLC 1.2. In Figure 4.100, the hourly damage to the t21 tendon is plotted against the combination of the significant wave height and the peak spectral period used in the simulations. From this figure, it can also be stated that damages related to the excitation of springing are still mitigated, which is mainly attributed to the inclination of the tendons. The greatest damages occur for a combination of high significant wave heights combined with low spectral periods, which is expected.

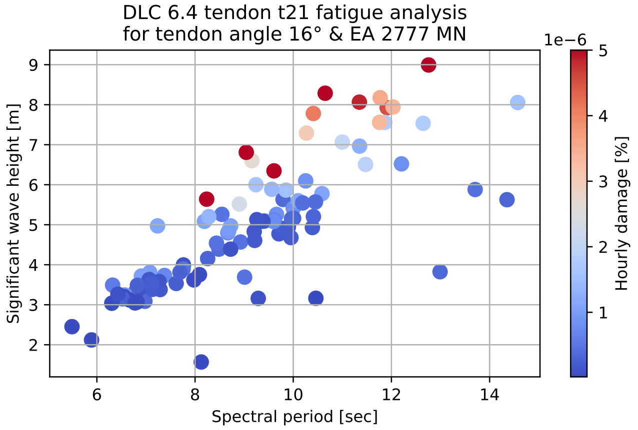

Figure 4.100: Fatigue calculation of DLC 6.4 for the mooring configuration where the tendon angle is 16° and the axial stiffness is 2777 MN. The values represent the hourly damage of tendon t21 for different combinations of significant wave height and peak spectral period.

5

Conclusions

In this research, an attempt is made to minimise the effects on the mooring system caused by the high-frequency responses of a TLP supporting a wind turbine. High frequency means that the response has frequency components that are above the incoming wave frequencies. From the literature review, it was concluded that there are several phenomena that matched this criterion, namely springing and ringing, where the thesis is devoted solely to springing. Ringing has been included in the literature study to signify the properties of this response and how this differs from a springing response. The objectives of this research are to gather already available information from the oil & gas industry, therefore creating clarity on the subject, and to optimise the mooring system in such a way that the effects of springing can be minimised.

From the literature review, it is concluded that springing is a periodic steady-state response due to the excitation of the constrained DOFs of the TLP. These constrained DOFs are generally in the higher frequency ranges caused by the high stiffness properties of the mooring system. Therefore, excitation of such a DOF will influence tendon fatigue, as the resonance characteristics of the floater will incite a high-frequency cyclic load on the tendons. Eigenfrequencies of these constrained DOFs are located in the high-frequency tail of the first-order loading spectrum and in the spectrum of the second-order wave forces. Thus, both first- and second-order wave forces are incorporated in the simulations, which are evaluated with the use of a diffraction analysis.

In this research, an extensive diffraction analysis is performed using two diffraction programmes named OrcaWave and Hydrostar. The results for the case model TLP are validated by applying a step simplification study, where the model is built in phases to have more resemblance to the TLP and each step is validated by comparing it with the available literature. The study resulted in a calibrated analysis method, which may serve as a guide for any future research involving diffraction analyses. The main discovery from this analysis is the importance of including tower flexibility. This is often overlooked in common literature and may result in incorrect results. The flexibility of the tower causes the roll/pitch eigenfrequency to be much lower than anticipated by the diffraction software as these are not able to incorporate the DOF of the tower. A new method is suggested by altering the inertia term in such a way that the roll/pitch eigenfrequency matches that of the model including the tower flexibility. This only affected the results for second-order loading, as these depend on first-order body motions. For a TLP with vertical tendons, the method was shown to be a good solution.

The simulations for the analysis of springing are performed in the time domain, using commercially available software, called OrcaFlex, capable of simulating coupled aero-hydro-servo-elastic models. To evaluate the performance of the TLP, the following key parameters were used: for cases related to ULS, the maximum values for tendon tensions, tower base bending moments, and nacelle accelerations are considered, and for cases related to FLS, tendon damage calculated with an S-N curve is considered. From the first simulations performed, to identify whether springing is indeed a problem for the current TLP design, resulted in the following observations.

- For the DLCs considered, springing is indeed present in the currently applied TLP model and is mainly related to the pitching motion of the structure.
- A springing response for a TLP supporting a wind turbine is mainly the result of first-order forces. This is the result of a relatively "low" pitch eigenfrequency, caused by the increased inertia due to the presence of the RNA and due to the flexibility of the tower.
- Springing plays an important role in the fatigue life of the tendons.
- Slack tendon events are present to a greater degree in tension signals, causing structural limits to be exceeded.

For the mooring system, several properties are identified that can influence the occurrence of springing. All these properties influence the eigenfrequencies of the system, since springing is identified as a resonance problem. A set of variables is chosen, which is believed to have the greatest influence. These are the inclination and the axial stiffness of the tendons. For every mooring adjustment, a new diffraction analysis is required because the second-order wave force terms containing the first-order body motions change because of different stiffness properties. For the new diffraction analyses, incorporation of the inclination of the tendons resulted in some discrepancies. The inclination of the tendons causes a stronger coupling between the surge and the pitch DOFs, which is not easily captured with the use of a globally applied stiffness matrix. This results in differences between the motion RAOs generated with OrcaWave/Hydrostar and the spectral response graphs generated with OrcaFlex (which can incorporate the flexibility of structural elements). This difference consequently results in an incorrect solution for the second-order diffraction analysis. An upper limit of 21° is established, as the values tend to diverge too much above this limit.

The time-domain analyses for these mooring adjustments result in the following conclusions. Adjusting axial stiffness univariately has little to no effect on ULS calculations. This is the result of not being able to prevent slack tendon events from occurring. The shock loads caused by these events lead to the exceedance of ULS limits. For the FLS calculations, increasing the axial stiffness results in a decrease in tendon damage. This is due to the increased tendon area, which consequently reduces the stresses in the tendons. However, the source of the largest tendon damage, namely springing, does not decrease with the change in axial stiffness. In the end, the possible increase is too marginal and is unable to invoke any change, as the values for the axial stiffness are already on the limit of the industry. Therefore, this option does not produce the desired result.

Adjusting the tendon angle univariately shows more promising results. For the ULS calculations, an optimal inclination of 16° is found, which, compared to the base case, reduces the maximum tendon tensions with ±40%, the tower base bending moment with ±50%, and the nacelle accelerations with ±65%. This reduction is linked to an increase in the coupling of the surge and pitch motions. Inclining the tendons causes the system to rotate around a particular focal point. For 16°, this focal point is located at the RNA, which forces the TLP to rotate around the RNA instead of the other way around. This in turn also mitigates the occurrence of slack tendon events and greatly reduces the occurrence of springing. Therefore, fatigue damage to the tendons also reduces to less than 1% compared to the base case. However, caution is advised towards the results, as these are site-specific due to the fact that water depth and pontoon length can greatly affect the initial stability of the floater.

An additional set of simulations is performed using a combination of the mooring adjustments mentioned before. For this combination, the optimal tendon angle of 16° is used, while ranging over the axial stiffness values. The analysis shows that an axial stiffness of 2100 MN results in the lowest tendon tensions, while an axial stiffness of 2777 MN results in the lowest maximum tower base moments and nacelle accelerations. The progression of the maximum values is related to the shifting and excitation of the eigenfrequencies of the total system. Therefore, it is concluded that an optimal configuration of the mooring system is to use an inclination of 16° for the mooring tendons and to apply an axial stiffness of 2468/2777 MN. The choice of choosing a configuration with slightly larger tendon tensions is because the tensions do not increase significantly, while the accelerations of the RNA are notably reduced, therefore increasing its service life. Additionally, increasing axial stiffness reduces fatigue damage in the tendons due to its increased tendon area.

To recapitulate, concise answers are given to the research questions mentioned in the introduction.

- *What is the cause for springing to occur in the motion of a TLP?*

  The root cause for a springing response is linked to the resonance of the constrained DOFs of the TLP. Contrary to what is seen for oil & gas related TLPs, the response is not mainly the result of a second-order wave force. The inclusion of a 15 MW wind turbine with a flexible tower causes the pitch eigenmode to have a low eigenfrequency (also much lower than seen in comparable research on floating wind TLPs). This eigenfrequency is located in the range of the high-frequency tail of the first-order loading spectrum, therefore, reducing the importance of second-order wave forces.

- *To what extent is it possible to model springing of a TLP with the use of available software?*

  It is possible to model springing with the use of time-domain analyses performed with OrcaFlex, for which hydrodynamic models are derived based on potential theory with the use of OrcaWave and Hydrostar. The range of software is not limited to the ones mentioned here. A multitude of software, encountered during the course of this thesis, showed similar capabilities. For example, the use of WAMIT might be an alternative for diffraction analyses, and the use of OpenFast might serve as a replacement for simulations with coupled aero-hydro-servo-elastic models.

- *Which properties of the mooring design have an influence on the response of a TLP due to springing types of loading?*

  Properties that could influence the response are properties related to altering the natural periods of the constrained DOFs of the TLP, because springing is a resonance problem. In the analysis, the following are identified: tendon angle, axial stiffness, number of tendons per pontoon arm, weight of tendons, and tendon length. For the case study used for this thesis, the adjustment of the tendon angles is shown to be the most effective.

- *To what extent can optimal ranges for mooring design properties be identified to minimise the occurrence and effect of springing?*

  For the case model, an optimum is found for a tendon angle of 16° and an axial stiffness of 2777 MN. A notion is regarded to this conclusion, as it is discovered that the stability of the floater heavily depends on the length of the pontoons and the water depth at the installation site.

Regarding the answers given to the sub-questions above, the following answer can be formulated for the main research question.

What aspects of a mooring system for a TLP supporting a wind turbine have to be considered during the preliminary design to minimise the influence of springing on the structural integrity of the mooring tendons?

Since the response is identified as a resonance problem, adjustments in the mooring system which will influence eigenfrequencies of the system should be considered in order to minimise the effect of springing. Furthermore, although not part of the mooring system, the length of the pontoons should be considered for adjustment, as this will help the stability of the floater if angled tendons are used. In general, the adjustment should be made so that the eigenfrequencies of the system do not coincide with the frequency components of other significant forces, such as wave, wind, etc.

6

Recommendations

Following the development of this thesis, several topics are encountered, which are regarded as necessary for further investigations, or subjects that are not completed during this thesis due to time restrictions. A list of these topics is provided below.

- As mentioned in this thesis, the evaluation of ringing is not incorporated. However, it is still believed that the response has a significant impact on the mooring system. It would therefore still be a necessary topic to investigate. A possible method for evaluating such a response is mentioned in the Appendix.
- One of the main problems encountered for the case model TLP is the low pitch eigenfrequency of the system, caused by the interaction between the floater and the combined turbine and RNA, which heavily influences the magnitudes motion and the occurrence of springing. A topic for research would be to design the tower in such a way that the pitch eigenfrequency moves away from first-order wave loading frequencies, or to use damping to minimise motion amplitudes at the RNA.
- It was initially planned to also use a fibre tendon model for the mooring lines of the TLP. However, this is not performed due to time restrictions. Fibre tendons show advantageous properties to minimise the loads in the tendons and to reduce the motions of the floater. One of these properties is the availability of damping in the system due to the viscoelastic and viscoplastic behaviour of the material. Furthermore, the rope has an increased stiffness when subjected to higher loading, which may be beneficial in avoiding resonance behaviour in the system. Including such models for floating wind TLP analyses can result in essential information for the industry.
- In this research, the effects of high-frequency loading transferred from the tendon to the soil was not considered. However, this forms an essential part of the total design. Therefore, a topic would be what the effects of springing (and ringing) are on the anchors and soil.

To close off this recommendation page, a request is made towards the academic world. During the course of this thesis, several difficulties were encountered in the acquisition of model test data and general information on floating wind turbines supported by a TLP. At the time of writing, it is believed that there is a dire need for more research regarding this topic, especially considering the importance of the energy transition. A great potential is seen for the use of this concept in the floating wind industry, and an increased effort to generate knowledge will have significant benefits towards the development and eventual installation of such structures. It is believed that academic institutions should play a leading role in this and that more effort should be invested in generating publicly available information.

7

References

American Petroleum Institute (API). (2005). *Design and analysis of station keeping systems for floating structures* (Tech. Rep.). Washington: API.

Bachynski, E., & Moan, T. (2014). Ringing loads on tension leg platform wind turbines. *Ocean Engineering*, *84*, 237–248. doi: 10.1016/j.oceaneng.2014.04.007

Bluewater. (2022). *Vision & mission.* Retrieved 10-05-2022, from `https://www.bluewater.com/corporate-about-us/vision-mission/`

Botros, F., Wilson, T., & Johnson, C. (1996). The Heidrun field: Global structural design and analysis of the Heidrun TLP. *All Days.* doi: 10.4043/8099-ms

Bridon. (2011). *Bridon-Oil and Gas catalogue* (5th ed.). Bridon Bekaert.

Cape Holland. (2022). *Monopile installation.* Retrieved 12-03-2023, from `https://capeholland.com/applications/monopile-installation/`

Chakrabarti, S. K. (2005). *Handbook of offshore engineering.* Elsevier.

Chen, X.-B. (2004). Middle-field formulation for the computation of wave-drift loads. *Journal of Engineering Mathematics*, *59*(1), 61–82. doi: 10.1007/s10665-006-9074-x

Davies, K. B., Leverette, S. J., & Spillane, M. W. (1994). Ringing response of TLP and GBS platforms. *Proc 7th Int Conf Behavior Offshore Structures*, *2*, 569–585.

Den Hartog, J. (1947). *Mechanical vibrations* (3rd ed.). McGraw-Hill Book Company, INC.

Den Hartog, J. (2012). *Strength of materials.* Dover Publications.

Det Norske Veritsas (DNV-OS-E301). (2020). *Position mooring* (Tech. Rep.). Høvik: DNVGL-OS-E301.

Det Norske Veritsas (DNV-OS-E304). (2020). *Offshore mooring steel wire rope* (Tech. Rep.). Høvik: DNVGL-OS-E304.

Det Norske Veritsas (DNV-RP-0286). (2019). *Coupled analysis of floating wind turbines* (Tech. Rep.). Høvik: DNVGL-RP-0286.

Det Norske Veritsas (DNV-RP-C205). (2019). *Environmental conditions and environmental loads* (Tech. Rep.). Høvik: DNV-RP-C205.

Det Norske Veritsas (DNV-RP-F205). (2019). *Global performance analysis of deep water floating structures* (Tech. Rep.). Høvik: DNV-RP-F205.

DTU. (2016). *Design load basis for offshore wind turbines* (Tech. Rep.). Frederiksborgvej: Department of Wind Energy.

Eatock Taylor, R., & Hung, S. (1987). Second order diffraction forces on a vertical cylinder in regular waves. *Applied Ocean Research*, *9*(1), 19–30. doi: 10.1016/0141-1187(87)90028-9

Faltinsen, O. M. (1990). *Sea loads on ships and offshore structures.* Cambridge University Press.

Faltinsen, O. M., Newman, J. N., & Vinje, T. (1995). Nonlinear wave loads on a slender vertical cylinder. *Journal of Fluid Mechanics*, *289*, 179–198. doi: 10.1017/s0022112095001297

Gaertner, E., Rinker, J., Sethuraman, L., Zahle, F., Anderson, B., Barter, G., … et al. (2020). *Definition of the iea 15-megawatt offshore reference wind.*

Grue, J., Bjorshol, G., & Strand, O. (1993). *Higher harmonic wave exciting forces on a vertical cylinder* (Tech. Rep.). Oslo: Matematisk Institutt Oslo.

Grue, J., & Huseby, M. (2002). Higher-harmonic wave forces and ringing of vertical cylinders. *Applied Ocean Research*, *24*(4), 203–214. doi: 10.1016/s0141-1187(02)00048-2

Gueydon, S., Wuillaume, P., Jonkman, J., Robertson, A., & Platt, A. (2015, Jun). Comparison of second-order loads on a tension-leg platform for wind turbines. *NREL.*

Guha, A. (2012). Development of a computer program for three dimensional frequency domain analysis of zero speed first order wave body interaction. *Master thesis Ocean Engineering.*

Gurley, K. R., & Kareem, A. (1998). Simulation of ringing in offshore systems under viscous loads. *Journal of Engineering Mechanics*, *124*(5), 582–586. doi: 10.1061/(asce)0733-9399(1998)124:5(582)

Haselsteiner, A. F., Sander, A., Ohlendorf, J.-H., & Thoben, K.-D. (2020). Global hierarchical models for wind and wave contours: Physical interpretations of the dependence functions. *Volume 2A: Structures, Safety, and Reliability.* doi: 10.1115/omae2020-18668

Haselsteiner, A. F., & Thoben, K.-D. (2020). Predicting wave heights for marine design by prioritizing extreme events in a global model. *Renewable Energy*, *156*, 1146–1157. doi: 10.1016/j.renene.2020.04.112

Horwath, S., Hassrick, J., Grismala, R., & Diller, E. (2020).

IEC-61400-1. (2019). *Wind energy systems - Design requirements* (4th ed.).

IEC-61400-3-2. (2019). *Wind energy systems generation systems - Design requirements for floating offshore wind turbines* (1st ed.).

Jefferys, E. R., & Rainey, R. C. (1994). Slender body models of TLP and GBS ringing. *Proc Int Conf Behavior Offshore Structures*, *2*, 587–605.

Johannessen, T. B. (2012, Feb). Nonlinear superposition methods applied to continuous ocean wave spectra. *Journal of Offshore Mechanics and Arctic Engineering*, *134*(1). doi: 10.1115/1.4003518

Jonkman, J. (2010). *Definitiion of the floating system for phase IV of OC3* (Tech. Rep. No. WE101211). Golden, Colorado: NREL U.S. Department of Energy.

Journée, J., & Massie, W. (2008). *Offshore hydromechanics* (2nd ed.). Delft University of Technology.

Kim, C. H. (2008). *Nonlinear waves and offshore structures.* World Scientific.

Kim, M. (1991). Second-order sum-frequency wave loads on large-volume structures. *Applied Ocean Research*, *13*(6), 287–296. doi: 10.1016/s0141-1187(05)80052-5

Kim, M., & Yue, D. K. (1990). The complete second-order diffraction solution for an axisymmetric body part 2. Bichromatic incident waves and body motions. *Journal of Fluid Mechanics*, *211*, 557–593. doi: 10.1017/s0022112090001690

Kim, S.-J., Kim, M.-H., & Koo, W. (2021). Higher-order diffraction forces on vertical circular cylinders by using a three-dimensional fully-nonlinear potential numerical wave tank. *Ocean Engineering*, *232*, 109065. doi: 10.1016/j.oceaneng.2021.109065

Kim, T., & Kim, Y. (2015). Study on extreme springing and ringing loads on TLP tethers. *Proceedings of the Japan Society of Naval and Marine Engineering*, *20*, 53–56.

Koo, B., Goupee, A. J., Lambrakos, K., & Kimball, R. W. (2012). Model tests for a floating windturbine on three different floaters. *Volume 7: Ocean Space Utilization; Ocean Renewable Energy.* doi: 10.1115/omae2012-83642

Krokstad, J. R., Stansberg, C. T., Nestega, A., & Marthinsen, T. (1998). A new nonslender ringing load approach verified against experiments. *Journal of Offshore Mechanics and Arctic Engineering*, *120*(1), 20–29. doi: 10.1115/1.2829515

Kvittem, M. I., Bachynski, E. E., & Moan, T. (2012). Effects of hydrodynamic modelling in fully coupled simulations of a semi-submersible wind turbine. *Energy Procedia*, *24*, 351–362. doi: 10.1016/j.egypro.2012.06.118

Lavidas, G., & Polinder, H. (2019). North sea wave database (nswd) and the need for reliable resource data: A 38 year database for metocean and wave energy assessments. *Atmosphere*, *9*(1), 551-578. doi: https://doi.org/10.3390/atmos10090551

LeMéhauté, B. (1976). *An introduction to hydrodynamics and water waves.* Springer-Verlag.

Malenica, S., & Molin, B. (1994). Third order triple frequency wave forces on fixed vertical cylinders. *9th Workshop on water waves and floating bodies.*

Matha, D. (2010). Model development and loads analysis of an offshore wind turbine on a tension leg platform with a comparison to other floating turbine concepts. *NREL.* doi: https://doi.org/10.2172/973961

Milano, D., Peyard, C., & Capaldo, M. (2018). Impact of high order wave loads on a 10 MW tension-leg platform floating wind turbine at different tendon inclination angles. *16th Journal for Hydromechanics.*

Natvig, B. (1994). A proposed ringing analysis model for higher order tether response. *Proceedings of the Fourth Interational Offshore and Polar Engineering Conference*, *1*, 40-51.

Newman, J. N. (1996). Nonlinear scattering of long waves by a vertical cylinder. *Waves and Nonlinear Processes in Hydrodynamics*, 91–102. doi: 10.1007/978-94-009-0253-4_8

Pinkster, J. A. (1980). *Low frequency second order wave exciting forces on floating structures* (Unpublished doctoral dissertation). Veenman.

Roald, L., Jonkman, J., & Robertson, A. (2014). *The effects of second-order hydrodynamics on a floating wind turbine* (Tech. Rep. No. WE11.5070). Golden, Colorado: NREL U.S. Department of Energy.

Stansberg, C. T., Huse, E., Krogstad, J. R., & Lehn, E. (1995). Experimental study of non-linear loads on vertical cylinders in steep random waves,". *ISOPE*, *1*, 78–82.

Telste, J. G., & Noblesse, F. (1986). Numerical evaluation of the green function of water-wave radiation and diffraction. *Journal of Ship Research*, *30*(02), 69–84. doi: 10.5957/jsr.1986.30.2.69

Teng, B., & Kato, S. (2002). Third order wave force on axisymmetric bodies. *Ocean Engineering*, *29*(7), 815–843. doi: 10.1016/s0029-8018(01)00047-6

Viswanathan, S., Holden, C., Egeland, O., & Greco, M. (2021). An open-source python-based boundary-element method code for the three-dimensional, zero-froude, infinite-depth, water-wave diffraction-radiation problem. *Modelling, Identification and Control: A Norwegian Research Bulletin*, *42*(2), 47–81. doi: 10.4173/mic.2021.2.2

Wang, T., & Zou, J. (2006). Hydrodynamics in deep water TLP tendon design. *Journal of Hydrodynamics*, *18*(S1), 377–384. doi: 10.1007/bf03400476

WindEurope. (2021). *Getting fit for 55 and set for 2050.* Retrieved from `https://etipwind.eu/publications`

Winterstein, S. R., Ude, T. C., & Marthinsen, T. (1994). Volterra models of ocean structures: Extreme and fatigue reliability. *Journal of Engineering Mechanics*, *120*(6), 1369–1385. doi: 10.1061/(asce)0733-9399(1994)120:6(1369)

Xu, F., & Wang, Y. (2021). Numerical simulation of ringing responses of a vertical cylinder. *Ocean Engineering*, *226*, 108815. doi: 10.1016/j.oceaneng.2021.108815

Zou, J., & Kim, C. H. (2000). Generation of strongly asymmetric wave in random seaway. *Proc. 10th Int. Offshore Polar Eng. Conf., ISOPE*.

Zou, J., Xu, Y., & Kim, C. H. (1997). Time domain simulation of a TLP's response due to laboratory-generated asymetric irregular waves. *Proc. 7th Int. Offshore Polar Eng. Conf., ISOPE*, *1*, 193–200.

Appendix A

Supplementary derivations

A.1 Derivation of linear incoming wave potential

For the derivation of Φ^w it is assumed that the slope of the surface of the water is very small, which means that the harmonic pressures have a linear relationship with the elevation of the surface of the wave. Thus, the equation representing Φ^w can be written as follows:

$$\Phi^w(x, z, t) = P(z) \cdot \sin(kz - \omega t). \tag{A.1.1}$$

This equation must meet particular boundary conditions:

- Continuity condition or Laplace equation
- Seabed boundary condition
- Free surface boundary condition
- Free surface kinematic boundary condition

Laplace equation

$$u = v_x = \frac{\partial \Phi^w}{\partial x}, \qquad v = v_y = \frac{\partial \Phi^w}{\partial y}, \qquad w = v_z = \frac{\partial \Phi^w}{\partial z}. \tag{A.1.2}$$

These can be substituted into the continuation condition (A.1.3) resulting in the Laplace equation (A.1.4).

$$\frac{\partial u}{\partial x} + \frac{\partial v}{\partial y} + \frac{\partial w}{\partial z} = 0, \tag{A.1.3}$$

$$\frac{\partial^2 \Phi^w}{\partial x^2} + \frac{\partial^2 \Phi^w}{\partial y^2} + \frac{\partial^2 \Phi^w}{\partial z^2} = 0 = \nabla^2 \Phi^w. \tag{A.1.4}$$

For the derivation, it is assumed that the flow is uniform on the y-axis, and thus the water particles move only in the x-z plane.

$$v = \frac{\partial \Phi^w}{\partial y} = 0 \qquad and \qquad \frac{\partial v}{\partial y} = \frac{\partial^2 \Phi^w}{\partial y^2} = 0. \tag{A.1.5}$$

Thus:

$$\frac{\partial^2 \Phi^w}{\partial x^2} = -P(z) \cdot k^2 \cdot \sin(kx - \omega t), \tag{A.1.6}$$

$$\frac{\partial^2 \Phi^w}{\partial z^2} = \frac{\partial^2 P(z)}{\partial z^2} \cdot \sin(kx - \omega t). \tag{A.1.7}$$

Combining these derivations with the Laplace equation results in Equation A.1.8, which is a basic differential equation with a known solution as represented in Equation A.1.9.

$$\frac{d^2P(z)}{d^2} - k^2P(z) = 0, \tag{A.1.8}$$

$$P(z) = C_1e^{kz} + C_2e^{-kz}. \tag{A.1.9}$$

Seabed boundary condition

Next boundary being substituted is the boundary condition on the seabed. There should be no flow through the seabed, so $\frac{\partial \Phi_w}{\partial z}\Big|_{z=-h} = 0$, as can be seen in Figure A.1.

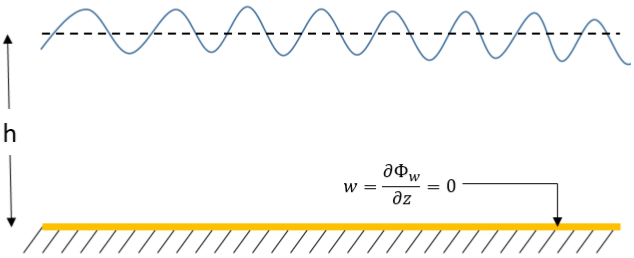

Figure A.1: Vertical velocity at the seabed.

Substituting the boundary condition leads to:

$$\begin{aligned} \frac{\partial \Phi^w}{\partial z}|_{z=-h} =& k \cdot (C_1e^{-kh} - C_2e^{kh}) \cdot \cos(kx - \omega t) = 0, \\ & k \cdot (C_1e^{-kh} - C_2e^{kh}) = 0, \\ & C_1e^{-kh} - C_2e^{kh} = 0, \\ & C_1e^{-kh} = C_2e^{kh}. \end{aligned} \tag{A.1.10}$$

Introducing C, it can be defined that:

$$\frac{C}{2} = C_1e^{-kh} = C_2e^{kh}. \tag{A.1.11}$$

Which can be substituted into Equation A.1.9.

$$\begin{aligned} P(z) &= \frac{C}{2} \cdot e^{kh}e^{kz} + \frac{C}{2} \cdot e^{-kh}e^{-kz}, \\ &= \frac{C}{2} \cdot \left(e^{k(h+z)} + e^{-k(h+z)}\right). \end{aligned} \tag{A.1.12}$$

The definition of cosh is as follows:

$$\cosh(s) = \frac{e^{+s} + e^{-s}}{2}. \tag{A.1.13}$$

Thus Equation A.1.12 can be rewritten as follows:

$$P(z) = C \cdot \cosh(k(h+z)). \tag{A.1.14}$$

Thus the incoming wave potential can be written as:

$$\Phi^w(x, z, t) = C \cdot \cosh(k(h+z)) \cdot \sin(kx - \omega t). \tag{A.1.15}$$

Dynamic boundary condition of the free surface

The following boundary condition to be substituted is the dynamic boundary condition of the free surface. This boundary condition states that the pressure on the free surface ($z = \zeta$) is equal to the atmospheric pressure (p_0), as can be seen in Figure A.2.

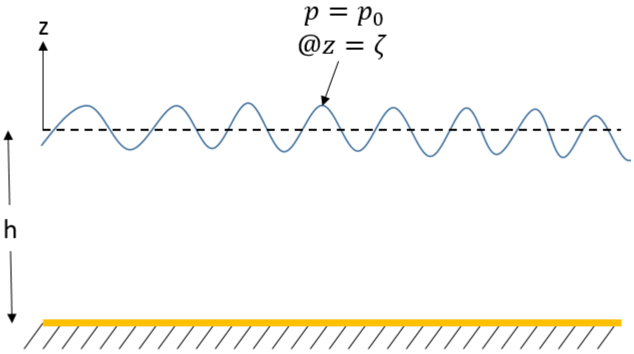

Figure A.2: Free surface dynamic boundary condition.

The pressure is derived from the Bernoulli equation (A.1.16). In this equation, it is assumed that the wave steepness is very small, therefore cancelling the $\frac{1}{2}\nabla^2\Phi^2$ part, turning the equation into the first order Bernoulli equation.

$$\frac{\partial\Phi^w}{\partial t} + \frac{p}{\rho} + \frac{1}{2}\nabla^2\Phi^2 + gz = C^*. \tag{A.1.16}$$

Substituting the boundary condition in the reduced Bernoulli equation leads to:

$$\begin{aligned} @Free\ surface \rightarrow & \frac{\partial\Phi^w}{\partial t} + \frac{p_0}{\rho} + g\zeta = C^*, \\ & \frac{\partial\Phi^w}{\partial t} - C^* + \frac{p_0}{\rho} + g\zeta = 0. \end{aligned} \tag{A.1.17}$$

$\frac{p_0}{\rho} - C^*$ can be included in $\frac{\partial\Phi^w}{\partial t}$. This can be done as it will not influence the velocities obtained from the potential (Journée & Massie, 2008). Thus:

$$\frac{\partial\Phi^w}{\partial t} + g\zeta = 0 \quad \text{for z=0.} \tag{A.1.18}$$

This equation is evaluated at the instantaneous position of the free surface, but it is necessary to know what this equation is at the mean position of the wave (z=0). Therefore, a Taylor expansion of t is performed at z = 0.

$$\begin{aligned} \left\{\frac{\partial\Phi^w}{\partial t}\right\}_{z=\zeta} &= \left\{\frac{\partial\Phi^w}{\partial t}\right\}_{z=0} + \zeta \cdot \left\{\frac{\partial^2\Phi^w}{\partial t^2}\right\}_{z=0} + ... \\ \left\{\frac{\partial\Phi^w}{\partial t}\right\}_{z=\zeta} &= \left\{\frac{\partial\Phi^w}{\partial t}\right\}_{z=0} + \mathcal{O}\left(\epsilon^2\right) \end{aligned} \tag{A.1.19}$$

This shows that the time derivative of the wave potential at the instantaneous position of the free surface can be compared with the one at mean water level, since the higher-order terms can be neglected as the derivation focusses on finding the first order potential. Thus, Equation A.1.18 can be rewritten to:

$$\frac{\partial\Phi^w}{\partial t} + g\zeta = 0 \quad \text{for z=0,} \tag{A.1.20}$$

$$\begin{aligned}\zeta &= -\frac{1}{g}\cdot\frac{\partial\Phi^w}{\partial t},\\ &= -\frac{1}{g}\cdot -\omega\, C\cdot\cosh(kh)\cos(kx-\omega t), \qquad\text{(A.1.21)}\\ &= \zeta_a\cdot\cos(kz-\omega t)\rightarrow\zeta_a=\frac{\omega\, C}{g}\cosh(kh),\end{aligned}$$

$$C=\frac{\zeta_a g}{\omega}\cdot\frac{\cosh(k(h+z))}{\cosh(kh)}\cdot\sin(kx-\omega t). \qquad\text{(A.1.22)}$$

Thus the wave potential becomes:

$$\boxed{\Phi^w=\frac{\zeta_a\, g}{\omega}\cdot\frac{\cosh(k(h+z))}{\cosh(kh)}\cdot\sin(kx-\omega t)} \qquad\text{(A.1.23)}$$

And for deep waters:

$$\boxed{\Phi^w=\frac{\zeta_a\, g}{\omega}\cdot e^{kz}\cdot\sin(kx-\omega t)} \qquad\text{(A.1.24)}$$

Free surface kinematic boundary condition

An additional boundary condition applied on the fluid particle is that the vertical velocity of a water particle on the free surface is the same as the vertical velocity of the free surface itself. Thus at the free surface, it holds that:

$$\frac{dz}{dt}=\frac{\partial\zeta}{\partial t}+\frac{\partial\zeta}{\partial x}\frac{dx}{dt}. \qquad\text{(A.1.25)}$$

which, after a Taylor expansion, is valid at $z=0$. Substituting the obtained first-order potential and rearranging the terms, the equation becomes:

$$\frac{\partial z}{\partial t}+\frac{1}{g}\cdot\frac{\partial^2\Phi^w}{\partial t^2}=0\quad\text{for z=0.} \qquad\text{(A.1.26)}$$

A.2 Method for solving the first order radiation and diffraction potentials

In this Appendix, a method for solving the potentials in question is given. To solve the radiation and diffraction potentials, boundary conditions have to be applied. These are the same as for the nonlinear forcing case as explained in the introduction of Chapter 2.2. Detail is given to the second boundary equation, which states that the component of the fluid velocity normal to the hull should equal the normal component of the velocity of the hull itself. Thus, for the potential on the hull:

$$\frac{\partial\Phi}{\partial n}=v_n(\vec{x},t). \qquad\text{(A.2.1)}$$

Due to the linearisation of the solution for the potential, this equation can be written as follows:

$$\frac{\partial\Phi}{\partial n}=v_n(\vec{x},t)=\sum_{j=1}^{6}v_j(t)\cdot f_j(\vec{x}), \qquad\text{(A.2.2)}$$

$$\begin{aligned} f_i, i = 1..3 &= (\vec{n})_i\,, \\ f_i, i = 4..6 &= (\vec{n} \times \vec{x})_i\,. \end{aligned} \tag{A.2.3}$$

And subsequently for the radiation potentials (Φ^r):

$$\begin{aligned} \Phi^r(\vec{x}, t) &= \sum_{j=1}^{6} \Phi_j^r(\vec{x}, t), \\ &= \sum_{j=1}^{6} \phi_j(\vec{x}) \cdot v_j(t). \end{aligned} \tag{A.2.4}$$

To remove $\dfrac{\partial \Phi}{\partial n}$ from Equation A.2.2, Equation A.2.4 is substituted and results in the following equation, which holds for the boundary of the submerged hull:

$$\sum_{j=1}^{6} \frac{\partial}{\partial n} \left(\phi_j(\vec{x}) \cdot v_j(t)\right) = \sum_{j=1}^{6} v_j(t) \cdot f_j(\vec{x}), \tag{A.2.5}$$

$$\frac{\partial \phi_j(\vec{x})}{\partial n} = f_j(\vec{x}) = n_j(\vec{x}) \text{ for } j = 1, ..., 6. \tag{A.2.6}$$

Thus, the equation describes what the boundary conditions for the potentials at the hull are, written in terms of the unknown velocity potential ϕ_j. As described by Journée & Massie (2008), the linearity of the model equation allows the wave and diffraction potential to be written as described here below, where Equation A.2.7 represents the final boundary condition for the wave and diffraction potential.

$$\frac{\partial \phi_0}{\partial n} + \frac{\partial \phi_7}{\partial n} = 0. \tag{A.2.7}$$

Additionally, two additional conditions are imposed on the solution, one of which is the radiation condition, which implies that the influence of the potential at a large distance from the body tends to be zero (see Equation A.2.8) and a ship body tends to be symmetric, thus symmetry/anti-symmetry is to be expected for the potential equations (see Equation A.2.9).

$$\lim_{R \to \infty} \Phi \;=\; 0, \tag{A.2.8}$$

$$\begin{aligned} \Phi_2(-x, y) &= -\,\Phi_2(+x, y), \\ \Phi_3(-x, y) &= +\,\Phi_3(+x, y), \\ \Phi_4(-x, y) &= -\,\Phi_4(+x, y). \end{aligned} \tag{A.2.9}$$

Since the time element are eliminated from the boundary conditions, the solution now only depends on space-related variables. For this solution, the influence and interaction of the potential spread over the body should be taken into account. Thus, a particular point on the body influences the solution of the potential on a different point on the body and vice versa. To represent this interaction, the use of source potentials is considered. It is possible to solve these potentials with the use of Green's second identity (an expansion on Green's function is provided in Appendix A.3). In Equation A.2.10, the Green's function is applied over the mean submerged hull (S_0), which describes the influence of a unit source and an image source on a particular field point located at $\vec{x}$ and the influence of a source at the field point itself, describing the effect of waves on the body.

$$\phi(\vec{x}) = \iint_{S_0} \sigma(\vec{\xi})G(\vec{x}, \vec{\xi}, f)\partial S. \tag{A.2.10}$$

However, this function represents a problem. The Green's function depends on the location of the source ($\vec{\xi}$) and observation point ($\vec{x}$) (see Equation A.3.3), if these locations coincide with each other, a singularity appears in the Green's function. However, this can be resolved by applying a Cauchy principal value integral which results in Equation A.2.11,where if the locations coincide, the velocity potential is equal to $\frac{\sigma_j(\vec{x})}{2}$. Or, the singularity can be avoided by considering the source panels to be at a very small distance below the actual body panel in the 3D body panel model as described by Guha (2012).

$$\phi(\vec{x}) = \frac{\sigma(\vec{x})}{2} + \iint_{S_0} \sigma(\vec{\xi})G(\vec{x}, \vec{\xi}, f)\partial S. \tag{A.2.11}$$

Substituting Equation A.2.11 into the boundary conditions represented by Equations A.2.6 & A.2.7, will lead to the following condition equation.

$$\frac{\sigma_j(\vec{x})}{2} + \iint_{S_0} \sigma_j(\vec{\xi})\frac{\partial G(\vec{x}, \vec{\xi}, f}{\partial n(\vec{x})}\partial S = \begin{cases} n_j(\vec{x}), & j = 1...6 \\ -\dfrac{\partial \phi_0}{\partial n(\vec{x})}, & j = 7 \end{cases} \tag{A.2.12}$$

To solve these equations on an arbitrary formed body, a body panel method will be used. The body will then be represented by N flat panels, each with a constant source potential σ_p (see Figure A.3 for an illustration of this 3D body panel model). Equations A.2.10 & A.2.12 will then change to:

$$\phi(\vec{x}) = \sum_{p=1}^{N} \sigma_p(\vec{\xi}_p) \iint_{S_p} G_p(\vec{x}, \vec{\xi}_p; f)\partial S, \tag{A.2.13}$$

$$\sum_{p=1}^{N} \sigma_p(\vec{\xi}_p) \iint_{S_p} \frac{\partial G(\vec{x}, \vec{\xi}_p, f)}{\partial n(\vec{x})}\partial S = \begin{cases} n_j(\vec{x}), & j = 1...6 \\ -\dfrac{\partial \phi_0}{\partial n(\vec{x})}, & j = 7 \end{cases} \Bigg|_{\vec{x}\in\vec{\xi}_p} \tag{A.2.14}$$

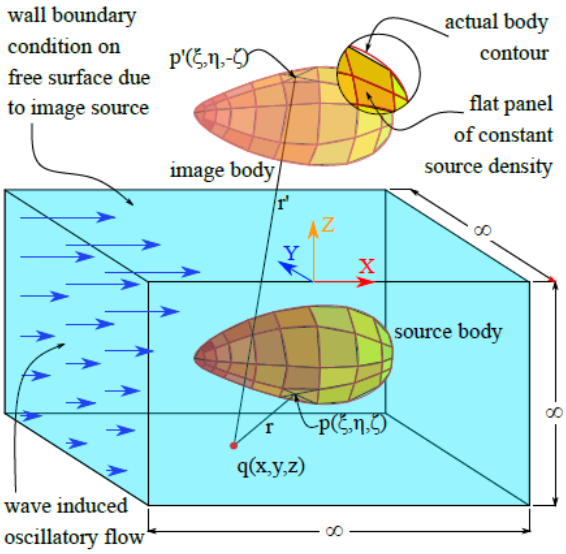

Figure A.3: 3D body panel representation (Viswanathan et al., 2021).

Using Equation A.2.14 will lead to N sets of algebraic equations for which $\sigma_j(\vec{x})$ is the only unknown. These can be gathered into what Viswanathan et al. (2021) calls 'the α matrix. σ^{ω}_{ps} in the matrix represents the induced normal velocity at body panel p, $p \in \{1, ...N\}$ due to a unit source density distribution on source panel s, $s \in \{1, ..., N\}$. This σ^{ω}_{ps} is also related to the wave frequency ω due to Green's function. These entries are either determined by the Cauchy principle value integral as described in Equation A.2.11 or by Equation A.2.14 in combination with the method described in Guha (2012). The right-hand side is complemented by $v^{n,\omega}_{j_p}$, $p \in \{1, ..., N\}$ for which $j \in \{1, ..., 6\} \to v^{n,p}_{j_p} = n_j$ and for $j = 7 \to v^{n,p}_{j_p} = \dfrac{-\partial \phi^{\omega}_0}{\partial n}$.

$$\begin{pmatrix} \alpha^{\omega}_{11} & \dots & \alpha^{\omega}_{1N} \\ \vdots & \ddots & \vdots \\ \alpha^{\omega}_{N1} & \dots & \alpha^{\omega}_{NN} \end{pmatrix} \cdot \begin{pmatrix} \sigma^{\omega}_{j1} \\ \vdots \\ \sigma^{\omega}_{jN} \end{pmatrix} = \begin{pmatrix} v^{n,\omega}_{j1} \\ \vdots \\ v^{n,\omega}_{jN} \end{pmatrix} \tag{A.2.15}$$

Equation A.2.15 can be solved which will result in unknown source distributions which comply with previously determined boundary conditions. To obtain the velocity potentials, a 'β-matrix' (Viswanathan et al., 2021) is used. These entries can be once again described by Equations A.2.11 or A.2.13.

$$\begin{pmatrix} \phi^{\omega}_{j1} \\ \vdots \\ \phi^{\omega}_{jN} \end{pmatrix} = \begin{pmatrix} \beta^{\omega}_{11} & \dots & \beta^{\omega}_{1N} \\ \vdots & \ddots & \vdots \\ \beta^{\omega}_{N1} & \dots & \beta^{\omega}_{NN} \end{pmatrix} \cdot \begin{pmatrix} \sigma^{\omega}_{j1} \\ \vdots \\ \sigma^{\omega}_{jN} \end{pmatrix} \tag{A.2.16}$$

A.3 Green's function

In Appendix A.2, the Green's function is introduced to solve the source potentials that cover the floating object as a sheet. In this Appendix, a closer look is provided to give insight into the Green's function. The work of Viswanathan et al. (2021) and Telste & Noblesse (1986) is being used as a source of information.

In the paper from Viswanathan et al. (2021), it starts with the velocity potential ϕ_Q used in a fluid domain:

$$\phi_Q = \frac{-1}{4\pi} \iint_S \left(\frac{\partial \phi}{\partial n} - \frac{\partial \phi'}{\partial n} \right) \frac{1}{r} \partial S. \tag{A.3.1}$$

Where ϕ and ϕ' represent potentials outside and inside the closed body surface S and r is the distance between $Q(\vec{x})$ with $\vec{x} = (x, y, z)$ and the source located at $P(\vec{\xi})$ with $\vec{\xi} = (\xi, \eta, \zeta)$. These source potentials can be represented by $\sigma(\vec{\xi}) = \left(\dfrac{\partial \phi}{\partial n} - \dfrac{\partial \phi'}{\partial n} \right)$ and a free-space Green function is introduced as $G^* \left(\vec{x}, \vec{\xi} \right) = \dfrac{-1}{4\pi r}$, resulting in the following equation:

$$\phi(\vec{x}) = \iint_S \sigma(\vec{\xi}) G^*(\vec{x}, \vec{\xi}) \partial S. \tag{A.3.2}$$

This free space Green function is transformed into a free surface Green function given by Telste & Noblesse (1986), which will take into account the boundary condition on the free surface.

$$G(\vec{x},\vec{\xi},f) = \frac{-1}{4\pi}\cdot\left(\frac{1}{r}+\frac{1}{r'}\right)+\tilde{G}(\vec{x},\vec{\xi},f). \tag{A.3.3}$$

Where:

$$\tilde{G}(\vec{x},\vec{\xi},f) = \frac{-1}{4\pi}\left[2f\left\{R_0(h,v)-i\pi J_0(h)\exp(v)\right\}\right], \tag{A.3.4a}$$

$$f = \frac{\omega^2 L}{g} \quad \text{L is the reference length}, \tag{A.3.4b}$$

$$p = \left\{(x-\xi)^2+(y-\eta)^2\right\}, \tag{A.3.4c}$$

$$r = \left\{p^2+(z-\zeta)^2\right\}^{1/2}, \tag{A.3.4d}$$

$$r' = \left\{p^2+(z+\zeta)^2\right\}^{1/2}, \tag{A.3.4e}$$

$$h = fp, \tag{A.3.4f}$$

$$v = f(z+\zeta). \tag{A.3.4g}$$

A relation between these parameters is illustrated in Figure A.4.

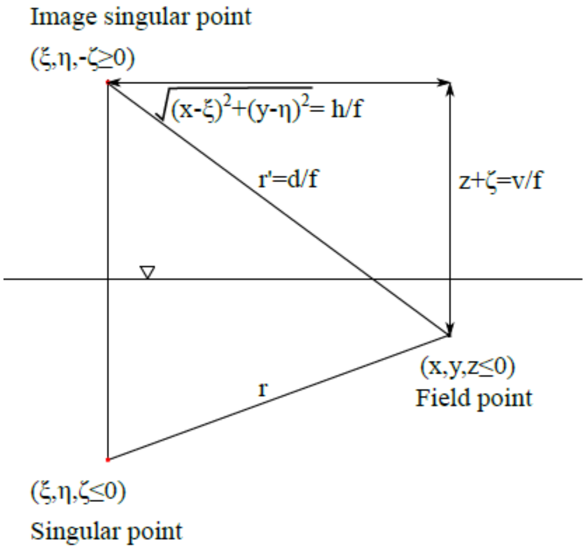

Figure A.4: Definition sketch (Telste & Noblesse, 1986).

The first term represents the sum of all potentials of the unit source and the image source. The image source accounts for the interaction between the body and the linearised free surface. The second term ($\tilde{G}$) represents the inclusion of waves in the model. This wavy part of the Green's function has the following partial derivatives.

$$\frac{\partial\tilde{G}}{\partial x} = \frac{\partial\tilde{G}}{\partial p}\frac{(x-\xi)}{p}, \tag{A.3.5a}$$

$$\frac{\partial \tilde{G}}{\partial y} = \frac{\partial \tilde{G}}{\partial p}\frac{(y-\eta)}{p}, \tag{A.3.5b}$$

$$\frac{\partial \tilde{G}}{\partial z} = \frac{1}{4\pi}\left[-2f^2\left\{\frac{1}{d} + R_0(h,v) - i\pi J_0(h)e^v,\right\}\right] \tag{A.3.5c}$$

$$\frac{\partial \tilde{G}}{\partial p} = \frac{1}{4\pi}\left[2f^2\left\{R_1(h,v) + iJ_1(h)e^v\right\}\right], \tag{A.3.5d}$$

$$d = (h^2+v^2)^{1/2} = fr'. \tag{A.3.5e}$$

The variables R_0 & R_1 are extensively described by Telste & Noblesse (1986), J_0 & J_1 are Bessel functions of the first kind. These partial derivatives can be substituted into the derivative $\frac{\partial G}{\partial n}$ in the following matter.

$$\frac{\partial G}{\partial n} = \frac{\partial G}{\partial x}n_x + \frac{\partial G}{\partial y}n_y + \frac{\partial G}{\partial z}n_z. \tag{A.3.6}$$

A.4 Environmental contour plot estimation

For the determination of environmental contour plots, the IFORM method is used. This uses a Rosenblatt transformation using the probability distributions of metocean variables. For the determination of probability functions, a model from design code C205 (DNV-RP-C205, 2019) or the OMAE model described by Haselsteiner et al. (2020). Both models are developed and their fit to the data are compared. This comparison can be seen in Figure A.5. The fit to the OMAE model is better compared to the model from DNV. In the remainder of this chapter, the calculation of the OMAE will be explained.

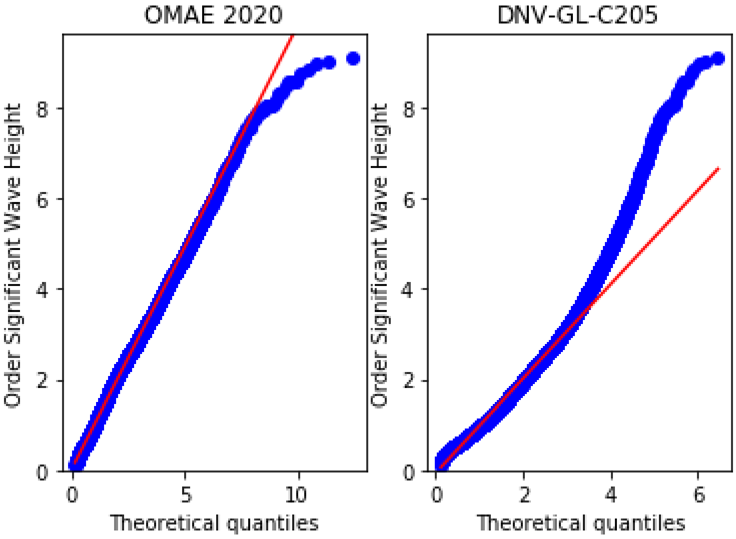

Figure A.5: Comparison study between DNV and OMAE environmental contour models

In the OMAE model, a contour plot method is given for the combination of the significant wave height and conditional zero-up crossing period (HS-TZ) and for the combination of the wind speed and the conditional wave height (UW-HS).

A.4.1 HS-TZ environmental contour

For the HS-TZ model, the significant wave height data are fitted to an exponentiated Weibull distribution (see Equation A.4.1) using a quadratic Weighted Least Squares Estimate (WLSQ) method as described by Haselsteiner & Thoben (2020) in Appendix A.

$$f(x,\alpha,\beta,\delta) = \delta \cdot \frac{\beta}{\alpha} \cdot \left[\frac{x}{\alpha}\right]^{\beta-1} \cdot \left[1 - \exp\left(-({}^{x}\!/\!_{\alpha})^{\beta}\right)\right]^{\delta-1} \cdot \exp(-({}^{x}\!/\!_{\alpha})^{\beta}). \tag{A.4.1}$$

The WLSQ method is coded in Python and validated by comparing the results with the values calculated in the paper. These are summarised in the following table.

Data set	Parameters paper			Parameters Python		
	α	β	δ	α	β	δ
A	0.207	0.684	7.79	0.2070	0.6973	7.7864
B	0.0988	0.584	36.6	0.0988	0.5835	36.575
C	0.227	0.697	9.85	0.2269	0.6973	9.846

Table A.1: Validation WLSQ method (HS-TZ model)

The WLSQ model shows an exact fit to the parameter data presented in the paper and can therefore be stated to be valid. The next step is to fit a log-normal distribution (see Equation A.4.2) to the zero-up crossing period conditional on the significant wave data. The paper suggests a wave bin of 0.5 metres.

$$f(x,\mu_{Tz},\sigma_{Tz}) = \frac{1}{x\sigma_{Tz}\sqrt{2\pi}} \cdot \exp\left(-\frac{(\ln(x)-\mu_{Tz})^2}{2\sigma_{Tz}^2}\right). \tag{A.4.2}$$

For each bin, the mean and standard deviation are calculated with the fitting function from Scipy in Python. For each parameter, the fitting functions (see Equation A.4.3) are estimated to speed up the calculation of a variable significant wave height. Parameters c are compared with the values described in the article in Table A.2.

$$\mu_{Tz}(h_s,c_1,c_2) = \ln\left(c_1 + c_2 \cdot \sqrt{\frac{h_s}{9.81}}\right), \tag{A.4.3a}$$

$$\sigma_{Tz}(h_s,c_3,c_4,c_5) = c_3 + \frac{c_4}{1 + c_5 \cdot x}. \tag{A.4.3b}$$

Param \ Data sets	Values paper			Values Python		
	A	B	C	A	B	C
c_1	3.62	3.54	2.71	3.619	3.545	2.714
c_2	5.77	5.31	6.51	5.767	5.311	6.511
c_3	0	0	0.109	0	0	0.01090
c_4	0.324	0.241	0.147	0.3239	0.2412	0.1468
c_5	0.404	0.256	0.236	0.4041	0.2564	0.2358

Table A.2: Validation fitting parameters (HS-TZ model)

Once again, the values are an exact match, and thus the Python model can be validated.

A.4.2 UW-HS environmental contour

For the UW-HS model, the wind speed is fitted to the same exponentiated Weibull distribution function used in the HS-TZ model (see Appendix A.4.1). Comparison of the calculated values with the values presented in the paper (Haselsteiner et al., 2020) are provided in Table A.3. The values are an exact match.

Data set	Parameters paper			Parameter Python		
	α	β	δ	α	β	δ
D	10.0	2.42	0.761	10.00	2.421	0.7606
E	10.8	2.48	0.683	10.775	2.483	0.6829
F	11.5	2.56	0.534	11.512	2.558	0.5339

Table A.3: Validation WLSQ method (UW-HS model)

For the conditional fit of the significant wave height for particular bins of wind speeds, a bin size of 2 m/s is selected, as suggested in the paper. Instead of a log-normal distribution fit, the exponentiated Weibull distribution is fitted to bins of significant wave heights. In this fitting procedure, the parameter δ of the function is set to a value of 5, as suggested in the paper. The resulting values for α and β are fitted to the following fitting functions.

$$\alpha_{Hs}(u_w, c_6, c_7, c_8) = (c_6 + c_7 \cdot u_w^{c_8})/2.0445^{1/\beta_{Hs}(u_w)} \tag{A.4.4a}$$

$$\beta_{Hs}(u_w, c_9, c_{10}, c_{11}, c_{12}) = c_9 + \frac{c_{10}}{1 + e^{-c_{11}(u_w - c_{12})}} \tag{A.4.4b}$$

First, the fitting of the function for β_{Hs} is done, which is consequently used in the fitting of the function for α_{Hs}. The parameter values are once again compared in Table A.4.

Data sets / Param	Values paper			Values Python		
	D	E	F	D	E	F
c_6	0.488	0.617	1.09	0.4876	0.6170	1.095
c_7	0.0114	0.0174	0.0251	0.01144	0.01737	0.02513
c_8	2.03	1.87	1.80	2.027	1.874	1.796
c_9	0.714	0.724	0.726	0.7138	0.7242	0.7256
c_{10}	1.70	2.01	1.89	1.695	2.013	1.887
c_{11}	0.304	0.309	0.194	0.3036	0.3086	0.1938
c_{12}	8.77	9.59	13.4	8.769	9.589	13.37

Table A.4: Validation fitting parameters (UW-HS model)

A.4.3 Plotting contour with IFORM

To plot an environmental contour plot with a particular probability of occurrence, Inverse First-Order Reliability Method (IFORM) is used. The steps for calculating this are explained below.

1. Select a return period in years and calculate its probability in hours.

$$\alpha_{SI} = \frac{1}{365.25 \cdot 24 \cdot \text{return period}}. \tag{A.4.5}$$

2. Calculate the safety index β_{SI} using a standard normal marginal distribution function ($-\Phi^{-1}$).
$$\beta_{SI} = -\Phi^{-1}(1 - \alpha_{SI}). \tag{A.4.6}$$
3. Calculate the uncorrelated Gaussian variables, which together should result in the safety index.
$$\sqrt{u_1 + u_2} = \beta_{SI}, \tag{A.4.7a}$$
$$u_1 = \beta_{SI} \cdot \cos(\varphi), \tag{A.4.7b}$$
$$u_2 = \beta_{SI} \cdot \sin(\varphi). \tag{A.4.7c}$$
Here φ is set to range across an entire circle.

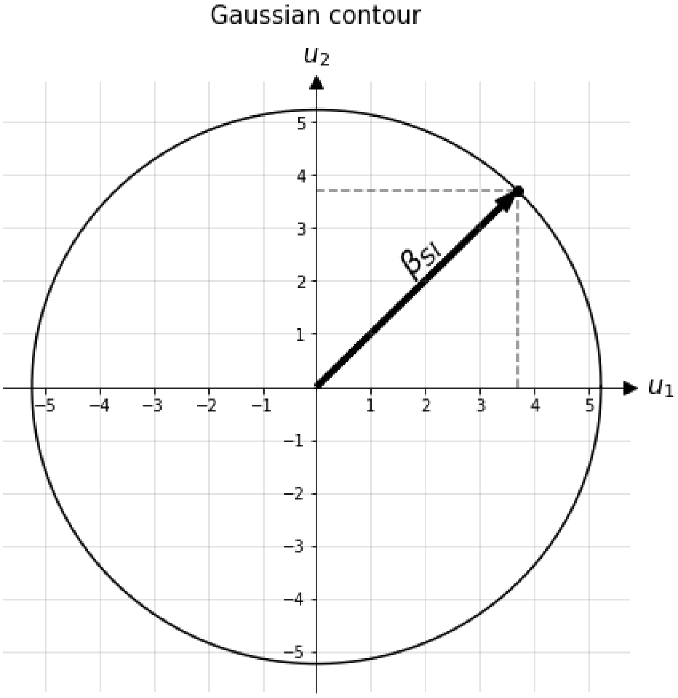

Figure A.6: Gaussian contour of variables u_1 & u_2

4. Now, having the coordinates of the Gaussian variables, the values for the metocean variables can be calculated using a Rosenblatt transformation. For the model HS-TZ, the Rosenblatt transformation uses the distributions determined in Appendix A.4.1 for calculating the value of the corresponding metocean variable.
$$h_s = F_{Hs}^{-1}(\Phi(u_1)) \tag{A.4.8a}$$
$$t_z = F_{Tz|Hs}^{-1}(\Phi(u_2)) \tag{A.4.8b}$$
Here $\Phi()$ is once again the standard normal distribution function. The resulting h_s and t_z can be plotted and will result in the contour line for the specified return period in step 1. In Figure A.7 a validation plot is shown, comparing it with the contour lines of the paper. The lines are an exact match, and thus the Python model can be said to be validated.

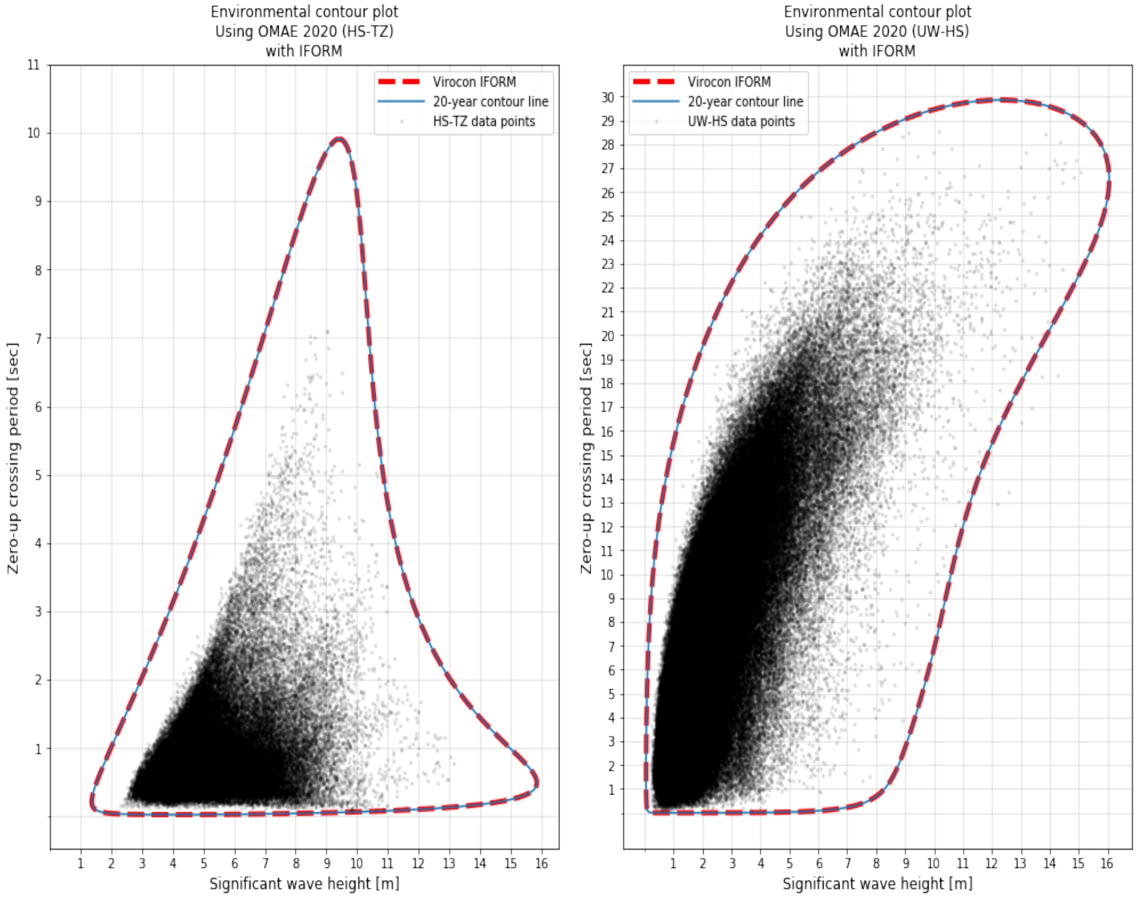

(a) **(b)**

Figure A.7: Validation for the environmental contour plot. The red dotted line is the IFORM contour line computed by the Virocon package. In the left figure, the HS-TZ contour plot with a 20-year return period for data set A is plotted, and in the right picture, the UW-HS contour plot with a 20-year return period for data set F is plotted.

A.5 Load evaluation for ringing

The computation of third-order loading forces is a complicated matter, as it is needed to solve the potential for an approximation of the non-homogeneous free surface boundary condition upto third order, which will be a computationally intensive model. The derivation for the third-order forces, including the contribution from the third-order potential, can be found in the paper from Malenica & Molin (1994). The application of this method can be found in work from Teng & Kato (2002), Krokstad et al. (1998) or more recently in S.-J. Kim et al. (2021).

Due to the complexity of the generic third-order potential loading model, a decision is made to settle for the FNV model, which describes this specific third-order load for a vertical cylinder column with a circular cross section, therefore excluding the third-order force acting on the pontoon arms. The choice of selecting FNV for the calculation of ringing loads for the TLP is based on available literature on the subject in question, where Krokstad et al. (1998) validated the use of FNV with experimental data and where recent examples of the use of FNV for the calculation of ringing loads in TLP structures can be read in articles from Bachynski & Moan (2014) and T. Kim & Kim (2015). Furthermore, DNV-RP-0286 (2019) recently suggested the use of this formula as a computationally inexpensive alternative to full-on CFD models to analyse ringing in structures.

The derivations of the FNV model and its application will be presented in the following chapters. First, the derivation of the FNV model is presented in Appendix A.5.1 based on the paper from Faltinsen et al. (1995). This derivation is based on a regular wave, Newman (1996) expanded the formula for irregular waves, and is addressed in Appendix A.5.2.

A.5.1 FNV regular wave

The applicability of the perturbation theory used in the derivation of the forces resulting from the first- and second-order potentials (see Chapters 2.2.1 & 2.2.2) is based on the following assumptions. The wave amplitude (ζ_a) is asymptotically small in relation to all other relevant length scales, for example, the wavelength ($k\zeta_a \ll 1$) and the characteristic geometry parameters of the structure. However, the observation of responses due to third-order loading is often found in severe sea states of $\zeta_a = 10m$ and $\lambda = 200m - 400m$ (Grue et al., 1993). The fact that a common radius of a vertical column for an offshore structure is $a = 10m$, contradicts the assumption that the wave amplitude is small with respect to all geometric aspects of a structure, since $\zeta_a/a = \mathcal{O}(1)$. In the literature, this suggests that significant nonlinear effects are likely to be expected near the column. For this region, Faltinsen et al. (1995) stated that the evaluation of the higher-order solution for the second-order diffraction regime is confined to the inner region. This simplifies the evaluation of the inhomogeneous boundary condition of the free surface (see Equation 2.2.13) as the left side only includes the vertical gradient of the potential, making it a Neumann boundary condition. As represented in Figure A.8, the inner coordinates are scaled with the radius of the column, while the coordinates in the outer domain are scaled with the wavelength.

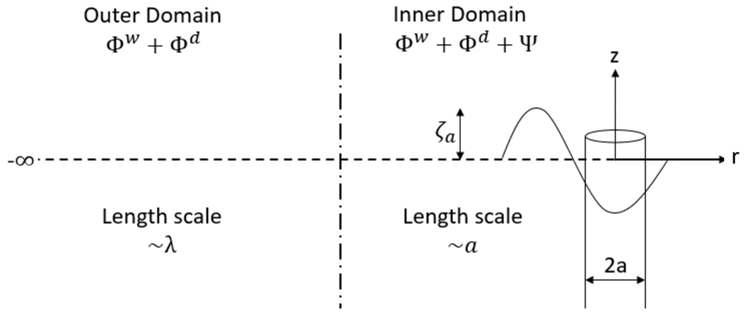

Figure A.8: Illustration of the inner and outer domain concept used in the derivation of higher-order wave forces.

Using the fact that the wave amplitude is not asymptotically small compared to the column radius, the application of the perturbation expansion is still justified as $k\zeta_a \ll 1$ and $ka \ll 1$, since the analysis is based in the long-wavelength regime ($\lambda = 200m - 400m$). An additional remark should be made that when the wave amplitude is large compared to the radius of the column, viscous drag forces are expected. This viscous drag force is not considered because potential theory assumes an inviscid flow. However, as mentioned in the paper from Faltinsen et al. (1995), viscous drag is not significant when $\zeta_a/a \approx 1$ and because it is expected that ringing occurs for low KC numbers (Grue & Huseby, 2002), it can therefore be neglected.

Evaluation of the potentials in the paper from Faltinsen et al. (1995) is done in polar coordinates (r, θ, z), as this simplifies the integration of the pressure over the rounded face of the column. The total potential is viewed as a linear part $(\Phi^w + \Phi^d)$ with a non-linear correction (Ψ). Thus:

$$\Phi_{FNV} = \Phi^w + \Phi^d + \psi + \mathcal{O}(\varepsilon^4). \tag{A.5.1}$$

Solving the potentials in a polar coordinate system, results in the following equations for the third-order force:

$$F^{(3)(\Phi^d+\Phi^w)} = -\pi\rho g k^2 a^2 \zeta_a^3 \cdot \cos(3\omega t), \tag{A.5.2a}$$

$$F^{(3)\Psi} = a\int_0^\infty \frac{1}{2}\rho g k^2 a \zeta_a^3 \cdot \left(\frac{3}{2}\Psi_1(1,Z) + 2\Psi_2(1,Z)\right) \cdot (\cos(\omega t) - \cos(3\omega t))dZ \tag{A.5.2b}$$

A.5.2 FNV irregular wave

To use the FNV model in a realistic environment, the irregular wave form is considered, where the derivation is based on the paper of Newman (1996). The assumptions for the wave conditions are identical to those for regular waves. Thus, each spectral component of every wave in the unidirectional irregular wave description is asymptotically large compared to the radius of the column and that significant HF loads in long irregular waves are caused by the interaction with the cylinder and not by the non-linear properties of the wave itself.

Where the relation to the wave number k in the planar description of waves (see Equation A.1.24) is extended to the following.

$$\frac{\omega^2}{g} = k \cdot (1 + (k\zeta_a)^2). \tag{A.5.3}$$

This ensures the potential to be accurate beyond linear theory and up to and including third order. Evaluating a bichromatic wave description with the planar wave potential represented in Equation A.1.24 and evaluating a component of the second-order free surface boundary condition represented by Equation 2.2.13, leads to Equation A.5.4, where there is only a dependency of a difference frequency term and not a sum frequency term. Therefore, it was stated by Newman (1996), when restricted to the force proportional to the incoming wave amplitude cubed (ζ_a^3), the incident wave system can be represented by a linear superposition of first-order potentials, thus confirming the use of the third-order force computed by the FNV method for irregular waves.

$$\nabla\Phi_1^w \cdot \nabla\Phi_2^w = \omega_1\omega_2 Re\left\{\zeta_{a,1}\zeta_{a,2}\exp\left((k_1+k_2)z + i(\omega_1-\omega_2)t - i(k_1-k_2)x\right)\right\}. \tag{A.5.4}$$

Subsequently, the third-order force is evaluated with the following equation:

$$\begin{aligned} F^{(3)(\Phi^d+\Phi^w)} =& \pi\rho a^2\Bigg(\zeta_1\left(\frac{\partial^2 u}{\partial z\partial t}\zeta_1 + 2w\frac{\partial w}{\partial x} + u\frac{\partial u}{\partial x} - \frac{2}{g}\frac{\partial u}{\partial t}\frac{\partial w}{\partial t}\right) - \\ & \frac{\partial u/\partial t}{g}(u^2+w^2)\Bigg), \end{aligned} \tag{A.5.5}$$

$$\begin{aligned} F^{(3)\Psi} =& a\int_0^\infty \frac{\pi\rho a}{g}u^2\frac{\partial u}{\partial t}(3\Psi_1(1,Z)+4\Psi_2(1,Z))dZ,\\ =&\frac{4\pi\rho a^2}{g}u^2\frac{\partial u}{\partial t}, \end{aligned} \tag{A.5.6}$$

where, for the application of an irregular wave, the description of the derivative of the linear wave potential (u & w) and wave surface description (ζ_1) depends on the amplitude (ζ_a) and frequency (ω) of each regular component in the description of irregular waves. It should be noted that Equation A.5.6 contains a difference-frequency term, which impedes the superposition principle. The research carried out by Johannessen (2012) derived a method to mitigate the effects of difference frequency when applying the FNV model. This method uses a bandwidth-limited window for interacting wave components, including the effects for selecting a cut-off frequency for the incoming wave spectra.

Appendix B

Case model TLP results (Diffraction)

B.1 Hydrodynamic coefficients

B.1.1 Added mass

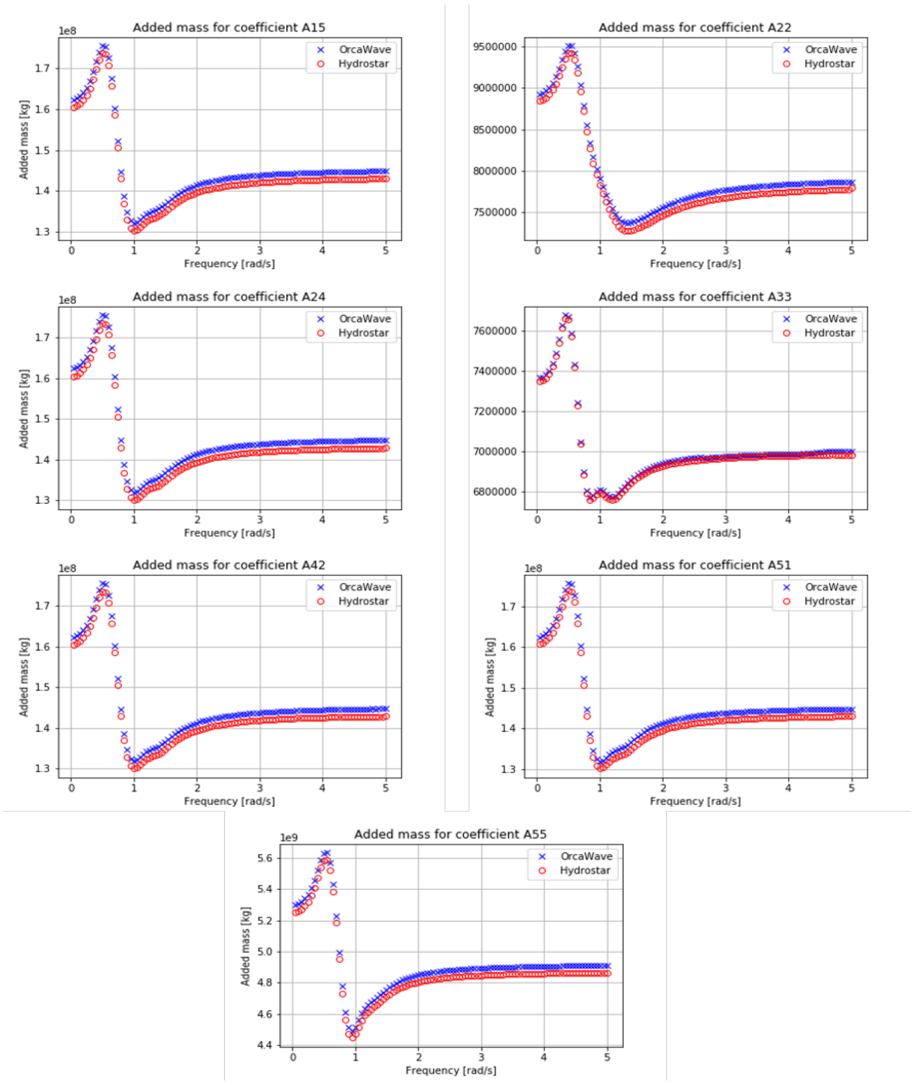

Figure B.1: Case study TLP added mass coefficients

B.1.2 Damping

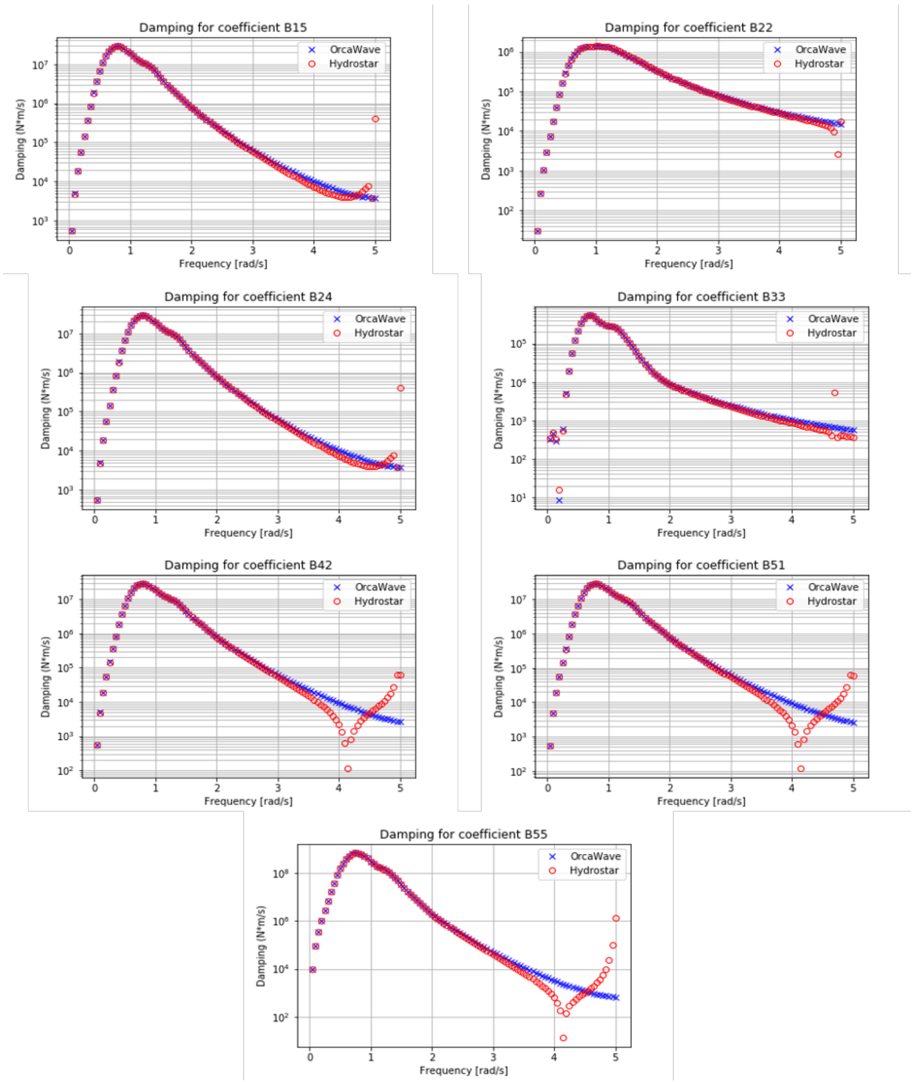

Figure B.2: Case study TLP damping coefficients

B.2 Second order

B.2.1 Second order convergence study

B.2.1.1 Partition radius (PartR)

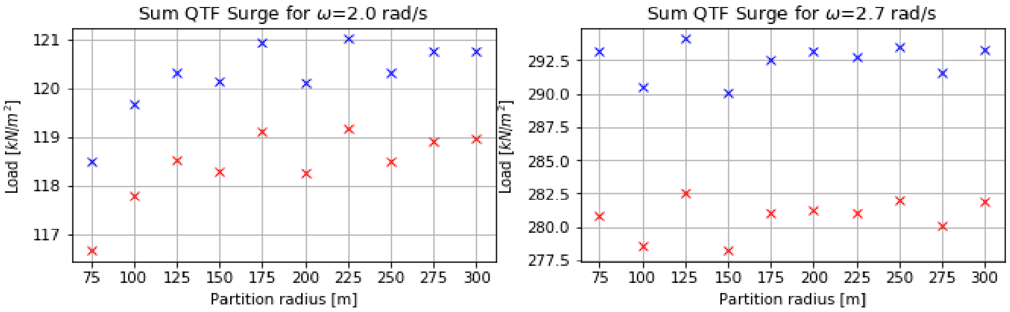

Figure B.3: Convergence study of second order potential force in Surge DOF. The partition radius is adjusted from 75m to 300m in 25m incremental steps. While keeping the scale of the free surface panels at 2 times the size of the average body panel (4000 panels variant). The blue and red crosses represent the solution for the direct and indirect method respectively.

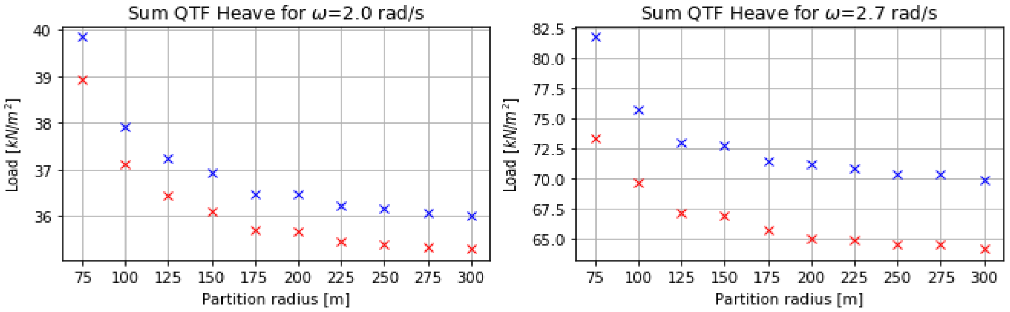

Figure B.4: Convergence study of second order potential force in Heave DOF. The partition radius is adjusted from 75m to 300m in 25m incremental steps. While keeping the scale of the free surface panels at 2 times the size of the average body panel (4000 panels variant). The blue and red crosses represent the solution for the direct and indirect method respectively.

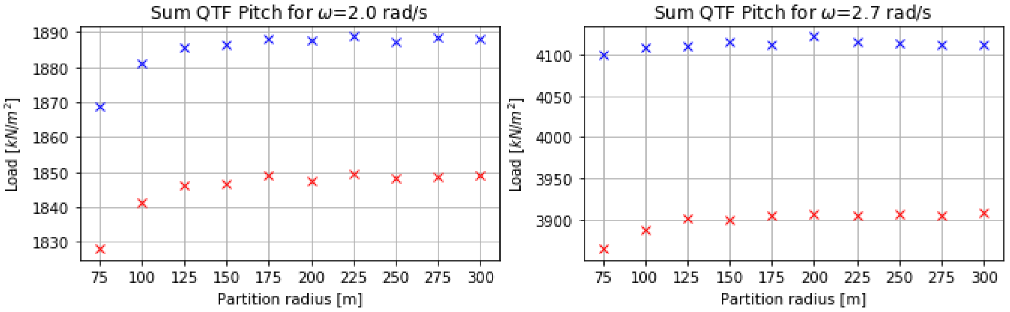

Figure B.5: Convergence study of second order potential force in Pitch DOF. The partition radius is adjusted from 75m to 300m in 25m incremental steps. While keeping the scale of the free surface panels at 2 times the size of the average body panel (4000 panels variant). The blue and red crosses represent the solution for the direct and indirect method respectively.

B.2.1.2 Free surface panel (Scale)

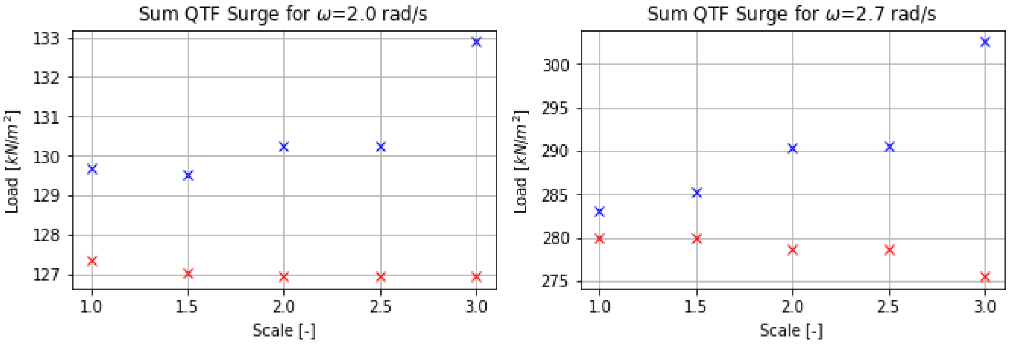

Figure B.6: Convergence study of second order potential force in Surge DOF. The partition radius is kept at 175m and a body mesh of 4000 panels is used. The blue and red crosses represent the solution for the direct and indirect method respectively.

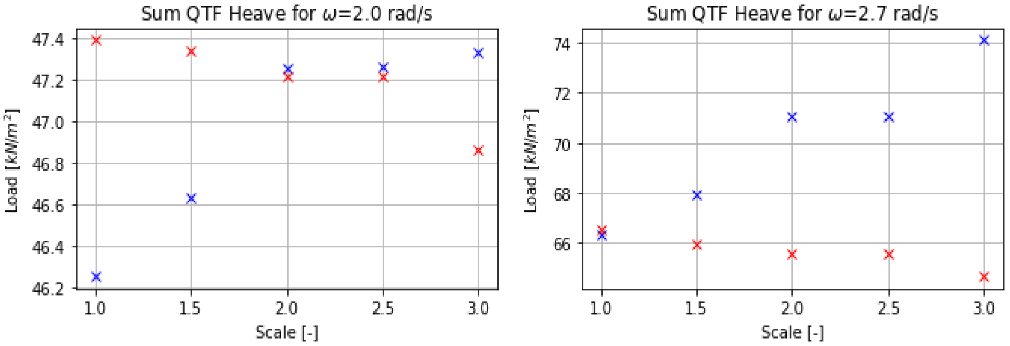

Figure B.7: Convergence study of second order potential force in Heave DOF. The partition radius is kept at 175m and a body mesh of 4000 panels is used. The blue and red crosses represent the solution for the direct and indirect method respectively.

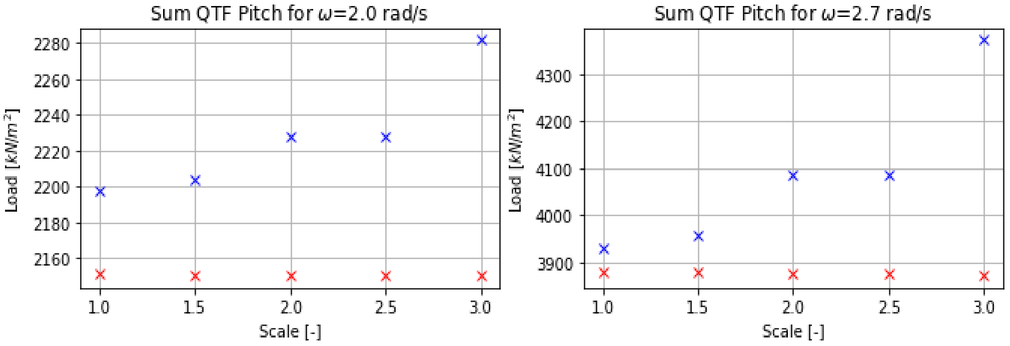

Figure B.8: Convergence study of second order potential force in Pitch DOF. The partition radius is kept at 175m and a body mesh of 4000 panels is used. The blue and red crosses represent the solution for the direct and indirect method respectively.

B.2.1.3 Body panels (NPan)

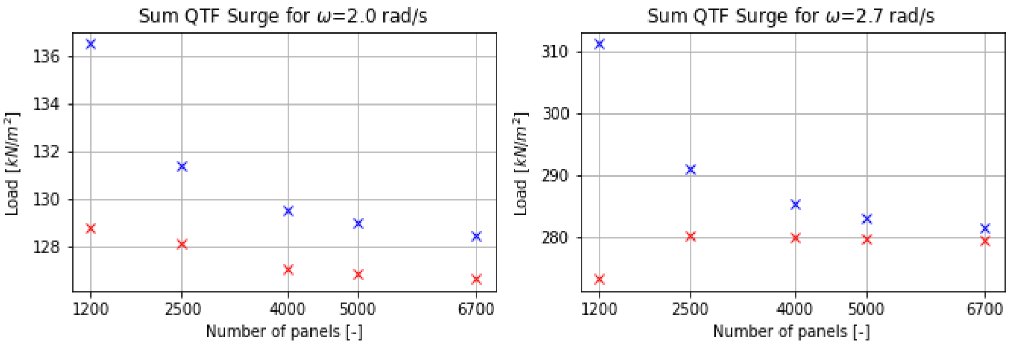

Figure B.9: Convergence study of second order potential force in Surge DOF. The partition radius is kept at 175m and the scale of the free surface is kept at 1.5. The blue and red crosses represent the solution for the direct and indirect method respectively.

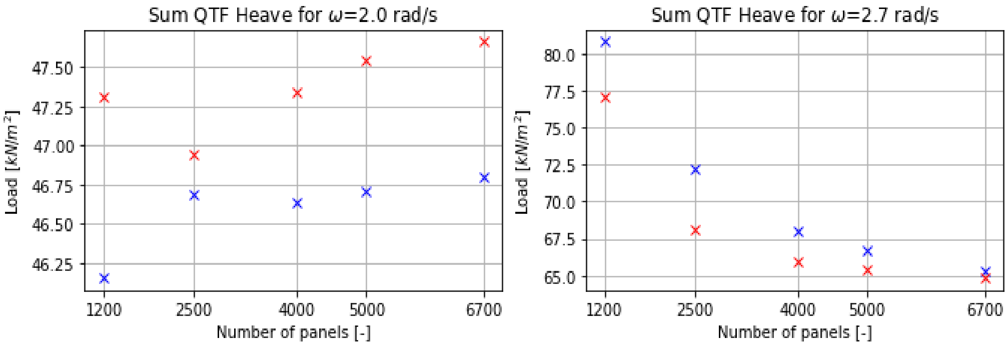

Figure B.10: Convergence study of second order potential force in Heave DOF. The partition radius is kept at 175m and the scale of the free surface is kept at 1.5. The blue and red crosses represent the solution for the direct and indirect method respectively.

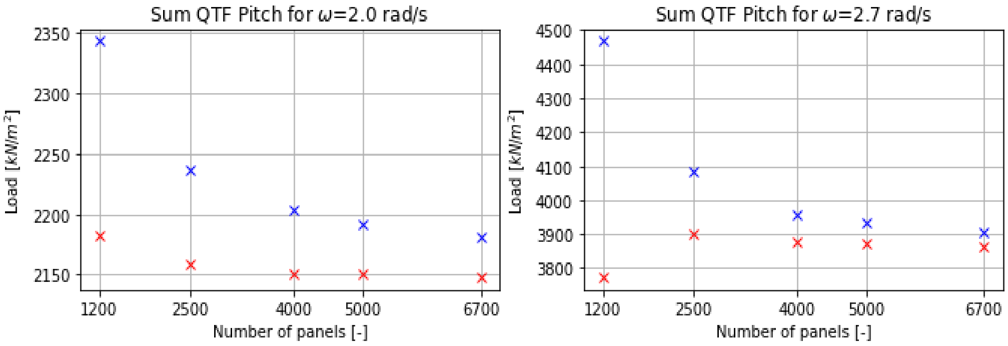

Figure B.11: Convergence study of second order potential force in Pitch DOF. The partition radius is kept at 175m and the scale of the free surface is kept at 1.5. The blue and red crosses represent the solution for the direct and indirect method respectively.

B.2.2 Difference frequencies QTFs

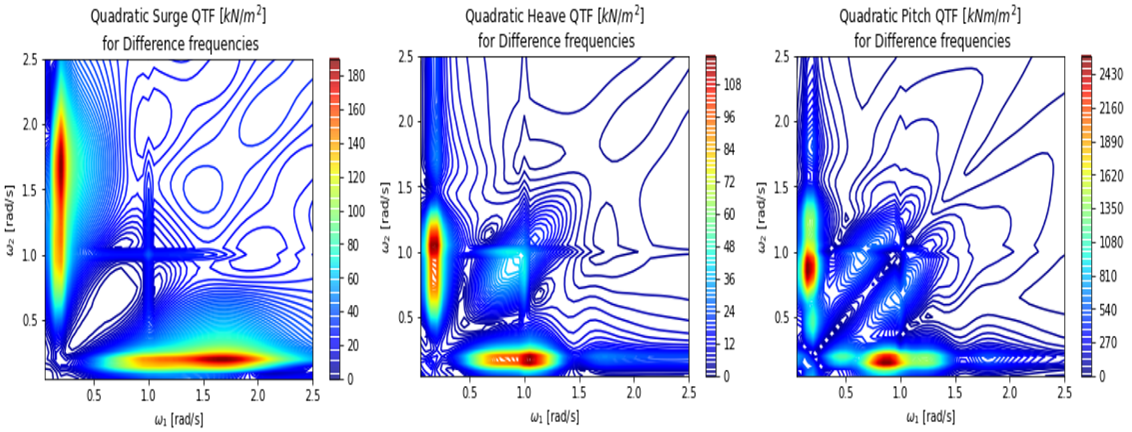
Quadratic Surge QTF [kN/m^2] for Difference frequencies

Quadratic Heave QTF [kN/m^2] for Difference frequencies

Quadratic Pitch QTF [kNm/m^2] for Difference frequencies

Figure B.12: Quadratic load part of the difference frequencies QTF for the case study TLP in DOFs surge, heave and pitch. Results are calculated with OrcaWave.

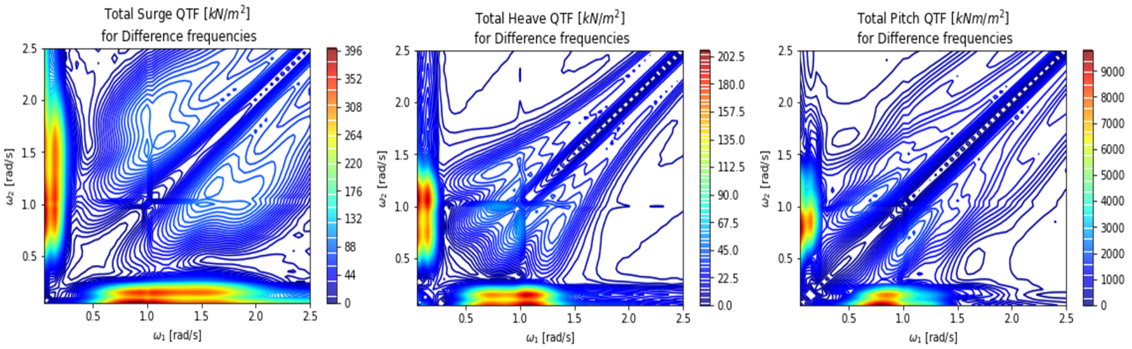
Total Surge QTF [kN/m^2] for Difference frequencies

Total Heave QTF [kN/m^2] for Difference frequencies

Total Pitch QTF [kNm/m^2] for Difference frequencies

Figure B.13: Quadratic and potential load part of the difference frequencies QTF for the case study TLP in DOFs surge, heave and pitch. Results are calculated with OrcaWave.

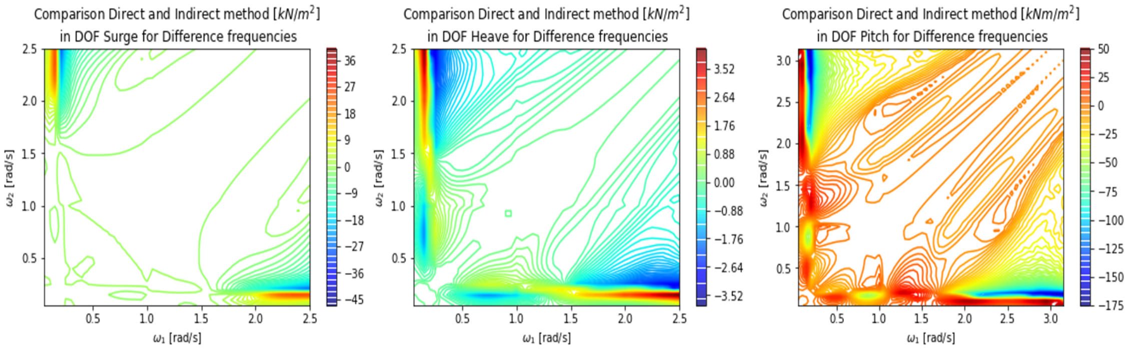
Comparison Direct and Indirect method [kN/m^2] in DOF Surge for Difference frequencies

Comparison Direct and Indirect method [kN/m^2] in DOF Heave for Difference frequencies

Comparison Direct and Indirect method [kNm/m^2] in DOF Pitch for Difference frequencies

Figure B.14: Comparison of direct and indirect method potential solution for the difference frequencies QTF of the case study TLP. Results are calculated with OrcaWave.

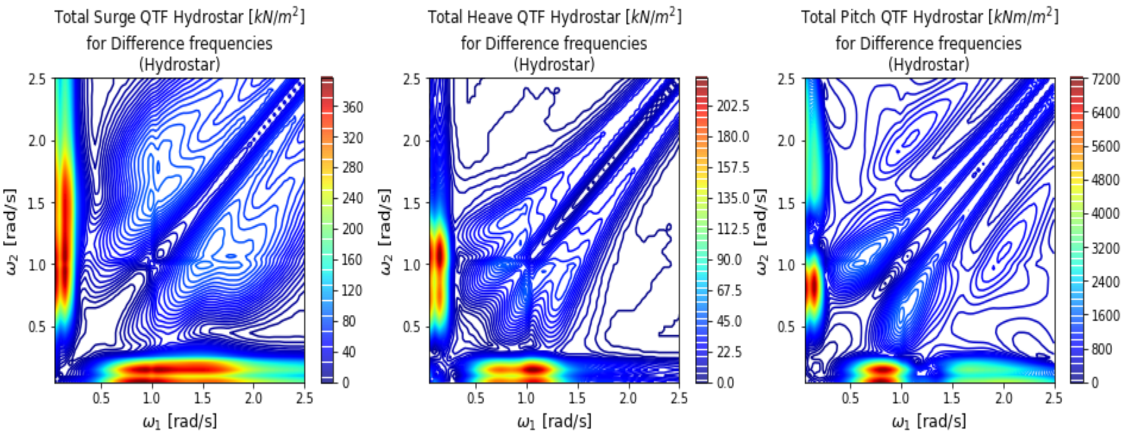
Total Surge QTF Hydrostar [kN/m^2] for Difference frequencies (Hydrostar)

Total Heave QTF Hydrostar [kN/m^2] for Difference frequencies (Hydrostar)

Total Pitch QTF Hydrostar [kNm/m^2] for Difference frequencies (Hydrostar)

Figure B.15: Quadratic and potential load part of the difference frequencies QTF for the case study TLP in DOFs surge, heave and pitch. Results are calculated with Hydrostar.

B.2.3 QTF calculation without tower flexibility

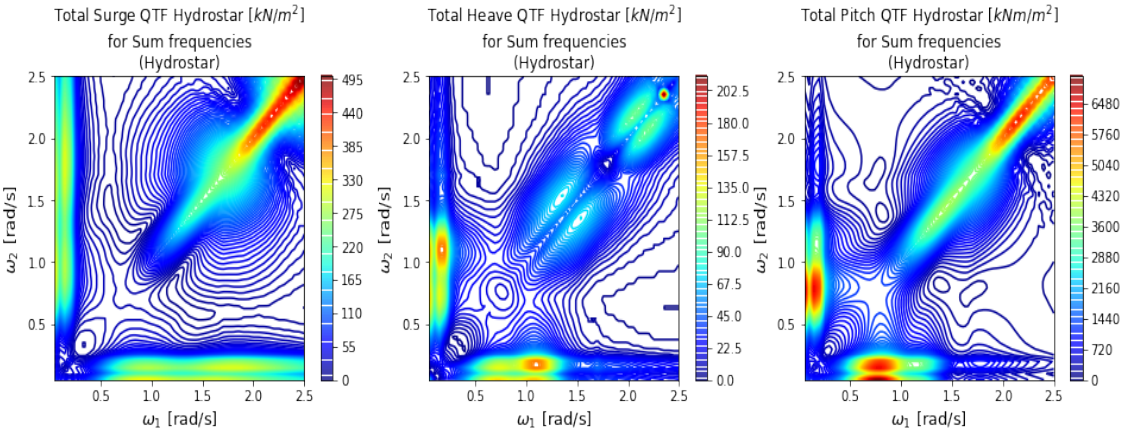
Total Surge QTF Hydrostar [kN/m^2] for Sum frequencies (Hydrostar)

Total Heave QTF Hydrostar [kN/m^2] for Sum frequencies (Hydrostar)

Total Pitch QTF Hydrostar [kNm/m^2] for Sum frequencies (Hydrostar)

Figure B.16: Quadratic and potential load part of the sum frequencies QTF for the case study TLP in DOFs surge, heave and pitch. Results are calculated with Hydrostar excluding the influence of tower flexibility.

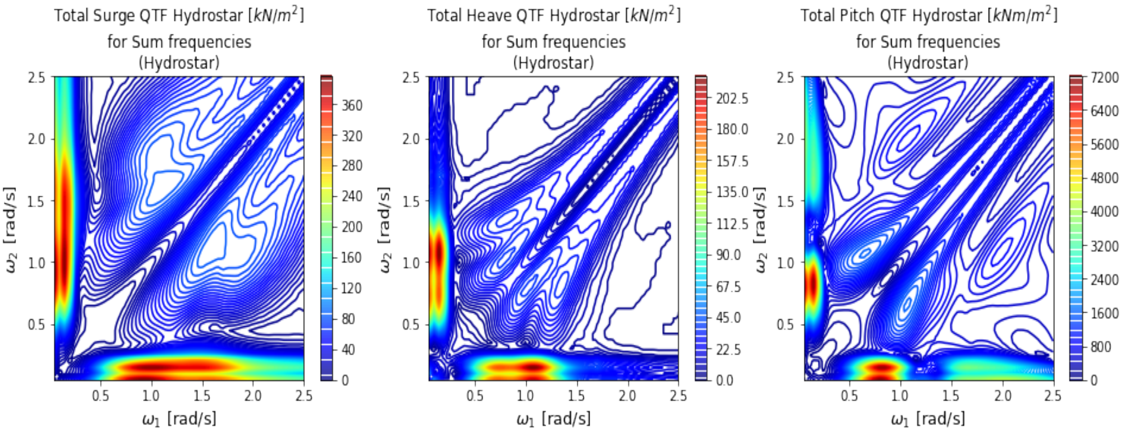

Figure B.17: Quadratic and potential load part of the difference frequencies QTF for the case study TLP in DOFs surge, heave and pitch. Results are calculated with Hydrostar excluding the influence of tower flexibility.

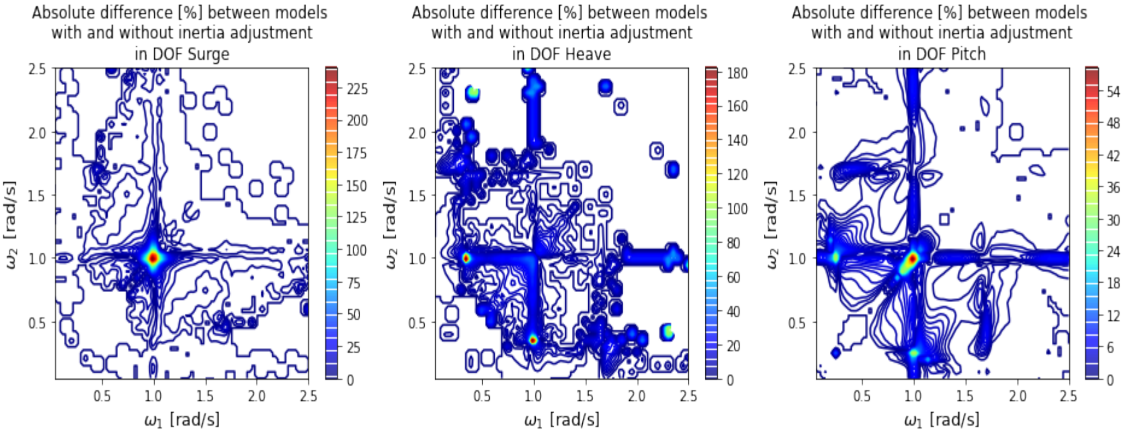

Figure B.18: Influence of tower flexibility on difference QTF calculation. The absolute difference between the adjusted and non adjusted model is shown in percentage. The results are calculated with the Hydrostar diffraction model.

B.3 Second order analysis of adjustments

B.3.1 Tendon angle adjustments (sum QTF)

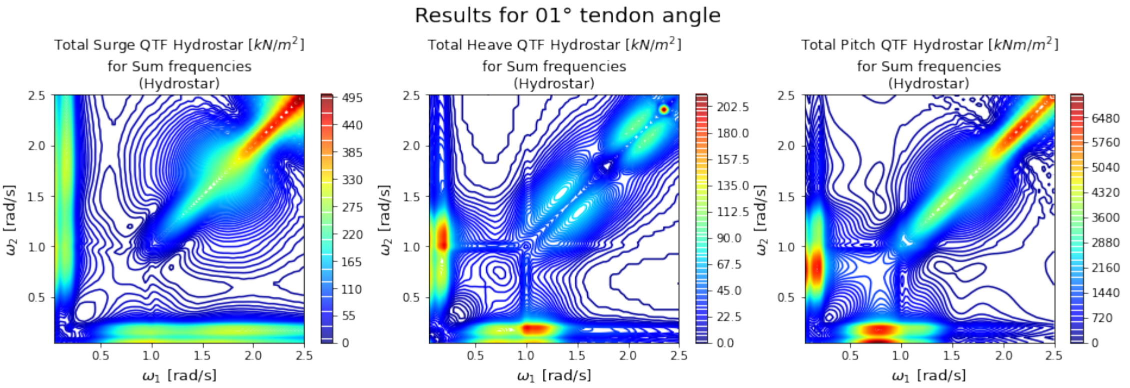

Figure B.19: Sum QTFs for the case study TLP where the tendons are inclined under an angle of 1°. The results are calculated with Hydrostar and tower flexibility is included.

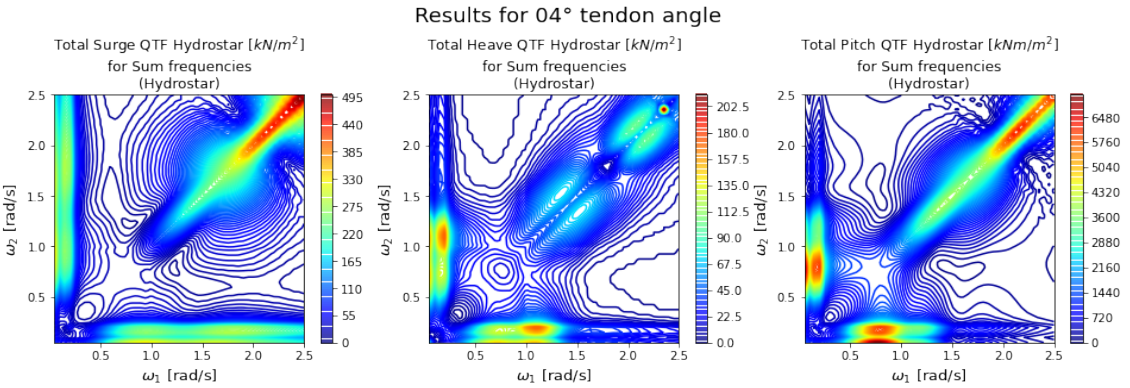

Figure B.20: Sum QTFs for the case study TLP where the tendons are inclined under an angle of 4°. The results are calculated with Hydrostar and tower flexibility is included.

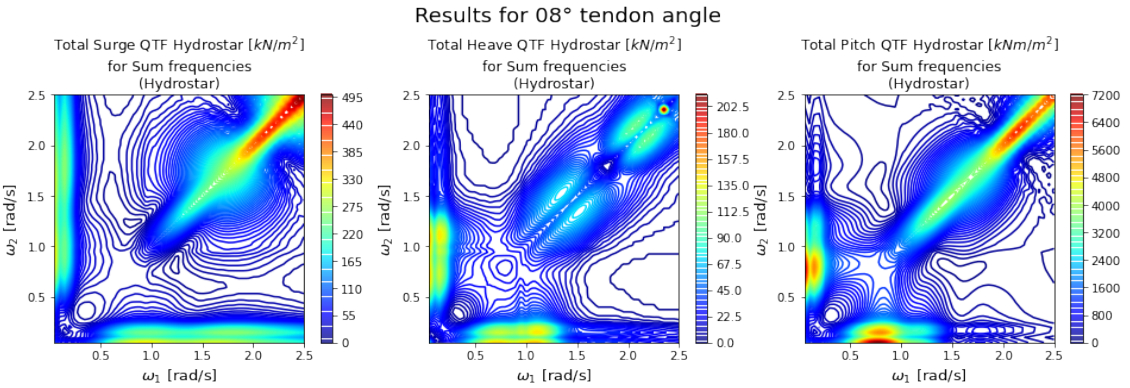

Figure B.21: Sum QTFs for the case study TLP where the tendons are inclined under an angle of 8°. The results are calculated with Hydrostar and tower flexibility is included.

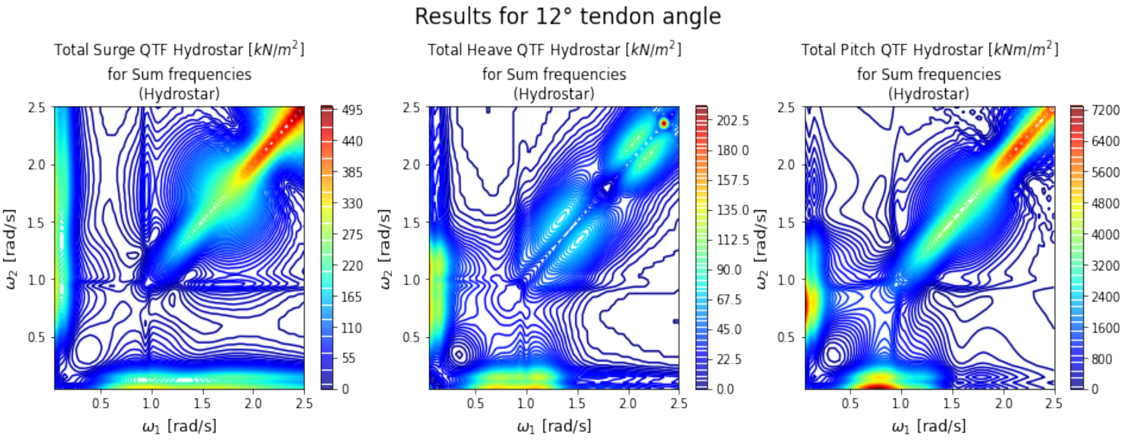

Figure B.22: Sum QTFs for the case study TLP where the tendons are inclined under an angle of 12°. The results are calculated with Hydrostar and tower flexibility is included.

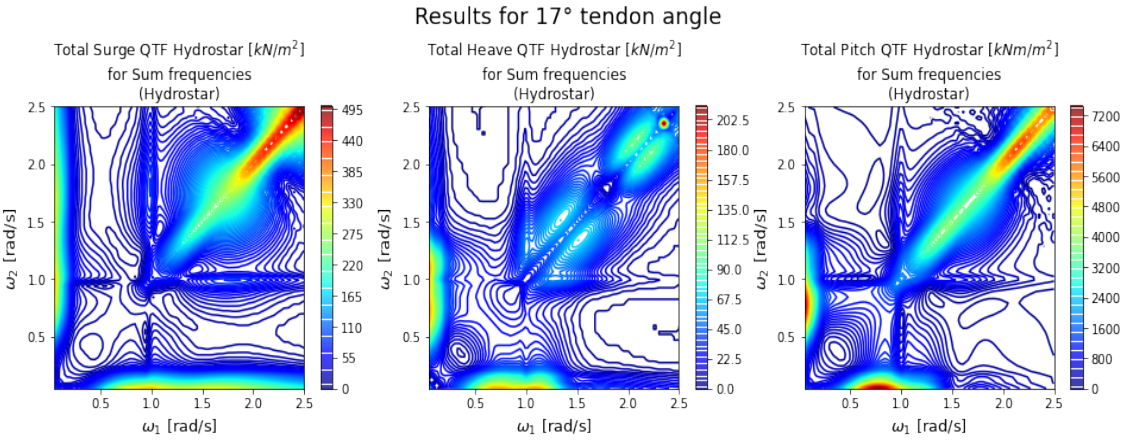

Figure B.23: Sum QTFs for the case study TLP where the tendons are inclined under an angle of 17°. The results are calculated with Hydrostar and tower flexibility is included.

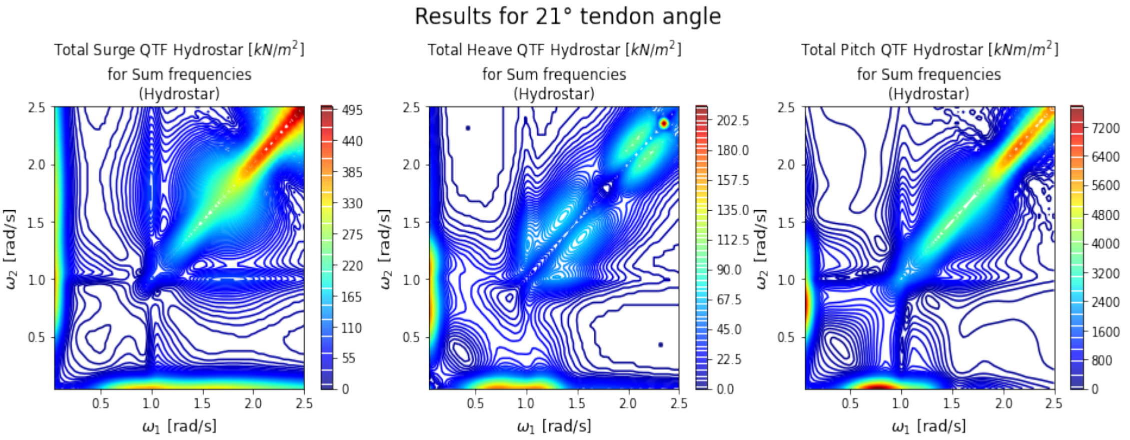

Figure B.24: Sum QTFs for the case study TLP where the tendons are inclined under an angle of 21°. The results are calculated with Hydrostar and tower flexibility is included.

B.3.2 Tendon angles adjustment (differences sum QTF with classical configuration)

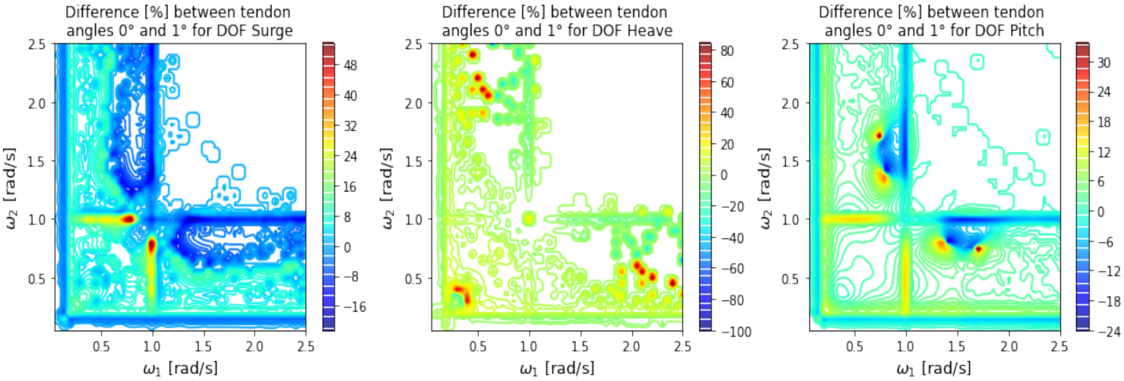

Figure B.25: Differences between the classical configuration and the adjusted tendon angle (1°) sum QTF for the case study TLP. The results are calculated with Hydrostar.

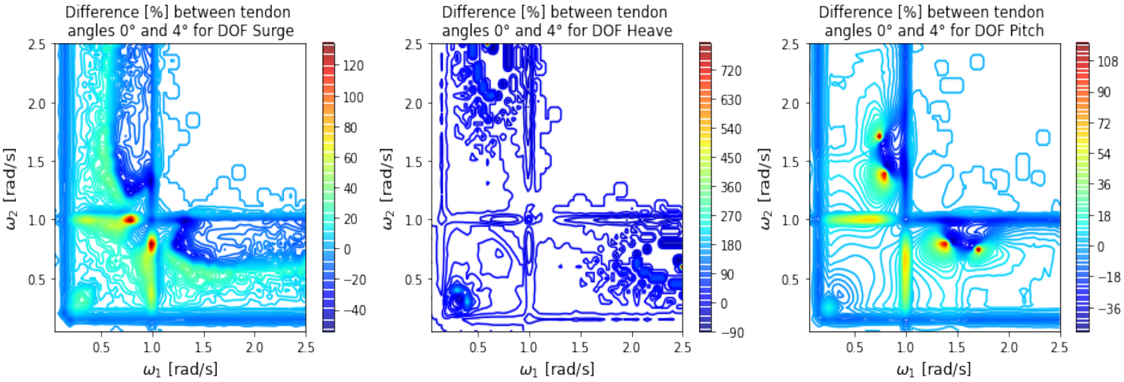

Figure B.26: Differences between the classical configuration and the adjusted tendon angle (4°) sum QTF for the case study TLP. The results are calculated with Hydrostar.

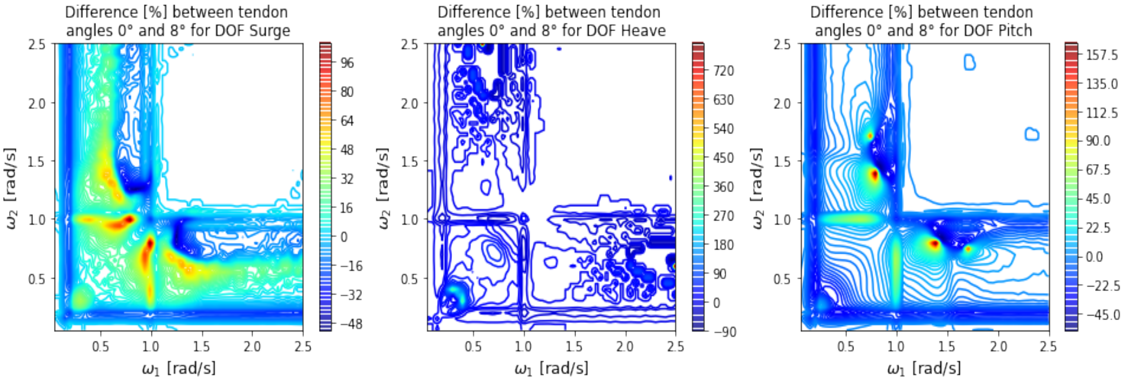

Figure B.27: Differences between the classical configuration and the adjusted tendon angle (8°) sum QTF for the case study TLP. The results are calculated with Hydrostar.

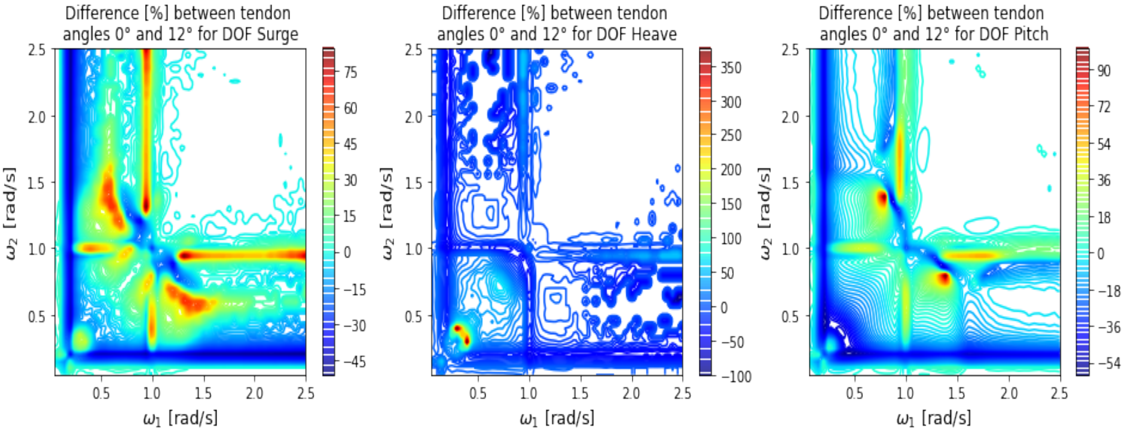

Figure B.28: Differences between the classical configuration and the adjusted tendon angle (12°) sum QTF for the case study TLP. The results are calculated with Hydrostar.

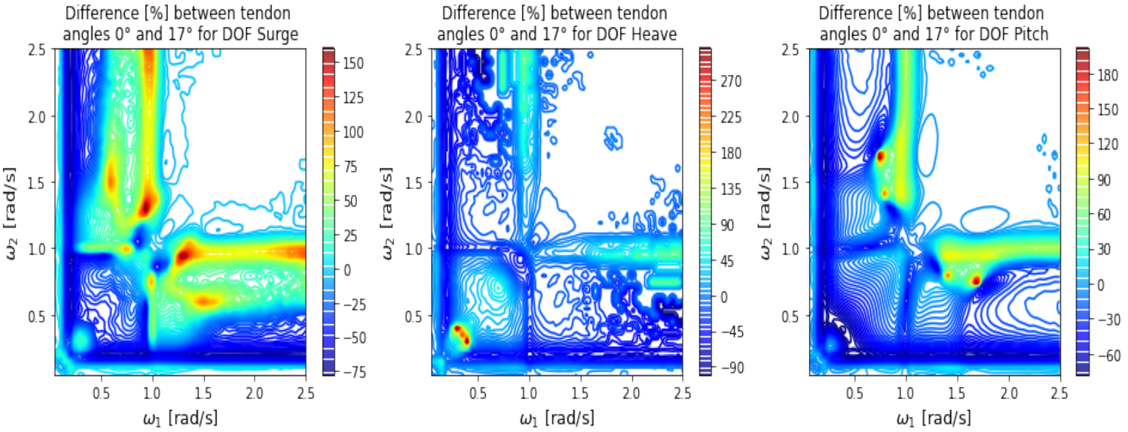

Figure B.29: Differences between the classical configuration and the adjusted tendon angle (17°) sum QTF for the case study TLP. The results are calculated with Hydrostar.

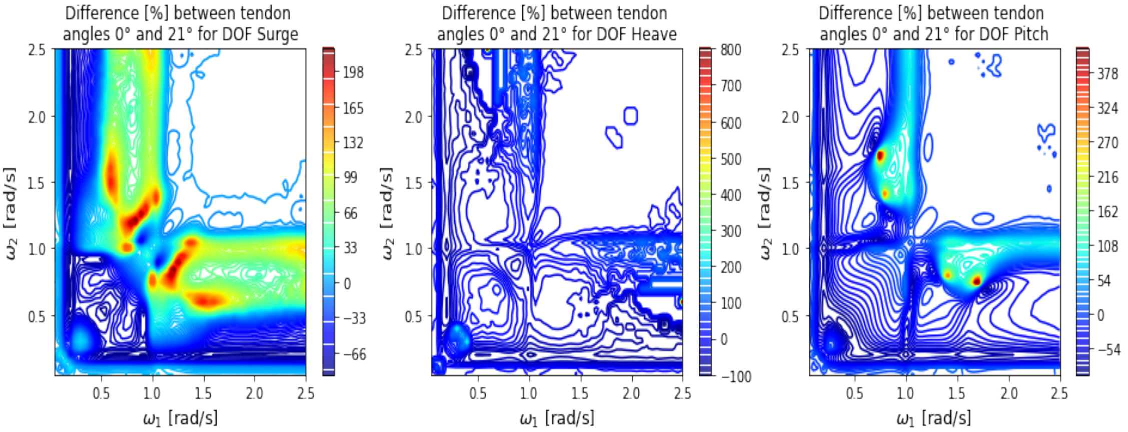

Figure B.30: Differences between the classical configuration and the adjusted tendon angle (21°) sum QTF for the case study TLP. The results are calculated with Hydrostar.

B.3.3 Tendon stiffness adjustments (sum QTF)

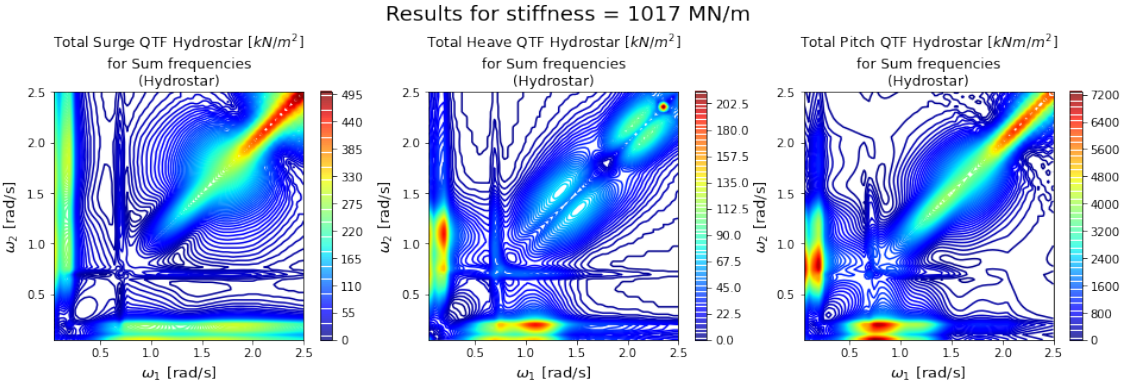

Figure B.31: Sum QTFs for the case study TLP with a tendon axial stiffness of 1017 MN. The results are calculated with Hydrostar and tower flexibility is included.

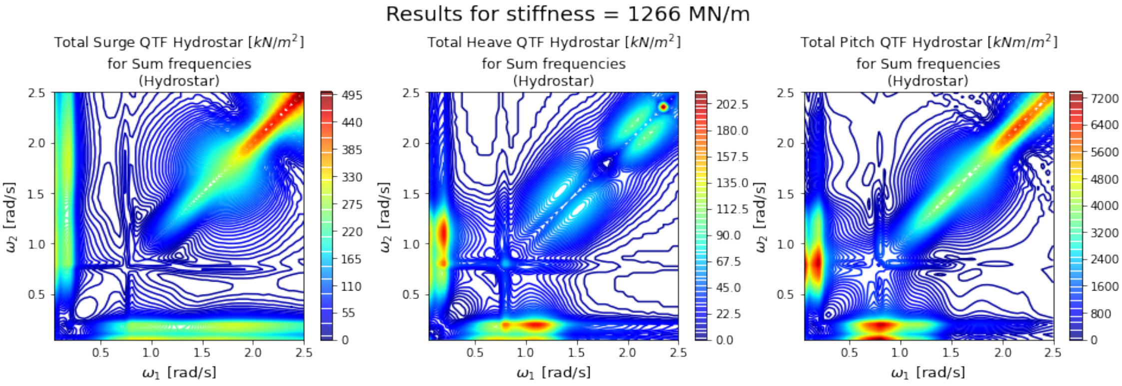

Figure B.32: Sum QTFs for the case study TLP with a tendon axial stiffness of 1266 MN. The results are calculated with Hydrostar and tower flexibility is included.

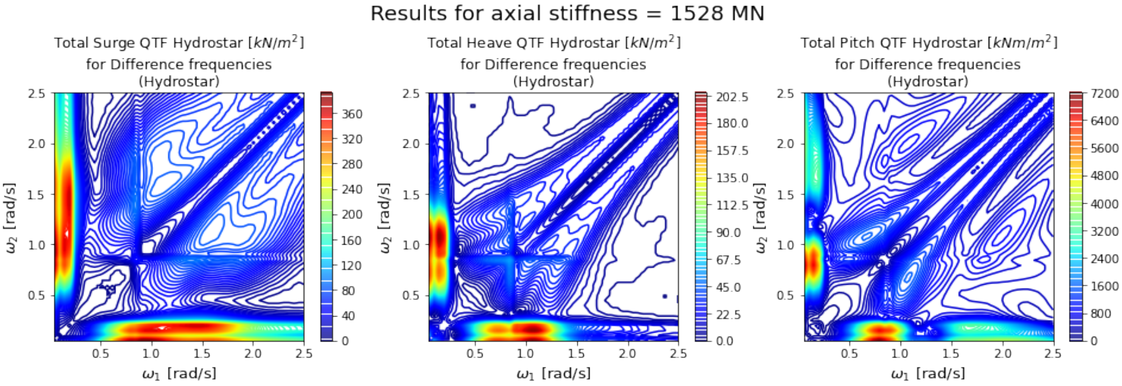

Figure B.33: Sum QTFs for the case study TLP with a tendon axial stiffness of 1528 MN. The results are calculated with Hydrostar and tower flexibility is included.

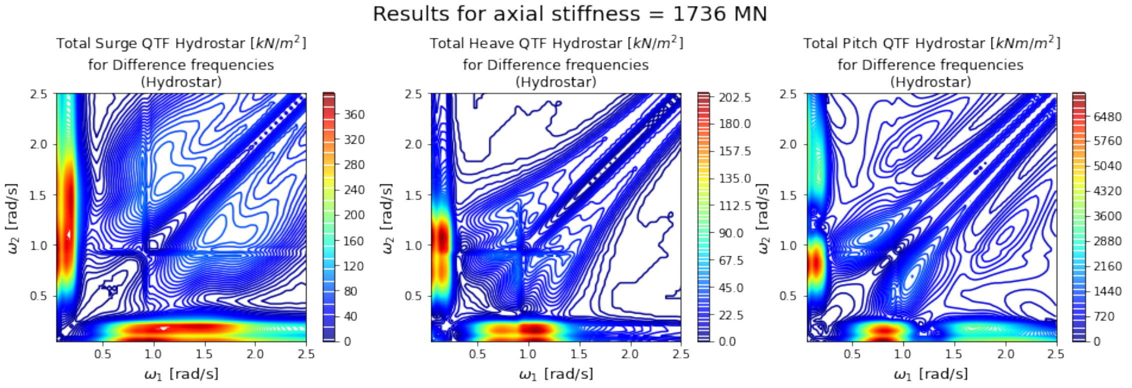

Figure B.34: Sum QTFs for the case study TLP with a tendon axial stiffness of 1736 MN. The results are calculated with Hydrostar and tower flexibility is included.

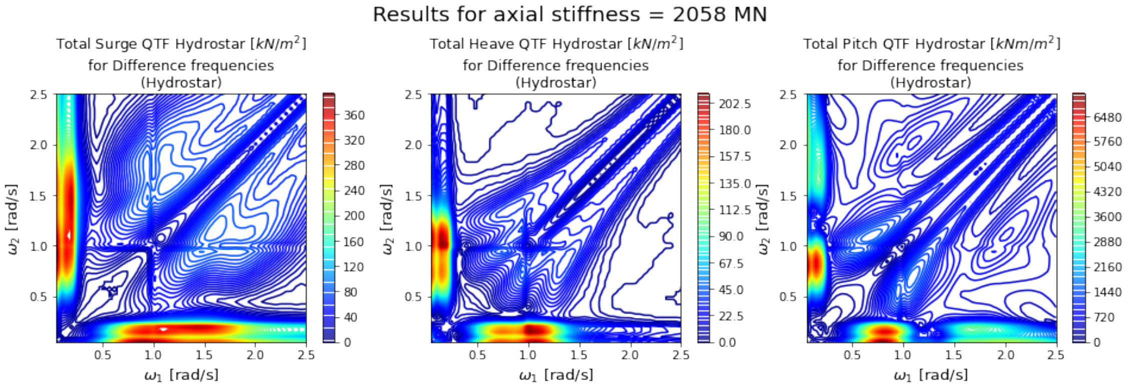

Figure B.35: Sum QTFs for the case study TLP with a tendon axial stiffness of 2058 MN. The results are calculated with Hydrostar and tower flexibility is included.

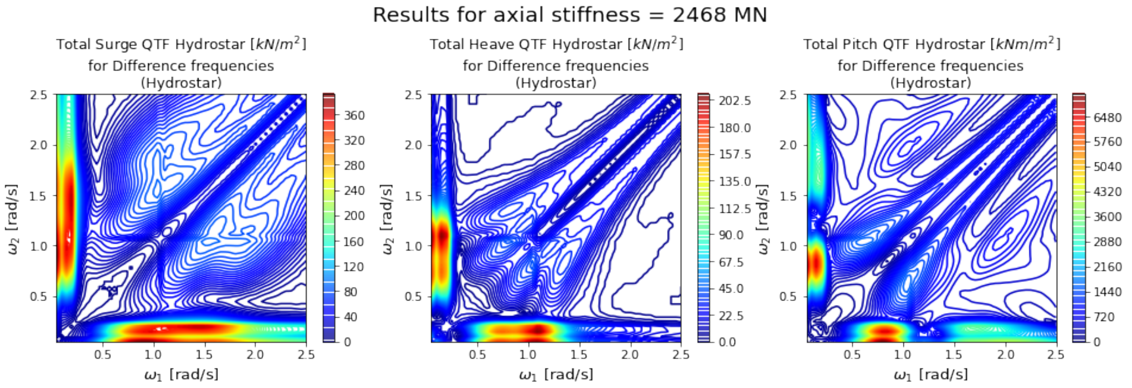

Figure B.36: Sum QTFs for the case study TLP with a tendon axial stiffness of 2468 MN. The results are calculated with Hydrostar and tower flexibility is included.

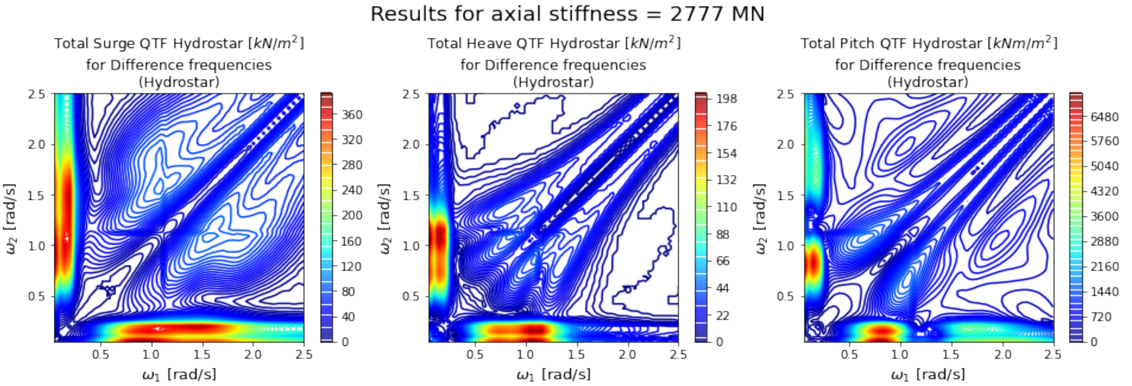

Figure B.37: Sum QTFs for the case study TLP with a tendon axial stiffness of 2777 MN. The results are calculated with Hydrostar and tower flexibility is included.

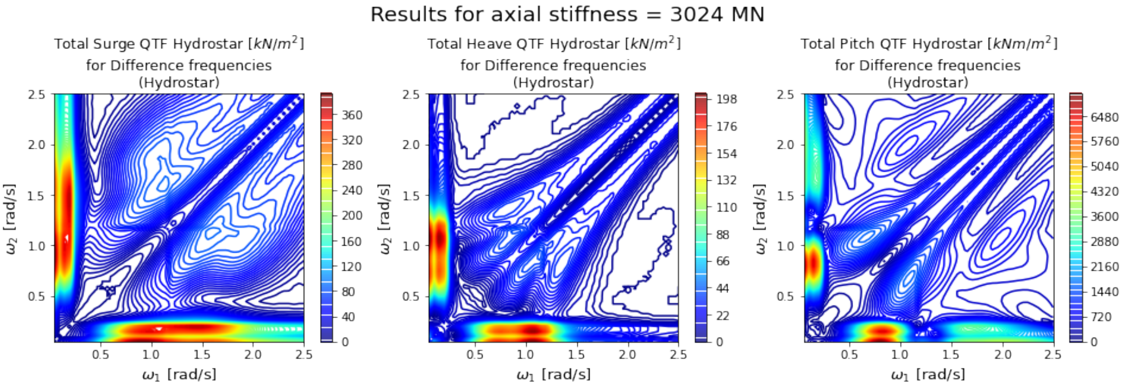

Figure B.38: Sum QTFs for the case study TLP with a tendon axial stiffness of 3024 MN. The results are calculated with Hydrostar and tower flexibility is included.

B.3.4 Tendon stiffness adjustment (differences sum QTF with reference stiffness)

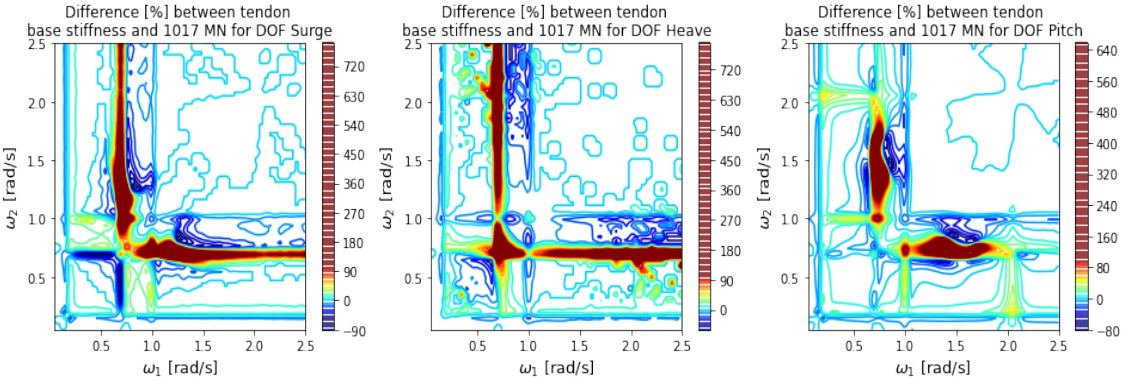

Figure B.39: Differences between the reference and the adjusted tendon axial stiffness (1017 MN) sum QTF for the case study TLP. The results are calculated with Hydrostar.

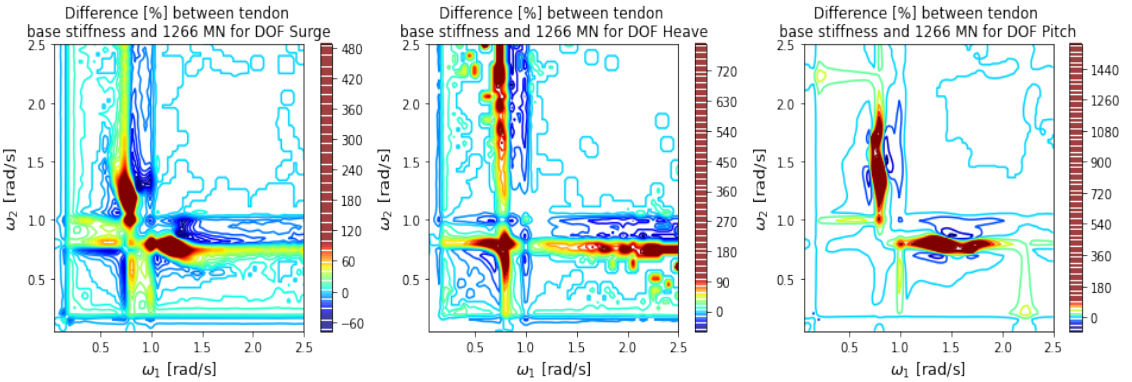

Figure B.40: Differences between the reference and the adjusted tendon axial stiffness (1266 MN) sum QTF for the case study TLP. The results are calculated with Hydrostar.

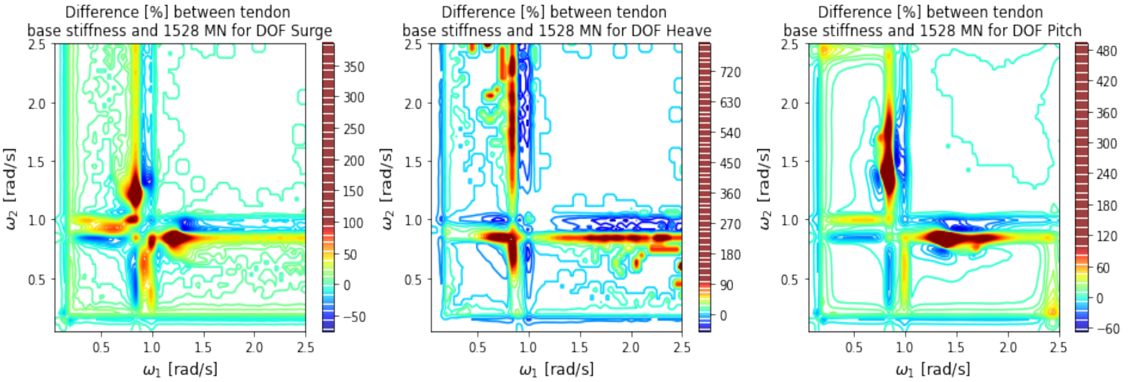

Figure B.41: Differences between the reference and the adjusted tendon axial stiffness (1528 MN) sum QTF for the case study TLP. The results are calculated with Hydrostar.

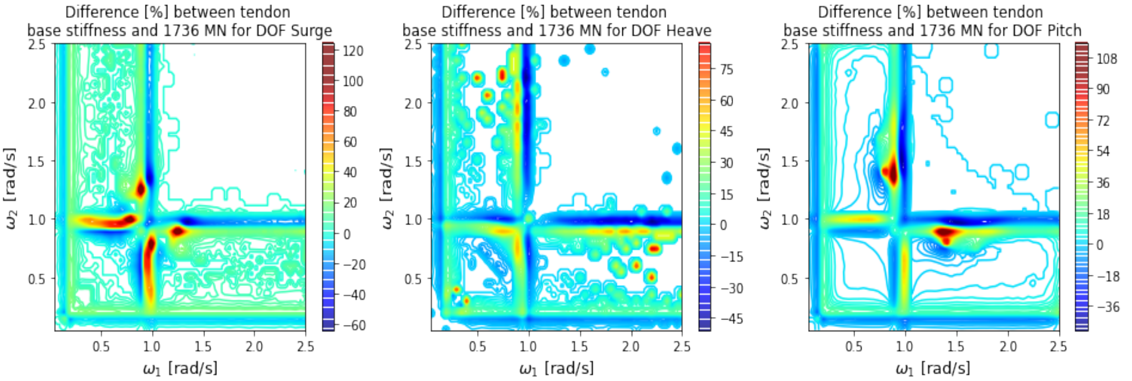

Figure B.42: Differences between the reference and the adjusted tendon axial stiffness (1736 MN) sum QTF for the case study TLP. The results are calculated with Hydrostar.

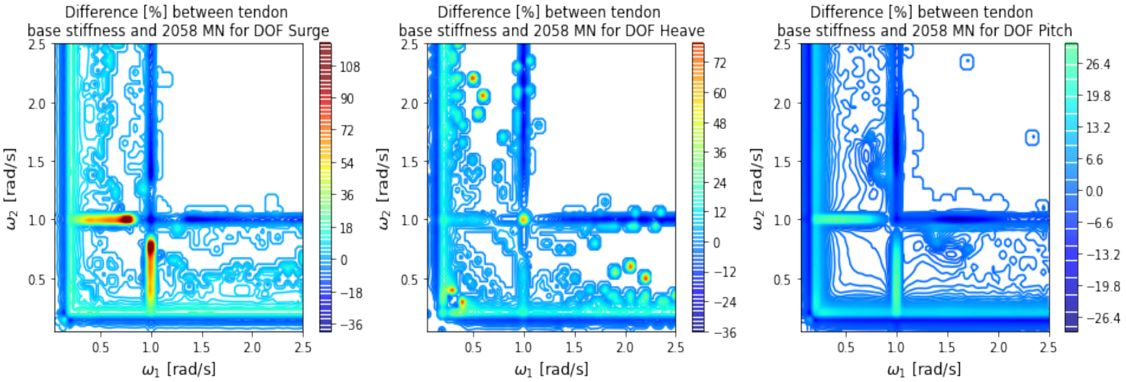

Figure B.43: Differences between the reference and the adjusted tendon axial stiffness (2058 MN) sum QTF for the case study TLP. The results are calculated with Hydrostar.

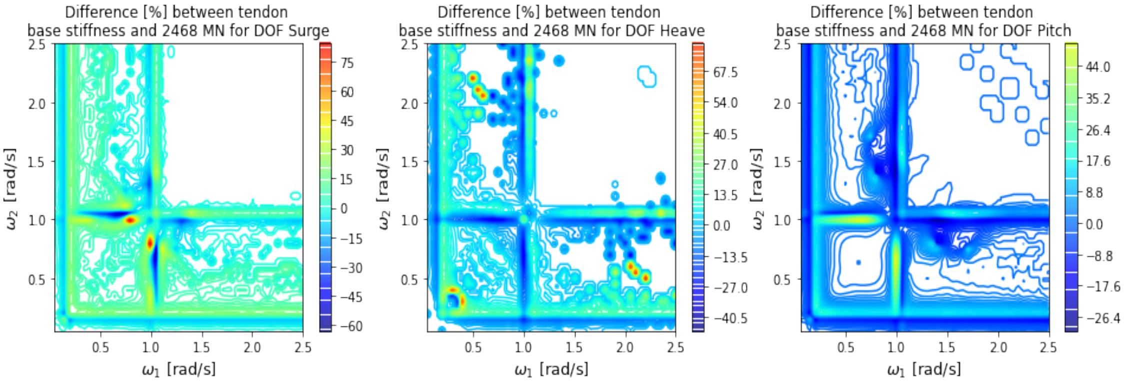

Figure B.44: Differences between the reference and the adjusted tendon axial stiffness (2468 MN) sum QTF for the case study TLP. The results are calculated with Hydrostar.

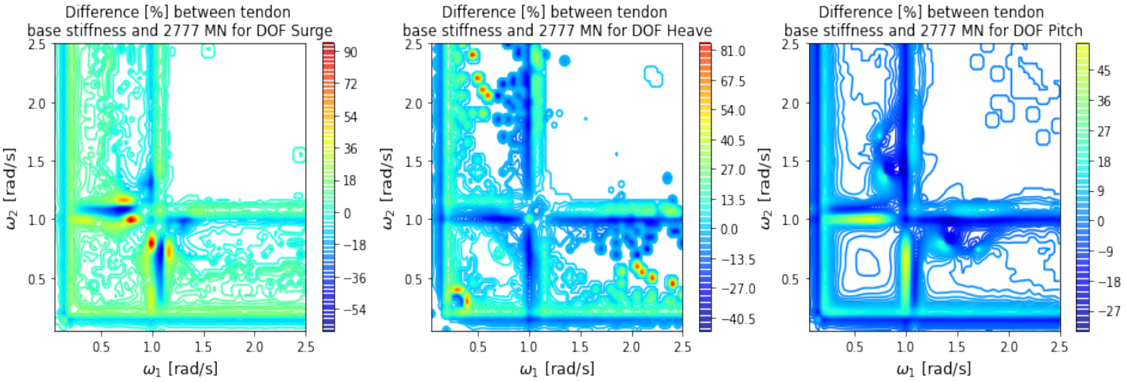

Figure B.45: Differences between the reference and the adjusted tendon axial stiffness (2777 MN) sum QTF for the case study TLP. The results are calculated with Hydrostar.

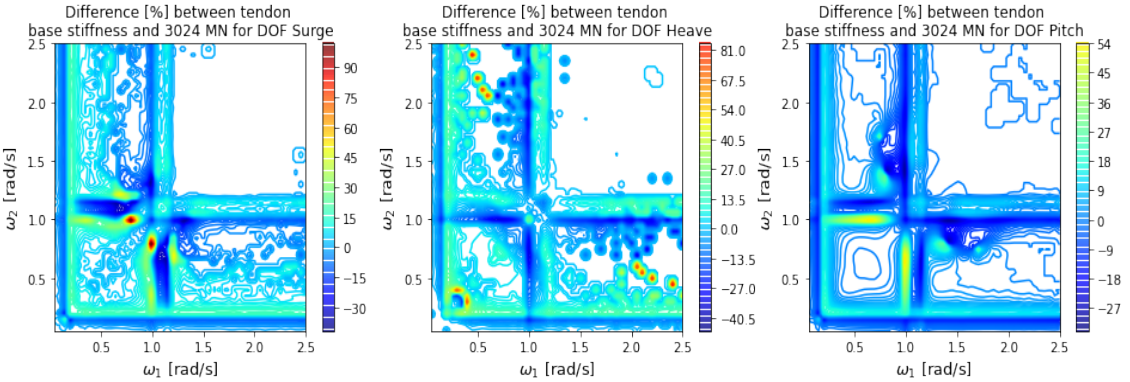
Difference [%] between tendon base stiffness and 3024 MN for DOF Surge

Difference [%] between tendon base stiffness and 3024 MN for DOF Heave

Difference [%] between tendon base stiffness and 3024 MN for DOF Pitch

Figure B.46: Differences between the reference and the adjusted tendon axial stiffness (3024 MN) sum QTF for the case study TLP. The results are calculated with Hydrostar.

B.3.5 Combination adjustment (sum QTF)

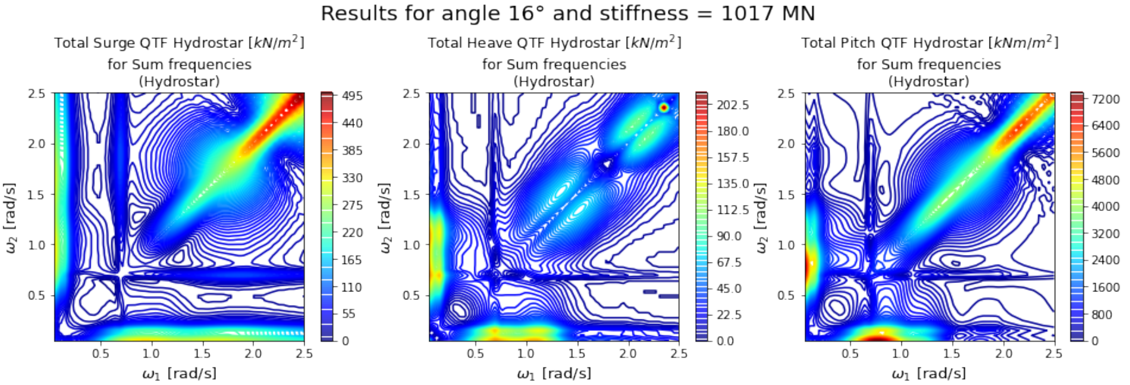
Results for angle 16° and stiffness = 1017 MN

Total Surge QTF Hydrostar [kN/m^2] for Sum frequencies (Hydrostar)

Total Heave QTF Hydrostar [kN/m^2] for Sum frequencies (Hydrostar)

Total Pitch QTF Hydrostar [kNm/m^2] for Sum frequencies (Hydrostar)

Figure B.47: Sum QTFs for the case study TLP with a tendon inclination of 16° and axial stiffness of 1017 MN. The results are calculated with Hydrostar and tower flexibility is included.

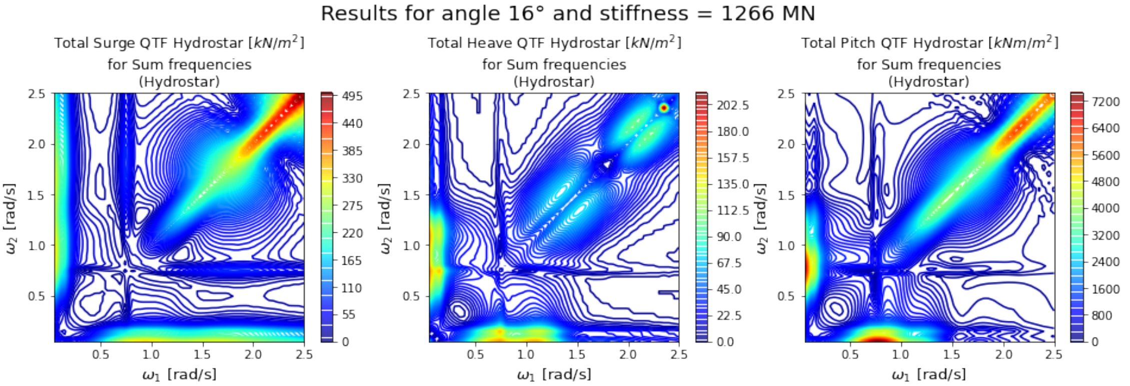
Results for angle 16° and stiffness = 1266 MN

Total Surge QTF Hydrostar [kN/m^2] for Sum frequencies (Hydrostar)

Total Heave QTF Hydrostar [kN/m^2] for Sum frequencies (Hydrostar)

Total Pitch QTF Hydrostar [kNm/m^2] for Sum frequencies (Hydrostar)

Figure B.48: Sum QTFs for the case study TLP with a tendon inclination of 16° and axial stiffness of 1266 MN. The results are calculated with Hydrostar and tower flexibility is included.

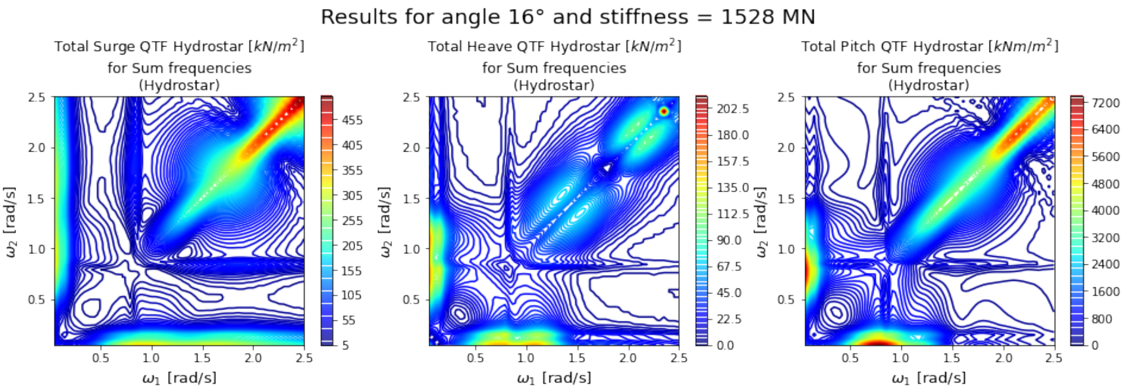

Figure B.49: Sum QTFs for the case study TLP with a tendon inclination of 16° and axial stiffness of 1736 MN. The results are calculated with Hydrostar and tower flexibility is included.

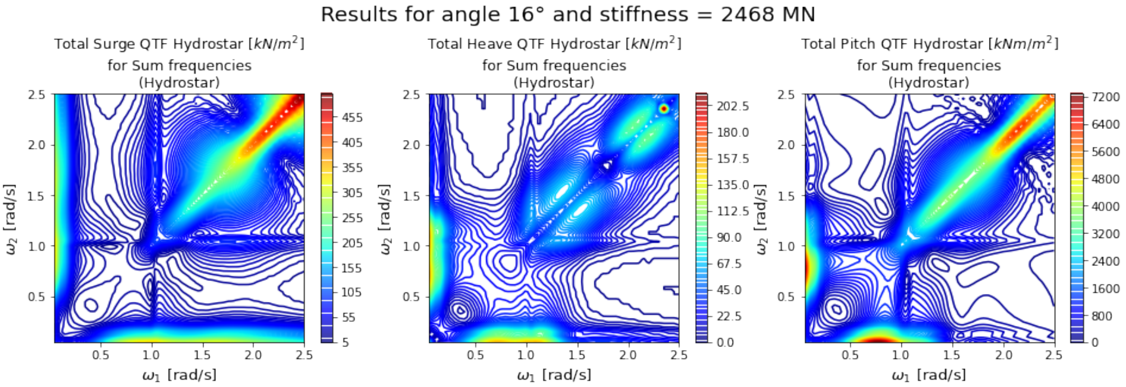

Figure B.50: Sum QTFs for the case study TLP with a tendon inclination of 16° and axial stiffness of 2468 MN. The results are calculated with Hydrostar and tower flexibility is included.

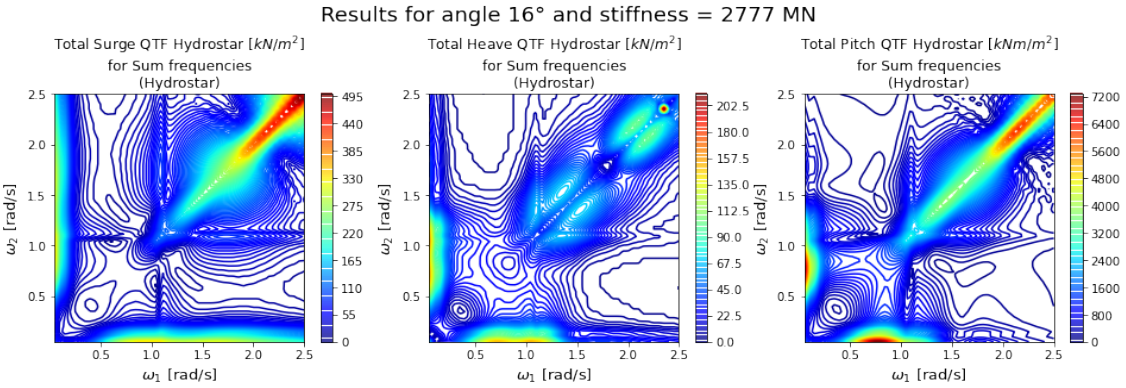

Figure B.51: Sum QTFs for the case study TLP with a tendon inclination of 16° and axial stiffness of 2777 MN. The results are calculated with Hydrostar and tower flexibility is included.

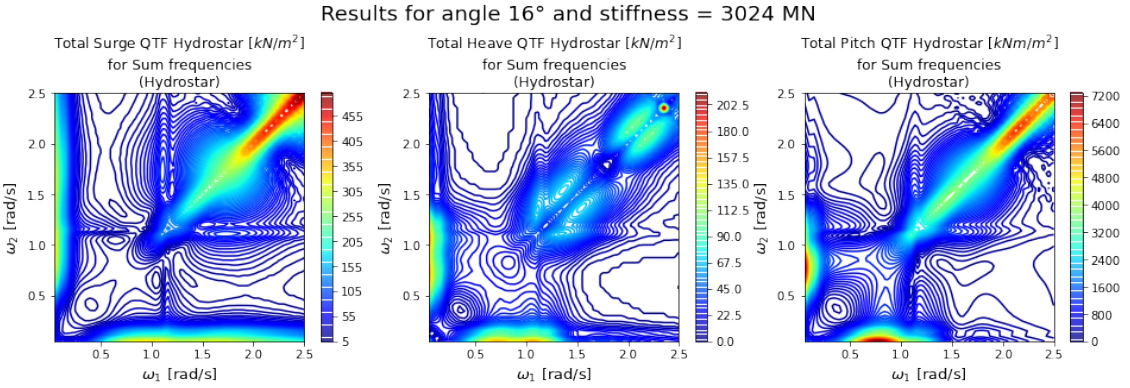

Figure B.52: Sum QTFs for the case study TLP with a tendon inclination of 16° and axial stiffness of 3024 MN. The results are calculated with Hydrostar and tower flexibility is included.

B.3.6 Combination adjustment (difference sum QTF with reference configuration)

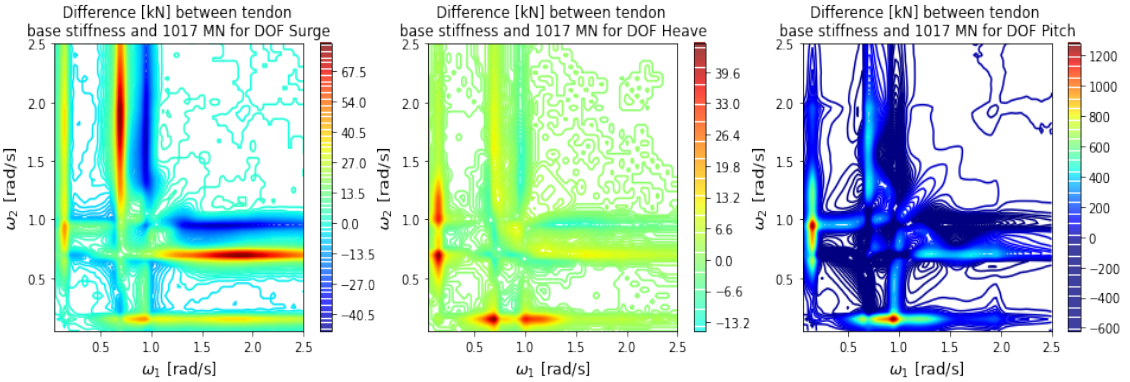

Figure B.53: Differences between the reference and the adjusted tendon axial stiffness (1017 MN) sum QTF for the case study TLP. The results are calculated with Hydrostar.

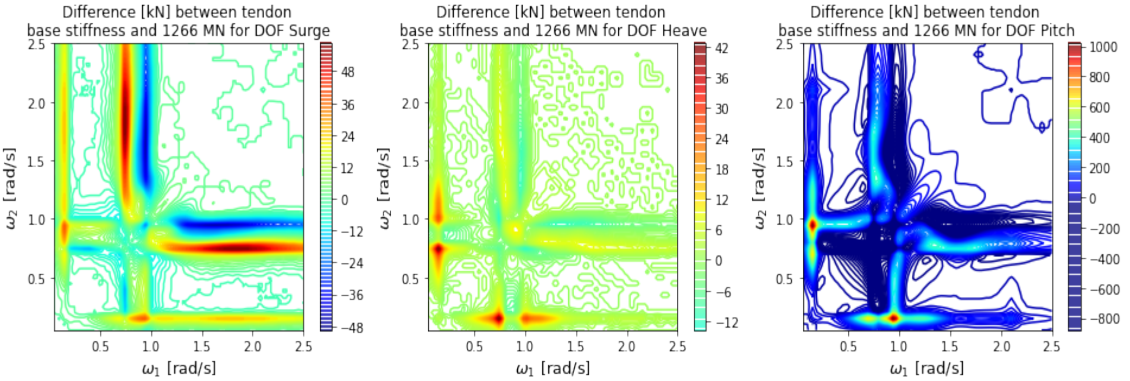

Figure B.54: Differences between the reference and the adjusted tendon axial stiffness (1266 MN) sum QTF for the case study TLP. The results are calculated with Hydrostar.

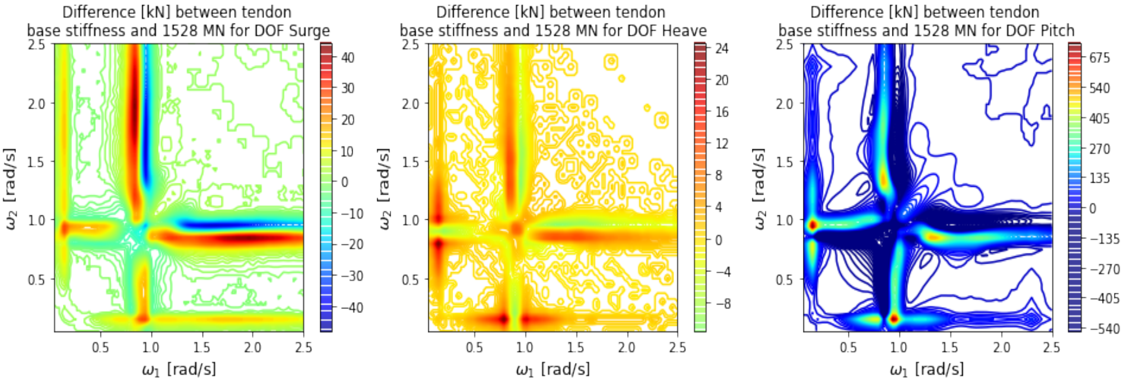

Figure B.55: Differences between the reference and the adjusted tendon axial stiffness (1528 MN) sum QTF for the case study TLP. The results are calculated with Hydrostar.

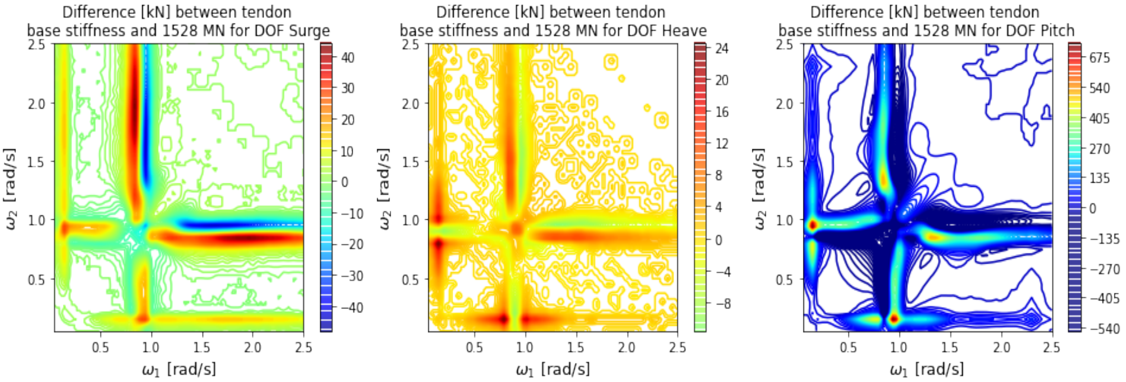

Figure B.56: Differences between the reference and the adjusted tendon axial stiffness (1736 MN) sum QTF for the case study TLP. The results are calculated with Hydrostar.

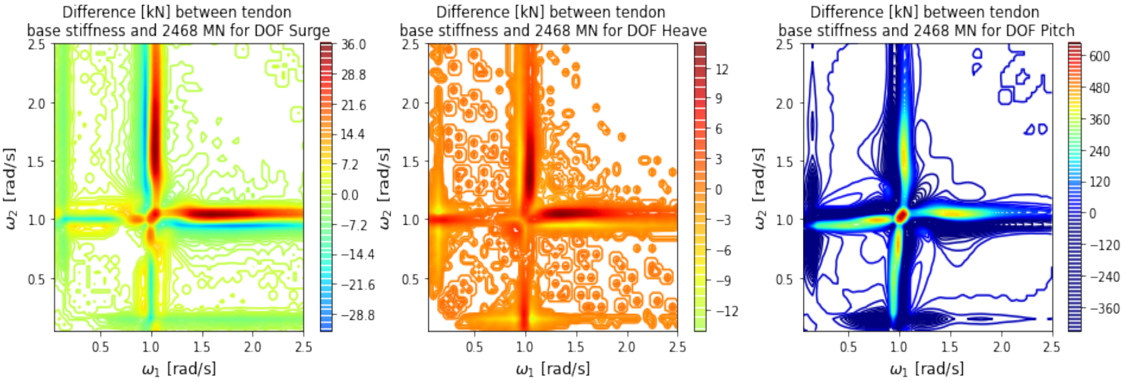

Figure B.57: Differences between the reference and the adjusted tendon axial stiffness (2468 MN) sum QTF for the case study TLP. The results are calculated with Hydrostar.

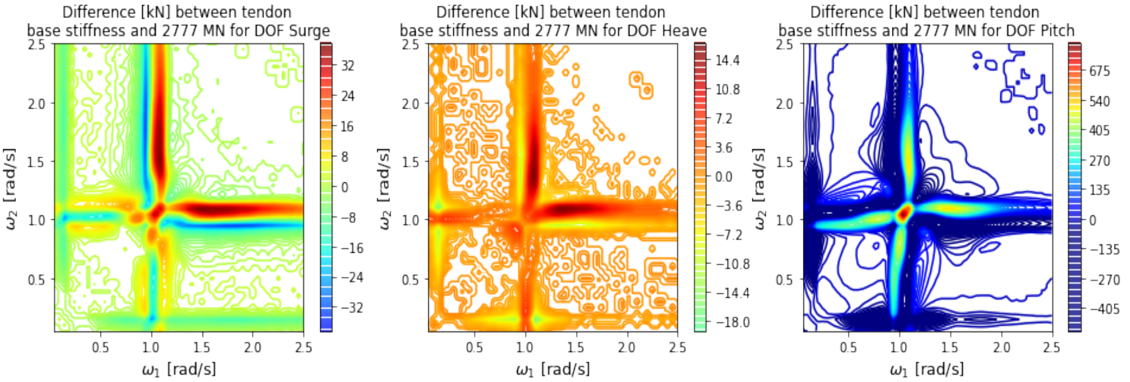

Figure B.58: Differences between the reference and the adjusted tendon axial stiffness (2777 MN) sum QTF for the case study TLP. The results are calculated with Hydrostar.

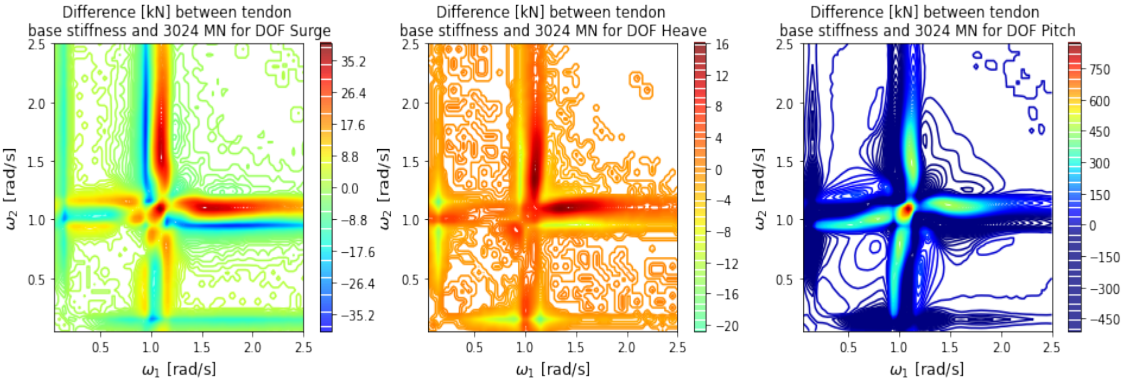

Figure B.59: Differences between the reference and the adjusted tendon axial stiffness (3024 MN) sum QTF for the case study TLP. The results are calculated with Hydrostar.

Appendix C

Extra information

C.1 NSS South-Korean Sea

No. sea	Hs	Tp	gamma	dir	vw	dir	vc	dir
	[m]	[s]	[-]	[deg]	[m/s]	[deg]	[m/s]	[deg]
698	2.45	5.82	4.4	180	28	180	0.25	180
881	1.57	7.74	1.0	60	28	240	0.25	0
939	2.12	5.89	3.0	60	28	60	0.25	120
1684	3.49	7.05	4.1	240	28	240	0.25	300
1685	4.83	8.94	2.9	240	28	300	0.25	300
1686	3.16	8.66	1.2	240	36	300	0.25	300
1695	3.89	8.13	2.8	240	28	240	0.25	240
1696	4.77	9.50	2.1	240	28	300	0.25	240
1703	4.54	8.68	2.9	240	28	240	0.25	180
1713	4.15	8.62	2.4	240	28	240	0.25	120
1722	4.39	8.64	2.7	240	28	240	0.75	240
1723	3.62	7.94	2.6	240	28	300	0.75	240
1731	3.81	7.57	3.6	240	28	240	0.75	180
1732	3.75	7.92	2.8	240	28	180	0.75	180
1739	3.24	7.05	3.5	240	28	240	1.25	240
1740	4.39	8.58	2.8	240	28	300	1.25	240
1753	3.26	7.19	3.2	180	28	180	0.25	180
1759	3.69	8.67	1.8	180	28	300	0.25	120
1763	3.73	7.78	3.1	180	28	240	0.75	240
1764	3.72	7.13	4.5	180	28	180	0.75	240
1767	3.09	7.00	3.2	180	28	180	0.75	180
1775	3.42	6.90	4.3	120	28	120	0.25	60
1776	3.38	7.17	3.5	120	28	60	0.25	60
1784	3.20	6.83	3.9	120	28	120	0.25	120
1789	3.33	6.98	3.8	120	28	120	0.75	60
1790	4.97	8.67	3.6	120	28	60	0.75	60
1792	4.97	8.16	4.7	120	36	120	0.75	180
1795	3.05	6.84	3.5	120	28	120	0.75	120
1796	4.80	8.64	3.4	120	28	120	1.25	60
1797	4.84	8.68	3.4	120	28	120	1.25	120
1803	3.23	7.06	3.4	60	28	60	0.25	60
1810	3.15	6.87	3.7	60	28	60	0.25	0

1811	3.12	6.72	4.0	60	28	0	0.25	0
1827	4.00	7.88	3.4	60	28	60	0.25	120
1833	3.04	6.60	4.0	60	28	120	0.75	60
1834	3.38	7.08	3.7	60	28	60	0.75	60
1835	3.07	6.80	3.6	60	28	0	0.75	60
1841	4.61	9.35	2.1	60	28	60	0.75	0
1849	4.91	9.57	2.2	60	28	60	1.25	60
1857	3.39	7.22	3.5	0	28	0	0.25	0
1860	3.30	6.14	5.0	0	28	0	0.25	300
1867	3.71	7.58	3.4	0	28	0	0.75	0
1869	4.48	8.73	2.7	0	28	0	0.75	300
1877	3.63	7.11	4.3	300	28	0	0.25	0
1883	3.26	6.63	4.6	300	28	0	0.25	300
1884	3.53	7.06	4.2	300	28	300	0.25	300
1889	3.58	7.35	3.6	300	28	0	0.25	240
1890	3.81	7.66	3.4	300	28	300	0.25	240
1898	3.53	7.49	3.2	300	28	240	0.75	300
1902	3.49	7.17	3.8	300	28	240	0.75	240
1924	4.93	10.58	1.3	240	28	300	0.25	0
1948	4.94	10.22	1.6	240	28	300	0.25	240
2001	4.68	10.18	1.4	60	28	60	0.25	0
2011	3.16	10.46	1.0	60	28	300	0.75	300
2038	3.83	12.99	1.0	300	28	300	0.25	240
2055	5.09	9.46	2.5	240	28	240	0.25	240
2057	5.08	9.61	2.3	240	28	240	0.25	180
2059	5.26	9.70	2.4	240	28	240	0.25	120
2061	5.20	8.71	3.9	240	28	240	0.75	240
2062	5.63	9.58	3.0	240	28	300	0.75	240
2063	5.12	9.48	2.5	240	28	240	0.75	180
2064	6.60	9.58	4.3	240	36	240	0.75	180
2065	5.41	9.61	2.7	240	28	240	0.75	120
2066	5.26	8.79	3.8	240	28	240	1.25	240
2067	6.00	9.28	4.0	240	36	240	1.25	180
2068	5.64	8.39	5.0	180	36	180	0.75	180
2069	6.35	9.46	4.2	180	36	300	0.75	180
2070	5.08	8.26	4.6	120	28	120	0.75	60
2071	5.52	8.82	4.2	120	28	120	0.75	120
2072	6.81	9.18	5.0	120	36	120	0.75	120
2073	5.20	9.76	2.3	60	28	60	0.25	0
2074	5.09	9.46	2.5	60	28	120	0.75	60
2075	5.13	9.32	2.8	60	28	0	0.75	0
2077	6.52	12.36	1.2	240	28	300	0.25	60
2080	5.63	14.22	1.0	240	28	300	0.25	0
2081	5.16	10.36	1.7	240	28	300	0.25	300
2084	5.60	10.40	2.0	240	28	240	0.25	240
2085	5.54	10.24	2.1	240	28	300	0.25	240
2088	5.87	10.43	2.2	240	28	240	0.25	180
2090	5.89	10.22	2.5	240	28	240	0.25	120
2093	7.07	11.59	2.1	240	36	300	0.75	300

2098	6.51	11.54	1.7	240	28	240	0.75	240
2101	5.78	10.41	2.2	240	28	240	0.75	180
2102	7.29	10.65	3.4	240	36	240	0.75	180
2106	5.15	10.11	1.9	60	28	60	0.25	0
2107	5.88	13.11	1.0	60	36	300	0.25	0
2108	5.57	10.81	1.6	60	28	60	0.25	180
2109	6.10	10.54	2.3	60	28	60	0.75	0
2110	6.97	11.33	2.3	60	36	60	1.25	60
2111	8.06	13.86	1.1	240	28	300	0.25	300
2112	7.54	12.85	1.4	240	28	300	0.25	240
2113	7.56	12.14	2.0	240	28	300	0.75	300
2114	8.06	11.67	2.8	240	36	300	0.75	300
2115	7.93	11.82	2.5	240	28	240	0.75	240
2116	7.56	11.70	2.4	240	28	240	0.75	180
2117	7.78	10.80	3.7	240	36	240	0.75	180
2118	7.94	11.71	2.6	240	36	300	0.75	180
2119	8.99	12.67	2.4	240	28	240	1.25	180
2120	8.29	11.05	3.8	240	36	240	1.25	180
2121	8.18	11.55	3.0	60	36	60	1.25	60

Table C.1: DLC 6.4. environmental input

C.2 Steel wire rope properties

Diameter [mm]	**MBL** kN	**Axial Stiffness** MN	**Dry Mass** [kg/m]
65	4553	416	21
68	4869	441	22.6
70	5344	484	24.8
73	5892	537	27.3
76	6416	584	29.7
79	7059	620	32.7
82	7635	671	35.4
86	8095	712	37.3
90	8706	766	40.1
92.5	9267	813	42.9
95.5	9917	870	45.9
98	10847	954	50.4
102	11558	1017	53.7
105.5	12071	1056	55.6
108	12814	1120	59
111.5	13675	1197	63.1
114	14468	1266	66.8
118	15177	1313	70.3
121.5	16008	1385	74.1
124	16760	1452	77.7
127	17631	1528	81.7
131	18300	1552	84.6
133	19204	1628	88.8
137.5	20542	1736	94.7
141	21509	1817	99.1
144	22259	1884	103
146.5	23257	1969	108
147.5	24259	2058	113
153.0	25302.0	2146.0	118
159.0	25463.7	2160.0	115
162.2	26207.3	2221.7	118
165.4	26951.0	2283.4	121
168.5	27694.6	2345.2	125
171.7	28438.3	2406.9	128
174.9	29181.9	2468.7	132
178.0	29925.6	2530.4	135
181.2	30669.2	2592.1	139
184.4	31412.9	2653.9	142
187.6	32156.5	2715.6	146
190.7	32900.2	2777.4	149
193.9	33643.8	2839.1	153
197.1	34387.5	2900.8	156
200.2	35131.1	2962.6	159

203.4	35874.8	3024.3	163
206.6	36618.4	3086.1	166
209.8	37362.1	3147.8	170
212.9	38105.7	3209.5	173
216.1	38849.4	3271.3	177
219.3	39593.0	3333.0	180
222.4	40336.6	3394.8	184

Table C.2: Steel wire rope properties (Bridon, 2011). Values are extrapolated after a tendon diameter of 155mm.